A STUDY OF UNCERTAINTY IN APPLICATIONS OF STATISTICAL ENERGY ANALYSIS

by

Adnan Dawood Mohammed

Institute of Sound and Vibration Research
Faculty of Engineering and Applied Science
University of Southampton

Thesis submitted for the degree of
Doctor of Philosophy

February 1990

Acknowledgments

I wish to express my sincere gratitude to my supervisor, Professor Frank J. Fahy. His wise guidance throughout this work, his care, patience and continuous encouragement made the completion of this thesis possible. The time he selflessly spent for me and the discussions on and beyond the particular subject are deeply appreciated.

Special thanks and appreciation are due to the Iraqi Government for giving me the opportunity of joining the University of Southampton and for the financial support.

Thanks are also extended to Dr. R. J. Pinnington and Dr. N. Ferguson for their many useful comments and suggestions.

Many thanks are due to ISVR technicians for their technical assistance throughout the experimental work of this project.

ABSTRACT

FACULTY OF ENGINEERING AND APPLIED SCIENCE
INSTITUTE OF SOUND AND VIBRATION RESEARCH

DOCTOR OF PHILOSOPHY

A STUDY OF UNCERTAINTY IN APPLICATIONS OF STATISTICAL ENERGY ANALYSIS

BY

Adnan Dawood Mohammed

Statistical Energy Analysis (SEA) is an approach to vibration analysis which provides estimates of the response of large and complex structures to broadband forces in terms of gross system parameters and simple explicit formulae. The penalty for the apparent simplicity of this approach is that the accuracy of response prediction for any individual practical system is subject to uncertainty. One source of uncertainty is purely physical and associated with variations in dimensions, damping, materials, force distributions, boundary conditions, etc., from the nominal values assumed in the models. The other source of uncertainty relates to the suitability of the coupled subsystems model employed, the validity of the SEA hypothesis as applied to the model, the choice of coupling loss factors, the centre frequency and the analysis bandwidth (i.e., the number of modes involved).

Since fine details of systems under analysis are not represented in the theoretical models, SEA may be considered to produce the ensemble average behaviour of a set of similar systems which have the same gross parameters but which differ from each other in detail. The practical justification for such an approach is that no physically realisable system corresponds exactly to any theoretical model, however detailed, and hence it is uneconomic and unrealistic to expend time and money on modelling of fine detail which only cause small variations about the ensemble mean. This is particularly true when many vibrational modes contribute to the total response of the system.

This thesis sets out to investigate the influence of perturbations of geometric subsystem parameters on power flow, energy levels and coupling loss factor as functions of subsystems modal densities, dissipation loss factors and analysis

bandwidth. Various cases of coupled, simple, multi-mode systems are investigated. The investigations are carried out by predicting the response of the coupled system, using exact analysis, and studying the sensitivity of the prediction to random perturbations of principal geometric parameters. The latter procedure is carried out by using the Monte Carlo method. The cases analyzed cover different spatially extended, coupled systems such as one-dimensional coupled systems (beams), two-dimensional coupled systems (plates) and a three-dimensional system (panel-box).

Results for the mean, the variance, and the confidence intervals for the frequency average values of the quantities of interest (power flow and coupling loss factor) are obtained across ensembles of similar systems as assumed in SEA. In addition, cumulative probability distributions for these quantities are presented. An empirical relationship which relates the variance of the coupling loss factor of coupled plates system to the modal overlap factor and the number of modes is also derived.

It is shown that the coupling loss factor derived from the analysis of energy flow between semi-infinite systems can grossly overestimate the actual coupling loss factor of the finite coupled systems when the average modal overlap factor of the coupled system is much less than unity. The discrepancy decreases as the modal overlap factor approaches unity. The estimates of coupling loss factor agree well with those obtained from the corresponding semi-infinite systems at high modal overlap. It is also shown that the variances of the coupling loss factor and of the power flow between subsystems associated with specific ranges of system perturbations decrease as the modal overlap factor increases. This is supported by the study of the cumulative distribution functions of the quantities above: the distributions approach normality with modal overlap. It is demonstrated on cases of coupling between a small subsystem and a large subsystem that only one subsystem needs to have a high modal overlap factor in order to obtain acceptable estimates for the coupling loss factor and the power flow. The numerical results are supported qualitatively by experimental investigations on coupled beams and coupled plates systems.

The most significant practical implications of the results of this investigation are that the application of conventional SEA to coupled systems of low modal overlap factor can greatly overestimate the transmission of energy from a directly driven subsystem to an undriven coupled system and that small variations in system parameters can produce large effects on system response.

TABLE OF CONTENTS

List of illustrations

CHAPTER 1

INTRODUCTION

Conventional analyses of structural and mechanical vibrations have been directed towards the lower few natural modes because these modes tend to have the greatest displacements, the highest stress levels, and are generally responsible for most gross structural failures. These analyses most commonly consist of determining the natural modes, and calculating the response of these modes to a specified excitation of interest, and of superposing these responses to determine the total structural response.

Continuous elastic structures have an infinite number of natural modes, but generally only a few of the lowest order modes can be reliably predicted by conventional theoretical and numerical analyses. At higher frequencies, and with broadband excitation, the use of conventional analysis becomes impractical and uneconomic, particularly for randomly excited, large, complex structures, and when the task is to predict structural fatigue, equipment failure or noise radiation. The reasons for this are: first, that the modes crowd together in broad frequency bands so that very large numbers of degrees of freedom need to be considered and therefore a great amount of expensive computation is required; second, the reliability of the modal response predictions decreases as the frequency increases (or as the vibration wave lengths become rather small and comparable with the size of structural details); and third, numerical accuracy decreases with mode order, even for rather idealized systems.

In the face of these difficulties it is frequently more appropriate to use statistical models and techniques to average out in a suitable way (over frequency bands, modes or populations of systems) the detailed modal behaviour. As the number of resonant modes in the frequency band of interest increases, the fluctuations in prediction of response due to small variations of system detail tend to diminish, making the average of the mean-squared response a quite reliable estimate. From the application point of view there is a need for statistical techniques. For example, mechanical and structural designers often need to make a response estimate at a certain stage of the design in order to qualify equipment and to design isolation, damping, or structural configurations to protect the equipment and to ensure the integrity of the structure. The

great detail of the structure is usually not known to the designer at this stage. Therefore a simple statistical estimate of the response that reveals parametric dependence is more appropriate.

Statistical Energy Analysis (SEA) is one of these statistical approaches to vibration analysis which has been developed over the past 30 years to deal with the broadband vibration problems of complex mechanical and acoustical systems. The word 'Statistical' expresses the fact that the ensemble of systems under analysis is presumed to be drawn from a population with random parameters. The word 'Energy' refers to the independent dynamical response variable which is common to the acoustical and mechanical systems; in principle, all other mean-squared quantities can be derived from it. Using the energy as the independent variable has an advantage that the total energy of an uncoupled subsystem equals the sum of the energies of the individual modes in that subsystem. Finally, the word 'Analysis' emphasizes that SEA is an approach to problems rather than an established engineering method, and allows the influences of the system parameters to be clearly revealed.

The general procedure of modelling in SEA regards complex mechanical systems to be composed of interconnected simpler elements (subsystems). Typically, these elements are idealized as beams, plates, acoustic cavities,etc. Each subsystem represents a group of similar oscillators (resonant modes) which form the energy storage elements of that subsystem (see appendix I). A subsystem is most simply characterized by its geometric boundaries and its material properties. There are no well-established criteria for the choice of subsystem boundaries. It is reasonable to suggest that an appropriate choice of boundaries would be at points or on surfaces, where freely propagating incident waves are substantially reflected. For any selected section of the system, there may be different classes of modes (e.g., flexural, torsional,etc.) that one may wish to identify and consider. Depending on the degree of coupling involved, these modes may be grouped together as one subsystem or they may be treated as separate subsystems. The next step is the evaluation of the following main quantities.

(a) Powers input to the energy storage elements by the external forces which operate on the different subsystems. These power inputs may be expressed in terms of certain input impedances for each subsystem.

(b) Powers dissipated in each subsystem which represent the vibrational energy lost by various mechanisms such as internal dissipation, friction at the boundaries and

acoustic radiation. This requires estimates of the dissipation loss factors of the subsystems.

(c) Powers transmitted from one subsystem to another which represent the rate of energy exchange between the different components. These may be expressed in terms of the impedances of the different subsystems at the interconnections or, alternatively, in terms of coupling loss factors which relate energy flow to stored energy. It is this latter form of relationship which forms the essential hypothesis on which SEA is based.

The quantities above represent the elements of the energy balance equations required for an SEA model. Energy levels of the different components of the coupled system can then be obtained by solving the set of linear, energy balance equations. A demonstration of the general procedure of SEA modelling and an explanation of the assumptions leading to the definition of modal average coupling loss factor are presented in appendix I.

Three different assumptions are made in the hypothesis of SEA. First, the average of power flow between two coupled multi-mode subsystems, excited by wide frequency band forces, is proportional to the difference in their average modal energies: this is an *ad hoc* extension of an exact relationship for two coupled oscillators. The proportionality constant is found to be dependent on the details of the geometry and the material properties of the coupled subsystems, but it is,in principle, independent of the type of excitation. Second, the rate of energy dissipation by a subsystem is proportional to the stored energy of that subsystem Third, the energy stored in a subsystem is distributed uniformly among the modes (equipartition of subsystem modal energy).

1.1 The Problem

Statistical Energy Analysis is an attractive approach because of the apparent simplicity of its general fundamental assumptions, described in the previous section, and its relatively simple manner of application to engineering problems. It provides estimates of the response of complex structures in terms of simple relationships, based upon a relatively simple description of system parameters, without going into the great detail as other (deterministic) approaches require. SEA leads to the concept of 'equipartition' of modal energy which serves as a first approximation for the prediction of component vibrational energies. For example it can be shown that, in a two

component system with only one of them directly driven, one obtains the maximum expected energy for the undriven component and the minimum for the driven one.

SEA estimates have been found to be (in general) more reliable and acceptable than those obtained from other approaches, especially at high frequencies, when the deterministic analysis of individual modes become less useful. But the crucial questions are: 'what are the criteria to quantify this reliability?', or, 'what uncertainty is associated with the prediction of the response when using this approach?'. These questions arise because of the fact that SEA is based on the concept of subsystems with random parameters in which the time-average response spectrum is calculated as an *average* across ensemble of similar systems. Such a spectrum, having been produced, is then integrated to give the total energy flow (or level), combining information from all frequencies. The answer is therefore probabilistic in nature and does not reveal the fine structure of frequency dependence of the response (i.e. no detail). Therefore, this answer is surely subject to some uncertainty. The degree of uncertainty will depend on many factors such as the range of variation of the dimensions of the coupled subsystems, the fabrication tolerances, the variations in the properties of the materials, the number of modes that are employed in the averaging process, uncertainties in the loss factors, and the modal densities (or the degree of modal overlap).

During the past 30 years most of the work carried out on SEA has been directed toward the prediction of the mean response of coupled systems. Very little attention has been given by the researchers to the problems of uncertainty of response estimates; namely, the variance, the associated probability distributions, and confidence limits. The present study was initiated in order to investigate this problem.

1.2 Literature Review

The development of Statistical Energy Analysis can be traced back to 1962 when Lyon and Maidanik [1] published one of the first papers that appeared on this subject. The paper described the result which forms the basis of SEA that the time-average power flow between two conservatively coupled, linear oscillators, excited by independent stationary white noise sources, is proportional to the difference in the average, uncoupled, energy levels of the oscillators. Their proof depended upon the linearisation of the power flow equations, on the basis of the smallness of the coupling force coefficients compared with the modal damping force coefficients.

Scharton and Lyon [2] first demonstrated that the power flow between randomly excited coupled oscillators is proportional to the difference between their actual time-average coupled energies. This proportionality is independent of the strength of the coupling if the oscillator energies are correctly defined. It was also found that the calculations needed to demonstrate the proportionality for two-oscillator systems become very tedious for an arbitrary system of even three oscillators. This was confirmed by Kakar [3] and Woodhouse [4].

The work on two coupled oscillators has been extended to cover the interactions of many modes in groups. Newland [5, 6] investigated the power flow between many oscillators for a special case of 'weak coupling'. The investigations have shown that there is a power flow-energy difference relationship between two sets of oscillators, which is analogous to the two-oscillator exact result, with the restriction that the external (modal) forces applied to the individual oscillators (modes) of each set are statistically independent. This result for mode group interactions has formed the basis of SEA hypothesis for the applications to the vibration analysis of coupled multi-mode structures. However, many exponents of the approach have assumed, without proof, that the power flow-energy difference relationship holds for any two subsystem, irrespective of the strength of coupling. The concept and the definition of weak coupling have been argued by many authors. One definition relates the strength of coupling between oscillators to the relative magnitude of coupling forces and the oscillator internal forces, or impedances [47, 48]. The other definition which appears to be more relevant is based upon the relative magnitude of the coupling loss factors and the internal loss factors of the coupled system [7, 4]. Coupling is weak if the ratio of the coupling loss factor to the internal loss factor of each oscillator is substantially less than unity.

The first attempt to apply the concepts of SEA to realistic structural systems was made by Lyon and Eichler [8]. They formulated and solved the problem of a simple oscillator attached to a plate, and then extended the basic ideas to beam-plate and plate-plate systems. For the second problem they applied the travelling wave method to the calculation of the coupling loss factor between the plates. They compared the measured coupling loss factor of the two plates with that obtained from the theoretical predictions. It was found that the agreement was good above a certain frequency where a reverberant wave field is well established. They explained the fall in the mean value in the lower frequency range as being due to a lack in the interacting mode pairs which are responsible for the power flow between the coupled subsystems. This result was also found by Gibbs and Gilford [36], when they compared the experimental observations

and the theoretical values of bending wave energies of coupled plates. They attributed this behaviour to the gradual breakdown of simple power flow concepts at low frequencies.

Lyon and Scharton [9] studied the vibration of three-element plate/beam/plate structures and the contribution of the different kinds of motions to the power flow. They found that the energy transfer is determined by beam flexure in the lower frequency bands, but that torsional motion contributed significantly at higher frequencies. In another paper [2] they studied the concept of the energy sharing process between the interacting modes in random vibration. They applied the coupled oscillator result to a simple coupled-beam example, in which two almost identical Euler-Bernoulli beams are lightly coupled together by a stiffness element. They calculated the coupling loss factor in three different modal cases and found that this factor was inversely proportional to the modal bandwidth or internal damping in the case of coinciding modal frequencies; proportional to internal damping in the case of modal frequency mismatch, but independent of damping when averaging over relative positions of the modes in frequency is carried out. They compared the different results of coupling loss factor with that obtained from the wave transmission calculation. They found that the results obtained by the statistical mode-location model were equivalent to those obtained from the travelling wave method, in that a finite structure behaves like an infinite structure when one performs an average over all possible locations of the modal resonance frequencies.

A large number of publications have followed, applying the concept of SEA hypothesis to engineering problems. The presentation of all the publications will not be given here, but instead only an outline of the work that is relevant to the present work. The reader may consult references [10, 11, 12, 13] where virtually all significant works until 1986 are summarized.

Davis [14, 15] gave the exact solution for the response of two coupled beams, utilizing two different coupling configurations, namely, translational and rotational springs. He discussed extensively the effects of the coupling element on the modal properties and the modal density of the coupled system. Cases of weak and strong couplings were also examined. In another paper [16], he discussed the random vibration of two beams strongly coupled at discrete points. He found that the weak coupling case is an asymptotic case of the general problem.

Davis and Wahab [17] developed an exact mathematical model for a beam with three simple supports subjected to randomly distributed, random loads (Rain-On-The-Roof). The loads on the two beam sections are independent. For this case it was proved that the power exchange was proportional to the uncoupled modal energies. The model enabled the investigation of the effects of various parameters such as damping level and modal overlap. They demonstrated that the results for the averaged, normalized power flow in an ensemble of 'similar systems' approached that obtained from the travelling wave method (SEA estimate) at high modal overlap. They also found that this average is much lower than the SEA estimate when low damping levels were introduced. This latter conclusion is confirmed by the present study.

Davis and Khandoker [18] extended the previous work of coupled beams to a case when one of the beams is driven by a point random force while the other one is driven indirectly. Similar conclusions to that of the previous work were obtained. In addition the dependence of the power flow on the position of the excitation is clearly exhibited in this paper.

Remington and Manning [19] obtained an SEA type solution for the longitudinal power flow between two rods. The results were compared with the broad band frequency averaged exact calculation. It was found that the agreement was fairly good for both strong and weak couplings. Note that the weak coupling assumption had been almost universally employed in the first few years of SEA history.

Using coupled plates as their model, Bies and Hamid [20] determined experimentally the coupling loss factor by the power injection method. They compared the results to an approximate solution by the travelling wave method [8] and found that large discrepancies are occuring at low frequencies. They also demonstrated the effect of the number of the observation positions on the above comparison.

Boisson, Guyader and Lesueur [21] presented a theoretical analysis of power flow based upon coupled system modes (energy influence coefficients) for different configurations of coupled plates. General expressions were obtained for the vibrational energies of the coupled structures. In a more recent paper [22], they compared their numerical results (energy ratio of L-shaped coupled plate systems) with those obtained by applying SEA. They found that SEA overestimates the prediction of energy ratio (a difference of 5 dB) at low frequencies (when the modal overlap factor is very small). Larger discrepancies between the two estimates were reported under the conditions of point excitations.

Keane and Price [23] investigated the underlying assumption of SEA theory and showed how it may be developed to cope with a problem involving strongly coupled subsystems with low modal densities. The discussion given in this paper is restricted to the problems that may be modelled by two, point spring coupled multi-mode subsystems and for these the effects of coupling strength and modal density were examined in detail. The paper also shows how the fundamental results of SEA may be recovered in the case of weak coupling and high modal density.

Dimitriadis and Pierce [24] presented analytical expressions for the power flow and the vibrational energies of a two strongly coupled, simply supported plates system. Numerical results for coupling loss factor, energy ratio, and modal density ratio were compared with those obtained by using SEA. The results suggest that SEA becomes progressively better with increasing frequency and internal damping.

Sun, Lalor, and Richards in two companion papers [25, 26] presented the theoretical and experimental analysis of non-conservatively coupled plates, excited by broad band random forces. They extended the work which had been done by Fahy and Yao [27] on of the power flow between non-conservatively coupled oscillators. The investigations have shown that the forms of the modified energy balance equations are the same as those used for the conservatively coupled systems, but the terms involving both internal loss factors and coupling loss factors are altered because of the introduction of coupling damping. They also found that the effect of the coupling damping on the power flow between the coupled plates is negligible. More recently, Sun and Ming [28] found that the coupling damping has an effect upon the power flow between coupled subsystems; the greater the coupling damping, the less the power flow. Note that this conclusion conflicts with their first finding mentioned above.

Work on the interaction between mechanical structures and acoustic fields has been widely studied. Lyon and Maidanik [1] applied the coupled oscillator, energy flow theory to a structure-reverberant acoustic field problem. Using this model, the steady-state partition of energy between the two systems and the parameters (namely the radiation and internal resistances) which govern this partition are computed. Experiments on a beam in a reverberant room were also conducted. A satisfactory agreement between the measurements and the theoretical predictions was found.

Maidanik [29] applied the above approach to the problem of a ribbed panel in a reverberant acoustic field. The analysis showed that the acceleration spectrum of the vibrational field was related to the pressure spectrum by a coupling factor which is a

simple function of the radiation and mechanical resistances of the structure. The radiation resistance of the ribbed panel was studied as a function of frequency. The results of experiments which were conducted to test the theory were reported. The agreement between theory and experiments was shown to be satisfactory.

Fahy, in two comprehensive papers [30, 31], studied the vibration of containing structures by sound in the contained fluid. He analyzed a system which consists of a rigid rectangular box with one simply supported flexible wall. He obtained numerical and statistical type results for the internal Acousto-Structural mode coupling factors and the corresponding modal average radiation efficiency. A lower limiting frequency was found, above which the radiation efficiency of the panel is equal to that of a baffled panel radiating into free-field conditions, but below which the radiation efficiency falls below the free field value. Measurements have confirmed the existence of the lower limiting frequency. This was also observed in the case of the cylindrical shell. The modelling procedure described in the first paper [30] is followed in the work presented in Chapter 6 of this thesis.

There is very little literature concerning the uncertainty of SEA predictions. The earliest was a treatment by Lyon [11], who discussed the dependence of the variance of the response on the uncertainties in the modal energy of subsystems, the coupling strength, the actual number of resonant modes and the response observation positions.

1.3 The Aims of the Work and the Approach Used

Vibration analysis of continuous systems is subject to uncertainties arising from two main sources. These are [32, 33]

(a) Uncertainties which are associated with variations in geometry, material properties, force distributions and boundary conditions from the nominal values assumed in the theoretical models.

(b) Uncertainties which relate to the accuracy of the modelling, the validity of the hypotheses and the type of analysis employed.

In addition to the effects of the above sources of uncertainties, Statistical Energy Analysis response estimates may also be affected by the uncertainty which originates

from the width of the analysis frequency band and the centre frequency of the band (i.e., the number of modes involved).

Since SEA models represent only the gross properties of the class of systems modelled, individual realizations of systems will differ in their behaviour from SEA prediction. Therefore, it is vital for users of SEA to be able to estimate the probability distribution and the confidence limits for such variations.

The degree of sensitivity of the dynamic behaviour of structures to parameter variations is of great importance to the structural designers. In particular, it is essential to determine if the small perturbations can result in significant changes in the responses of the structures under investigations (e.g, resonance tuning/detuning).

The principal objective of this work is to study the uncertainty of the predictions made by the application of Statistical Energy Analysis in terms of perturbation of subsystem geometry. This is achieved by analyzing various cases of multi-mode coupled systems using exact calculations and establishing the influence of the perturbations of the structural parameters on the sensitivity of the predictions of the quantities of interest in SEA. Such quantities are the time-average power flow and the coupling loss factor.

The sensitivity analysis of the predictions is carried out by employing the Monte Carlo technique [34]. An ensemble of similar systems is generated by random perturbations of one of the (input) structural variables of the coupled system under study. The input variable is assumed to have a normal distribution with a known mean and standard deviation. The normally distributed sample of the input variable is used in computing the frequency-average quantities of interest for each element in the system sample. Due to computation limitations, the size of the samples of the frequency-average quantities investigated is limited to 32 elements. This number is justified as being adequate according to the argument of Hodges and Woodhouse [58, 59], that the frequency averaging has a somewhat similar effect to including many more configurations (i.e., large sample) of the system under investigation.

The analysis will involve the calculations of the mean and the variance across the generated ensembles of the frequency averaged quantities of interest. The variance gives an idea of how the behaviour of our individual systems may deviate from the average system. If the deviation is a small fraction of the mean, we know that most realizations of the system will have a response that is close to the mean, which is

therefore of practical utility, while if the deviation is equal to the mean or greater, the probability that any realization is close to the mean will be small and the mean will lose its worth as an estimate. Confidence intervals for the means, which define the probabilities that one estimate lies in a given range or is less than a certain value, will also be presented.

The deviation or the scattering of the response data is demonstrated and judged by establishing the cumulative probability distribution curves. These curves are compared with each other for different values of a selected structural parameter such as damping or modal density (or modal overlap).

Some experiments are made on physical coupled systems, but the labour and time involved in realizing many perturbations precluded a more comprehensive experimental study.

1.4 Thesis Arrangement

The chapters of this thesis are arranged as follows. Two models of coupled beams are analysed in Chapter 2. The first model treated a case of coupling between two long beams, while the second one describes the analysis of interaction between a beam of high modal density (long) and another of low modal density (short). The latter model is analysed because Statistical Energy Analysis is quite frequently applied to systems with such characteristics.

Chapter 3 presents experimental work on two coupled multi-mode beams and also experimental work on two short beams. The latter case represents a coupling of only two resonant modes.

Chapter 4 describes the analysis of two coupled plates. A similar approach to that for the two coupled beams is used.

Chapter 5 deals with the analysis of two coupled rods. This simple system is studied to explain some of the conclusions which are drawn from the previous chapters and have importance in the analysis of all coupled structures.

Chapter 6 presents the analysis of coupling between a structure and an acoustic cavity. Statistical results for the panel radiation efficiency, which is proportional to the coupling loss factor, are presented.

Chapter 7 presents the experimental work on two coupled plates. The tests contain the measurements of energy ratio of the coupled plates and the sensitivity of the measurements to perturbations of the coupled system.

Conclusions are drawn and recommendations for future work made in Chapter 8. It is hoped that the present work will be helpful for future studies of Statistical Energy Analysis.

CHAPTER 2

POWER FLOW BETWEEN COUPLED BEAMS

2.1 Introduction

This chapter deals with the theoretical predictions of the time averaged response (namely, input power, power flow, and total energies) of two coupled beams to a random point force applied to one of them. An exact solution for the mathematical model of the problem is presented using the progressive wave approach. The beams under investigation are long cantilevers coupled at their free ends via a non-conservative, linear coupling. The predicted time averaged quantities are used to derive SEA parameters using the SEA relationship. The derived parameters are used to establish a statistical model with the aid of the coupled system perturbations and the use of the Monte Carlo technique.

A modified case of a long-short beam system is also analyzed which represents modal interactions between only one resonant mode of the short beam with the many resonant modes of the long beam in the frequency band of interest.

A comparison between the predicted results from the above cases and those obtained from the corresponding infinite model are made. In addition, results for the variance, confidence intervals for the means and the probability distributions of the predictions are also reported.

2.2 Two Coupled Beams; Mathematical Model and Assumptions

The differential equation for a bending wave in an undamped beam is of the form

$$B \frac{\partial^4 w(x)}{\partial x^4} + m' \frac{\partial^2 w(x)}{\partial t^2} = 0 \ , \qquad (2.1)$$

where w is the lateral displacement of the beam, B = YI is the bending stiffness of the beam, Y is the Young's modulus of elasticity, I is the second moment of area of cross section, m' is the mass per unit length and x represents the distance along the beam span.

Equation (2.1) is known as the Euler-Bernoulli equation which does not include the rotational inertia effects. It is shown [35] that when the bending wave length is large compared to the thickness of the beam, then these effects may be neglected. Since the present analysis is restricted to frequencies where the wave length is much larger than the thickness of the beams, this approximation may be considered as reasonable.

A possible solution to equation (2.1) may take the form

$$w(x,t) = W(x)\, e^{j\omega t} \ , \qquad (2.2)$$

which is a harmonic variation with time, (j denotes $\sqrt{-1}$). The substitution of this solution in equation (2.1) gives

$$B \frac{\partial^4 W(x)}{\partial x^4} - m' \omega^2 W = 0 \ , \qquad (2.3)$$

where ω is the frequency of vibration in radians per second. A solution of equation (2.3) is

$$W(x) = A_n\, e^{\beta_n x} \ , \qquad (2.4)$$

where

$$(B \beta_n^4 - m' \omega^2)\, A_n = 0 \ . \qquad (2.5)$$

Let $\beta_n = k$, where k is the bending wave number which is given by

$$k = \omega^{1/2} \left(\frac{m'}{B}\right)^{1/4} \quad .$$

Equation (2.5) provides four possible solutions, i.e.,

$$\beta_n = k, -k, jk, -jk \quad , \qquad (2.6)$$

which means that we will obtain terms of the form $e^{\pm jkx}$ which describe travelling waves along the beam which may transport energy. The speed of propagation of these type of waves is given by

$$C_b = \omega^{1/2} \left(\frac{B}{m'}\right)^{1/4} \quad ,$$

which is clearly a function of frequency. Therefore the bending wave is described as a 'dispersive wave'. Also, we will obtain terms of the form $e^{\pm kx}$ which represent distortion fields (evanescent fields) that decrease exponentially with the distance x from a discontinuity or the boundary. The evanescent fields decrease 2π Nepers per wave length; therefore they are of considerable importance only in the immediate vicinity of the discontinuity.

The total solution to the bending wave equation may now be written as

$$w(x,t) = (A_1 e^{-jkx} + A_2 e^{+jkx} + A_3 e^{-kx} + A_4 e^{+kx}) e^{j\omega t} \quad , \qquad (2.7)$$

where A_1-A_4 are the wave amplitudes of the different waves present. This solution is known as 'the progressive wave solution' which satisfies the boundary conditions of

the beam. A standing wave, or normal mode, may be regarded as a set of travelling waves which constructively interfere to form the nodes (points of zero deflection) or the antinodes of the vibrating beam.

Figure (2.1.a) shows two Euler-Bernoulli cantilever beams coupled at one point by a non-conservative, linear coupling element (damped translational spring). The coupling element has a stiffness K_c and dissipation loss factor η_c. It is represented by

$$\tilde{K}_c = K_c (1 + j\eta_c) \ .$$

Transverse vibration of beam 1 is generated by a point harmonic force. The force is located at a given position along the span of the beam. Vibrational energy is transmitted from beam 1 to beam 2 by a shear force and velocity at the coupling point.

The coupled beam system may be divided at the discontinuities into three simple beams (see figure (2.1.b)). The flexural motion of the free vibration of each beam is governed by the bending wave differential equation (2.1). It has been shown [36] that the consideration of wave types other than bending waves does not significantly affect the prediction of bending wave energy. The progressive wave solution (equation (2.7)) can now be used to obtain the exact, bending, displacement response of the different parts of the coupled beam system. This solution can be written as

$$w_I(x_1,t) = (A_1 e^{-jk_1x_1} + A_2 e^{+jk_1x_1} + A_3 e^{-k_1x_1} + A_4 e^{+k_1x_1}) e^{j\omega t} \ ,$$

$$w_{II}(x_2,t) = (A_5 e^{-jk_1x_2} + A_6 e^{+jk_1x_2} + A_7 e^{-k_1x_2} + A_8 e^{+k_1x_2}) e^{j\omega t} \ , \quad (2.8)$$

$$w_{III}(x_3,t) = (A_9 e^{-jk_2x_3} + A_{10} e^{+jk_2x_3} + A_{11} e^{-k_2x_3} + A_{12} e^{+k_2x_3}) e^{j\omega t} \ ,$$

where w_I , w_{II}, and w_{III} are the displacement responses of beams I, II, and III respectively. A_1 to A_{12} are the wave amplitudes, k_1 and k_2 are the flexural wave numbers of the coupled beams, and ω is the frequency of vibration. Equations (2.8)

satisfy the geometric and the natural boundary conditions at the excitation position, the coupling point, and the clamped ends of the coupled beams.

Beam damping is taken into account by assuming a complex Young's moduli i.e., $\tilde{Y}_i = Y_i (1 + j\eta_i)$, for $e^{j\omega t}$ time dependence, where η is the dissipation loss factor of the beam material and i = 1,2, represents the beam number. The friction losses modify the factor $\frac{B_i}{m_i'}$ to $\frac{B_i(1+j\eta_i)}{m_i'}$ in the differential equations of the coupled beams. The introduction of the damping leads to a complex representation of the bending wave numbers and the bending wave speeds. The latter two parameters can now be written respectively as

$$\tilde{k}_i = \omega^{1/2} \left(\frac{m_i'}{B_i(1+j\eta_i)}\right)^{1/4} ,$$

or

$$\tilde{k}_i = k_i \left(1 - \frac{j\eta_i}{4}\right) , \qquad (2.9)$$

and similarly,

$$\tilde{C}_{b_i} = C_{b_i} \left(1 + \frac{j\eta_i}{4}\right) . \qquad (2.10)$$

The complex wave number representation leads to the so-called complex evanescent (nearfield) waves. This result appears to have no physical meaning (as near waves do not transport energy). However, Tamm and Weis [60] have shown that such complex nearfields occur very often at high frequencies. Therefore, we do not feel that this is a problem in the present work.

The magnitude of each wave which is present in each simple beam is given by the complex coefficients $\tilde{A}_1$ - $\tilde{A}_{12}$ and these are found by substituting the general

solution (equations (2.8)) into the boundary conditions which apply to the discontinuities of the coupled beams. These boundary conditions are

$$\tilde{w}_I(L_1) = 0, \qquad \tilde{w}'_I(L_1) = 0, \qquad \tilde{B}_1\tilde{w}''_I(0) = \tilde{B}_1 w''_{II}(L_2)$$

$$\tilde{B}_1\tilde{w}'''_I(0) = \tilde{B}_1\tilde{w}'''_{II}(L_2) + \tilde{F}, \qquad \tilde{w}_I(0) = \tilde{w}_{II}(L_2), \quad \tilde{w}'_I(0) = \tilde{w}'_{II}(L_2),$$

$$\tilde{B}_1\tilde{w}''_{II}(0) = 0, \qquad \tilde{B}_2\tilde{w}''_{III}(L_3) = 0\ , \qquad \tilde{w}_{III}(0) = 0, \quad \tilde{w}'_{III}(0) = 0,$$

$$\tilde{K}_c(\tilde{w}_{II}(0) - \tilde{w}_{III}(L_3)) = -\tilde{B}_1\tilde{w}'''_{II}(0), \quad \tilde{K}_c(\tilde{w}_{II}(0) - \tilde{w}_{III}(L_3)) = -\tilde{B}_2\tilde{w}'''_{III}(L_3)\ ,$$

where (') denotes a spatial derivative. Note that the bending moments at the coupled ends of the beams are assumed to be zero (i.e., no rotation) because the calculations are carried out in a low frequency range.

After employing the above twelve boundary conditions, the unknown complex coefficients are related through a set of twelve simultaneous linear equations which have the matrix form

$$\begin{bmatrix} \tilde{a}_{11} & \tilde{a}_{12} & \tilde{a}_{13} & \tilde{a}_{14} & \cdots & \tilde{a}_{1N} \\ \tilde{a}_{21} & \tilde{a}_{22} & \tilde{a}_{23} & \tilde{a}_{24} & \cdots & \tilde{a}_{2N} \\ \vdots & & & & & \\ \tilde{a}_{N1} & \tilde{a}_{N2} & \tilde{a}_{N3} & \tilde{a}_{N4} & \cdots & \tilde{a}_{NN} \end{bmatrix} \begin{Bmatrix} \tilde{A}_1 \\ \tilde{A}_2 \\ \tilde{A}_3 \\ \tilde{A}_4 \\ \vdots \\ \tilde{A}_N \end{Bmatrix} = \begin{Bmatrix} \cdot \\ \cdot \\ \cdot \\ \tilde{F} \\ \cdot \\ \cdot \\ \cdot \end{Bmatrix}\ , \quad (2,12)$$

where N is the number of equations. Each row in the matrix equation corresponds to a given boundary condition.

Equation (2.11) is solved using a routine from the NAG-library with an IBM 3090 computer [37]. The routine gives an approximate solution for the equations using Crout's factorisation method. The time taken to perform the analysis is proportional to N^3.

Once the complex coefficients are obtained, the displacement of the coupled beams can be computed at any point along the coupled system and hence the time averaged quantities of interest can be predicted. These quantities are the injected power, the power flow, and the total energies of the beams. The frequency response curves of these quantities which are evaluated at individual frequencies are integrated (over the frequency band of interest) to give the band (equivalent white noise) quantities [11]. The justification for adding frequency components came from the fact that power quantities do not involve phase.

2.2.1 Calculation of input power

The input power is one of the quantities that is presumed known in SEA calculation. If the sinusoidal force $\tilde{F} = |F_o| e^{j\omega t}$ acting at the point $x_1 = 0$ ($x_2 = L_2$), (see figure (2.1.b)), of the driven beam (1) which has the point mobility $\tilde{H} = |H_o| e^{j\phi}$, causes a velocity of $\tilde{V}_d = |V_o| e^{j(\omega t+\phi)}$ at that point. Where ϕ is the relative phase of the velocity $\tilde{V}_d$ with respect to the force $\tilde{F}$ which is the phase of the mobility function $\tilde{H}$. The time averaged (averaged over a long time) input power is given by

$$\bar{P}_{in} = 1/2\ |\tilde{F}|\,|\tilde{V}_d| \cos\phi \ , \qquad (2.12)$$

$$= 1/2\ |\tilde{F}|^2\, Re\{\tilde{H}\} \ ,$$

$$= 1/2\ |\tilde{V}_d|^2\, Re\{\tilde{Z}\} \ ,$$

where $\tilde{V}_d$ is given by

$$\tilde{V}_d = j\omega\, w_I(0) \quad .$$

$\tilde{Z}$ is the point impedance, * denotes a complex conjugate, and Re{ } denotes a real part.

2.2.2 Calculation of power flow

The vibrational energy is transmitted from the driven beam (1) to the receiver beam (2) by means of the shear force and velocity at the coupling point. By using a similar formula to that for the injected power, the time averaged power flow is given by

$$\bar{P}_{12} = 1/2\ \mathrm{Re}\{\tilde{S}_{III}(L_3).\tilde{V}^{*}_{III}(L_3)\} \quad , \qquad (2.13)$$

where $\tilde{S}$ and $\tilde{V}_{III}$ are the shear force and the velocity at the coupled end of the receiver beam, respectively. The shear force can be written as

$$\tilde{S}_{III} = \tilde{K}_c\ \{\tilde{w}_{II}(0) - \tilde{w}_{III}(L_3)\} \quad . \qquad (2.14)$$

The time averaged power flow can now be written as

$$\bar{P}_{12} = 1/2\ \mathrm{Re}\{j\,\omega\,\tilde{K}_c\,|\tilde{w}_{III}(L_3)|^2 - j\,\omega\,\tilde{K}_c\,\tilde{w}_{II}(0).\tilde{w}^{*}_{III}(L_3)\} \quad (2.15).$$

2.2.3 Calculation of total energy

It is useful to introduce the vibrational energy content of the simple resonator before discussing the calculation of energies of the coupled beams model. The equation of motion of free damped vibration of a simple, linear oscillator of mass m_r and stiffness K_r is

$$\ddot{y} + \omega_o \eta_r \dot{y} + \omega_o^2 y = 0 \ , \qquad (2.16)$$

where y represents the displacement, $\omega_o = \sqrt{K_r/m_r}$ is the natural frequency and η_r is the dissipation loss factor. If we assume a form of solution $y(t) = Ce^{\beta t}$ we find that

$$\beta = -\frac{1}{2}\ \omega_o \eta_r \pm j\, \omega_d \ ,$$

where

$$\omega_d = \omega_o \sqrt{(1 - \eta_r^2/4)} \ .$$

The solution for the displacement y(t) is then

$$y(t) = A\, e^{-(1/2)\, \omega_o \eta_r t} \sin(\omega_d t + \theta) \ , \qquad (2.17)$$

where A is the initial amplitude of vibration. In this case the oscillation occurs at radian frequency ω_d and the amplitude of the oscillations decreases exponentially in time due to the extraction of energy by damping. If the loss factor η_r is small, then ω_d is very nearly equal to ω_o and the period of the damped oscillations is essentially the same as that for undamped oscillations.

The potential energy of vibration in this case is

$$(PE)_r = \frac{1}{2} K_r y^2 = 1/2\ K_r A^2 e^{-\omega_o \eta_r t} \sin^2(\omega_d t + \theta) \ , \qquad (2.18)$$

and the kinetic energy is

$$(KE)_r = \frac{1}{2} m_r \dot{y}^2 \ ,$$

$$= \frac{1}{2} m_r A^2 \omega_o^2 e^{-\omega_o \eta_r t} \left[\left(\frac{\omega_d}{\omega_o}\right) \cos(\omega_d t + \theta) + 1/2\ \eta_r \sin(\omega_d t + \theta) \right]^2 \qquad (2.19)$$

The time averaged quantities of potential energy and kinetic energy can be obtained by averaging equations (2.18) and (2.19) over one complete period of vibration. They can be written approximately as

$$(\bar{PE})_r = \frac{1}{4} K_r A^2 e^{-\omega_o \eta_r t} = (\bar{KE})_r = \frac{1}{2} (\bar{E})_r \quad . \qquad (2.20)$$

Thus, the time averaged kinetic and potential energies of a simple resonator are both equal to one half of the energy of vibration ($(\bar{E})_r$).

The time averaged energy of a beam may be calculated as follows. For a simple beam element having a length δx and a mean squared velocity $\bar{V}^2(x)$, the time averaged kinetic energy $\delta\bar{T}$ may be written as

$$\delta\bar{T} = \frac{1}{2} (m'\delta x)\, \bar{V}^2(x) \quad ,$$

where m' is the mass per unit length of the beam. $\bar{V}^2(x)$ may be written as

$$\bar{V}^2(x) = \frac{1}{2} \mathrm{Re}\{\tilde{V}(x) \,.\, \tilde{V}^*(x)\} \quad ,$$

therefore

$$\delta\bar{T} = \frac{1}{4} \omega^2 m' \,\mathrm{Re}\{\tilde{w}(x) \,.\, \tilde{w}^*(x)\} \quad .$$

For a beam of length l, the total kinetic energy is

$$\bar{T} = \frac{1}{4} m' \omega^2 \int_0^l Re\{w(x) \, . \, w^*(x)\} \, dx \quad . \qquad (2.21)$$

By using the approximation that only the resonant modes are contributing to the energy content in the frequency band of interest, and by employing the result of the simple oscillator energy (equation (2.20)), the time averaged total time averaged energy of the beam may be predicted to be twice the time averaged kinetic energy, i.e.,

$$\bar{E} = 2\bar{T} \quad .$$

The coupled total energies of the beams under investigation can easily be evaluated after the substitution for the displacement functions in equation (2.21). The integration over the beam length is carried out numerically by employing a routine which uses the Gauss 30-point and Kronrod 61-point rules [38].

2.3 Modal Density and Modal Overlap

The modal density of an elastic system can be defined as the expectation of the number of resonance frequencies per unit frequency interval. Modal density can either be measured or predicted using theoretical formulae (see references [10], [39], and [40] for these formulae). The measurement may in principle be done by exciting the structure with a pure tone and gradually varying the frequency. From the resultant frequency response curve the number of modes can be simply counted [41]. Although this method is simple to use, it has serious disadvantages. First, the magnitudes of the various peaks depend upon the positions of the driving point and the response measurement transducer. Second, at higher modal densities the mode count becomes difficult and one may miss some modes because of their closeness in frequency. Finally, there are no available criteria for the identification of the resonant peaks and hence measurement of the modal density with an acceptable degree of accuracy. An alternative experimental technique for measuring the modal density of a spatially uniform system is based upon the measurement of the frequency-average value of the

real part of the input mobility of the structure and the relationship between the latter parameter and the modal density [35].

Theoretical prediction of the modal density is considered to be a more accurate and reliable technique than the experimental one because of the experimental difficulties which are involved in the measurements. Reference [39] illustrates the formulae for the modal densities of some uniform elastic systems which are based on the calculations in reference [40]. Some of these formulae can be found in Appendix II. Note that these formulae apply strictly to frequencies which are considerably greater than the system fundamental natural frequency.

The expression for the modal density of a beam can be obtained by considering the values of bending wave number k_b which correspond to the natural modes of that beam. The number of modes below any value k is given by

$$N(k) = k/(\pi/l) = kl/\pi \ , \qquad (2.22)$$

and the modal density in k is given by

$$n(k) = dN(k)/dk = l/\pi \ . \qquad (2.23)$$

The modal density in frequency is found by the simple transformation

$$n(\omega) = n(k)\ (dk/d\omega) = l/(\pi C_g) \ , \qquad (2.24)$$

where C_g is the group velocity and is given by

$$C_g = d\omega/dk = 2\ C_b \ ,$$

where C_b is the bending wave speed; therefore,

$$n(\omega) = \frac{l(\omega\,\Gamma C_l)^{-1/2}}{2\pi}\ , \qquad (2.25)$$

where Γ is the radius of gyration of the cross section of the beam and C_l is the longitudinal wave speed. The modal density equation may also be written as

$$n(f) = (2\pi)^{-1/2}\, l\, (m'/B)^{1/4} f^{-1/2}\ , \qquad (2.26)$$

where B is the bending stiffness for a homogeneous beam and f is the frequency of vibration in Hz.

Equation (2.26) is used to calculate the modal density of the individual beams in the coupled beam system under consideration. In the high frequency range where the finite thickness effect becomes important, the beam will have an increasing modal density. However, in the low frequency range the modal density is relatively low and decreases with increasing frequency.

The modal overlap factor is a measure of the average separation between resonance frequencies in relation to the average modal bandwidth. Modal bandwidth ($\eta\omega$) can be defined as the frequency difference between the points at which the input power to a single resonator reaches half (3 dB down) its maximum value. The modal overlap factor (M) can be written as

$$M = \frac{\eta\,\omega}{\delta\omega}\ ,$$

or

$$M = n(\omega)\,\eta\,\omega\ . \qquad (2.27)$$

where $\delta\omega$ is the average frequency separation between adjacent resonance modes of the vibrating system. The modal overlap factor has been found to have a significant influence on the reliability of SEA calculations [41], a conclusion which is confirmed by the work presented in this thesis.

2.4 Perturbation Analysis

In order to create a statistical model for the quantities of interest in SEA, the mathematical model of the problem (described in section 2.2) is adopted. Long beams, having relatively high modal densities are used. The dimensions and properties of the beams and the coupling element are described in the table below.

Length (mean)	Beam 1 Beam 2	3.68 m 3.58 m
Width	Beam 1, 2	0.025 m
Thickness	Beam 1 Beam 2	0.003 m 0.002 m
Material	Beam 1, 2	Steel
Young's modulus	Beam 1, 2	1.95E+11 N/m^2
Density	Beam 1, 2	7700 Kg/m^3
Modal density $n(f)$	Beam 1 Beam 2	0.142 Mode/Hz 0.169 Mode/Hz
Coupling stiffness (K_c)		1.3E+4 N/m
Coupling dissipation loss factor (η_c)		0.15

Figures (2.2)-(2.5) display typical frequency distributions for the input power, power flow, and total energies of the coupled beams which are due to a point harmonic force located on the first beam. The figures show about 14 modes having natural frequencies in a frequency band of 50 Hz centered at 25 Hz (the calculations are carried out at each 0.1 Hz to ensure good frequency resolution). This number of resonant

modes is quite sufficient from the statistical point of view to obtain reliable averages for the predicted quantities. The main reasons for choosing the above mentioned frequency band are as follows; first, it is suitable for producing a relatively high modal density for the coupled beam system and hence provide the above mentioned number of resonant modes; second, higher frequency bands, with the selected beams lengths, above, will cause computing problem (namely, arithmetic overflow) when solving the system matrix equation.

In order to investigate the sensitivity of the computation of the quantities of interest to small alterations in one of the structural parameters, the Monte Carlo statistical method [43] is considered in the present work. This method can be defined in a wide sense as any technique that can be used for the generation of statistical distribution of a model using random parameters. One of the widely used applications of the Monte-Carlo method is known as 'the distribution sampling'. The purpose is to find the distribution, or some of the parameters of the distribution, of a certain random variable. This variable, that we call 'the output variable', is a known function of one or more other random 'input variables' which have a known statistical distribution. To estimate the distribution of the output variable we draw a value for each of the input variables and calculate the resulting output variable. Such sampling is then repeated many times and this yields an estimate of the distribution.

The distribution sampling application is adopted in the present analysis as follows: the length ratio (l_1/l_2) of the coupled beams is chosen as the input random variable for the purpose of perturbation analysis of the coupled beams system under study. A sample of 32 elements of (l_1/l_2) is drawn randomly from a normally distributed random population [44]. The generated sample has known values of mean and standard deviation which provide a coefficient of variation of 10% of the mean length ratio of the coupled beams. For each given value of (l_1/l_2), the time averaged quantities of input power, power flow, and total beams energies of the coupled system are calculated, as described in the previous sections, and the results are then integrated over the frequency range of interest (1-50 Hz) to simulate the response to a band of white noise. The computations are carried out for ten, randomly selected, points of excitation and the results are then averaged over the selected points. The reason for exciting the system at different points is to approximate the requirement of 'uncorrelated excitations' for the purpose of SEA. The effects of force position on the prediction is discussed in a subsequent chapter.

The computed quantities above form ensembles having the size of 32 elements. Each element in these ensembles represents an observation (output random variable) from one realization of the coupled beams system. Note that the produced ensembles of $\bar{P}_{in}$, $\bar{P}_{12}$, $\bar{E}_1$, and $\bar{E}_2$ are for a given value of internal loss factors of the coupled beams, i.e., for a given value of average modal overlap factor (M_{av}). The latter parameter is calculated as

$$M_{av} = \sqrt{M_1 M_2} \quad , \tag{2.28}$$

where M_1 and M_2 are the average modal overlap factors of beam 1 and beam 2 respectively. This is an *ad hoc* relationship which is justified by the fact that M_1 and M_2 are almost similar. The process of calculations described above is then repeated for different M_{av} values to study the effect of the latter parameter on the sensitivity of the predictions. The different values of the average modal overlap factor of the coupled beams are obtained by assuming different values of dissipation loss factors η_1 and η_2. An attempt to obtain the different values of M_{av} by assuming different modal densities for the coupled beams (by assuming different length or different cross section areas) was not practicable because of computation difficulties at high modal overlap.

The effects of small variations (perturbations) in the geometry of the coupled system on the sensitivity of the prediction are investigated by calculating the mean and the normalized variance of the computed ensembles of the quantities of interest. The quantities selected for these investigations are the power flow, from the driven beam to the receiver beam, and the coupling loss factor (described in the next section) of the coupled system because they represent the most important quantities in SEA formulation.

The sensitivity of the predictions is also investigated by studying the statistical distributions of the computed ensembles of the coupling loss factor and the power flow at different modal overlap conditions. Cumulative probability distributions for the above quantities are constructed using the following formula [45]

$$E[P\{r(i)\}] = \frac{i - \frac{3}{8}}{n + \frac{1}{4}} \quad , \tag{2.29}$$

where E[P{r(i)}] is the average cumulative distribution function of the random variable r. The variable r is represented by ordered sample as

$$r(i) < r(i+1) < r(i+2) <.....< r(n) \quad ,$$

where i is the element order and n is the sample size. The scale of cumulative distribution function can then be transformed to a scale of 'number of standard deviations' using the statistical tables of the standard normal distribution. The true values of the variable r(i) are then plotted against the new axis of P(r(i)) as shown in figures (2.10) and (2.11) for the coupling loss factor and the normalized power flow (power flow/input power) respectively. The results are discussed in a subsequent section.

2.5 Coupling Loss Factor

Vibrational energy in a system may be lost by either being dissipated or being transmitted to another system. Power in a two-coupled-components system apparently flows in both directions. The power that flows from component 1 to component 2 is independent of the energy content of component 2, but it is proportional to the energy content of component 1 (see Appendix I). This proportionality is known as the basic assumption in SEA hypothesis and can be written as

$$\bar{P}_{12} \sim \bar{E}_1 \quad , \tag{2.30}$$

and similarly

$$\bar{P}_{21} \sim \bar{E}_2 \quad , \tag{2.31}$$

where $\bar{E}_1$ and $\bar{E}_2$ are the total time-average energies of components 1 and 2 respectively. The proportionalities (2.30) and (2.31) can be written as

$$\bar{P}_{12} = \eta_{12}\,\omega\,\bar{E}_1 \ , \tag{2.32}$$

and

$$\bar{P}_{21} = \eta_{21}\,\omega\,\bar{E}_2 \ , \tag{2.33}$$

where $\eta_{12}\omega$ and $\eta_{21}\omega$ are the constants of proportionalities. η_{12} and η_{21} are termed coupling loss factors and they are of central importance in SEA. The coupling loss factor of two coupled subsystems may be estimated on the basis of SEA hypothesis that the power flow between the subsystems is proportional to the difference of subsystems energies. Coupling loss factor may be written as [2],

$$\eta_{12} = \frac{\left\{\bar{P}_{12}\right\}_{net}}{\omega\, N_1 \left\{ (\bar{E}_1/N_1) - (\bar{E}_2/N_2) \right\}} \ , \tag{2.34}$$

where N_1 and N_2 are the expected number of modes in subsystems 1 and 2 respectively, $(\bar{E}_1/N_1)$-$(\bar{E}_2/N_2)$ is the average modal energy difference and ω is the centre frequency of the band of the analysis. $\left\{\bar{P}_{12}\right\}_{net} = \bar{P}_{12} - \bar{P}_{21}$, is the net power flow between the coupled beams. Equation (2.34) hides two basic assumptions which achieve an indirect isolation of modal pair interactions. First, the coupling is weak which means only a very small fraction of power will be transferred per radian of oscillation. Second, it is assumed that the natural frequencies of the oscillator sets are distributed in a random manner [53] which means that the calculated quantities are only statistical averages over an ensemble of similar, but not identical systems.

On the basis of the above assumptions a number of techniques have been proposed, to calculate the coupling loss factor. One of these techniques is the natural frequency shift method [6] which is based on the changes in natural frequencies of the two uncoupled modes which occur when coupling elements are introduced. In practice this method was considered to be unsuccessful. The major difficulty in using this method is the achievement of a coupled motionless point between two coupled structures while other points are vibrating as normal.

The other technique is the travelling wave method [2] which considers the waves that propagate, reflect, and transmit through a lossless model of two coupled semi-infinite subsystems.

Scharton and Lyon [2] introduced an alternative technique for the estimation of coupling loss factor of two coupled beams which is the statistical distribution method. This method assumes that for a typical mode of beam 1 with resonant frequency ω_r there are, on average, (n_2/n_1) interacting modes of beam 2 (n denotes modal density), and that the natural frequencies ω_s of these modes are uniformly and independently distributed in a frequency bandwidth $(1/n_1)$ centred on ω_r. It is assumed that the damping is light and the excitation bandwidth is small compared with the centre frequency ω.

The applications of the first two techniques mentioned above to a problem of beam-beam coupling [46] have shown that the estimates of the coupling loss factors obtained from those methods differed by a factor of five. Crandall and Lotz [47] have improved on these estimates by treating the problem as one of 'strong coupling'. They compared the travelling wave method and the frequency shift method estimates of the coupling loss factor. They found that the factor of difference between the two estimates was $(\pi^2/4)$.

In the present work the coupling loss factor (η_{12}) of the beam-beam model is calculated on the basis of SEA hypothesis (equation (2.34)) for each realization in the set of similar (not identical) systems after the proper substitution for the time averaged quantities of $\bar{P}_{12}$, $\bar{E}_1$ and $\bar{E}_2$. Using the new ensemble of η_{12}, results for the mean and the normalized variance are calculated for different M_{av} values and displayed in figures (2.6) and (2.8) respectively. Another estimate for η_{12} is found by applying the travelling method. This method is chosen because it seems to have some advantages over the other available methods. It is more general and can easily be applied to any coupled structural elements without any mathematical complications compared with the other methods. Previous results, computed by this method, have shown more accurate estimates compared with their experimental measurements. In the present work, the travelling wave method is applied to the system shown in figure (2.12). This system consists of two semi-infinite beams coupled at their ends by a translational spring of stiffness K_c.

A sinusoidal incident wave propagates to the left in the lossless beam 1. At the coupling, reflected, transmitted, and nearfield waves are generated. The displacement of beam 1 can be written as

$$w_1(x,t) = (A_1\, e^{jkx} + A_2\, e^{-jkx} + A_3\, e^{-kx})\, e^{j\omega t} \ , \qquad (2.35)$$

which consists of two propagating waves and a non-propagating (nearfield) wave. A_1-A_3 are the waves amplitudes, and k_1 is the bending wave number. The displacement of beam 2 is

$$w_2(x,t) = (A_4\, e^{jkx} + A_5\, e^{kx})\, e^{j\omega t} \ , \qquad (2.36)$$

which consists of one propagating wave and one nearfield wave of amplitudes A_4 and A_5 respectively. k_2 is the wave number of beam 2. Equations (2.35) and (2.36) satisfy the boundary conditions at the coupling point. The boundary conditions are

$$B_1 w_1'' = 0 \ ,$$

$$B_2 w_2'' = 0 \ ,$$

$$K_c(w_1 - w_2) = -B_1 w_1''' \ ,$$

$$K_c(w_1 - w_2) = -B_2 w_2''' \ ,$$

where B_1 and B_2 are the bending stiffnesses of the beams.

As the time averaged power flow from beam 1 to beam 2 is proportional to the stored energy of beam 1, then the coupling loss factor may be written as [2]

$$\eta_{12} = \frac{\bar{P}_{12}}{\omega \bar{E}_1} \ . \qquad (2.37)$$

The time averaged power flow associated with the transmitted wave is given by

$$\bar{P}_{12} = B_1 k_1^3 \omega |A_4|^2 \cdot \qquad (2.38)$$

If we assume that the nearfield waves (generated at the junction) contribute negligibly to the flexural energy and, further, that the energy transmitted across the coupling is small so that the reflected wave has nearly the same energy as the incident wave, then the total time averaged flexural energy of beam 1 of length l_1 is given by

$$\bar{E}_1 = m_1' l_1 \omega^2 |A_1|^2 \ , \qquad (2.39)$$

where m_1' is the mass density of the beam 1. Substituting equations (2.38) and (2.39) into equation (2.37) yields the following expression for the beam-beam coupling loss factor:

$$\eta_{12\infty} = (k_1 l_1)^{-1} \frac{B_2 k_2^3}{B_1 k_1^3} \frac{|A_4|^2}{|A_1|^2} \ . \qquad (2.40)$$

The coupling loss factor $\eta_{12\infty}$ may also be written in terms of the transmission coefficient τ_∞ as

$$\eta_{12\infty} = (k_1 L_1)^{-1} \tau_\infty \ , \qquad (2.41)$$

where

$$\tau_\infty = \frac{B_2 k_2^3}{B_1 k_1^3} \frac{|A_4|^2}{|A_1|^2} \ .$$

The substitution of equations (2.35) and (2.36) into the boundary conditions yields the following expressions for the ratio $\frac{|A_4|^2}{|A_1|^2}$ as

$$\frac{|A_4|^2}{|A_1|^2} = \frac{\alpha}{\beta} ,$$

where

$$\alpha=4K_c^2G_1^2[8K_c^2G_1^2+16K_c^2G_1G_2 +8K_c^2G_2^2-8K_c^2G_1^2G_2-8K_cG_1^2G_2^2+4G_1^2G_2^2] ,$$

and

$$\beta=[4K_c^2G_1^2+8K_c^2G_1G_2+4K_c^2G_2^2-4K_c^2G_1^2G_2-4K_cG_1^2G_2^2+2G_1^2G_2^2]^2 ,$$

where

$$G_1 = B_1k_1^3 ,$$

and

$$G_2 = B_2k_2^3 .$$

Equation (2.40) is evaluated for the value of $\eta_{12\infty}$ using the properties and the dimensions of the finite coupled beams system under investigation . The result of $\eta_{12\infty}$ is plotted in figure (2.13) for the frequency range of interest. The frequency averaged value is obtained and plotted in figures (2.6) and (2.14) for the comparison with those obtained from the finite coupled beams models.

2.6 Long-short Beams Model

The mathematical model of the long coupled beams system of section (2.2) is modified to suit the case of coupling between a long and a short beam. The modification is made by making the modal density of one of the coupled beams to be about 10 times the other beam. This is simply done by choosing an average length ratio

of the same order. The resulting model represents modal interactions of a single resonant mode of the short beam with about seven resonant modes of the long beam in a frequency band of 50 Hz centred at 25 Hz. This type of analysis has great importance in engineering applications when an element (substructure) of low modal density is coupled to another of much higher modal density. Examples of such applications are a plate coupled acoustically to a large volume of fluid and a beam coupled to a large plate.

The same method of analysis for the previous model is used for this case. The coupling loss factor and the normalized power flow are obtained as a set of data which results from the geometric (length ratio) perturbation of the coupled system. The results are treated statistically and the mean values and the normalized variance of the sets of data are calculated for different values of modal overlap factor.

Figures (2.14) and (2.15) display the mean values of coupling loss factor and normalized power flow respectively. Figures (2.16) and (2.17) display the results of the normalized variances for the above quantities. Figures (2.18) and (2.19) present the cumulative probability distributions of the coupling loss factor and the normalized power flow respectively.

2.7 Results and Discussion

Figure(2.6) displays the mean values of the coupling loss factor (η_{12}) of the coupled, multi-mode, beams system against the average modal overlap factor (M_{av}) of the system. It also displays the estimate of coupling loss factor of the corresponding infinite system ($\eta_{12\infty}$). Figure (2.7) displays the mean values of the normalized power flow $\left\{\frac{\bar{P}_{12}}{\bar{P}_{in}}\right\}$. Figure (2.7.a) shows the modal energy ratio ($\bar{U}_2/\bar{U}_1$) of the coupled beams at different M_{av} values. This ratio is calculated for only one realization in the coupled beams systems set. This realization is chosen to be the one with mean length ratio. The computed means of η_{12} and $\left\{\frac{\bar{P}_{12}}{\bar{P}_{in}}\right\}$, which are obtained from the ensembles calculated previously, are considered to be representing the true estimates for the means of the populations of these quantities. But how accurate are these estimates? To answer this question we consider what would happen if we were to take repeated samples of the same sizes, from the same populations. The sample means would vary somewhat from sample to sample and form what is called the sampling distribution of

the mean. Of course, in the practical case under consideration, we took just one sample. The accuracy of the computed means are assessed by the construction of confidence intervals for these means. The intervals define the degree of confidence that the calculated means lie between two certain limits. The probability associated with the confidence intervals is called the confidence coefficient.

To establish confidence intervals for the calculated means, it is required to have a knowledge about the distributions of these means. In the present work it is assumed that the distributions of the means of coupling loss factor and the normalized power flow are approximately normal. This assumption is justified by the consideration of the *Central Limit Theorem.* This theorem states that, if random samples size n, are taken from a distribution with mean μ and standard deviation σ, the sampling distribution of the mean will be approximately normal with mean μ and standard deviation $(\frac{\sigma}{\sqrt{n}})$. The approximation improves as n increases.

Suppose a random sample, size n is taken from a distribution with an unknown mean μ and an unknown standard deviation σ. If the distribution is normal then the confidence interval for μ can be written as

$$C.I = \bar{r} \pm t_c \cdot \frac{s}{\sqrt{n}} \quad , \tag{2.42}$$

where $\bar{r}$ and s are the estimated sample mean and standard deviation. The quantity $(\frac{s}{\sqrt{n}})$ which is the standard deviation of the sampling distribution of the mean is often called the standard error of $\bar{r}$, t_c is a factor and has a value which depends on the required confidence coefficient and can be obtained from statistical tables [49]. Note that the value of t_c increases as n decreases. 95 per cent confidence interval is considered to be reasonable in the present work according to the size of the sample (n = 32) used. A useful approximation for n > 25, is that the 95 per cent confidence interval can be written as [49],

$$C.I = \bar{r} \pm 2.\frac{s}{\sqrt{n}} \tag{2.43}$$

Confidence intervals for the means of η_{12} and $\left\{\frac{\bar{P}_{12}}{\bar{P}_{in}}\right\}$ are obtained at different M_{av} values using equation (2.43) irrespective to the apparent distribution of the sample.

Figure (2.6) shows that η_{12} has the tendency to increase as M_{av} increases. η_{12} approaches asymptotically the estimate of coupling loss factor of the corresponding infinite system as the average modal overlap takes high values ($M_{av} \geq 1$). This result is a confirmation of those of Davis and Wahab [17] and Davis and Khandoker [18] for cases of coupling of two simply supported beams.

Figure (2.7) shows that the mean value of the normalized power flow is proportionally lower at high modal overlap than at low modal overlap. This result may be attributed to the high dissipation in the energy of the driven beam which is associated with the increase in the internal loss factors of the coupled beams over the range used to increase the modal overlap factors of the beams.

Figures (2.6) and (2.7) also display the 95 per cent confidence intervals for the calculated means of η_{12} and $\left\{\frac{\bar{P}_{12}}{\bar{P}_{in}}\right\}$. The widths of the intervals demonstrate the effect of M_{av} on the sensitivity of the predictions. The intervals are wider at low modal overlap than at high modal overlap. This suggests that at high modal overlap the probability of of obtaining estimates for the above quantities which are close to the means is high. This result is confirmed by calculating the normalized variance (variance/(mean)^2) values for η_{12} and $\left\{\frac{\bar{P}_{12}}{\bar{P}_{in}}\right\}$ at different modal overlap conditions. The results are plotted in figures (2.8) and (2.9) respectively. These figures show clearly that the normalized variance decreases as M_{av} increases. The normalized variance takes relatively small values at high modal overlap. A possible reason for this is that the frequency response of the coupled beams is dominated by the well separated resonant peaks at low modal overlap which are highly sensitive to small changes in structural details. The changes have no considerable effect on the smoothed frequency response at high modal overlap. The comparison between figure(2.8) and figure (2.9) shows that the normalized variance of coupling loss factor is always higher than that of the normalized power flow. This is because the coupling loss factor as computed from equation (2.32) is affected by the sensitivities of both power flow and the energy difference of the coupled beams to system parameter variations.

Figures(2.10) and (2.11) display the cumulative probability distributions for a given sample of coupling loss factor and the normalized power flow at different average modal overlap factor values respectively. From these figures it can be emphasized that as Mav increases, the probability that any realization of η_{12} or $\left\{\frac{\bar{P}_{12}}{\bar{P}_{in}}\right\}$ which is close to the mean value increases. This means that we are certain that the calculated means of the above quantities are more reliable and acceptable at high modal overlap than those at low modal overlap. The way of presentation of the cumulative probability distribution provides a simple, and quick method of testing for normality. It is clearly displayed that as M_{av} increases and takes values equal to unity and greater, the cumulative distribution curves will have the shape of a straight line. This result suggests that the observations came from a normal distribution [49], which is similar to the assumed distribution of the input perturbed parameter l_1/l_2.

Similar results to the above are obtained from the analysis of the Long-short model. Figures (2.14) and (2.15) displays the results for the means of η_{12} and $\left\{\frac{\bar{P}_{12}}{\bar{P}_{in}}\right\}$ against the modal overlap factor of the long beam (M_1). Figure (2.14) shows that as M_1 increases and approaches the value of unity, the average coupling loss factor of the finite system approaches the value of the corresponding infinite beams system. Figure (2.15) shows that the normalized power flow decreases as M_1 increases. The results for the normalized variances of η_{12} and $\left\{\frac{\bar{P}_{12}}{\bar{P}_{in}}\right\}$ are shown in figures (2.16) and (2.17) respectively. From these results we can conclude that only one beam needs to have high modal overlap when using SEA to analyse a case of two coupled beams. Cumulative probability distributions for this case of coupling are shown in figures (2.18) and (2.19) for given samples of η_{12} and $\left\{\frac{\bar{P}_{12}}{\bar{P}_{in}}\right\}$ respectively. Similar conclusions may be drawn to that of the long-long beams model.

2.7.1 The perturbations of the coupling element

In the previous sections of this chapter, we studied the sensitivity of the predicted means of η_{12} and $\left\{\begin{matrix}\bar{P}_{12}\\ \bar{P}_{in}\end{matrix}\right\}$ to small, random variations in the geometry of the coupled beams systems. This section deals with the investigation of the effects of possible random perturbations in the properties of the coupling element which represents the path of the power flow between the coupled beams. Normalized power flow is selected as the output quantity. A similar approach to that used previously is followed. The coupling stiffness K_c is perturbed according to a sample which is drawn from a normal distribution. The perturbed sample of K_c is fed to the mathematical model of the coupled beams and results for the normalized power flow are computed in ensembles for different average modal overlap factor values. The cumulative probability distributions are constructed and displayed in figure (2.20). This figure shows that the distribution of $\left\{\begin{matrix}\bar{P}_{12}\\ \bar{P}_{in}\end{matrix}\right\}$ is normal at all M_{av} values. This concludes that the computed value of power flow is slightly sensitive to the perturbations of the stiffness of the coupling element.

2.8 Conclusions

The conclusions which can be drawn from the analysis of two coupled beams are

(a) The travelling wave method overestimates the coupling loss factor of the coupled beams system when the average modal overlap factor is small (M_{av} <1).

(b) The variances of coupling loss factor and the power flow across ensembles of coupled beams decreases as the M_{av} increases. In addition the 95% confidence interval, for the means of the above quantities, decreases as M_{av} increases.

(c) The probability of obtaining estimates for the coupling loss factor and the power flow which are close to the means increases when the average modal overlap factor is large. This conclusion can be noted from the

shapes of the cumulative probability distributions of the above quantities. The distributions approach normality as M_{av} increases.

(d) When a large multi-mode system is coupled to a small system, the modal overlap factor of the large system was found to be more dominant than that of the small system.

(e) At a given value of average modal overlap factor of the coupled system, random perturbations of the coupling stiffness have slight effects on the sensitivity of prediction of the power flow between the coupled beams.

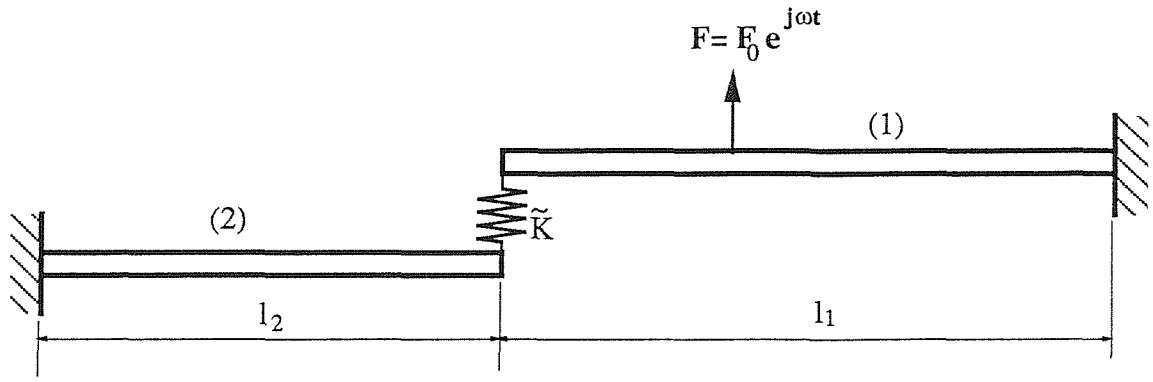

Figure (2.1.a)

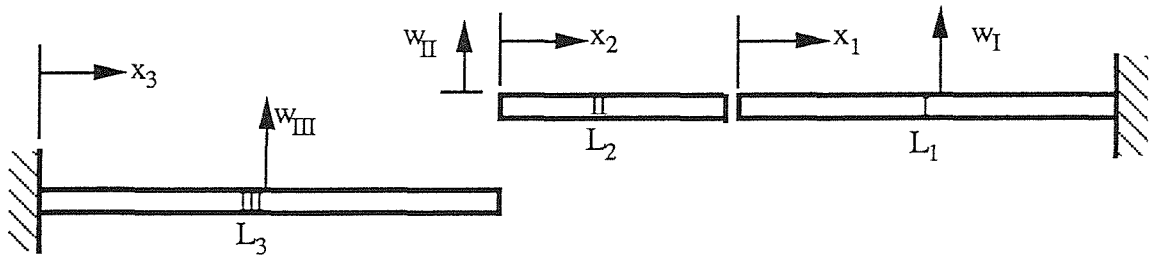

Figure (2.1.b)

Figure (2.1) Coupled beams system

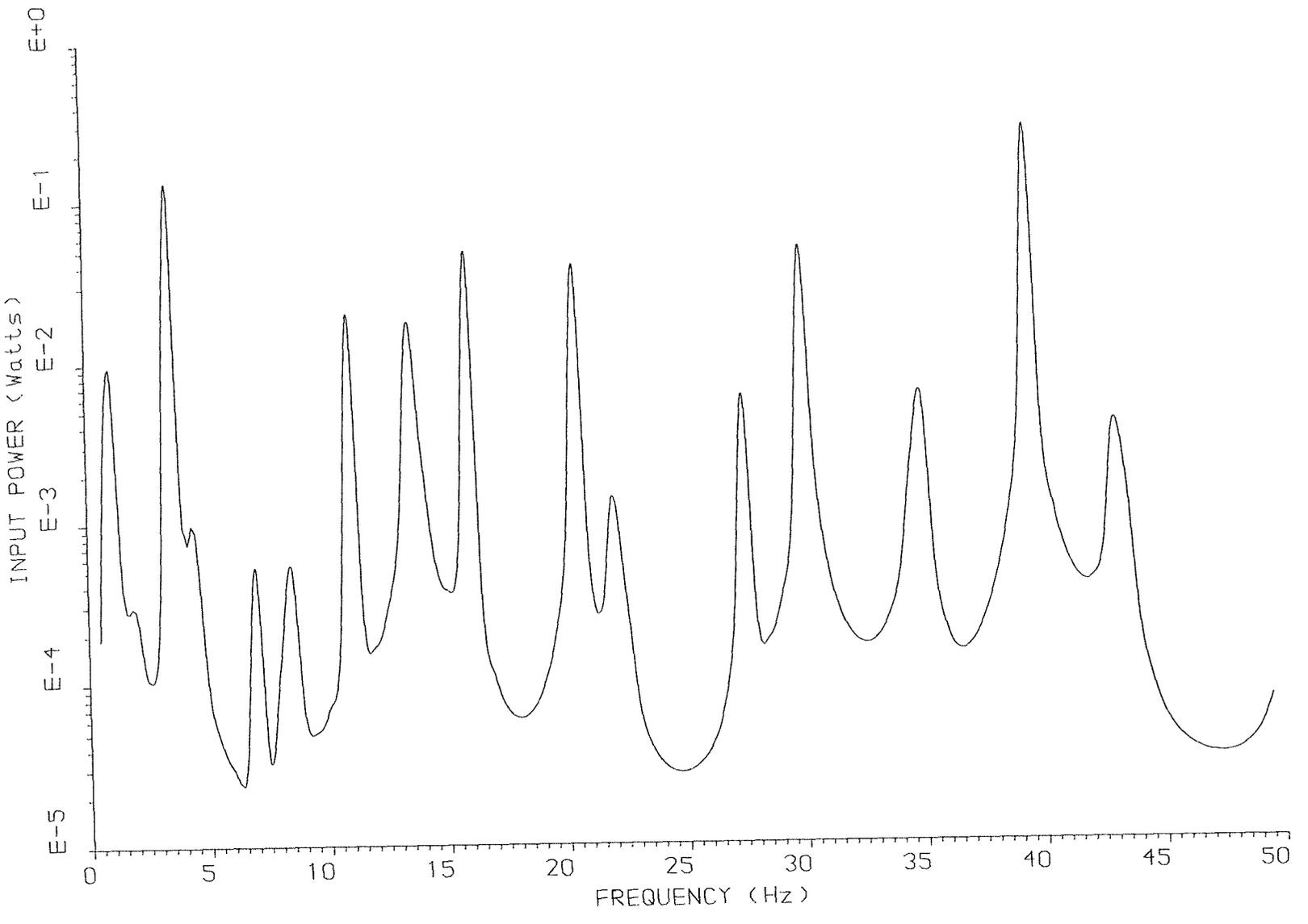

FIG. (2.2) INPUT POWER TO A TWO COUPLED BEAMS SYSTEM

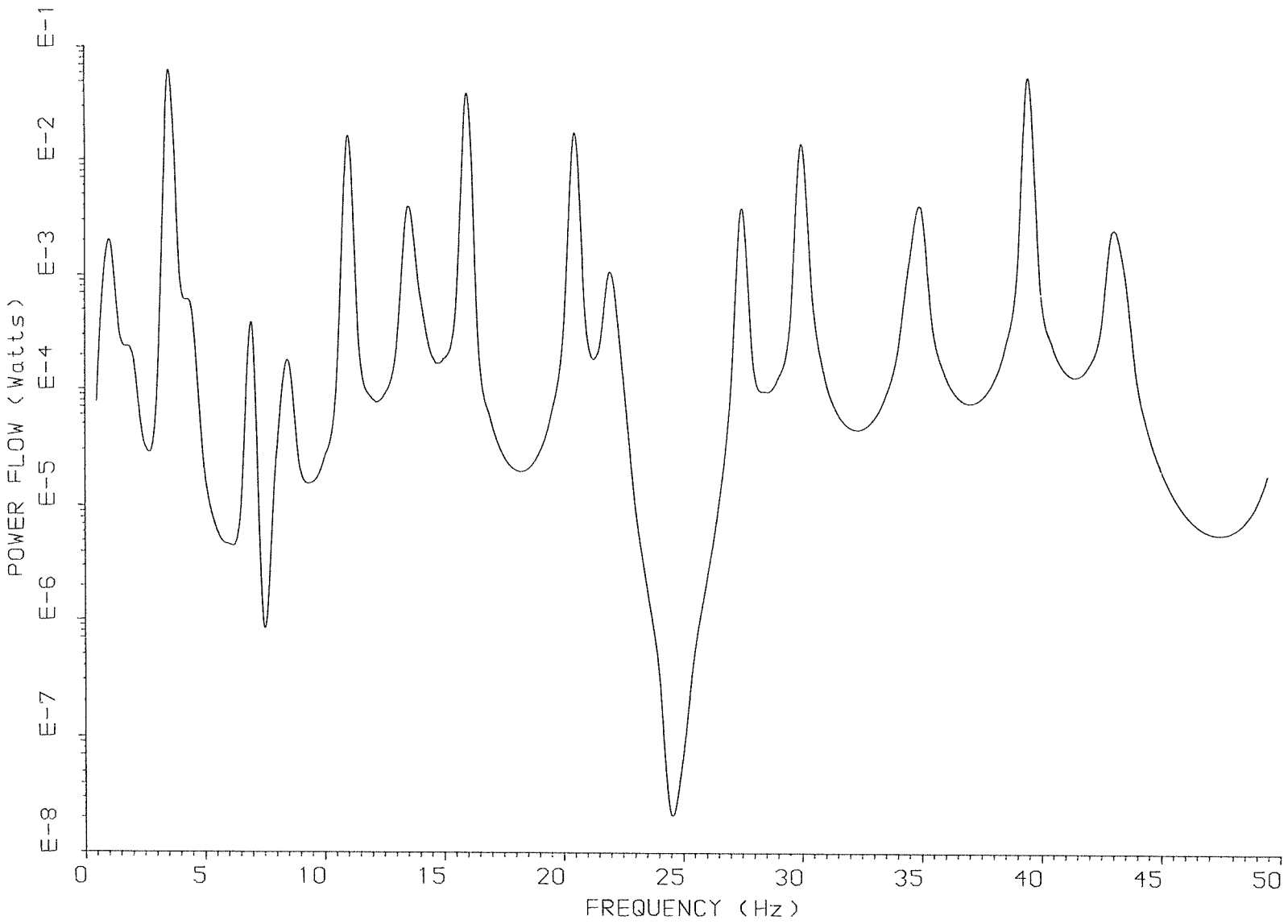

FIG. (2.3) POWER FLOW BETWEEN TWO COUPLED BEAMS

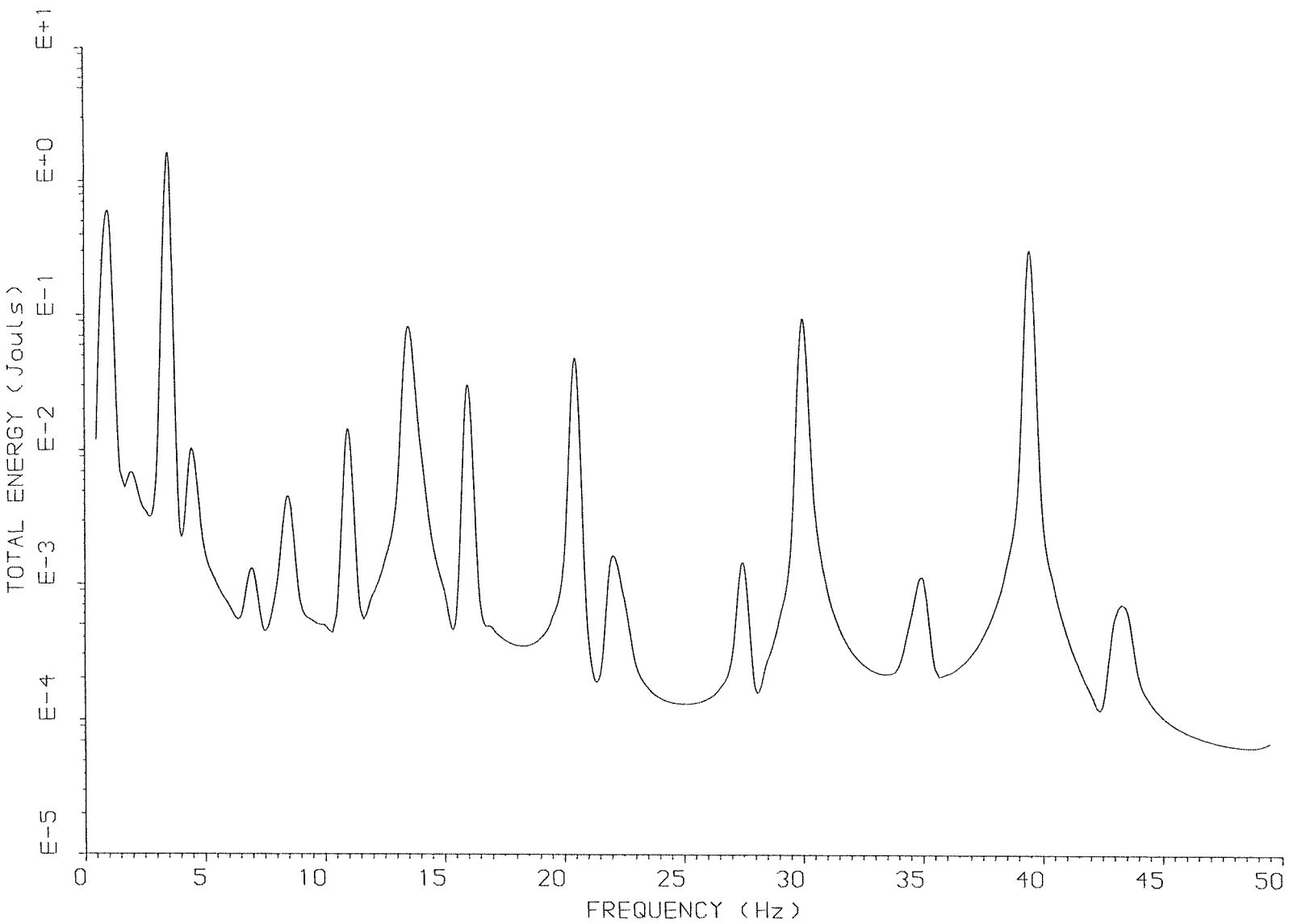

FIG. (2.4) TOTAL ENERGY OF THE DRIVEN BEAM

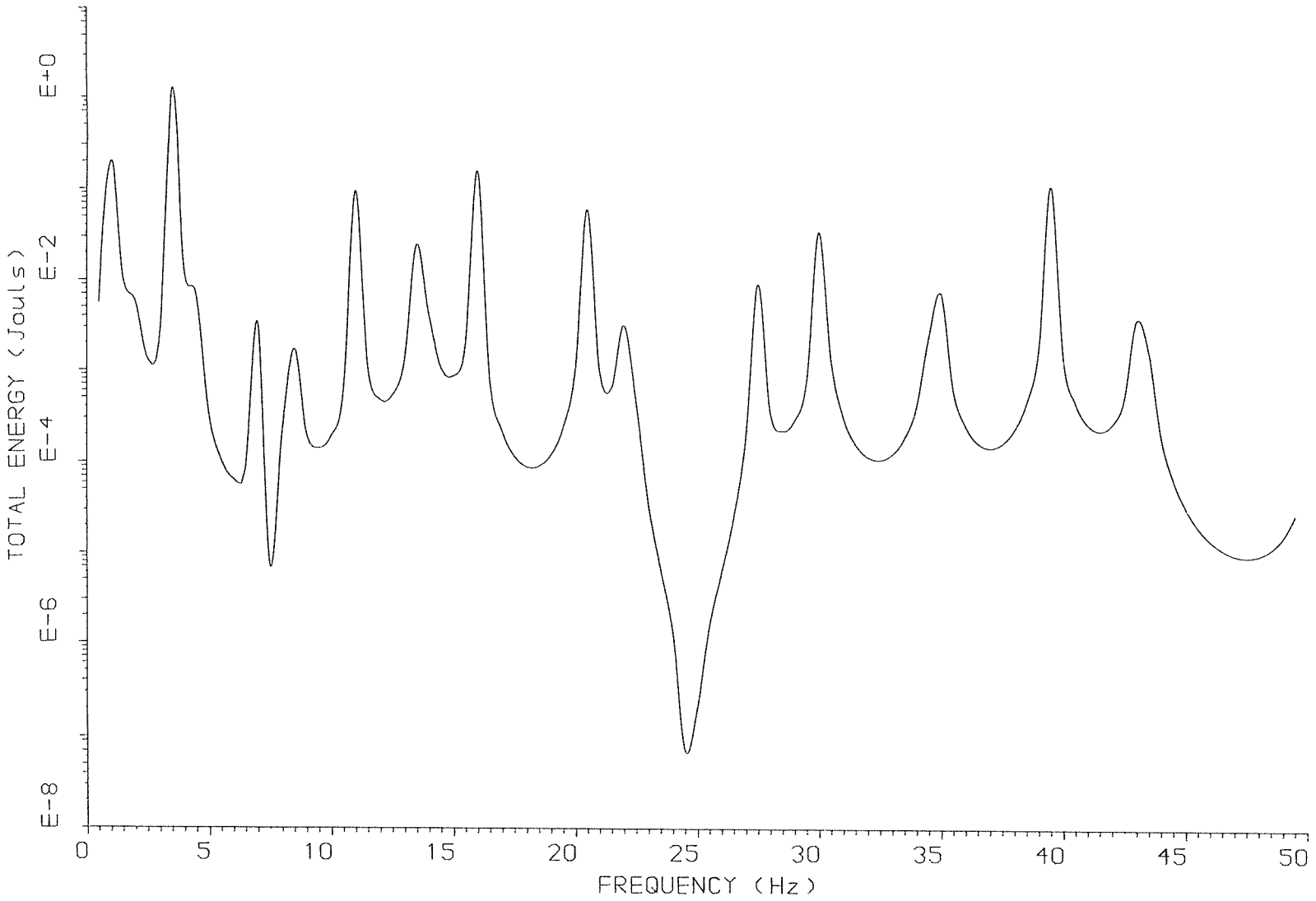

FIG. (2.5) TOTAL ENERGY OF THE RECEIVER BEAM 2

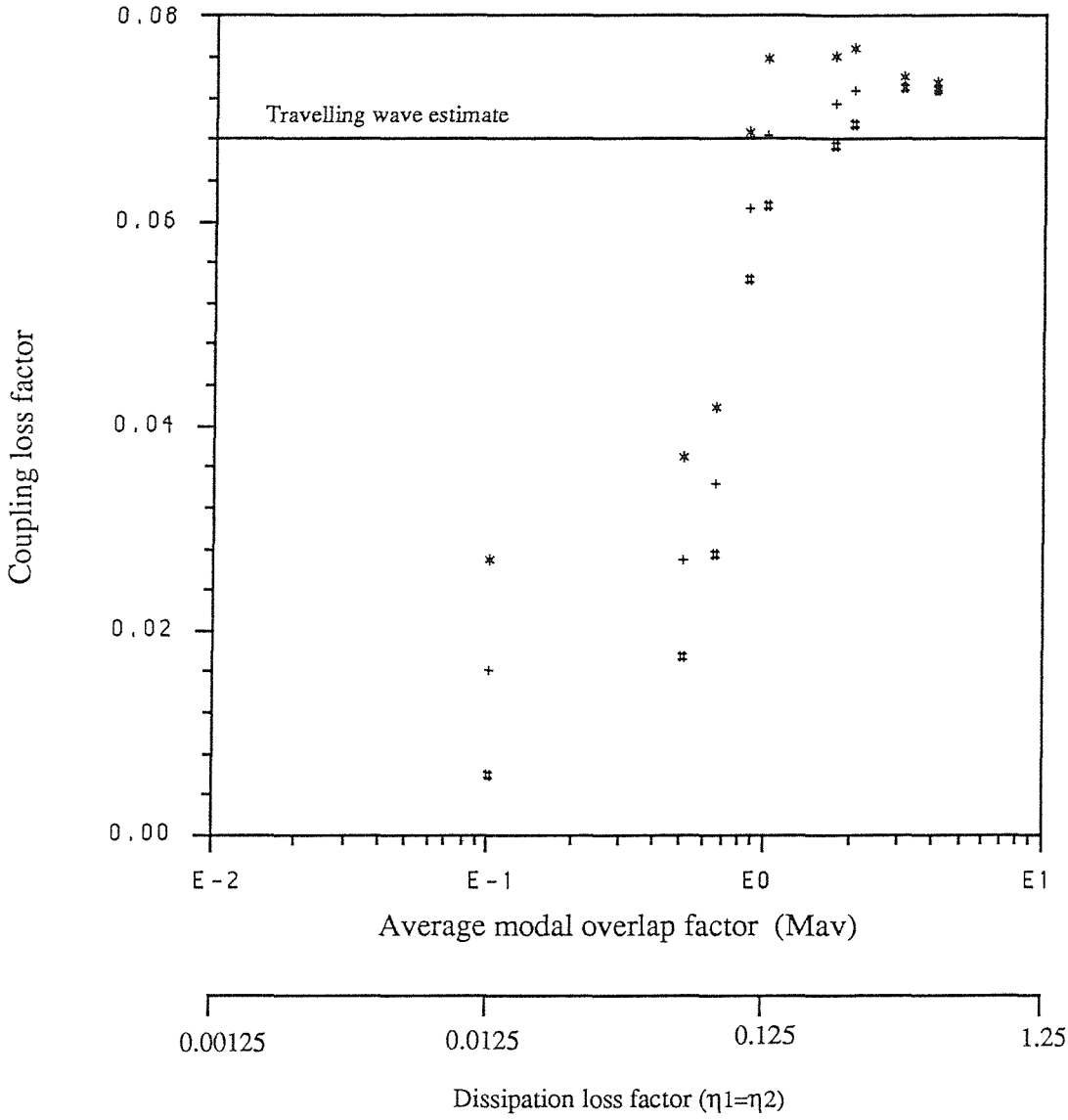

Figure (2.6) : The predicted coupling loss factor of coupled beams system

+ Mean value, * 95% confidence interval.

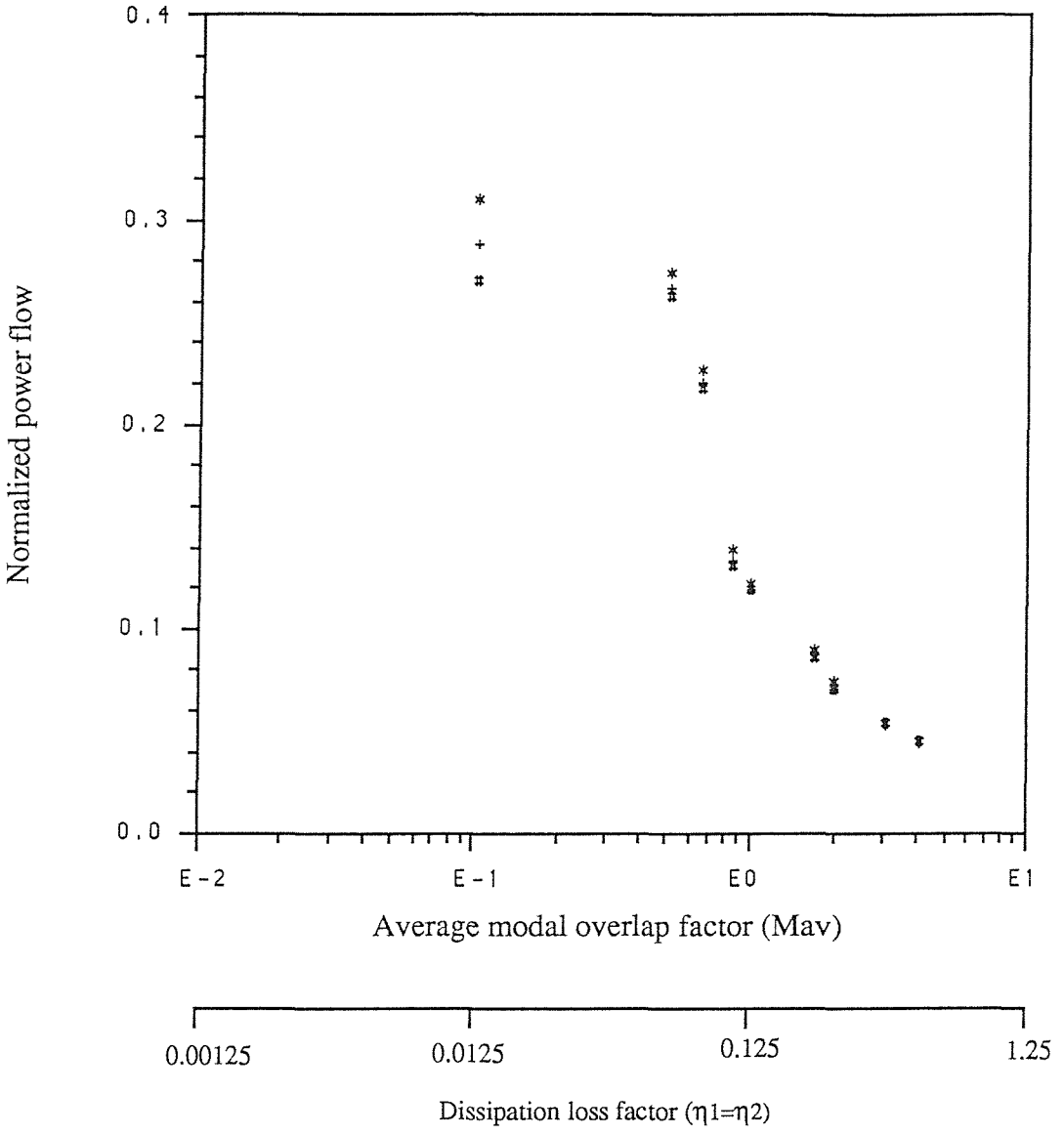

Figure (2.7) : The predicted normalized power flow of coupled beams system. + Mean value, * 95% Confidence interval #

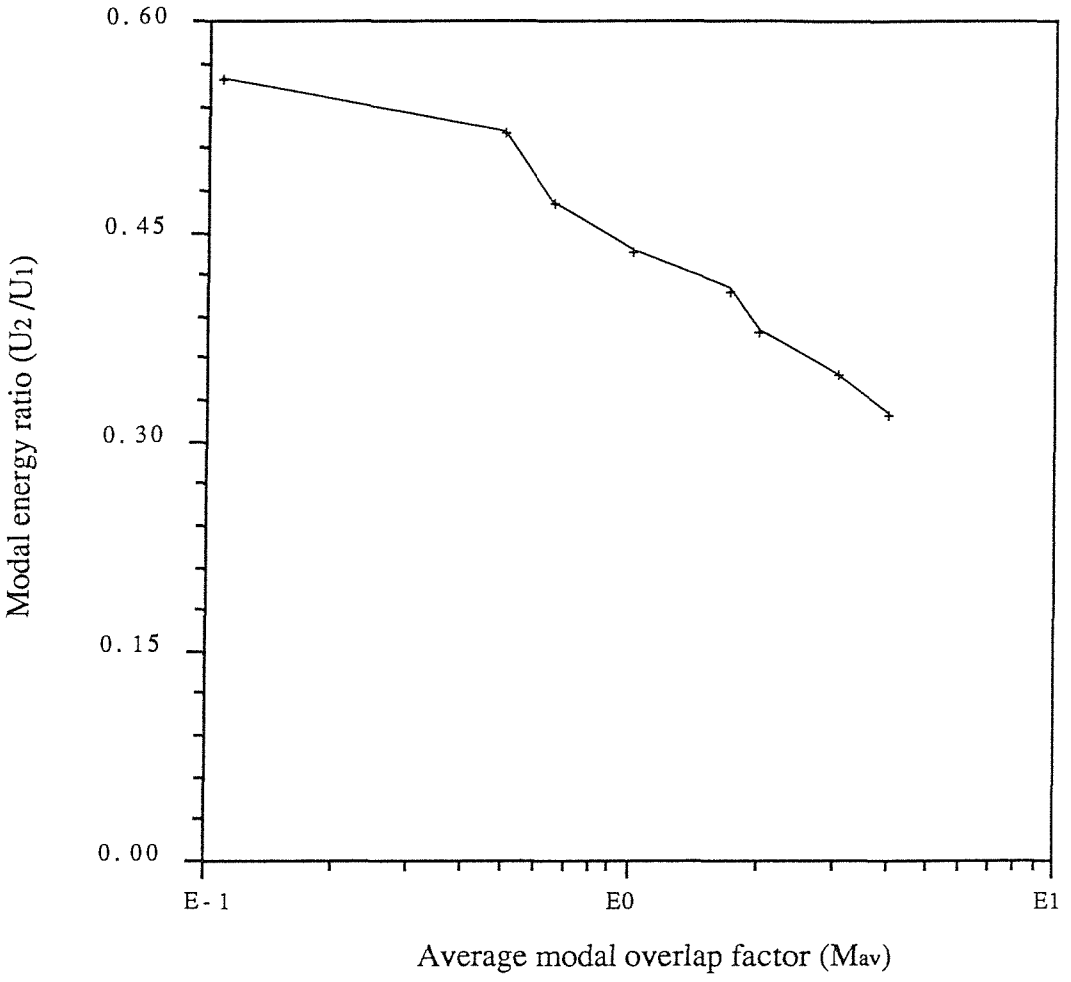

Figure (2.7.a) : Modal energy ratio of two coupled beams

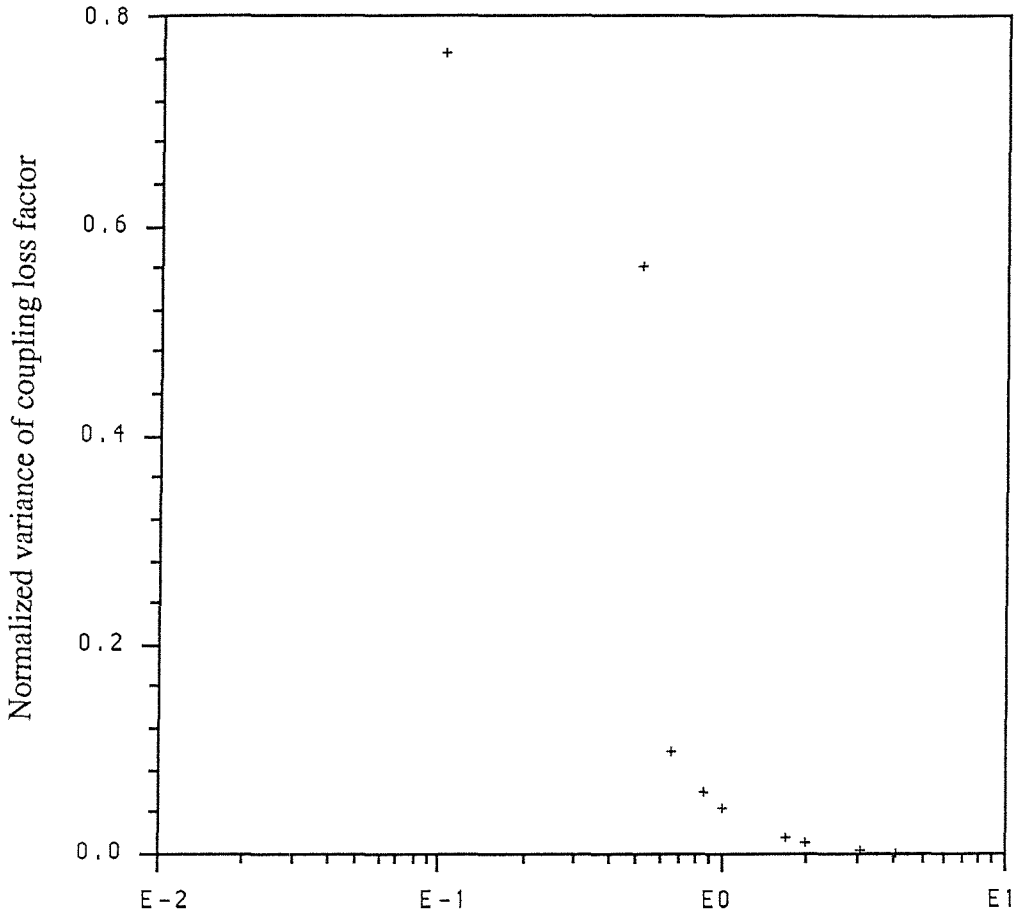

Figure (2.8) : The predicted normalized variance of coupling loss factor of coupled beams system.

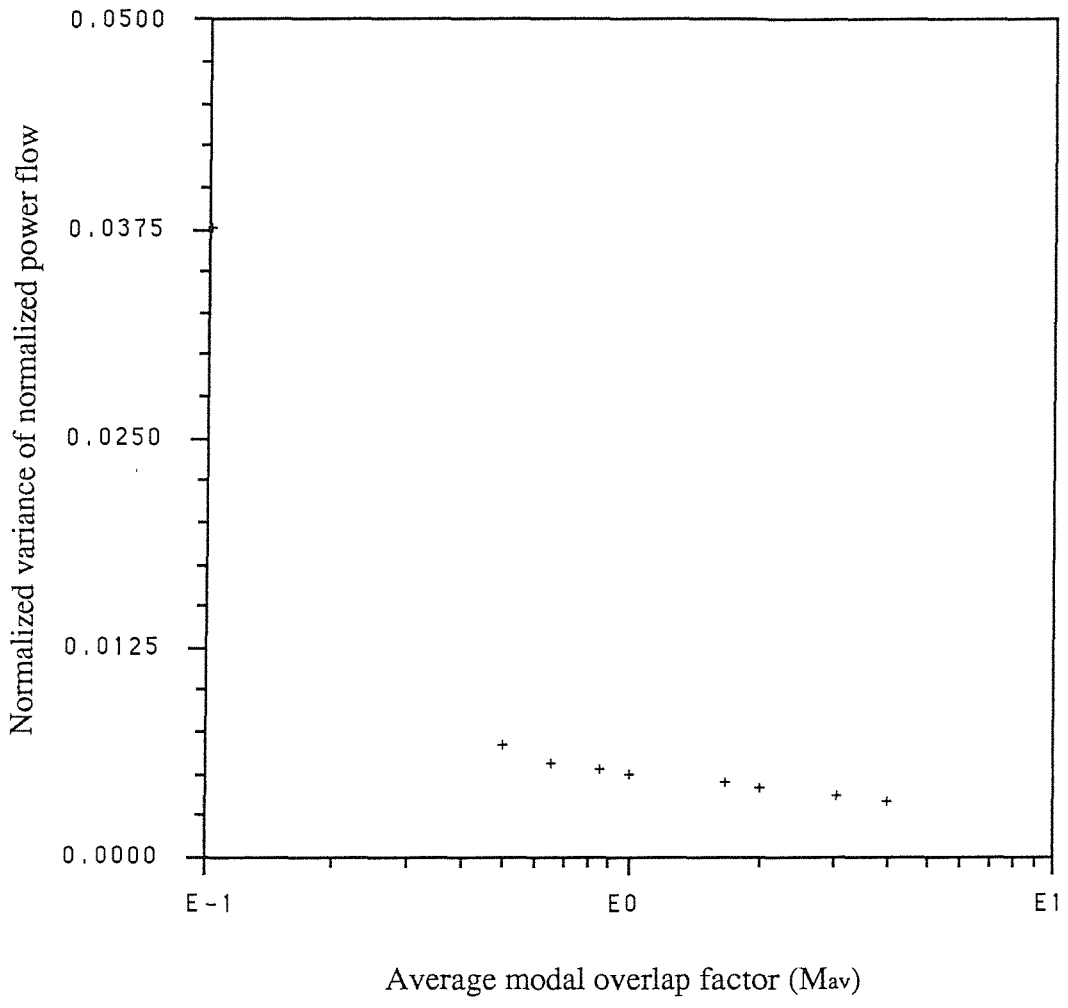

Figure (2.9) : The predicted normalized variance of normalized power flow between coupled beams.

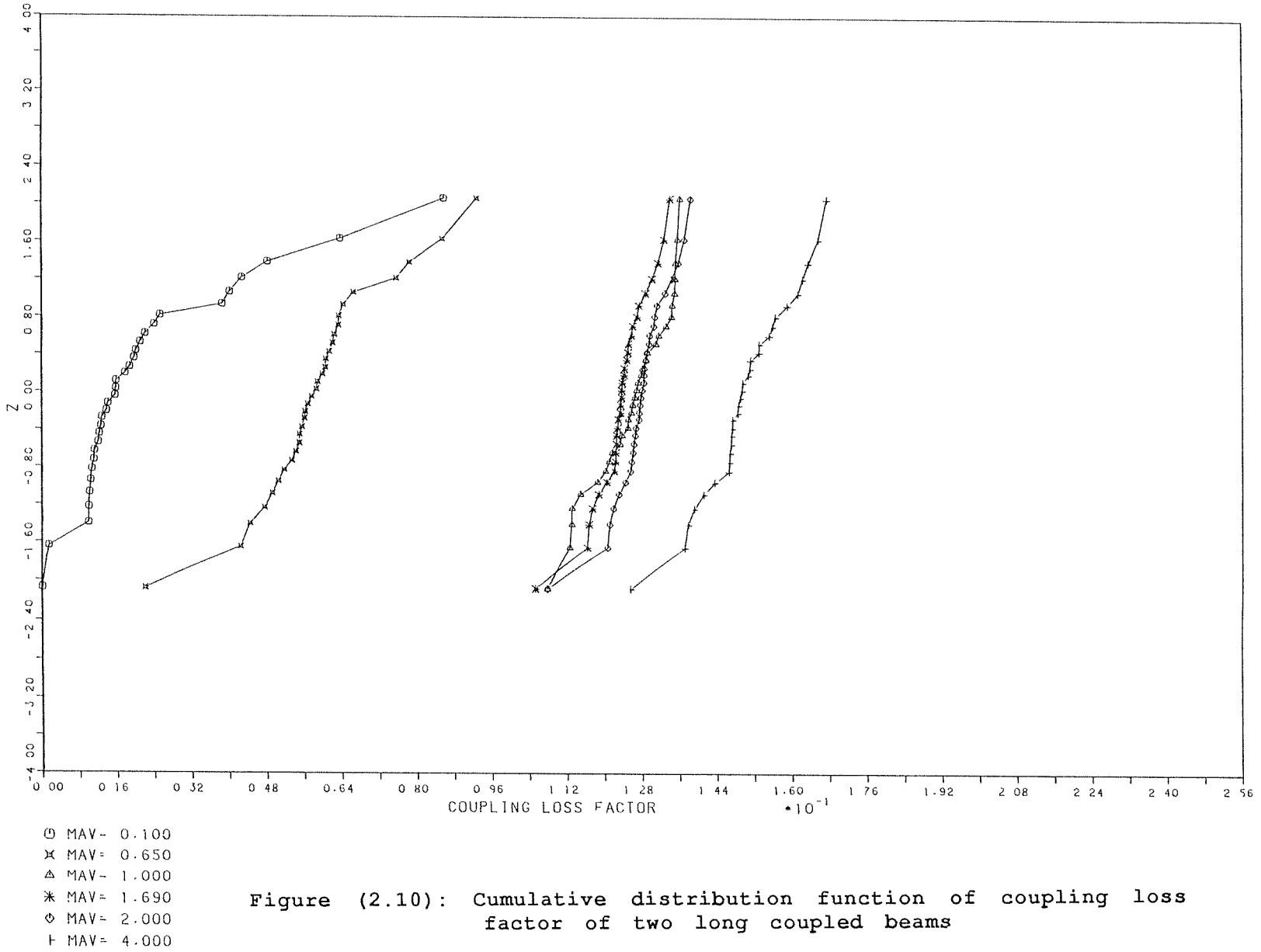

Figure (2.10): Cumulative distribution function of coupling loss factor of two long coupled beams

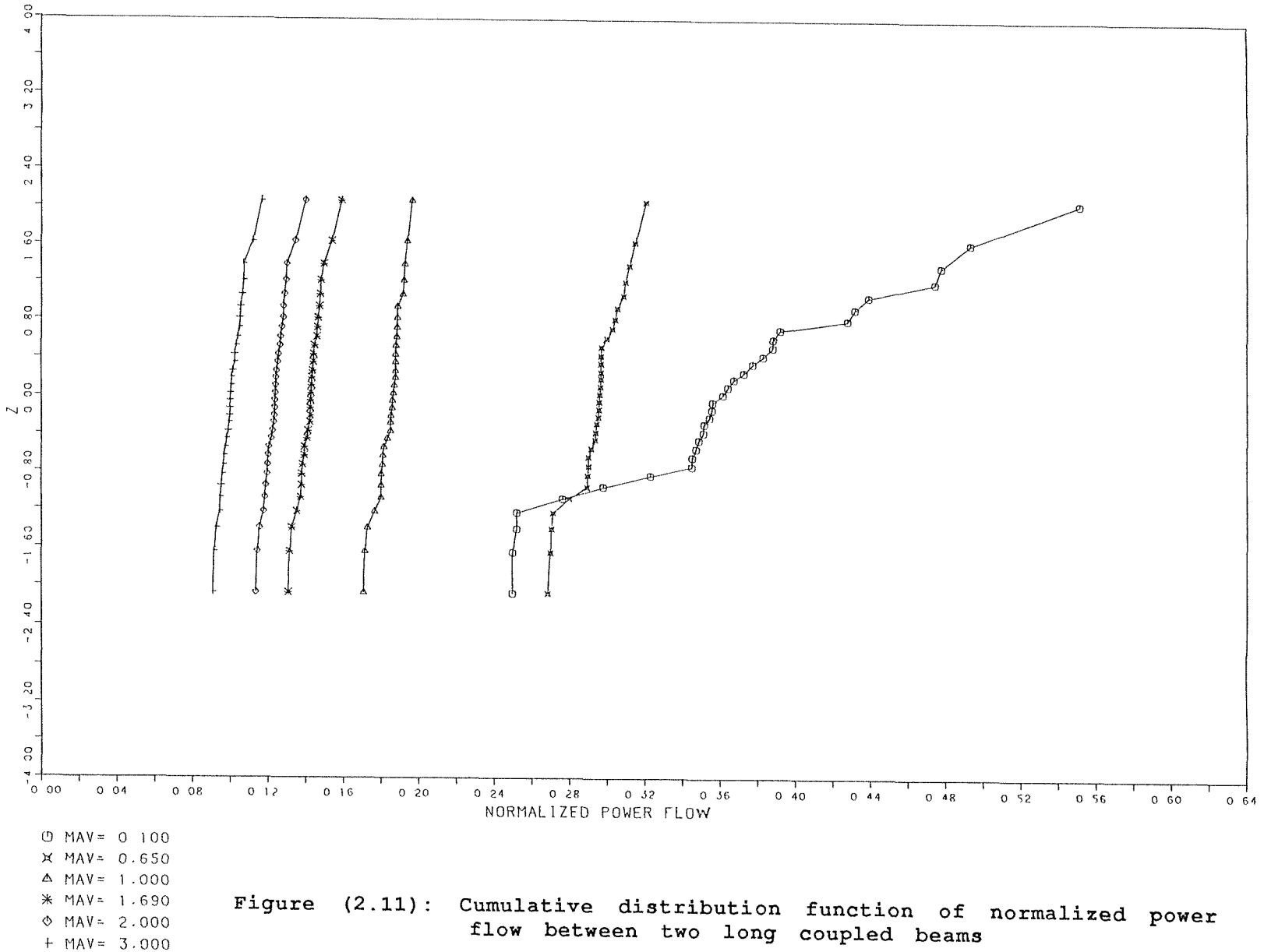

Figure (2.11): Cumulative distribution function of normalized power flow between two long coupled beams

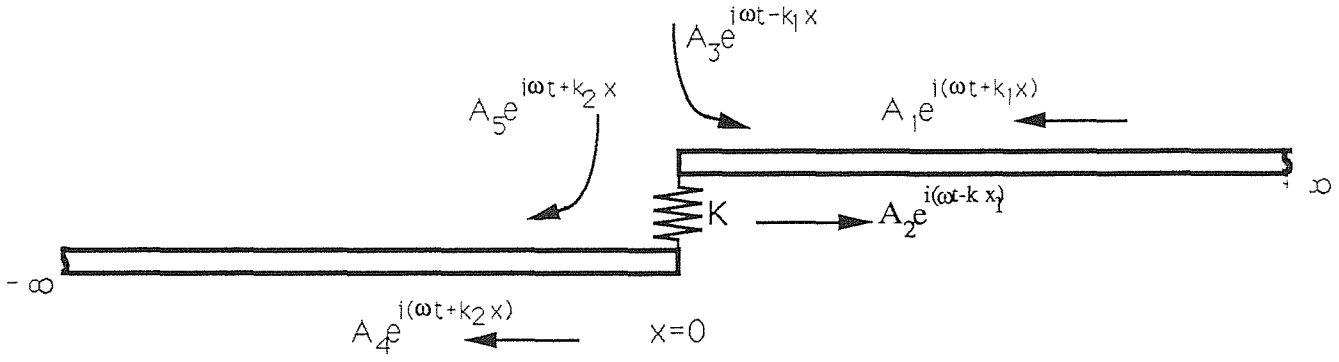

Figure (2.12) : semi -infinite coupled beams

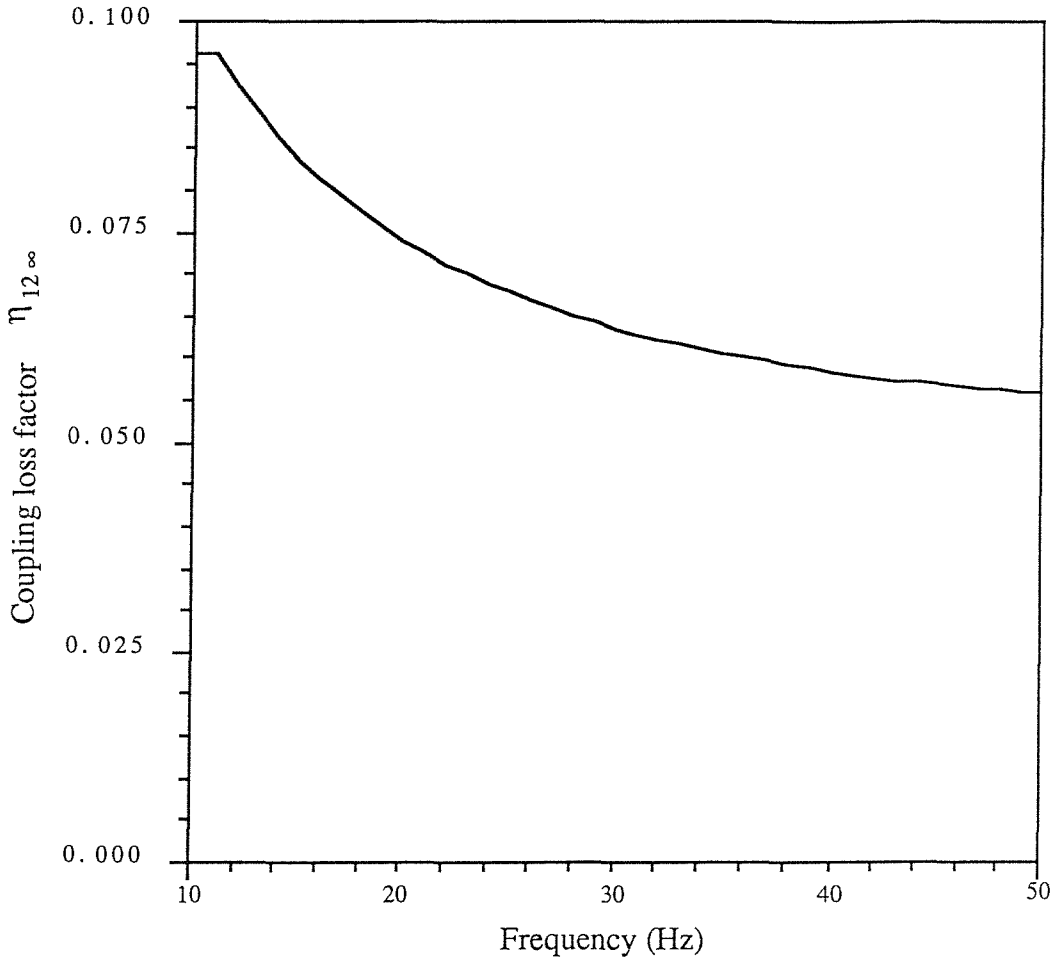

Figure (2.13) : Coupling loss factor of an infinite coupled beams system

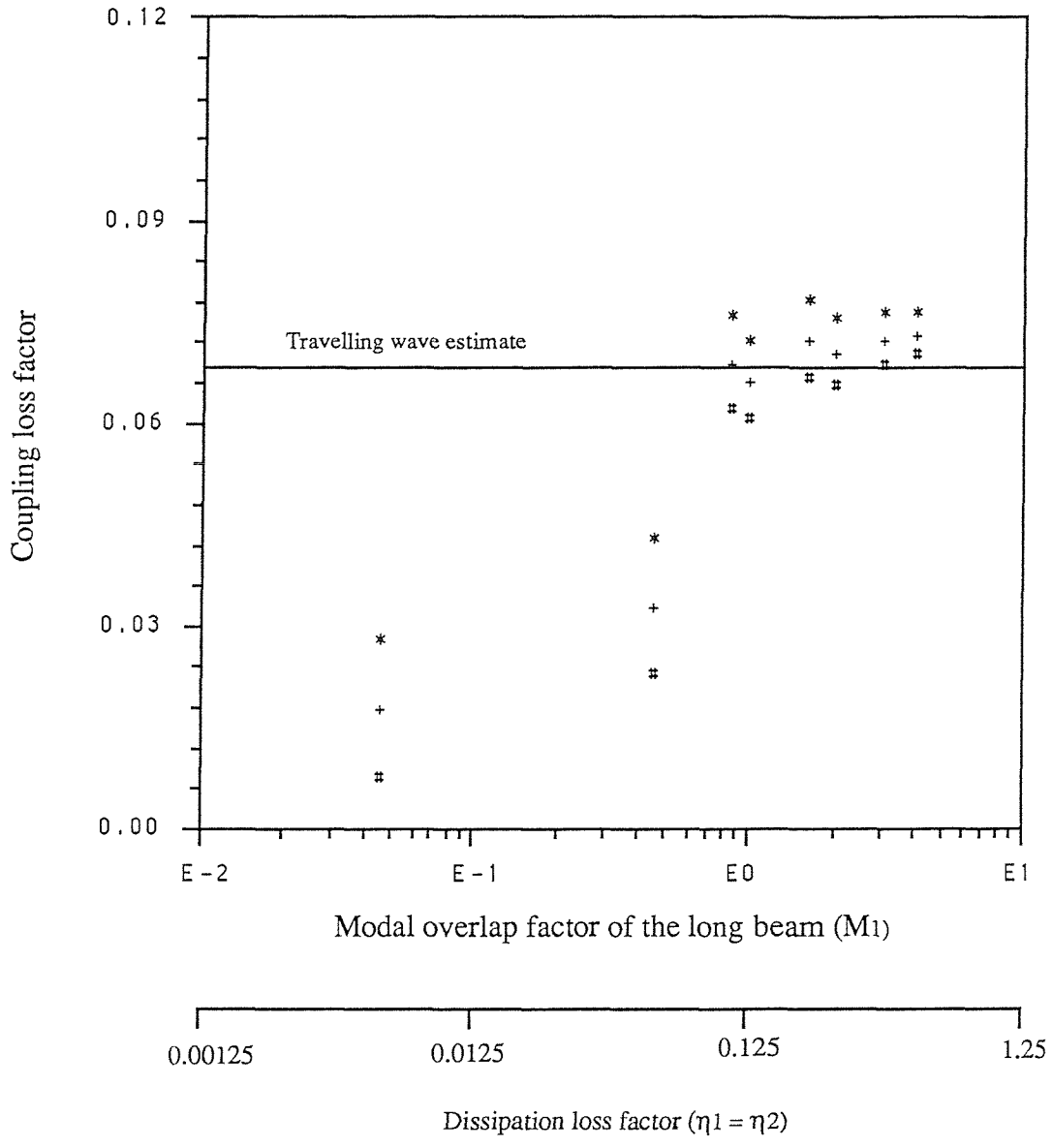

Figure (2.14) : The predicted coupling loss factor of coupled long-short beams.

+ Mean value, * # 95% confidence interval

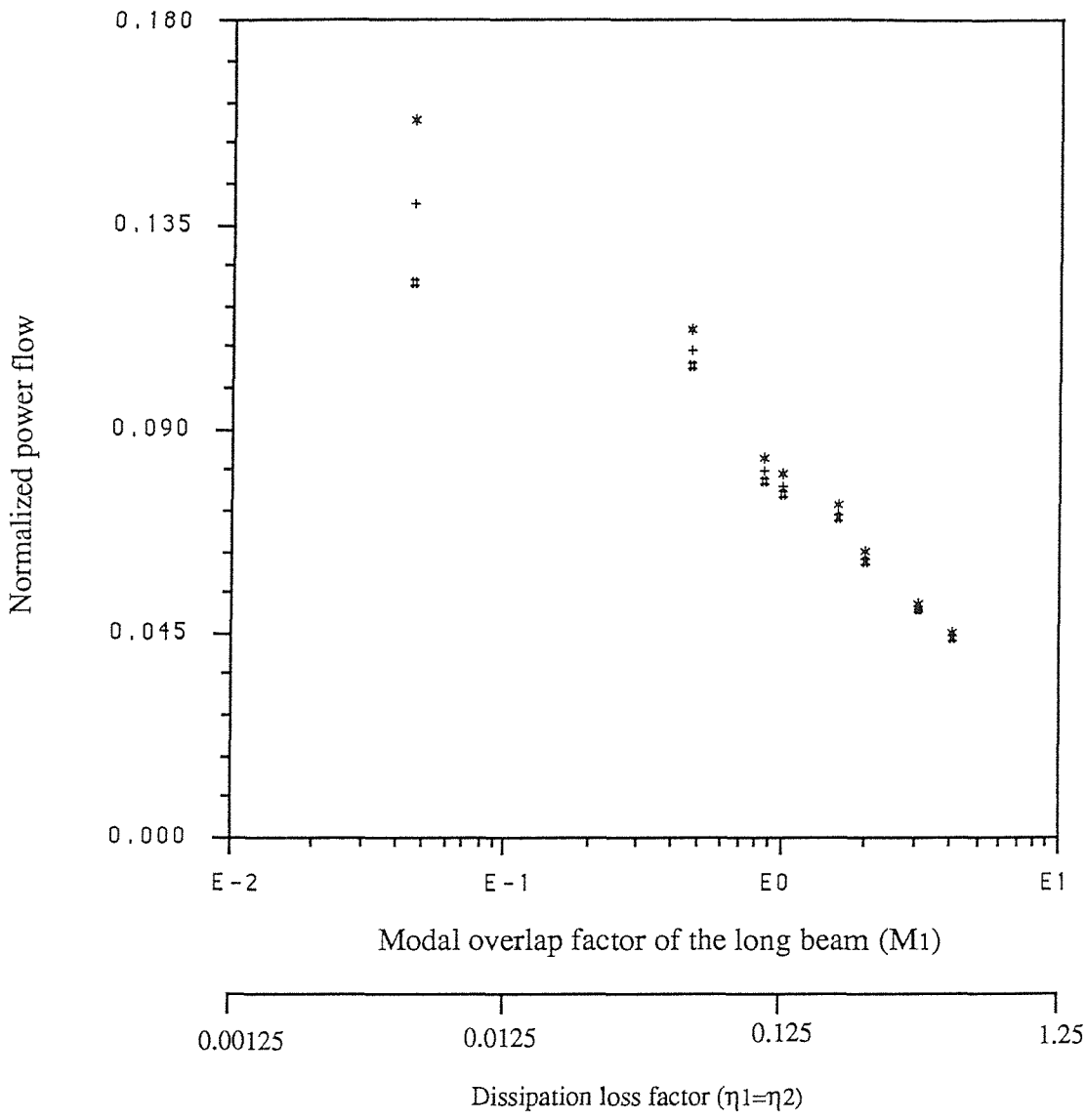

Figure (2.15) : The predicted normalized power flow of coupled long-short beams.
+ Mean value, * 95% confidence interval.

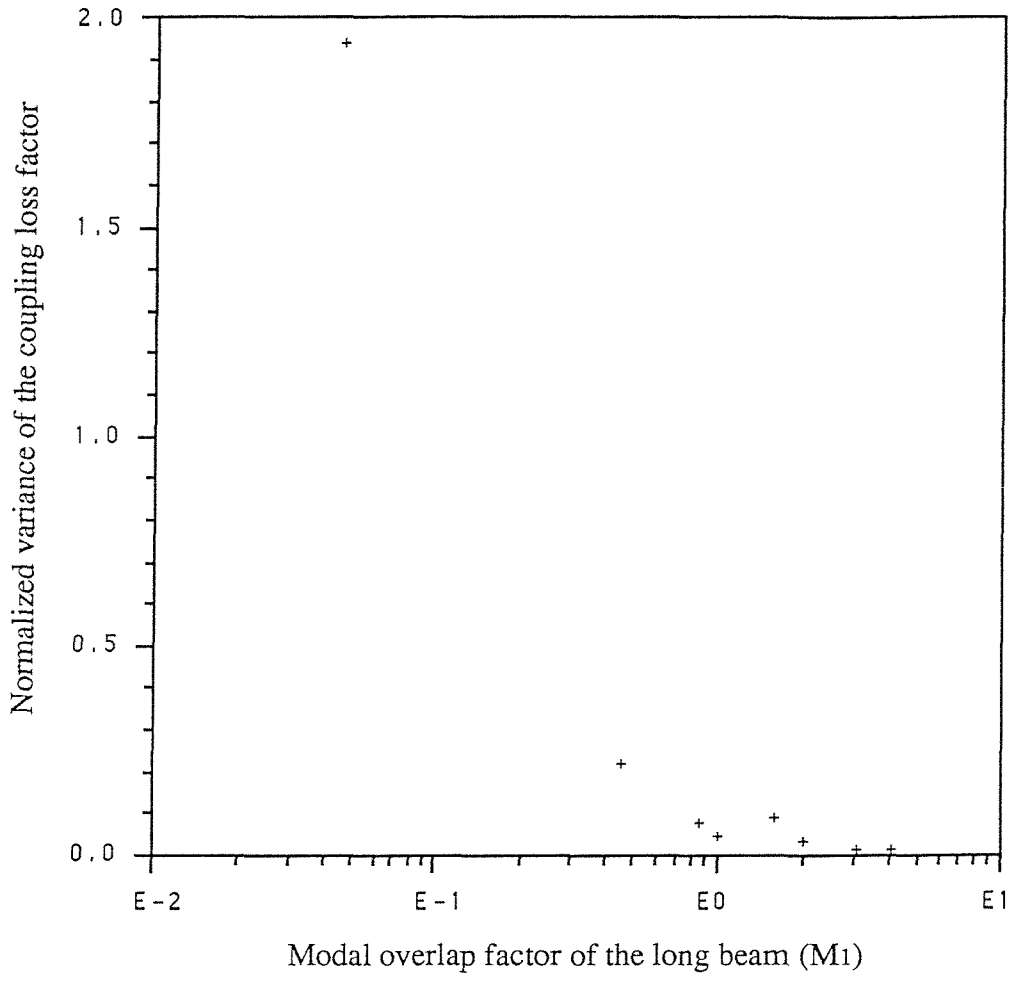

Figure (2.16) : The predicted normalized variance of the coupling loss factor of coupled long-short beams.

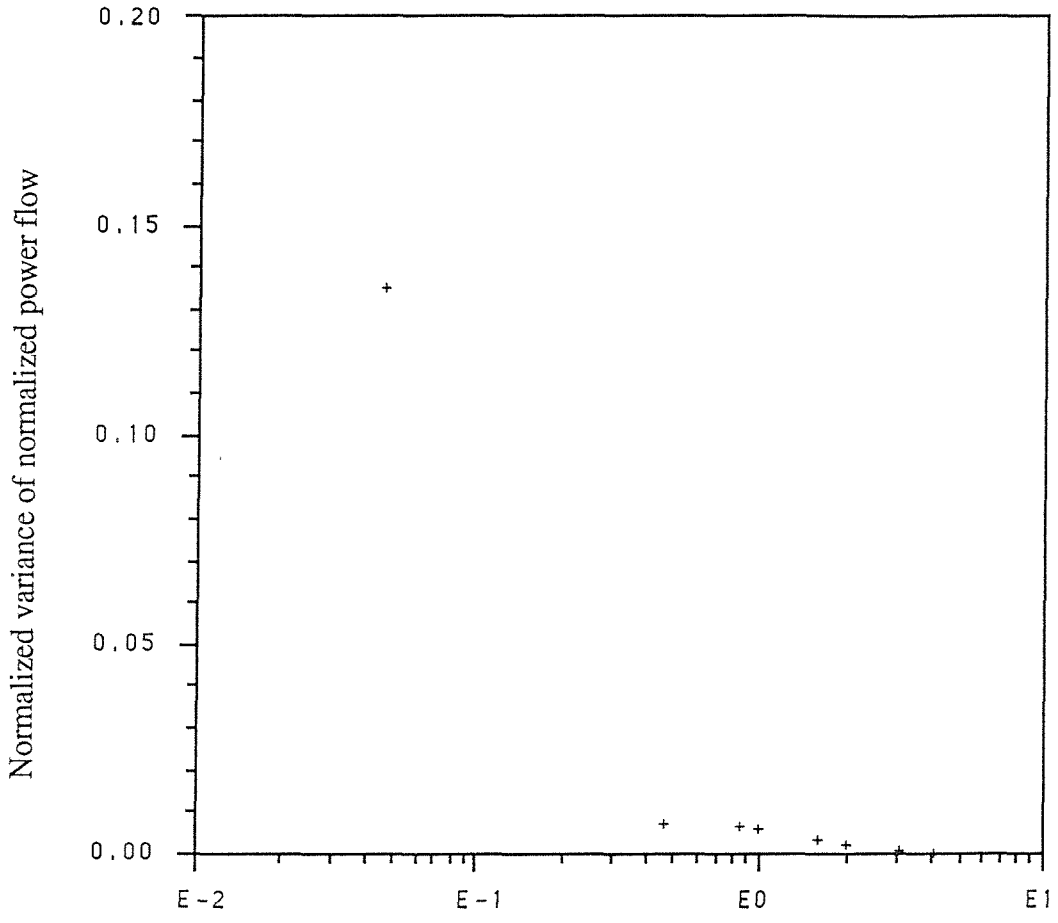

Figure (2.17) : The predicted normalized variance of the normalized power flow between coupled long-short beams.

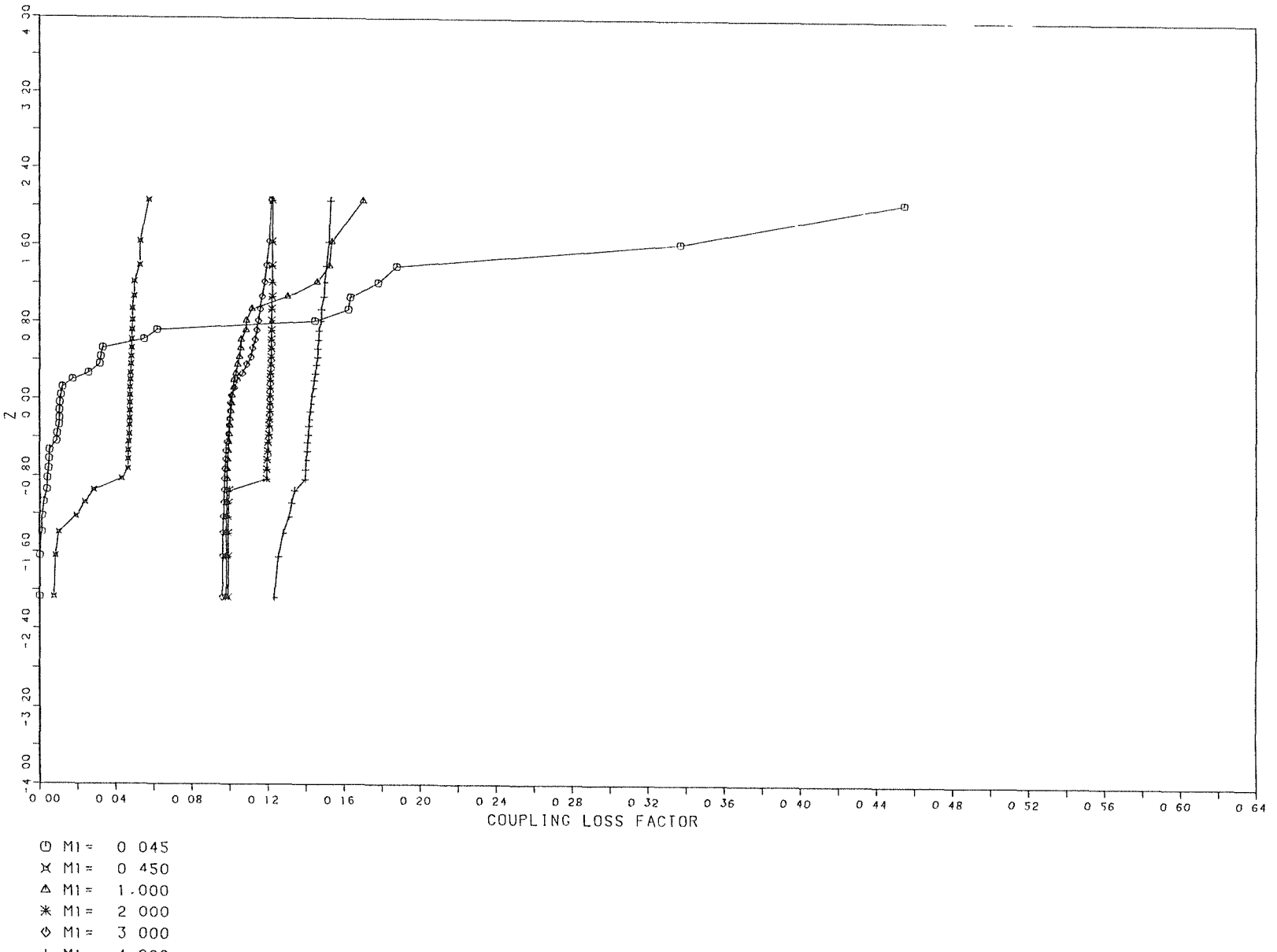

Figure (2.18): Cumulative distribution function of coupling loss factor of a long-short beams system

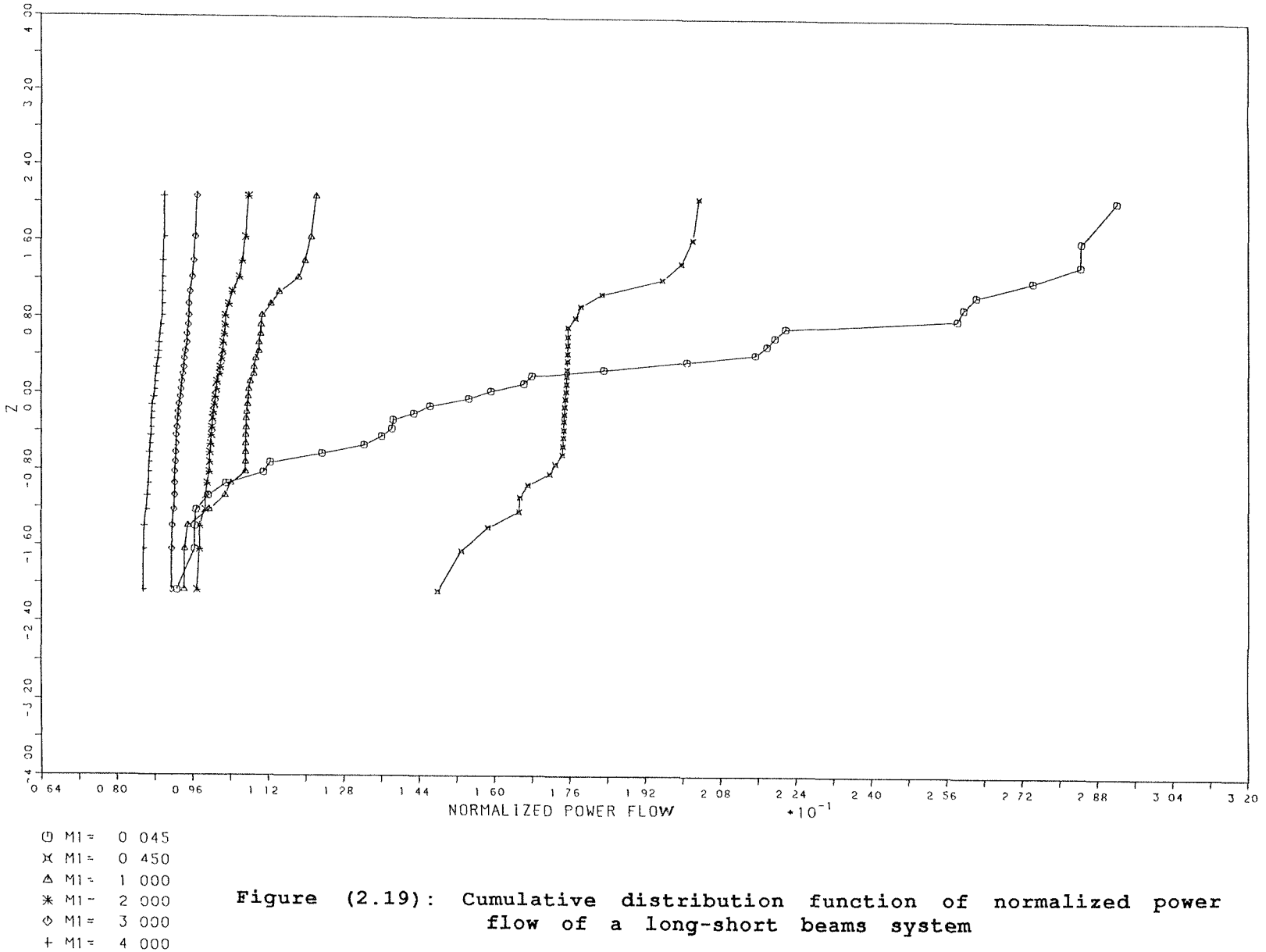

Figure (2.19): Cumulative distribution function of normalized power flow of a long-short beams system

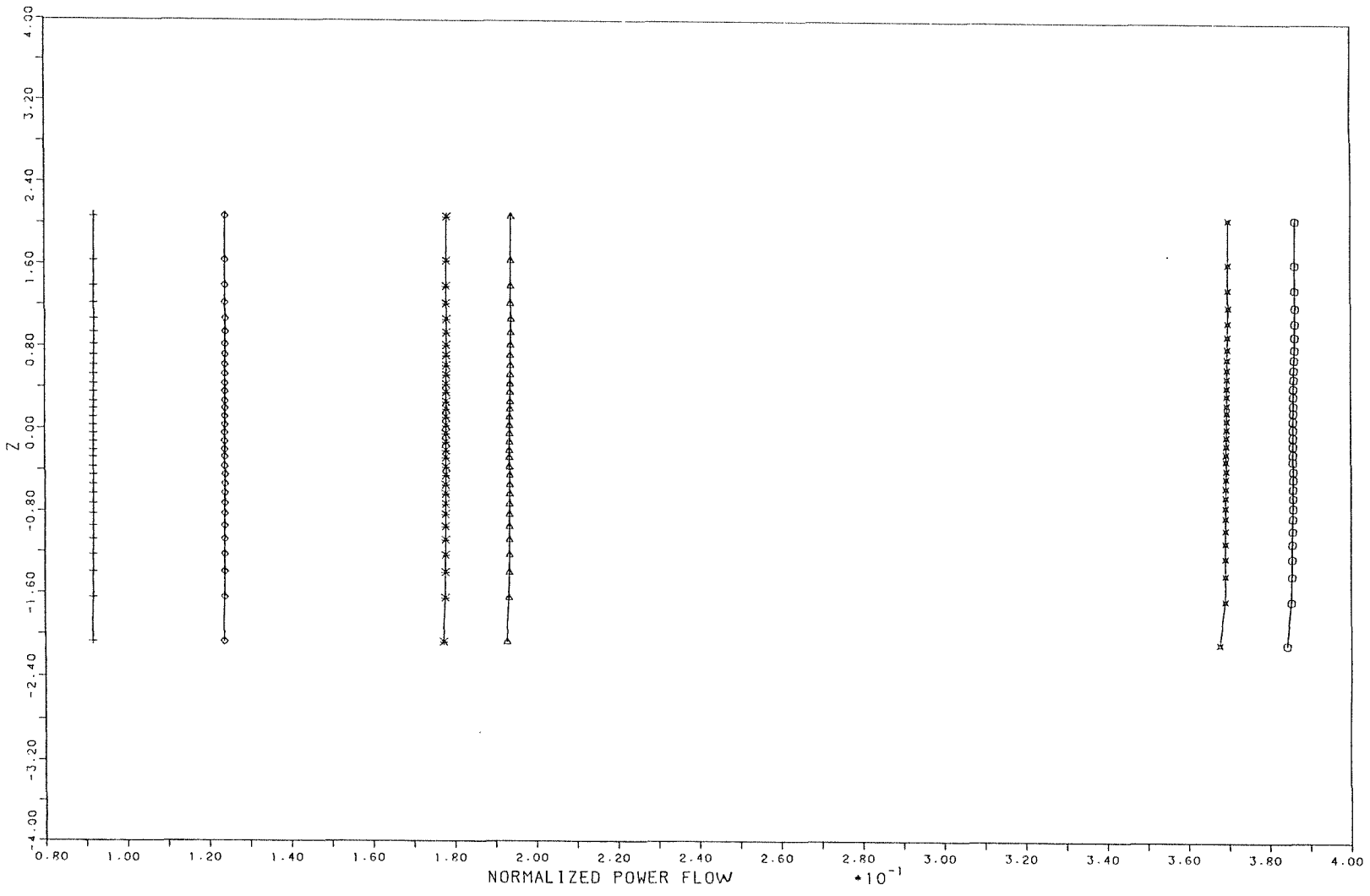

Figure (2.20): Cumulative distribution function of normalized power flow between two long coupled beams (from coupling stiffness perturbations)

CHAPTER 3

MEASUREMENTS OF POWER FLOW BETWEEN COUPLED BEAMS

3.1 Introduction

This chapter describes experimental investigations on coupled beams systems. It includes the following two main parts:

(a) Experimental work on two long, coupled beams, which represents a case of coupling between many resonant modes contributing to the energy sharing process in the frequency band of interest.

(b) Experimental work on a coupled system of short beams which represents a system of two coupled oscillators (resonant modes).

The same physical configuration has been used for both cases. It consists of two cantilever beams coupled at their free ends by a rubber vibration isolation pad. For both cases the power was input to the coupled system by applying a force to one of the coupled beams by a coil and magnet arrangement. The main objectives of these experiments were:

(i) To measure the time averaged quantities of the input power to the system, the power flow from the driven beam to the receiver beam, and the total energies of the coupled beams.

(ii) To study the sensitivity of the measured quantities to small variations in structural details of a long-long beams system by using the same approach which has been described in the theoretical presentation of the problem (Chapter 2). The sensitivity is judged by the interpretation of the results of the mean and the variance of the quantities of interest .

Both parts of this chapter may be divided into the following sections. A description of the properties of the individual components of the experimental model, the measured quantities and the method of the measurement, and a discussion of the results.

3.2 Measurements of Power Flow between Two Coupled Long Beams

3.2.1 Model description

The experimentally investigated coupled system consisted of two aluminium cantilever beams forming the configuration shown in figure (3.1.a). The dimensions of the beams are given in the table below. The beams are coupled at their free ends via a flexible, non-conservative coupling element. The clamped boundaries of the beams were achieved by using massive steel jaws which were fixed on heavy concrete blocks. Each concrete block had the dimensions of $(0.5 \times 0.5 \times 0.5)$ m^3, which ensured good isolation of the experimental rig from the ground. The coupled beams system was suspended, at six positions along the span, from an overhead frame using thin steel wires. The distances between the suspension points were selected to be equal to ensure a uniform distribution of the beams weights. The complete lay-out of the rig can be seen in figure (3.1.b).

Length (mean)	Beam 1 (L_1) Beam 2 (L_2)	3.42 m 3.40 m
Width	Beam 1, and 2	0.05 m
Thickness	Beam 1 Beam 2	0.005 m 0.005 m
Material	Beam 1, and 2	Aluminium
Modulus of elasticity (assumed)	Beam 1, and 2	7.1E+10 N/m^2
Density (assumed)	Beam 1, and 2	2700 Kg/m^3
Modal density	Beam 1 Beam 2	0.032 Mode/Hz 0.032 Mode/Hz

The dimensions of the beams were selected such that there were seven modes having natural frequencies in the frequency band of interest (100-300 Hz) contributing to the frequency response function of each uncoupled beam as shown in figure (3.2). The transfer function between the force and the velocity at the driving point can be seen in figure (3.3). This figure shows a typical example of the coupled mode frequencies of the coupled system.

The coupling element which was used to couple the free ends of the beams was manufactured from natural rubber. It had a translational stiffness of 1.3E+4 N/m and a dissipation loss factor of 0.15 (established in earlier investigations [50]). It had a thickness of 1 cm and cross section dimensions of 1.2×1.2 cm. The square faces of the natural rubber were glued to 2 mm thick aluminium plates. These plates had the same area as that of the coupling material. The coupling element was glued to the free ends of the beams (see figure 3.1.c).

3.2.2 Instrumentation

The instrumentation used in the measurements consisted of a vibration exciter, vibration accelerometers, and FFT signal analyzer which also produced the pseudo random binary sequence (PRBS) input signal.

The electro-dynamic vibration exciter consisted of a small, light electrical coil placed in the annular gap of a small magnet. This simple mechanism was held horizontally on an elevator system. The latter was mounted on a heavy steel support and permitted fine, vertical and horizontal adjustments for the coil-magnet mechanism, minimizing any pre-deflection of the coupled beam system. The generated input signal was fed to a power amplifier before it was received by the vibration exciter. A force transducer was screwed to the tip of the electrical coil from one side and tightly fixed to the face of the driven beam from the other side.

The signal from the force transducer was fed through a coaxial cable to a charge amplifier and then into the measuring equipment. The piezoelectric element in the transducer produces a small charge which is proportional to the acceleration or the force. This charge is transformed into a voltage signal in the charge amplifier. The charge amplifiers used for these experiments had three-digits charge sensitivity

calibrators and two integrators in series; these provide the options of measuring directly velocity or displacement.

The measuring equipment consisted primarily of the vibration pick-up transducers and the signal analyzer. The vibration transducers had a weight of 2.6 grams which was expected to have negligible mass loading effects on the vibrating system, and hence mass loading corrections of the measured quantities were unnecessary.

The vibration signal was fed to the signal analyzer via a charge amplifier. A two-channel digital signal analyzer was used for the signal processing part of the experiments. The analyzer is equipped with software which can perform the time and frequency domain analysis of the acquired signals. A digital plotter was connected to the analyzer for the screen dumping of the results.

A spectrometer and level recorder were also used in the experiments for the purpose of the measurement of the internal loss factor using the decay rate method.

The complete set-up of the instruments and the rig is shown in figure (3.4).

3.2.3 Measurements

The accelerometers are accompanied by the manufacturer's calibration charts, which stated their sensitivity in volts/g. Since this sensitivity may change with time and usage, all the accelerometers were calibrated when connected to a charge amplifier and the digital signal analyzer. The calibrator consisted of an electromagnetic vibration exciter, which generates a known amplitude at a fixed frequency. The measured values for all accelerometers confirmed the values provided by the manufacturers. The experiments were conducted to measure the following quantities:

(a) The dissipation loss factors of the uncoupled beams. This kind of measurement was carried out on bare beams, and also while the beams had damping material attached.

(b) The measurement of time averaged injected power to the system by the vibration exciter. This was carried out using the acquired acceleration signals at the excitation point.

(c) The measurement of time averaged power flow between the coupled beams using the acceleration signals at the coupled ends of the beams.

(d) The measurements of the time averaged kinetic energies of the coupled beams which were then doubled to obtain the total energies. These measurements were done using the signals acquired at a number of positions along the beam spans.

3.2.3.1 *Internal loss factor measurement*

The measurements of the dissipation loss factors of the uncoupled beams were conducted for different damping levels. The reason for this was to provide different values for the modal overlap factors of the beams. The damping was applied to the beams by attaching layers of thin, self-adhesive damping tape on both sides of the beams.

Two basic experimental techniques were involved in these measurements. These techniques are (i) the decay rate method and (ii) the steady-state (half-power bandwidth) method. The reason for employing different methods rather than relying on only one is that, for very low damping levels, one generally obtains more accurate results by using the decay rate method than using the half-power bandwidth method and vice-versa.

For the decay rate method, the band limited PRBS excitation was suddenly turned off, and the decay of the vibration was observed. If T_{60} is the reverberation time with which the energy of the vibration is reduced by 60 dB from its initial value and f_c is the centre frequency of the band, then the loss factor may be written approximately as [33]

$$\eta = \frac{2.2}{f_c \, T_{60}}$$

The measurements were conducted over a frequency band from 100 Hz centred at 300 Hz. The uncoupled beam was driven at a number of randomly selected points while an accelerometer was attached at another randomly selected point on the beam. The acceleration signal was fed to a charge amplifier. The signal was next fed to a

spectrometer that drives a level recorder. The decay time was measured on the smooth decay curve which was plotted on the level recorder.

The resulting value of the loss factor was then arithmetically averaged over various input points and the observation points. The measurements were repeated several times and the loss factor measured by this method gave values up to 0.05.

The half-power bandwidth method makes use of the frequency response function of the uncoupled beam to measure the dissipation loss factor. The beam was excited by a PRBS signal in the frequency band 100 Hz to 300 Hz. The signal from the force transducer and the accelerometer were input to the analyser which was set-up to display the frequency response function. By performing the measurement over narrow enough bands, to ensure an adequate frequency resolution, the half power modal bandwidths were easily measured on a linear-log plot of the frequency response function as demonstrated in figure (3.5) for a typical resonant mode. Seven resonant modes were included for the measurements in the frequency band selected above for each uncoupled beam under investigation. The dissipation loss factor may be written as

$$\eta = \frac{\Delta f}{f_n}$$

where Δf is the half power modal bandwidth and f_n is the resonance frequency of the mode n. The values of loss factor obtained from each single resonance response were averaged over the available number of resonant modes to obtain the averaged modal dissipation loss factor. Note that this method was used on beams having many damping layers attached to both sides of the beams. The range of loss factor measured by this method was 0.05-0.15.

3.2.3.2 *Vibrational input power measurement*

The power was input to the coupled beams by the vibration exciter. The later was driven by the PRBS signal in the frequency band of 100 Hz to 300 Hz. The time averaged input power at any frequency may be written as

$$\bar{P}_{in} = 1/2\ \mathrm{Re}\{\tilde{F}.\tilde{V}^{*}\} \qquad (3.1.a)$$

or in spectral terms as

$$\bar{P}_{in}(\omega) = \mathrm{Re}\{\tilde{G}_{FV}(\omega)\} \qquad (3.1.b)$$

where $\tilde{F}$ and $\tilde{V}$ are the complex amplitudes of the force and the velocity respectively, $\tilde{G}_{FV}$ denotes the one-sided cross spectral density function between the force and the velocity. A force transducer and a light piezoelectric accelerometer was placed on axis on the driven beam. The driving point was at a distance of 1.2 m from the coupled end of beam 1.

Both the signals from the force transducer and the accelerometer were fed after charge amplification to the two channels of the analyzer. Using the built-in software of the analyzer, the real part of the cross power spectrum of the force and the integrated acceleration (velocity) signals were obtained. The resulting function was then integrated between the two specified frequency limits (100-300 Hz) to give the injected power in the band. A typical input power spectrum is shown in figure (3.6).

3.2.3.3 *Power flow measurement*

The vibrational power flow from the driven beam to the receiver beam was measured at the coupling point. This measurement was conducted by placing accelerometers on both sides of the coupling element as shown in the figure (3.1.c). The accelerometers picked up the acceleration levels of the coupled beams at the coupling point.

Using the same principles as for the previous section, the power flow can be measured by performing the dot product between the force of the coupling $\tilde{F}_c$ and the velocity at the coupled end of the receiver beam $\tilde{V}_2$, i.e.,

$$\bar{P}_{12} = 1/2\ \mathrm{Re}\{\tilde{F}_c.\ \tilde{V}_2^{*}\}\ , \qquad (3.2)$$

$$= 1/2\ \mathrm{Re}\{\tilde{K}(\tilde{w}_1-\tilde{w}_2).\ \tilde{V}_2^*\} \quad , \qquad (3.2.a)$$

where $\tilde{K}=K(1+j\eta_c)$ is the complex stiffness of the coupling element and η_c is the coupling dissipation loss factor. Equation (3.2.a) can be written approximately as

$$\approx 1/2\ \mathrm{Re}\{\tilde{K}(\tilde{w}_1.\ \tilde{V}_2^*)\} \quad \text{for } \eta_c \ll 1 \ , \qquad (3.3)$$

or in spectral terms

$$\bar{P}_{12}(\omega) = \mathrm{Re}\{\tilde{G}_{w_1 v_2}(\omega)\} \qquad (3.3.a)$$

where $\tilde{w}_1$ and $\tilde{w}_2$ are the displacements of the driven beam and the receiver beam at the coupling point respectively. The results of equation (3.3.a) were then integrated over the frequency limit of interest (100-300 Hz) to produce the power flow in that band. A typical picture of the cross spectrum can be seen in figure (3.7).

3.2.3.4 *Vibrational energy measurement*

The time averaged kinetic energies of the coupled beams were estimated from vibration measurements and then doubled to obtain the total energies. An accelerometer was successively attached on eight randomly selected points on each beam. The vibration energy was supplied by the vibration exciter which was driven by the signal described in the previous sections. The accelerometers were chosen for both their light weight and the flat response over the frequency range of the experiments. The signals from the accelerometers, already amplified via the charge amplifiers, were fed into the signal analyzer. These signals were integrated and the mean squared velocities were obtained by setting the analyzer to calculate the auto-spectrum of the acquired signals. The measurements were repeated for the number of selected points on the beams, and then integrated over the frequency band of the experiment. The results were then averaged over the selected points of observation.

The time-averaged kinetic energies were then calculated by multiplying the results by the total mass of the beams. Typical examples of the velocity auto-spectrum can be seen in figures (3.8) and (3.9).

3.3 Perturbation Analysis

In order to study the sensitivity of the measurements of the present work to the small variations in the details of the coupled structure under investigation a statistical population model was created from the measured quantities of interest. A similar approach to that described in the previous chapter was followed. It may be summarized by the following steps:

(a) The internal loss factors (η_1, η_2) of the uncoupled beams were measured using the methods described previously and the average modal overlap factor (M_{av}) was calculated as

$$M_{av} = \sqrt{M_1 M_2} ,$$

where M_1 and M_2 are the modal overlap factors of beam 1 and beam 2 respectively. M is given by

$$M = \eta\, n(\omega)\, \omega_c ,$$

where ω_c is the centre frequency of the band and $n(\omega)$ is the modal density of the beam which given by

$$n(\omega) = (1/2\pi)\, (1/\sqrt{\omega})\, (m'/YI)^{0.25} ,$$

where m' is the mass density of the beam, Y is the Young's modulus of the material and I is the second moment of area of the cross section.

(b) The length of the receiver beam (L_2) was perturbed according to a randomly selected length sample. The sample of L_2 had 16 elements and was drawn from a normally distributed population. The coefficient of variation applied was about 10% of the mean value of the length of the beam. The required length for each realization of coupled beams was obtained by releasing the screws of the steel block (the fixed boundary) and moving the boundary with the heavy concrete block the required distance along the span of the beam.Tight fixing of the steel block was then remade.

(c) For each different value of L_2 in the normally distributed sample, the time averaged input power, time averaged power flow, and time averaged total energies were measured as described in the previous sections in the frequency band of 100-300 Hz. The results formed ensembles of 16 elements.

(d) The coupling loss factor was then calculated from the measured ensembles as

$$\eta_{12} = \frac{\bar{P}_{12}}{n_1(\omega)\ \omega\ \{(\bar{E}_1/n_1)-(\bar{E}_2/n_2)\}}$$

(e) An estimate for the coupling loss factor of the corresponding infinite, coupled beams system was obtained by employing the travelling wave method, as described in the previous chapter. This estimate was used as a reference to be compared with the results obtained from the finite system under investigation.

(f) The modal overlap factors of the coupled beams were then progressively increased by attaching a layer(s) of damping material to the coupled beams.

(g). Steps (a)-(f) were then repeated for the new values of modal overlap factor.

Results for the mean and the 95% confidence interval of the mean of the coupling loss factor (η_{12}) and the normalized power flow $\frac{\bar{P}_{12}}{\bar{P}_{in}}$ were calculated from the measured ensembles and plotted against M_{av} in figures (3.10) and (3.11) respectively. The confidence interval for the mean which has been defined previously (chapter 2) was calculated as

$$C.I = \text{mean} \pm 2\ (s/\sqrt{n})\ ,$$

where s denotes the standard deviation and n is the sample size. Figures (3.12) and (3.13) display the normalized variance (variance/mean^2) of η_{12} and $\frac{\bar{P}_{12}}{\bar{P}_{in}}$ respectively.

3.4 Results and Discussion

Figure (3.10) displays the mean values, together with their 95% confidence intervals of the coupling loss factor, as a function of the average modal overlap factor of the experimentally investigated coupled beams system. The figure shows that the mean value increases rapidly as the average modal overlap factor (M_{av}) of the coupled system approaches the value of unity. It approaches the estimate of that for the corresponding infinite system as M_{av} takes (approximately) the value of 1 or greater. This result supports that obtained from the theoretically investigated coupled beams model (Chapter 2).

As described in the previous chapter, it is important to present the confidence interval of the mean of the quantity of interest. This interval defines the probability that any one realization in the acquired random sample of the specified quantity will occur within the limits of that interval. Figure (3.10) shows that the 95% confidence interval of η_{12} is relatively wider at low modal overlap cases than that at higher modal overlap. Again, this result supports that obtained in the previous chapter.

Figure (3.11) displays the results of another quantity of interest which is the normalized power flow $\frac{\bar{P}_{12}}{\bar{P}_{in}}$. It shows that the power flow decreases as M_{av} increases. This is because the amount of energy absorbed by the directly excited beam increases with its damping. The power flow reaches a relatively low value at higher modal overlap. The 95% confidence interval of the mean of $\frac{\bar{P}_{12}}{\bar{P}_{in}}$ shows a similar trend to that of the coupling loss factor. This result also supports those of the previous chapter.

Figures (3.12) and (3.13) show the results for the normalized variance of the coupling loss factor and the power flow respectively. The normalized variance in both figures has the tendency to decrease rapidly as the modal overlap factor increases. The comparison between these two figures shows that the normalized variance of $\frac{\bar{P}_{12}}{\bar{P}_{in}}$ is less than that of η_{12}. The reason for this may be attributed to the fact that the coupling loss factor is a more sensitive quantity than the power flow, because η_{12} is a ratio

between the power flow and the energy difference of the coupled system. The latter may be very sensitive to perturbations when it is small.

It should be noted here that the reason for not reporting M_{av} values greater than 1.16 was because of the experimental difficulties in obtaining damping levels that satisfy the higher modal overlap conditions for the selected lengths of beams.

Figure (3.14) shows the cumulative probability distributions of the coupling loss factor for different modal overlap factor values. Again this figure supports the results obtained from the theoretical investigations that the distribution approaches the normality as M_{av} takes values near unity and greater.

3.5 Measurements of Power Flow between Two Coupled Modes

3.5.1 Model description

A physical configuration of the beam-beam system similar to that used in the previous section (3.1) was used for the experimental set-up in this case. This case represents modal interactions of only two resonant modes of the coupled beams in the frequency band of interest.

The system investigated consisted of two, short, steel beams having the dimensions and the properties described in the table below.

Length	Beam 1 (L_1) Beam 2 (L_2)	0.164 m 0.220 m
Width	Beam 1, and 2	0.025 m
Thickness	Beam 1 Beam 2	0.003 m 0.002 m
Material	Beam 1, and 2	Steel
Modulus of elasticity	Beam 1, and 2	1.95E+11 N/m^2
Density	Beam 1, and 2	7700 Kg/m^3

Light damping was applied to both beams by attaching thin layers of damping material to the faces of the beams. The coupling element had the same properties and dimensions as that of the previously described long beams tests.

The object of this experimental work was to measure the time averaged input power, time averaged power flow, and time averaged energies of the two coupled beams and compare the spectra of these quantities with those obtained from the theoretical model in chapter 2.

3.5.2 Instrumentation

Similar instrumentation to that of the previous experimental work has been used. However, there were some differences that should be mentioned here. These differences were:

(a) Beam 1 was driven by a point harmonic force in the frequency range 20-200 Hz. The excitation was supplied by an electrodynamic exciter (coil and magnet).

(b) The input signal to the exciter was generated by an oscillator via a power amplifier.

(c) A digital phase meter was used to measure the phase angles of the quantities of interest.

(d) The received analogue signals (force and response) were monitored on B & K analogue voltmeters. The voltage readings were then calibrated to give the required engineering units of interest.

3.5.3 Measurements

The internal loss factors of the uncoupled beams were measured using the decay rate method which has been described previously. Loss factors values of 0.0013 for beam 1 and 0.0023 for beam 2 were found.

The acceleration level and the phase angle were measured at the required positions on the coupled beams from which the input power, power flow and the total energies were calculated in a number of frequencies in the frequency range of 20-

200 Hz, using principles similar to those described for the previous experimental work.

Using the mathematical model of the coupled beam system described in Chapter 2, the above quantities were predicted after the modification of the model to suit the case under investigation.

The computed and the measured results were compared and displayed in figures (3.15), (3.16), (3.17), and(3.18) for the input power, power flow, total energy of beam 1, and total energy of beam 2 respectively.

3.5.4 Results and discussion

Figure (3.15)-(3.18) display the theoretical and experimental results for the input power, power flow, and the total energies in two coupled modes as function of frequency in the range of 20-200 Hz. The figures show good agreement between the measured and the predicted natural frequencies of the system under investigation. These natural frequencies were found to be 53 Hz for the first mode and 125 Hz for the second mode of the coupled system.

The comparison between the measured and predicted results indicates fairly good agreement at the natural frequencies of the coupled system. This good agreement is a more significant result than the disagreement shown in the off-resonance regions, because only the resonance regions contribute significantly to the power flow and energy contents of the coupled beams. The disagreement in the off-resonance regions may be attributed to the relatively low amplitudes which lead to poor experimental estimates. Care had to be taken to ensure that the vibrational behaviour was properly linear, which it was found not to be at moderately high amplitudes. Figure (3.17) and (3.18) show relatively better agreement between the measured and the computed total energies of the beams than those of input power and power flow shown in figures (3.15) and (3.16). The reason for this may be related to the fact that energy measurements do not involve phase information (i.e., it is easy to measure) as input power and power flow measurements do. The comparison between total energy of beam 1 (E_1) and that of beam 2 (E_2) show that at off-resonance E_1 is smaller than E_2. This is an interesting observation because the excitation is applied on beam 1. A conclusion can be drawn from this observation that SEA is an inapplicable method for harmonic excitation. In other words, we cannot use the power flow energy difference

relationship for such a case because it clearly violates the assumption that energy can only flow from a component of high energy level to another of lower energy level.

3.6 Conclusions

Mean, variance and 95 per cent confidence interval for the mean for the coupling loss factor and the normalized power flow across an ensemble of coupled beams are obtained from experimental measurements. The following conclusions can be drawn from these results.

(a) The mean value of the coupling loss factor agreed with that obtained from the travelling wave method when the average modal overlap is high ($M_{av} \geq 1$), but at smaller values of modal overlap the coupling loss factor fell well below the travelling wave value. This result supports the theoretical analysis previously obtained.

(b) The normalized power flow decreases as M_{av} increases. This is because of the increase in the energy absorbed by the directly excited beam as the damping increases.

(c) Normalized variance results for coupling loss factor and the normalized power flow decreases as M_{av} increases. At any given modal overlap factor, normalized variance value for the normalized power flow is very much less than that for the coupling loss factor.

(d) The width of the 95 per cent confidence interval for the means of coupling loss factor and normalized power flow decreases as M_{av} increases. This will increase the probability of obtaining estimates for the above quantities which are close to the means. This result is confirmed by the construction of the cumulative probability distributions. The distributions for these quantities approach the normality as M_{av} increases ($M_{av} \geq 1$).

(e) The agreement between the theoretical and experimental values of input power, power flow, and total energies of two coupled modes is found to be good near the resonance frequencies of the coupled modes, but not so good near the anti-resonance frequencies.

(f) It is demonstrated that the power flow energy difference relationship cannot be applied for coupled systems under harmonic excitation because it violates the assumption that energy can only flow from high energy subsystems to low energy coupled subsystems.

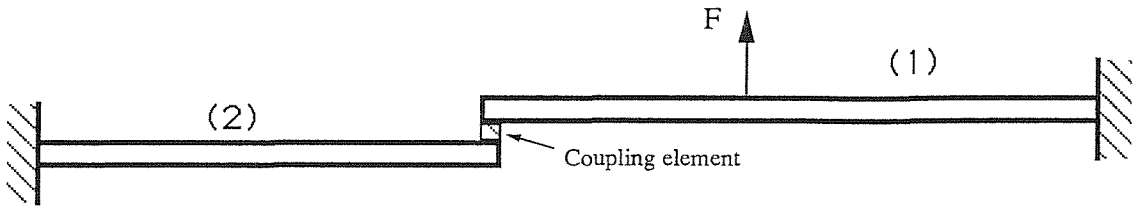

Figure (3.1.a) : Coupled beams system.

1.Coupled beams
2.Concrete block
3.Suspension wire
4.Supporting frame
5.Trolly
6.Fixed boundary

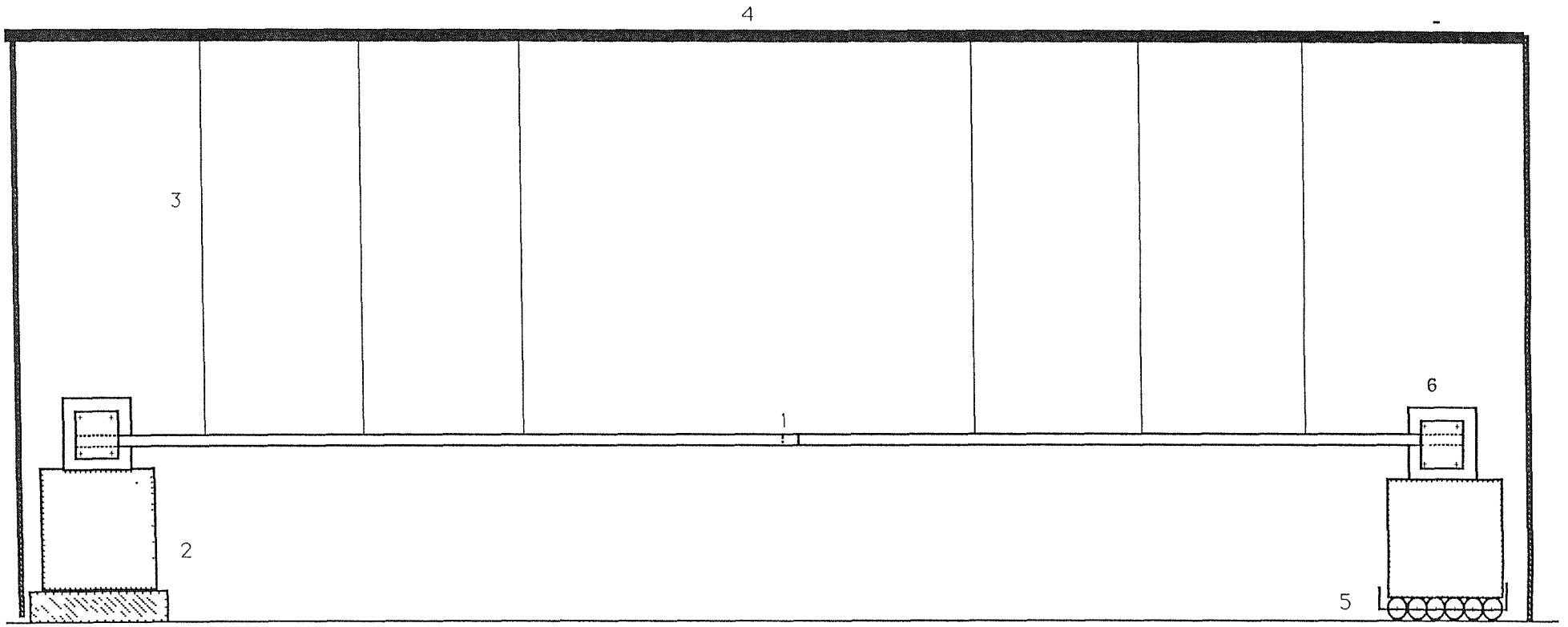

Figure (3.1.b) : The test rig.

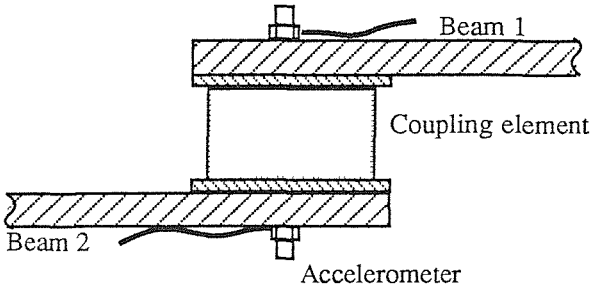

Figure (3.1.c) : The coupling element

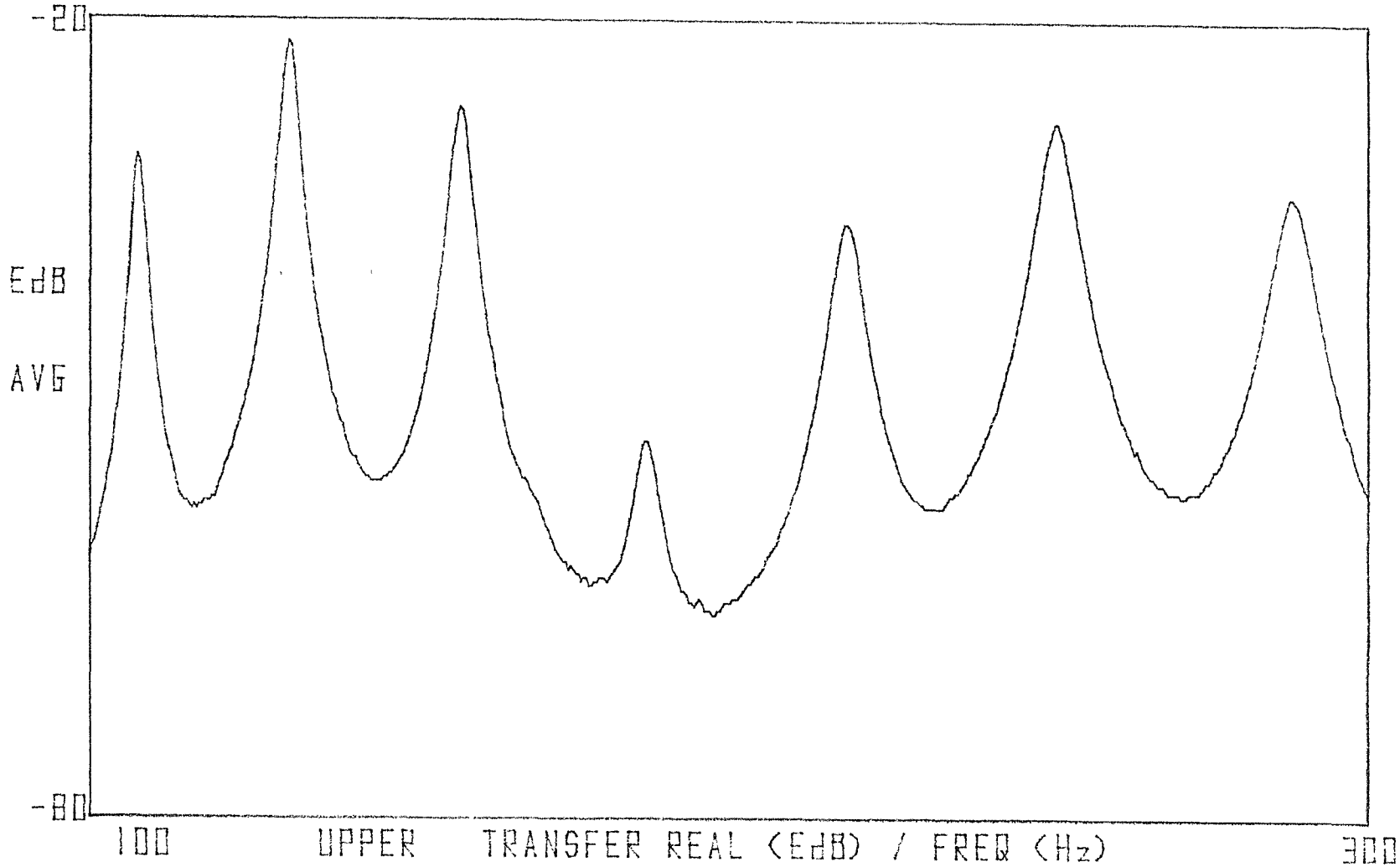

Figure (3.2): The real part of the driving point transfer function, between a force and a velocity, of uncoupled beam, L=3.4 m, η=0.015.

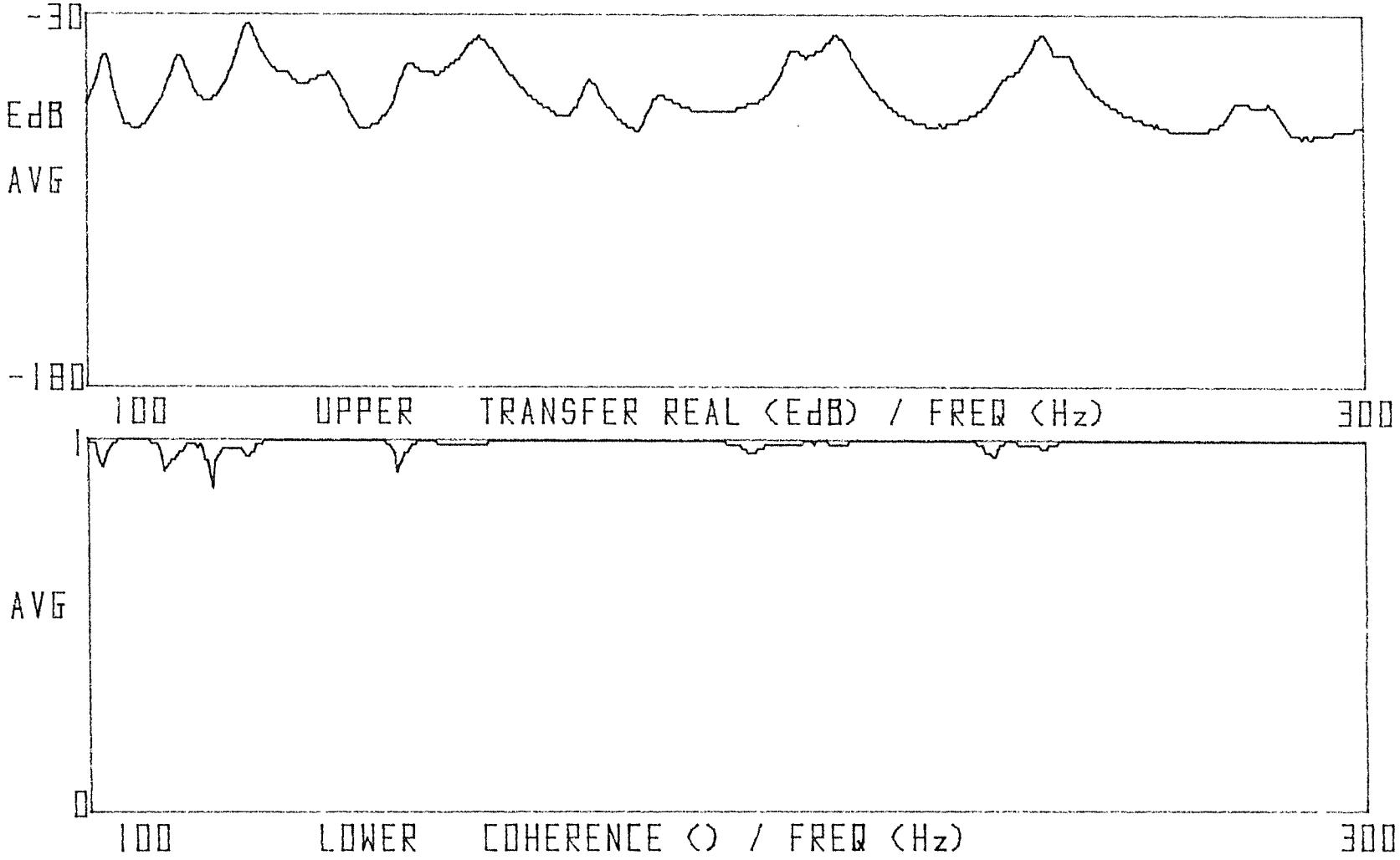

Figure (3.3): The real part of the driving point transfer function and the coherence function, between a force and a velocity, of coupled beams system, L_1=3.42 m, L_2=3.22 m, $\eta_1 = \eta_2$=0.03.

1. 2-Channel Digital Analyzer
2. Power Amplifier
3. Electrodynamic exciter
4. Accelerometer
5. Force Transducer
6. Charge Amplifier
7. Spectrometer
8. Level Recorder
9. Digital Plotter
10. Coupled BeamsSystem

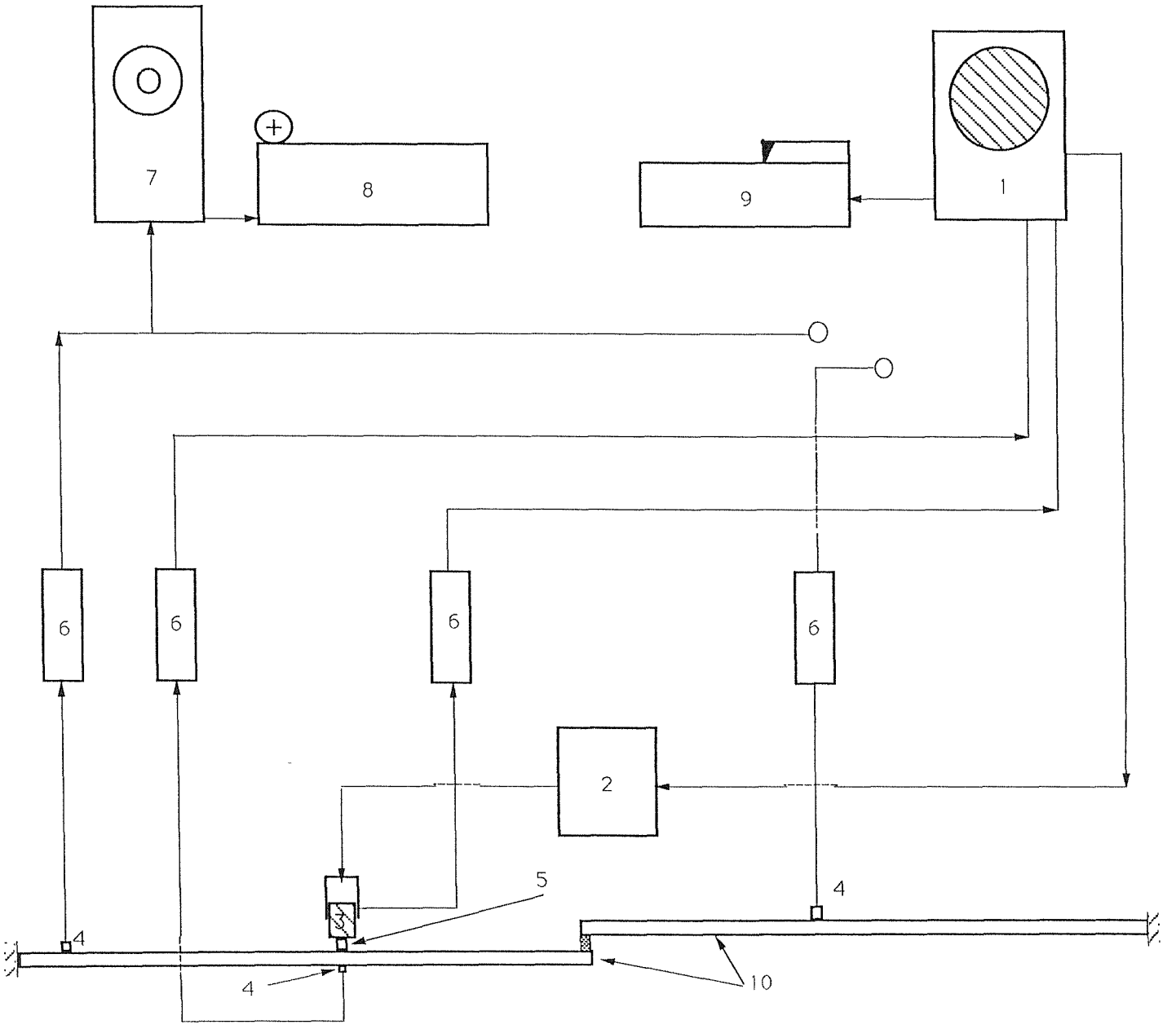

Figure (3.4) : The instrumentation.

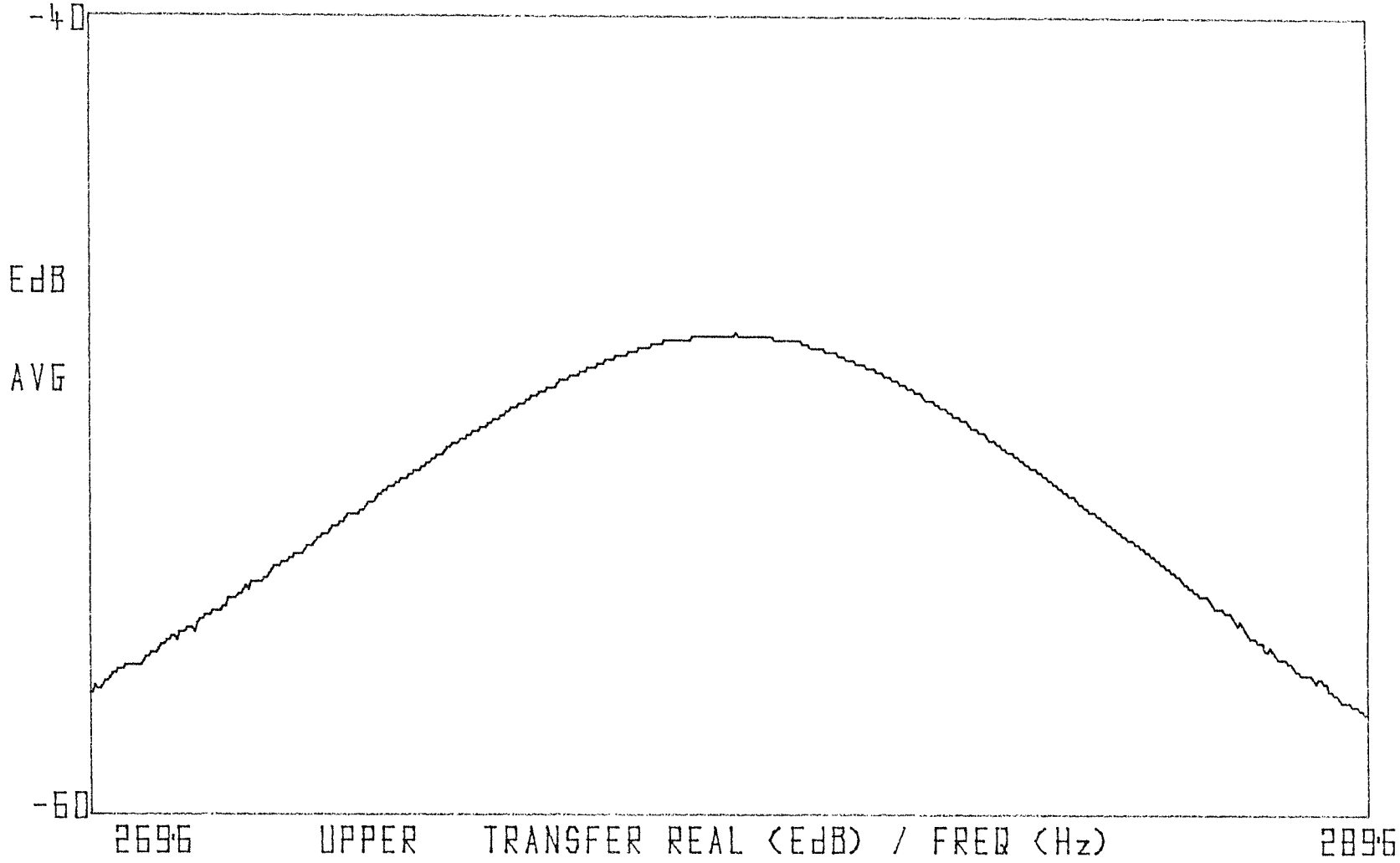

Figure (3.5): A typical resonant mode of an uncoupled beam having natural frequency of 280 Hz.

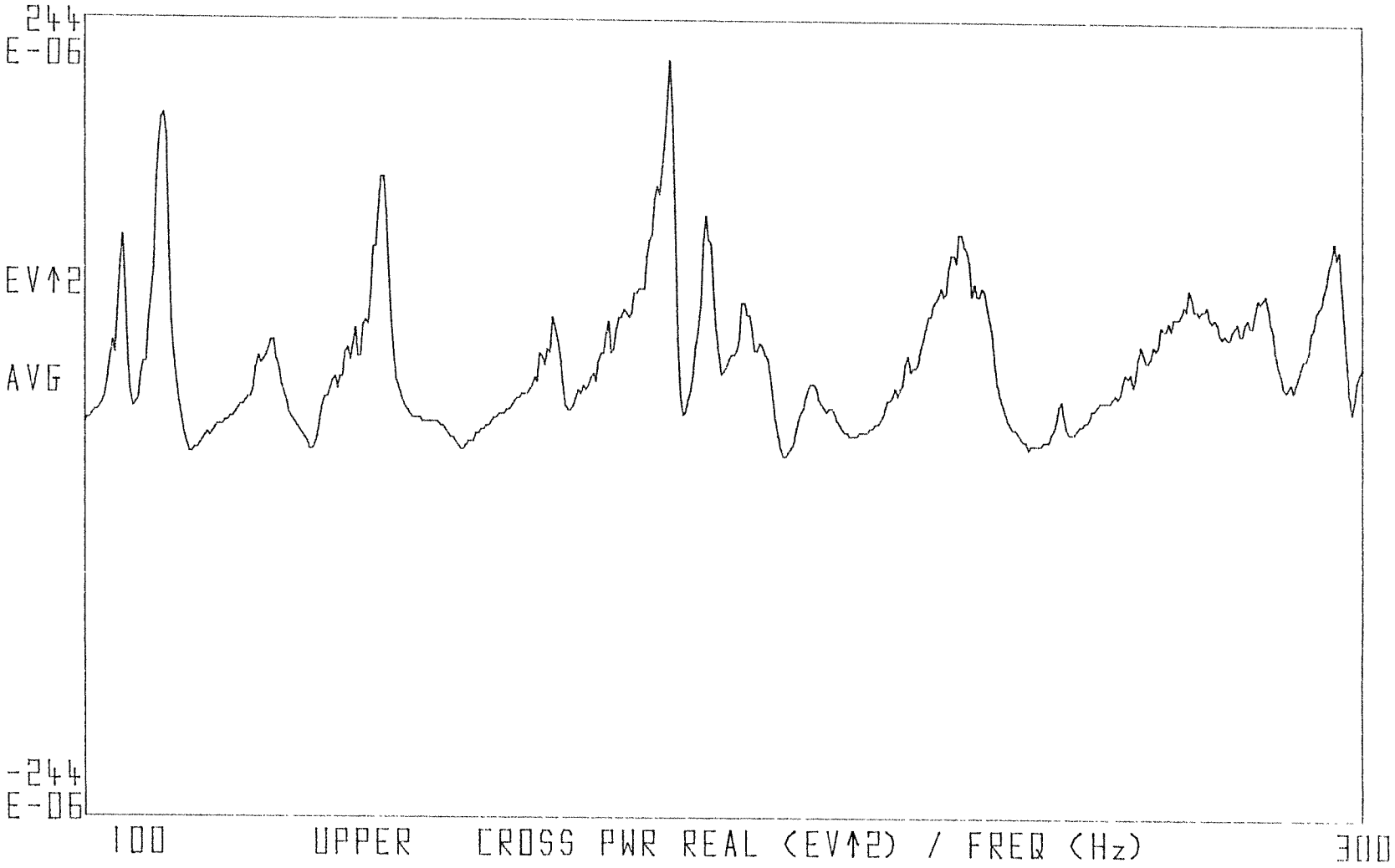

Figure (3.6): A typical real part of a cross power spectrum, between a force and a velocity at the driving point of the coupled beams system.

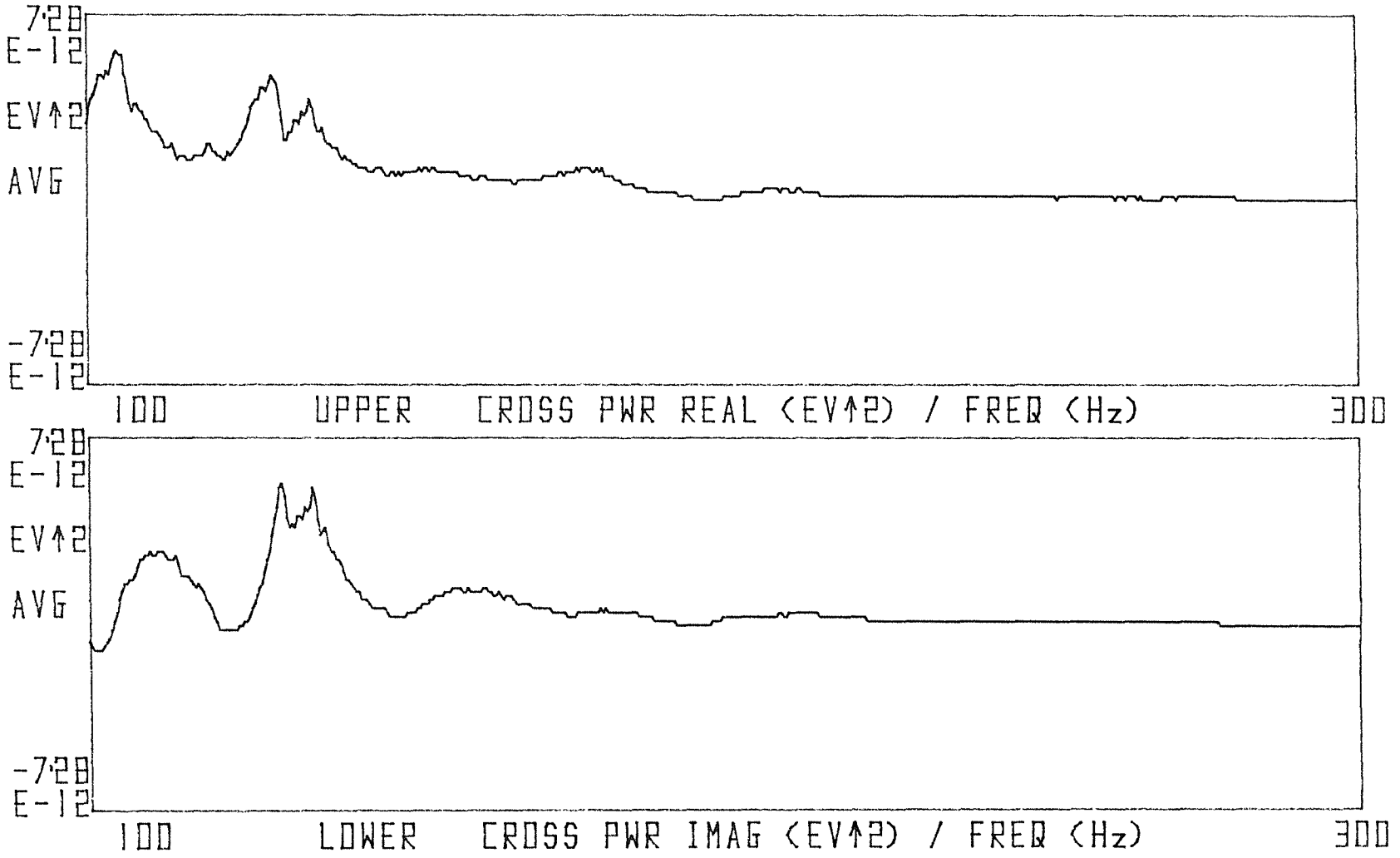

Figure (3.7): The real part and the imaginary part of the cross spectrum between the displacement of the directly driven beam and the velocity of the receiver beam at the coupling point. $\eta_1=\eta_2=0.09$, $L_2=3.3$.

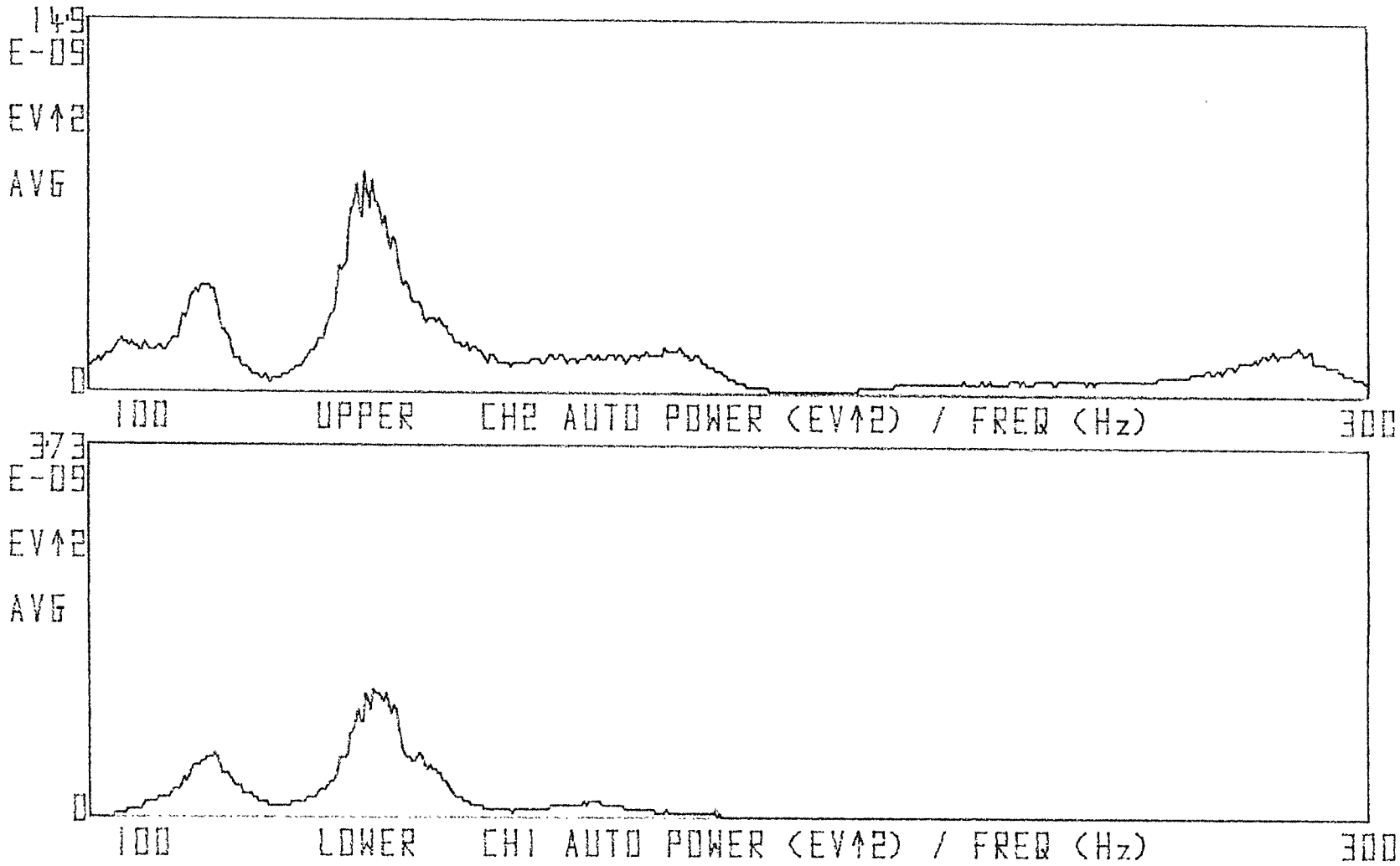

Figure (3.8): Auto power spectra of the velocities of the coupled beams. $\eta_1=\eta_2=0.055$, $L_2=3.05$ m. Top: driven beam, bottom: receiver beam.

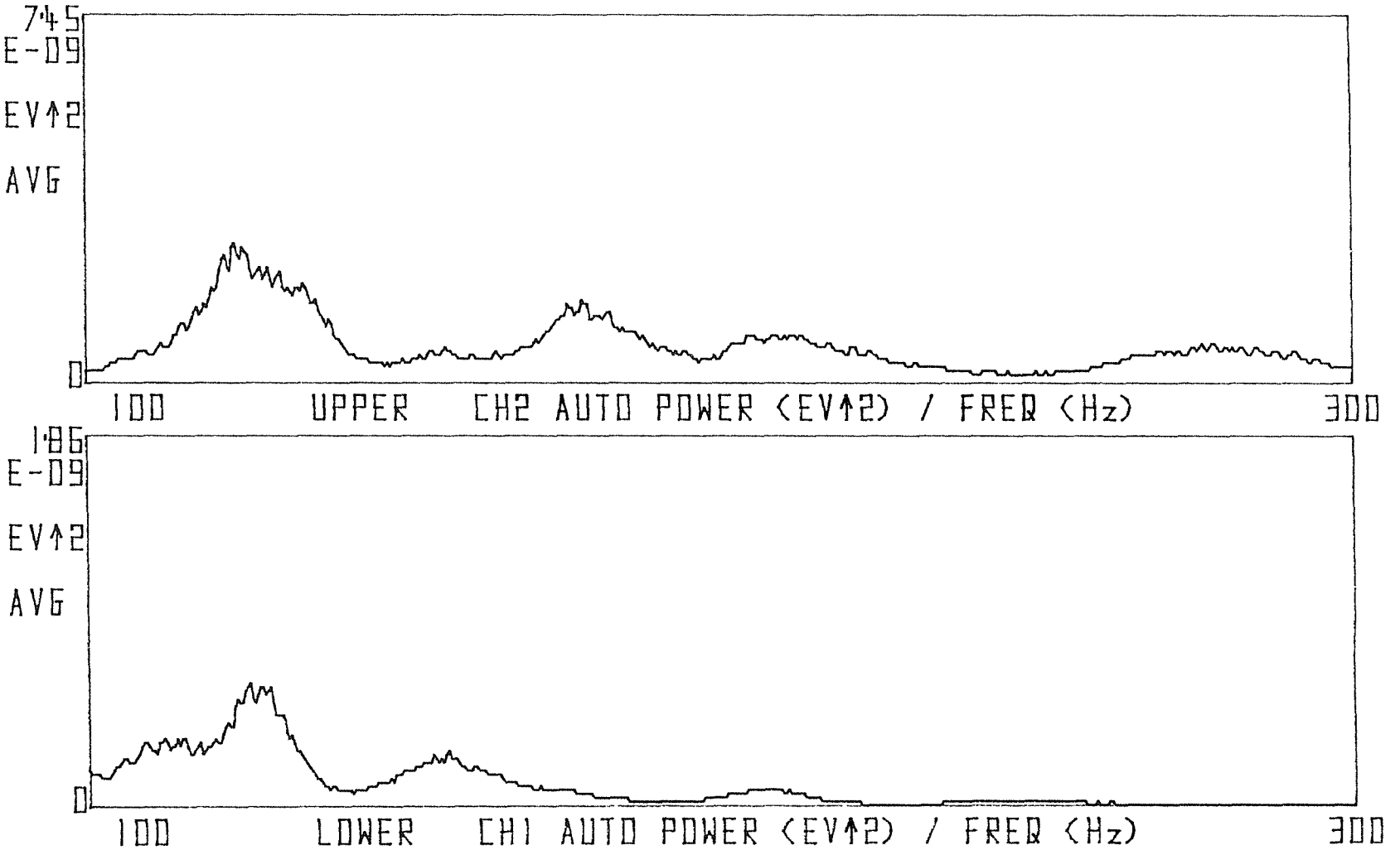

Figure (3.9): Auto power spectra of the velocities of the coupled beams. $\eta_1=\eta_2=0.09$, $L_2=3.3$ m. Top: driven beam, bottom: receiver beam.

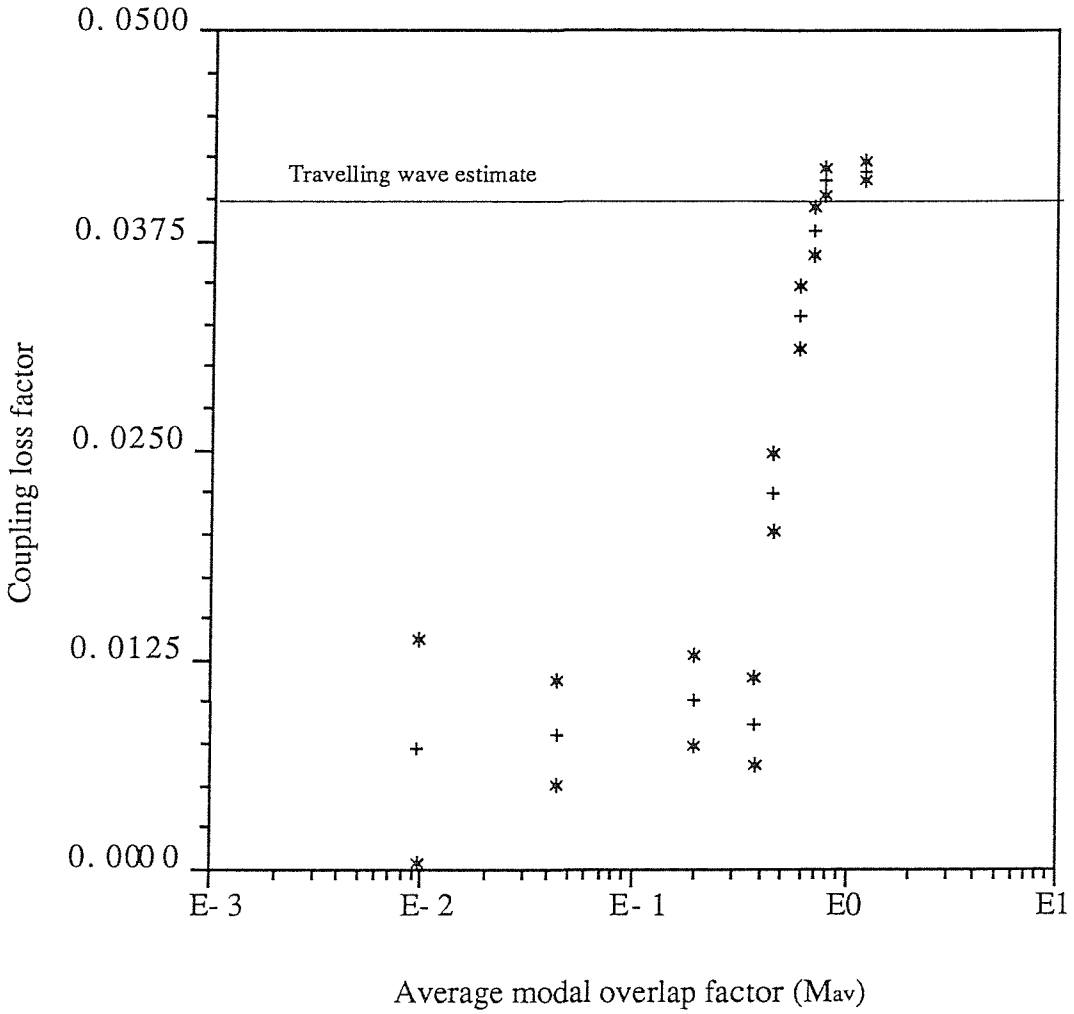

Figure (3.10) : The experimentally determined coupling loss factor of coupled beams. + Mean value, * * 95% confidence interval.

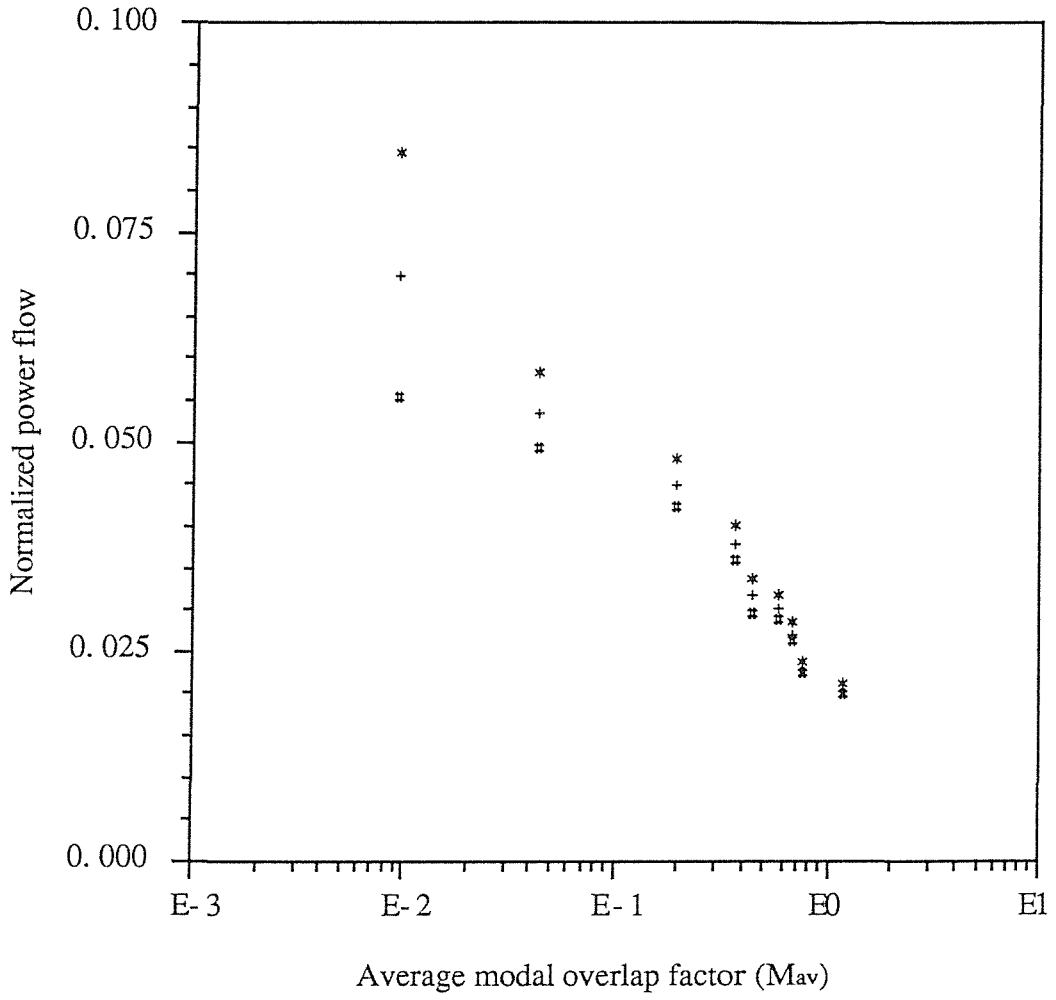

Figure (3.11) : The experimentally determined normalized power flow between two coupled beams. + Mean value, * # 95% confidence interval

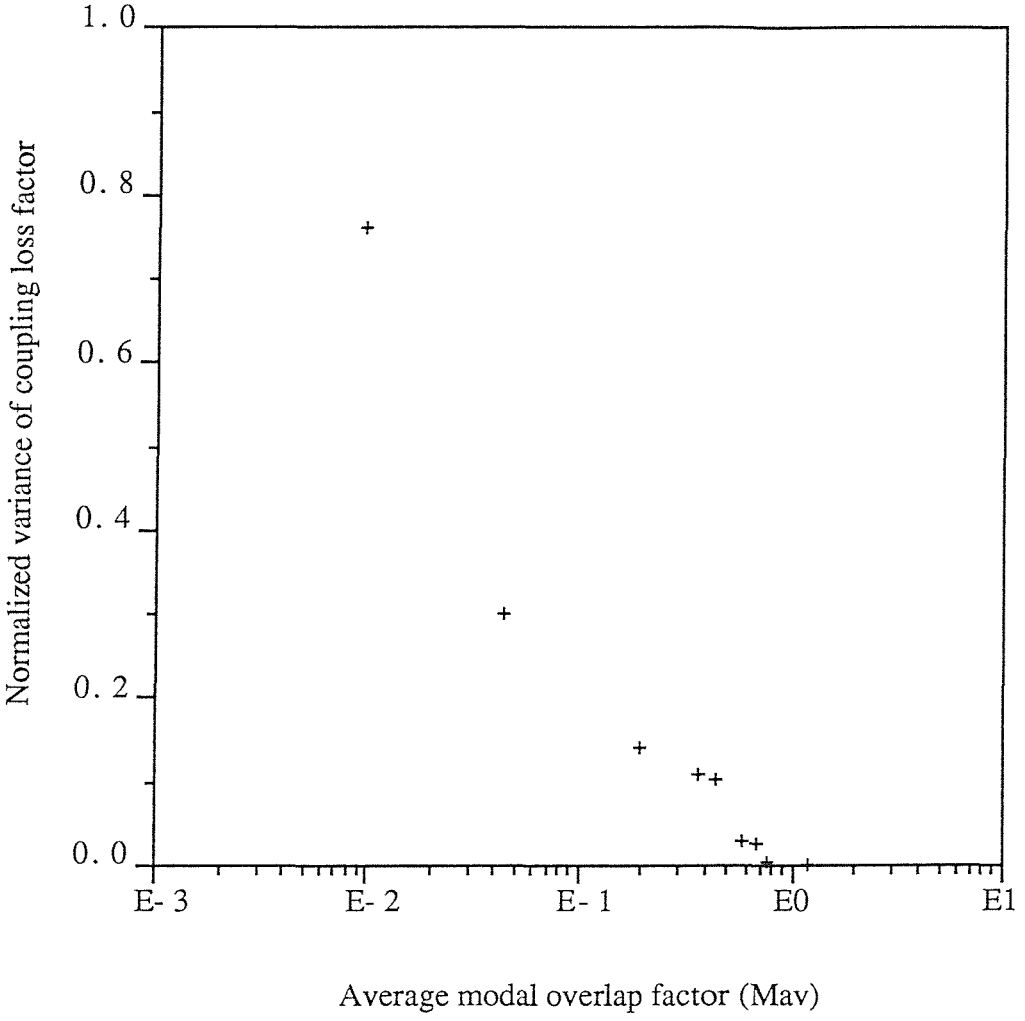

Figure (3.12) : Normalized variance of the experimentally determined coupling loss factor of coupled beams system.

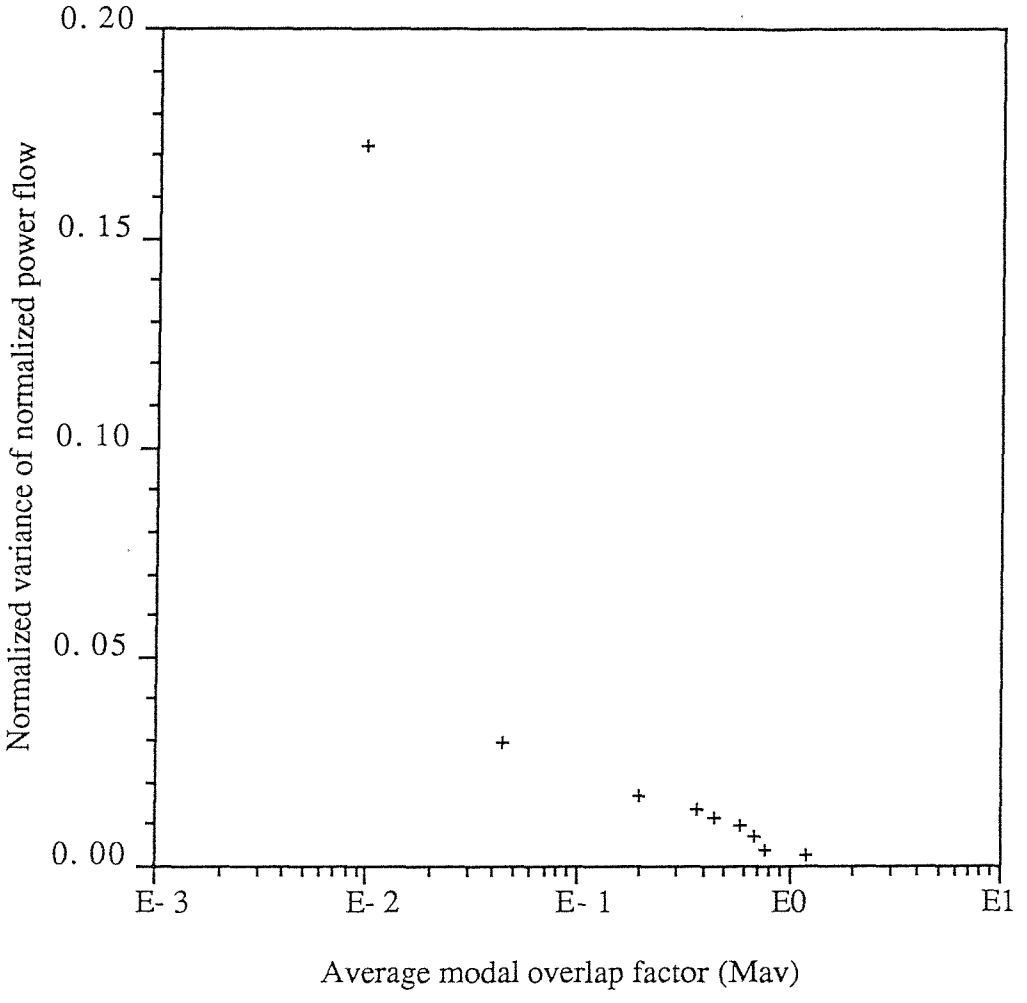

Figure (3.13) : Normalized variance of the measured normalized power flow between two coupled beams.

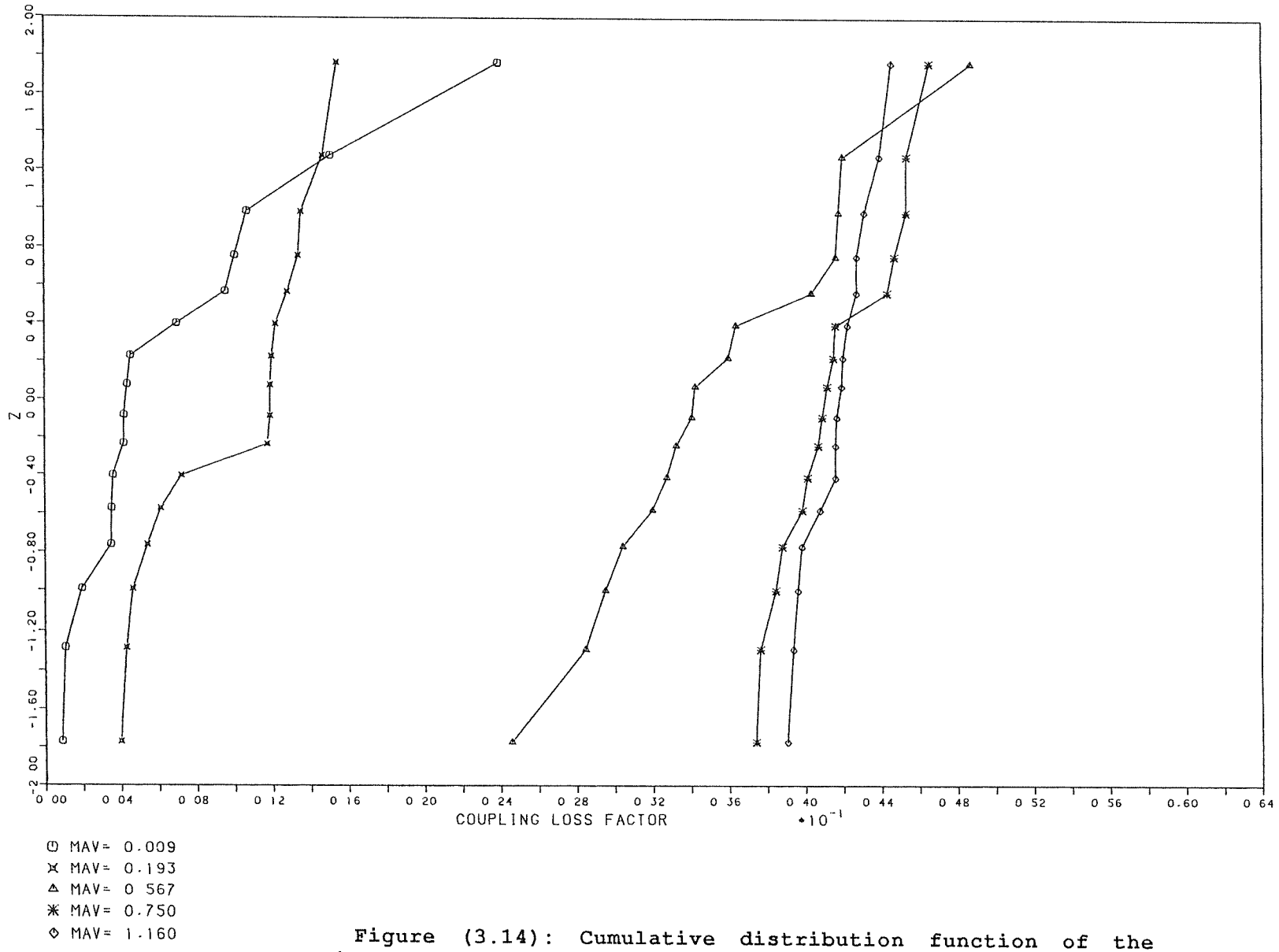

Figure (3.14): Cumulative distribution function of the experimentally determined coupling loss factor of two long coupled beams

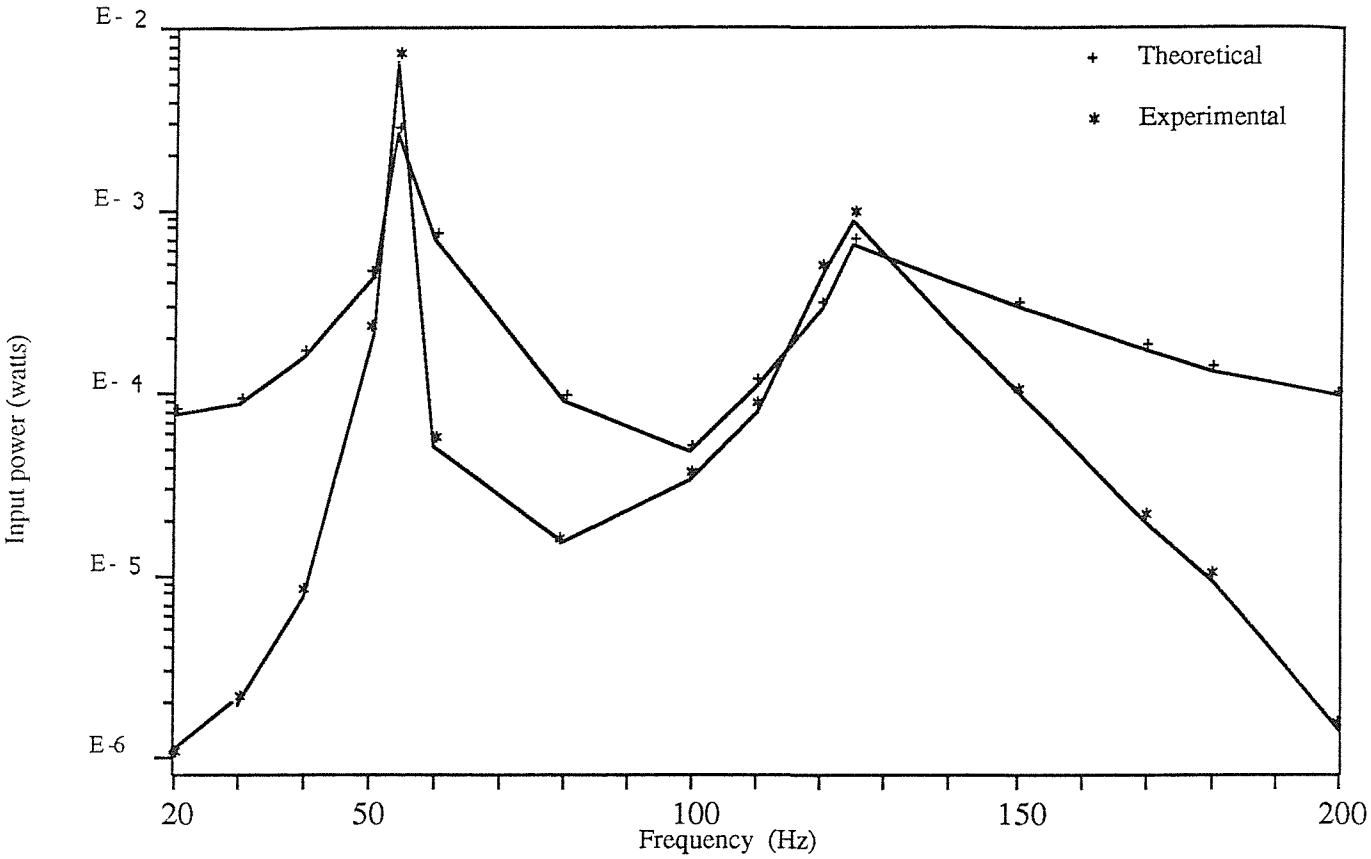

Figure (3.15) : A comparison between the measured and the calculated spectra of input power to a two, short coupled beams system.

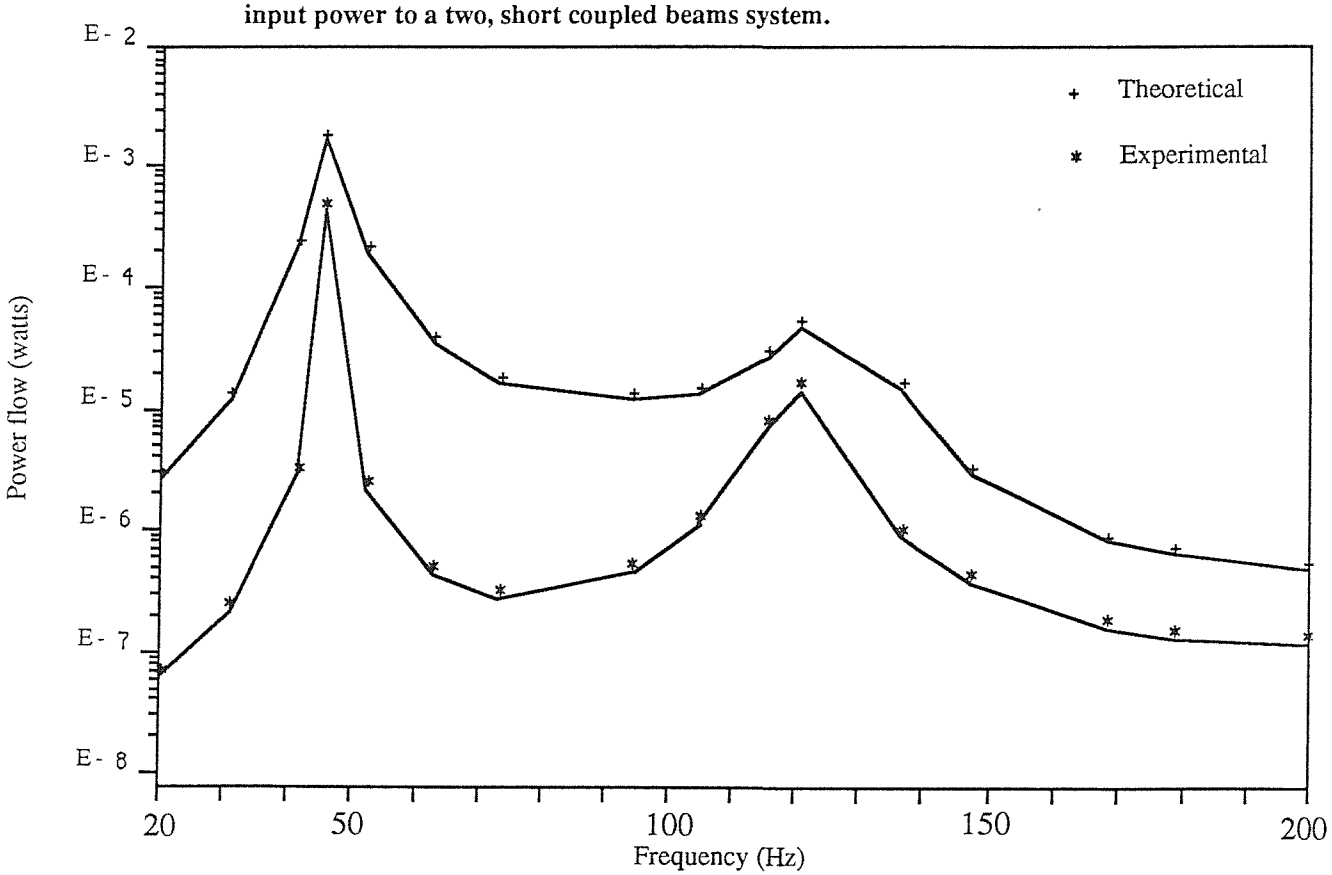

Figure (3.16) : A comparison between the measured and the calculated spectra of power flow between two, short, coupled beams.

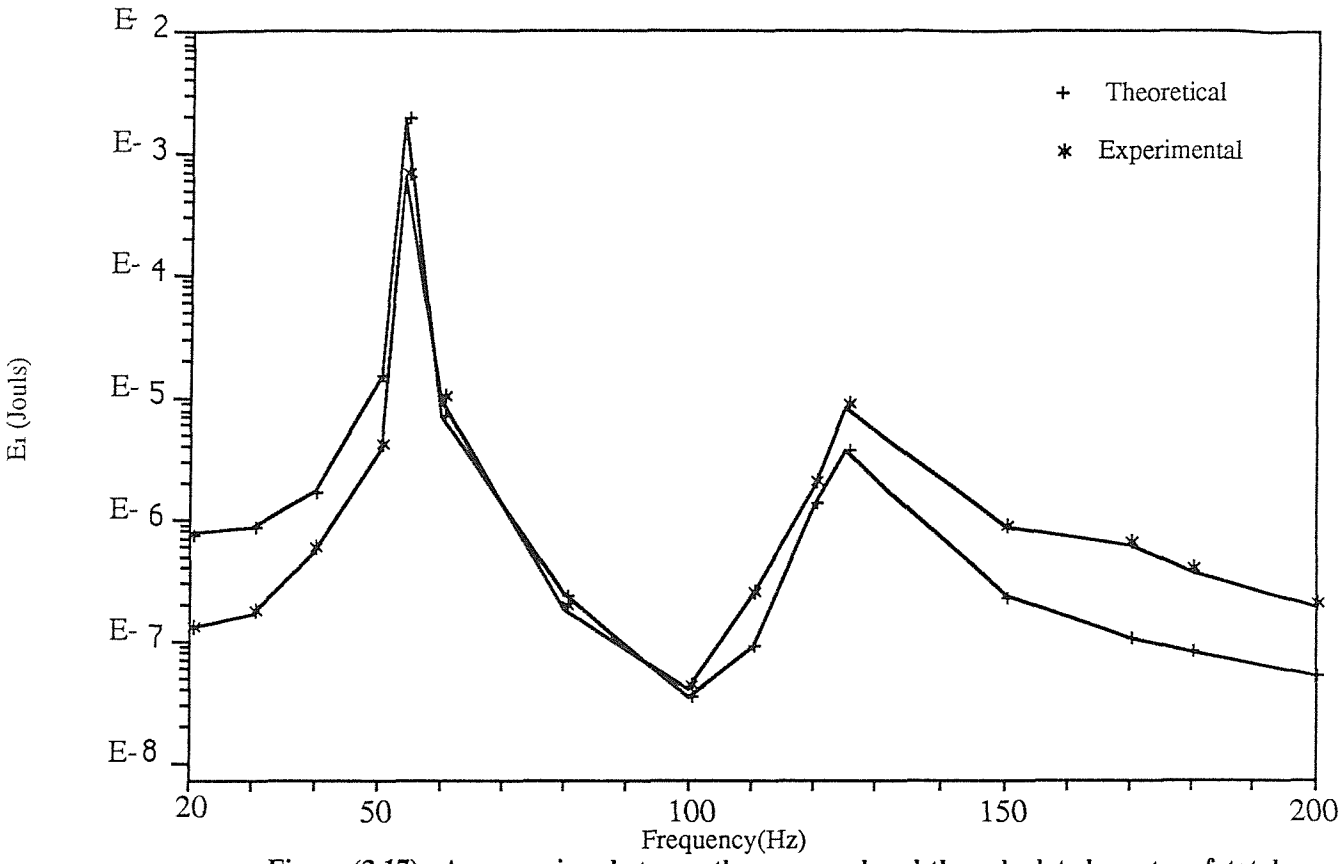

Figure (3.17) : A comparison between the measured and the calculated spectra of total energy of the directly driven beam of a two coupled beams system.

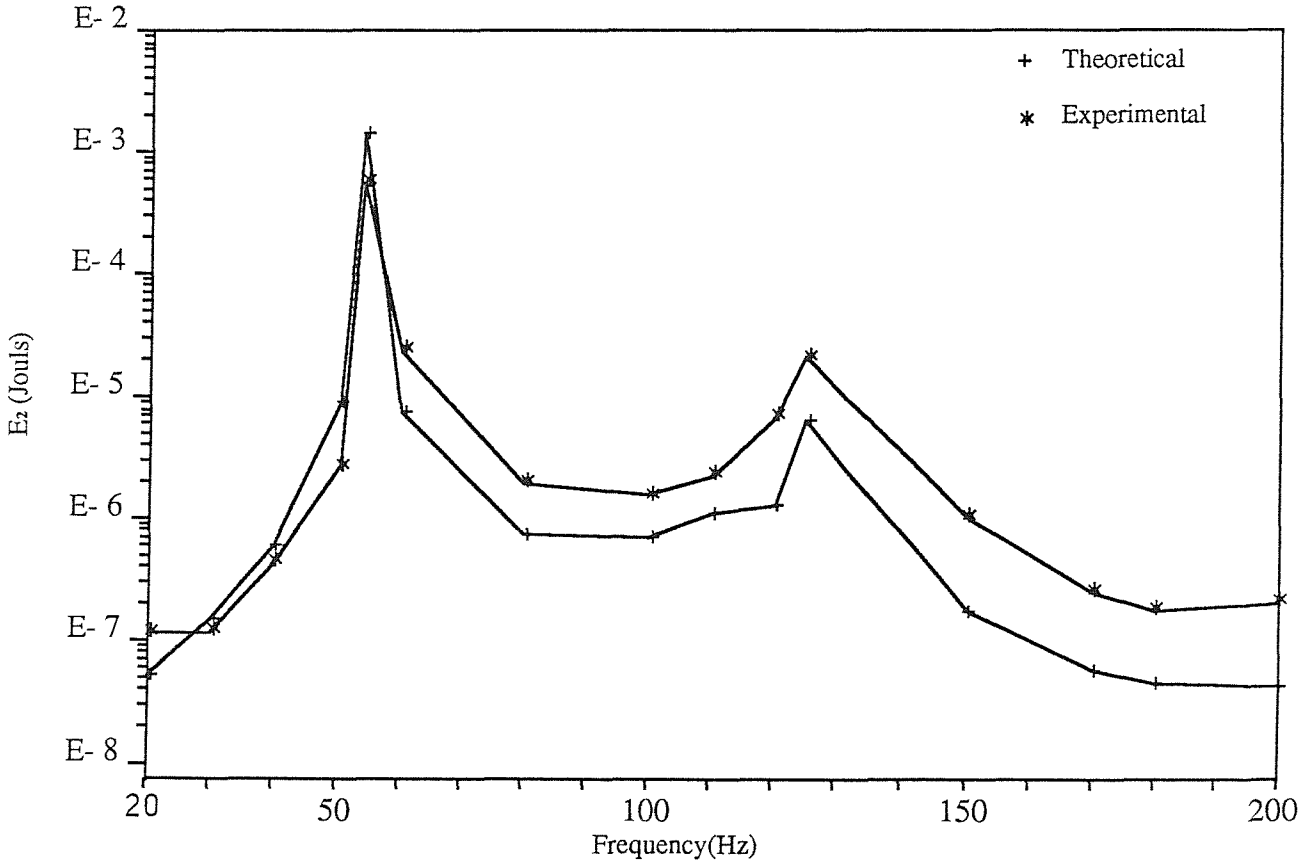

Figure (3.18) : A comparison between the measured and the calculated spectra of total energy of the receiver beam of a two coupled beams system.

CHAPTER 4

POWER FLOW BETWEEN COUPLED PLATES

4.1 Introduction

This chapter describes a study of the energy transmission between coupled plates due to the excitation of one of the plates by a (simulated) white noise source. Use is made of the general plate equation of motion. A closed form, separable type solution is used to predict the displacement response of the coupled structures under investigation. The solution is used to predict the quantities of interest, namely, the time averaged input power to the system, the time averaged power flow between the subsystems, the time averaged total energies of the coupled subsystems, and the coupling loss factor.

Ensembles of the predicted quantities are performed as results of the perturbations of the geometry of the coupled plates system using the distribution sampling application of the Monte Carlo method. The system analyzed is considered to be one realization taken from a set of similar, but not identical, systems having a known statistical distribution.

The objective of this work is to investigate the sensitivity of predictions of the model to the proposed perturbations. Results for the mean and variance of the ensembles are obtained and studied with respect to other structural parameters.

Two main cases are investigated in this chapter, namely, two coupled plates, and three coupled plates.

4.2 Two Plates System; Mathematical Model and Assumptions

The coupled system under investigation is shown in figure (4.1). It consists of two rectangular steel plates; each has two opposite sides simply-supported at the positions y = 0 and y = b. The plates are coupled together along one edge via an elastic, non-conservative coupling element which allows for translational as well as rotational motions of the coupled edges. The coupling element has a translational stiffness of $\tilde{K}_t$ and a rotational stiffness of $\tilde{K}_r$ where

$$\tilde{K}_t = K_t (1 + j\eta_c) \quad ,$$

and

$$\tilde{K}_r = K_r (1 + j\eta_c) \quad .$$

η_c is the dissipation loss factor of the coupling element. Damping is allowed for by means of hysteretic damping (η_1 and η_2 for plate1 and plate 2 respectively). The edges of the plates along which the coupling occurs have the same length ($b_1 = b_2 = b$). It is assumed that the plates are homogeneous, isotropic, and thin. The assumption 'thin' plates leads us to ignore the shear deformation and rotational effects. With the above-mentioned assumptions, classical thin plate vibration theory is valid.

The first plate (driven) is exited by a point harmonic force of a unit amplitude. For the purpose of analysis, the coupled system under investigation is divided into three simple plates (1, 2, and 3) as shown in figure (4.1). The division lines are considered to be the locations of the discontinuities (force position at $x_1 = 0$, and coupling position at $x_2 = 0$). Each simple plate will have its own geometric and natural boundary conditions. The free vibration of each plate is governed by the fourth order differential equation

$$\tilde{B}_i \left[\frac{\partial^2}{\partial x_i^2} + \frac{\partial^2}{\partial y^2} \right]^2 w_i + \rho_i h_i \frac{\partial^2 \tilde{w}_i}{\partial t^2} = 0 \quad , \qquad (4.1)$$

where w_i is the displacement, $\tilde{B}=\frac{\tilde{Y}h^3}{12(1-\upsilon^2)}$ is the flexural rigidity of the plate, $\tilde{Y} = Y(1+j\eta)$ is the complex Young's modulus, η is the loss factor, υ is the poisson's ratio, ρ is the density, h is the thickness, and i denotes the plate number (i = 1,2,3). The solution of the equation of motion will be sought in the form

$$\tilde{w}(x_i,y,t) = \sum_n \tilde{\varphi}_n(x_i) \sin(\frac{n\pi y}{b}) e^{j\omega t} , \qquad (4.2)$$

where $\varphi_n(x_i)$ is a function of x_i for plate i, n is an integer and j denotes $\sqrt{-1}$. This solution satisfies automatically the boundary conditions imposed by the simple supports at the positions y=0, and y=b. It remains to find the function $\varphi_n(x_i)$ for each value of "n" in the series.

The externally applied force distribution on the coupled structure at the position $x_1 = 0$, (or $x_2 = L_2$), and $y = y_o$ is represented by

$$F(y,t) = F_o \delta(y-y_o) e^{j\omega t} , \qquad (4.3)$$

where F_o is the force amplitude and ω is the frequency of vibration. δ is the Dirac delta function. This force may be expanded in a Fourier series of sine-terms, i.e

$$F(y,t) = \sum_n F_n \sin(\frac{n\pi y}{b}) e^{j\omega t}. \qquad (4.4)$$

By the usual method, we find

$$F_n = \frac{\int_0^b F(y,t)\,\sin(\frac{n\pi y}{b})\,dy}{\int_0^b \sin^2(\frac{n\pi y}{b})\,dy}\ , \qquad (4.5)$$

or

$$F_n = \frac{2F_o}{b}\,\sin\,\frac{n\pi y_o}{b}\ . \qquad (4.6)$$

The expression in equation (4.6) will appear in one of the boundary conditions at the excitation point. Therefore,

$$F(y,t) = \sum_n\ (2/b)F_o\,\sin(\frac{n\pi y_o}{b})\,\sin(\frac{n\pi y}{b})\ e^{j\omega t}. \quad (4.7)$$

In order to find the function $\varphi_n(x_i)$ we consider equation (4.2). Each term of this equation must satisfy the differential equation (4.1) on its own. When such a term is substituted into the differential equation, the term $\sin(\frac{n\pi y}{b})\ e^{j\omega t}$ may be cancelled out leaving an ordinary equation in terms of $\tilde{\varphi}_n(x_i)$. This is of fourth order and so has the solution which can be written for the individual simple plate as

$$\tilde{\varphi}_n(x_1) = \sum_{m=1}^{4}\ \tilde{A}_{nm}\ e^{\tilde{K}_m x_1}\ ,$$

$$\tilde{\varphi}_n(x_2) = \sum_{m=5}^{8}\ \tilde{A}_{nm}\ e^{\tilde{K}_m x_2}\ , \qquad (4.8)$$

$$\tilde{\varphi}_n(x_3) = \sum_{m=9}^{12}\ \tilde{A}_{nm}\ e^{\tilde{K}_m x_3}\ .$$

The four k_m's in the above equations occur in two +/- pairs and are the wave numbers of the different wave forms for two positive going and two negative going waves of the different simple plates (1,2, and 3). They are the routes of the bi-quadratic equation (obtained from the differential equation), i.e.,

$$k_m^4 - 2\acute{\alpha}k_m^2 + \acute{\beta} = 0 \qquad (4.9)$$

where

$$\acute{\alpha} = \frac{n^2\pi^2}{b^2} = k_y^2$$

$$\acute{\beta} = \frac{n^4\pi^4}{b^4} - \omega^2\left(\frac{\rho h}{B}\right) = k_y^4 - k_p^4 \quad .$$

$k_p = \sqrt{\omega}\left\{\frac{\rho h}{B}\right\}^{0.25}$ is the flexural, free wave number. Therefore, equation (4.9) may be written as

$$k_m^4 - 2k_y^2 k_m^2 + (k_y^4 - k_p^4) = 0 \quad . \qquad (4.10)$$

Therefore, for each simple plate there four wave numbers such that equations (4.8) may be written

$$\tilde{\varphi}_n(x_1) = \tilde{A}_{n1}\, e^{\tilde{K}_1 x_1} + \tilde{A}_{n2}\, e^{\tilde{K}_2 x_1} + \tilde{A}_{n3}\, e^{\tilde{K}_3 x_1} + \tilde{A}_{n4}\, e^{\tilde{K}_4 x_1} \quad , \qquad (4.11)$$

$$\tilde{\varphi}_n(x_2) = \tilde{A}_{n5}\, e^{\tilde{K}_5 x_2} + \tilde{A}_{n6}\, e^{\tilde{K}_6 x_2} + \tilde{A}_{n7}\, e^{\tilde{K}_7 x_2} + \tilde{A}_{n8}\, e^{\tilde{K}_8 x_2} \, , \qquad (4.12)$$

$$\tilde{\varphi}_n(x_3) = \tilde{A}_{n9}\, e^{\tilde{K}_9 x_3} + \tilde{A}_{n10}\, e^{\tilde{K}_{10} x_3} + \tilde{A}_{n11}\, e^{\tilde{K}_{11} x_3} + \tilde{A}_{n12}\, e^{\tilde{K}_{12} x_3} \, , \qquad (4.13)$$

for plates 1, 2, and 3, respectively, where $\tilde{k}_2 = -\tilde{k}_1$, $\tilde{k}_4 = -\tilde{k}_3$, $\tilde{k}_6 = -\tilde{k}_5$, $\tilde{k}_8 = -\tilde{k}_7$, $\tilde{k}_{10} = -\tilde{k}_9$, and $\tilde{k}_{12}=-\tilde{k}_{11}$. Note that, because the original coupled plates are assumed to have the same width, thickness, and material properties, then,

$$|\tilde{k}_1| = |\tilde{k}_5| = |\tilde{k}_9| = |\tilde{k}_{x1}|$$

and (4.14)

$$|\tilde{k}_3| = |\tilde{k}_7| = |\tilde{k}_{11}| = |\tilde{k}_{x2}|$$

where

$$\tilde{k}_{x1} = \sqrt{k_y^2 + k_p^2}$$

and

$$\tilde{k}_{x2} = \sqrt{k_y^2 - k_p^2} \ .$$

Note also that, below the cut-off frequency (the frequency at which the propagation starts and when $k_y^2 = k_p^2$) in an undamped plate, k_{x1} and k_{x2} are real quantities while above this frequency k_{x1} is real and k_{x2} is imaginary. Equations (4.11)-(4.13) can now be written as

$$\tilde{\varphi}_n(x_1) = \tilde{A}_{n1} e^{\tilde{k}_{x1}x_1} + \tilde{A}_{n2} e^{-\tilde{k}_{x1}x_1} + \tilde{A}_{n3} e^{\tilde{k}_{x2}x_1} + \tilde{A}_{n4} e^{-\tilde{k}_{x2}x_1} \ , \qquad (4.15)$$

$$\tilde{\varphi}_n(x_2) = \tilde{A}_{n5} e^{\tilde{k}_{x1}x_2} + \tilde{A}_{n6} e^{-\tilde{k}_{x1}x_2} + \tilde{A}_{n7} e^{\tilde{k}_{x2}x_2} + \tilde{A}_{n8} e^{-\tilde{k}_{x2}x_2} \ , \qquad (4.16)$$

$$\tilde{\varphi}_n(x_3) = \tilde{A}_{n9} e^{\tilde{k}_{x1}x_3} + \tilde{A}_{n10} e^{-\tilde{k}_{x1}x_3} + \tilde{A}_{n11} e^{\tilde{k}_{x2}x_3} + \tilde{A}_{n12} e^{-\tilde{k}_{x2}x_3} \ . \qquad (4.17)$$

The magnitude of each wave which is present is given by the coefficients A_{n1}-A_{n12}. These coefficients may be found by substituting equations (4.15)-(4.17) into the

boundary conditions of each separate simple plate along the edges $x_1=0$, $x_1=L_1$, $x_2=0$, $x_2=L_2$, $x_3=0$, and $x_3=L_3$, for a given value of "n". These boundary conditions are

$$\tilde{w}_1(L_1) = 0 \ ,$$

$$\tilde{w}_1'(L_1) = 0 \ ,$$

$$\tilde{w}_1(0) = \tilde{w}_2(L_2) \ ,$$

$$\tilde{w}_1'(0) = \tilde{w}_2'(L_2) \ ,$$

$$\tilde{M}_{x1}(0) = \tilde{M}_{x2}(L_2) \ ,$$

$$\tilde{Q}_{x1}(0) = \tilde{Q}_{x2}(L_2) + F \ ,$$

$$\tilde{K}_t \cdot (\tilde{w}_2(0) - \tilde{w}_3(L_3)) = -\tilde{Q}_{x_2}(0) \ ,$$

$$\tilde{K}_t \cdot (\tilde{w}_2(0) - \tilde{w}_3(L_3)) = -\tilde{Q}_{x_3}(L_3) \ ,$$

$$\tilde{K}_r \cdot (\tilde{w}_2'(0) - \tilde{w}_3'(L_3)) = \tilde{M}_{x_2}(0) \ ,$$

$$\tilde{K}_r \cdot (\tilde{w}_2'(0) - \tilde{w}_3'(L_3)) = \tilde{M}_{x_3}(L_3) \ ,$$

$$\tilde{w}_3(0) = 0 \ ,$$

and

$$\tilde{w}_3'(0) = 0 \ ,$$

where $\tilde{Q}_x$ is the shear force per unit width and $\tilde{M}_x$ is the bending moment per unit width. They are written as

$$\tilde{Q}_x = \tilde{B}\left\{\frac{\partial^3 \tilde{w}}{\partial x^3} + \frac{\partial^3 \tilde{w}}{\partial x \partial y^2}\right\} \ ,$$

and

$$\tilde{M}_x = \tilde{B}\left\{\frac{\partial^2 \tilde{w}}{\partial x^2} + \upsilon \frac{\partial^2 \tilde{w}}{\partial y^2}\right\} \quad .$$

The substitution will produce a set of twelve simultaneous linear equations. The set of equations have to be solved for as many as "n" values as required to make the series converge. They are solved by employing a routine from the Nag-library in an IBM 3090-150 machine [37]. A straightforward solution for this equation is made difficult by the fact that one of the (real) k_x values gets large enough to cause an arithmetic overflow problem. This problem can be circumvented by choosing suitable scaling factors for the linear equations.

4.2.1 Calculation of input power

Once the coefficients of equations (4.15)-(4.17) are evaluated, the time averaged energy flowing into the coupled system due to the external driving can be simply calculated as,

$$\bar{P}_{in} = 1/2 \; . \; \mathrm{Re}\,\{\tilde{F}. \overset{*}{\tilde{V}_d}\} \quad , \tag{4.18}$$

where $\tilde{F}$ represents the complex force amplitude, $\tilde{V}_d$ is the complex velocity amplitude at the driving point, and (*) denotes a complex conjugate. The velocity at the driving point can be written as

$$\tilde{V}_d(x_1,y,t) = \sum_n j\,\omega\,\tilde{w}_1(0)_n . \sin\left(\frac{n\pi y}{b}\right) e^{j\omega t}. \tag{4.19}$$

By substituting equation (4.7) and equation (4.19) into (4.18), the time averaged input power may now be written as

$$\bar{P}_{in} = \sum_n \frac{F_o}{2} .\sin\left(\frac{n\pi y_o}{b}\right) \mathrm{Re}\{-j\,\omega\,\tilde{w}_1^*(0)_n .\} \tag{4.20}$$

Equation (4.20) is evaluated numerically in the frequency range 1-50 Hz. The results are then integrated over the above frequency range to simulate an input power due to a band of white noise excitation. A typical input power spectrum is shown in figure (4.2).

4.2.2 Calculation of power flow

The power flow from the first plate (driven) to the second plate (receiver) through the coupling element, is obtained by considering the rate of work done by internal forces at the coupling position, which are the shear force (Q_x), the bending moment (M_y) and the twisting moment (M_{xy}). The latter is written as

$$\tilde{M}_{xy} = \tilde{B}\,(1-\upsilon)\,\frac{\partial^2 \tilde{w}}{\partial y \partial x} \quad .$$

The two bending moments act at right angles to each other. The complete set of internal forces on a plate element are shown in figure (4.3).

Since only plates of uniform thickness are considered here, the shear force and the two bending moments may be expressed as force or moment per unit length. There are thus three main components of power flow at any point across the coupling line, each given by the time average of force (or moment) with velocity (or angular velocity). The total time averaged power flow at any point along the coupling line can be written as

$$\bar{P}_{12} = \bar{P}_{12s} + \bar{P}_{12m} + \bar{P}_{12t} \quad , \qquad (4.21)$$

where the first term on the right hand side represents the component of the shear force, the second term is related to the bending moment, and the last term represents the

twisting moment component. (-) indicates a time average. These power flow components can be written as

$$\bar{P}_{12s} = 1/2 \,.\, \mathrm{Re}\, \{ \tilde{Q}_x \, \tilde{\dot{w}}_3 \}_{x_3=L_3} \ ,$$

$$\bar{P}_{12m} = 1/2 \,.\, \mathrm{Re}\, \{ \tilde{M}_x \, (\frac{\partial \tilde{\dot{w}}_3}{\partial x_3})^* \}_{x_3=L_3} \ ,$$

$$\bar{P}_{12t} = 1/2 \,.\, \mathrm{Re}\, \{ \tilde{M}_{xy} (\frac{\partial \tilde{\dot{w}}_3}{\partial y})^* \}_{x_3=L_3} \ ,$$

where w_3 is the complex displacement amplitude of the second plate at the coupling line ($x_3 = L_3$), and (.) indicates a time derivative. The total power flow across the coupling line can be found by integrating equation (4.21) with respect to the length of the coupling, i.e.,

$$\bar{P}_{12T} = \int_0^b \bar{P}_{12}(y) \, dy \ , \qquad (4.22)$$

Equation (4.21) is used to compute the power flow in the frequency range 1-50 Hz. The band quantity is obtained by integrating the results over the frequency range of interest. A typical power flow spectrum is displayed in figure (4.4).

4.2.3 Plates vibrational energies

Following a similar procedure to that for the coupled beams model (Chapter 2), the total energy of a plate is calculated as twice the time averaged kinetic energy. The kinetic energy of a plate having an area S and mass per unit area ρh , can be calculated as

$$\bar{T} = \frac{1}{2} \rho h \int_S \overline{\dot{w}^2} \, (x,y) \, ds \qquad (4.23)$$

where $\overline{\dot{w}^2}$ represents the mean squared velocity of the plate which is given by

$$\overline{\dot{w}^2} = \frac{1}{2} \mathrm{Re} \left\{ \tilde{\dot{w}} \, . \, \tilde{\dot{w}}^* \right\} \quad ,$$

The kinetic energy of the plate can now be written as

$$\bar{T} = \frac{1}{4} \rho h \, \omega^2 \int_S |\tilde{w}(x)|^2 \, ds \quad , \qquad (4.24)$$

Band quantities of the total time averaged energies of the coupled plates $\bar{E}_1$ and $\bar{E}_2$ ($\bar{E} = 2\bar{T}$) are calculated in the frequency range 1-50 Hz. Typical energy spectra are shown in figures (4.5.a).and (4.5.b).

4.3 Modal Density and Modal Overlap.

Consider a simply supported plate of dimensions a and b along the axes x and y respectively. The modal density may be found by considering the area included by the quarter circle of radius k_p shown in figure (4.6). Note that

$$k_p^2 = k_x^2 + k_y^2 \ ,$$

$$= \left(\frac{m^2 \pi^2}{a^2}\right) + \left(\frac{n^2 \pi^2}{b^2}\right) \ .$$

The area which may be assigned to each mode in figure (4.6) is $\{\frac{\pi^2}{ab}\}$. The number of modes included up to a wave number $k_p = k$ is

$$N(k) = \frac{k^2 \, a \, b}{4\pi} \ ,$$

The modal density in k is

$$n(k) = \frac{dN(k)}{dk} \ ,$$

$$= \frac{k \, a \, b}{2\pi} \ ,$$

Using $n(\omega) = n(k).\frac{dk}{d\omega} = \frac{n(k)}{C_g}$, the modal density in frequency can be written as

$$n(\omega) = \frac{k_p ab}{4\pi C_b}$$

$$= \left(\frac{S}{4\pi}\right) . \left(\frac{m''}{B}\right)^{1/2} \ , \qquad (4.25)$$

where $S = ab$, $k = \frac{\omega}{C_b}$, and C_b is the phase speed. Equation (4.25) shows that the modal density of the simply supported plate is independent of frequency. This result, however, was found to be a good approximation for any other boundary conditions where the modes will not occur regularly as in the considered case [39]. Equation (4.25) was used to calculate the modal densities of the uncoupled plates of the system under study.

Modal overlap factors of the plates are calculated as

$$M = n(\omega)\ \eta\ \omega_c \quad ,$$

and the average modal overlap factor of the coupled plates system under study is calculated as

$$M_{av} = \sqrt{M_1\ M_2}$$

4.4 Coupling Loss Factor

The coupling loss factor (η_{12}) of the coupled plates under investigation is evaluated on the basis of SEA hypothesis, i.e.,

$$\eta_{12} = \frac{\bar{P}_{12T}}{\omega\, n_1(\omega)\left\{\frac{\bar{E}_1}{n_1(\omega)} - \frac{\bar{E}_2}{n_2(\omega)}\right\}}$$

where $\bar{P}_{12T}$, $\bar{E}_1$ and $\bar{E}_2$ are the time averaged band quantities of power flow, total energy of the driven plate, and total energy of the receiver plate respectively which are obtained from sections (4.2)-(4.4).

An estimate for the coupling loss factor of an infinite system is obtained using the travelling wave method [8]. Consider the system shown in figure (4.7). It consists of two coupled semi-infinite, lossless plates, lying in the plane x-y, joined along the line x = 0. The thickness and the properties of the plates and the coupling element are similar to those for the finite system under study (described in table 4.1 below).

Assume that the coupled plates system is excited by a diffuse vibrational field, which means that many bending waves, statistically independent of each other, will travel about the structure in all directions. Consider a flexural wave of a unit amplitude on plate I, incident on the junction at angle θ. Reflected and transmitted waves will be generated. In addition nearfield (non-propagating) waves will be generated at both sides of the junction.

A solution for the total displacement of plate I will be sought to have the form

$$w_I(x,y,t) = \left\{ A_1 e^{jkpcos\theta x} + A_2 e^{-jkpcos\theta x} + A_3 e^{-kpcos\theta x} \right\} e^{jkpsin\theta y} e^{j\omega t} \quad (4.26)$$

where A_1 is the incident wave amplitude, A_2 is the reflected wave amplitude, and A_3 is the nearfield amplitude. Similarly, the displacement of plate II can be written as

$$w_{II}(x,y,t) = \left\{ A_4 e^{jkpcos\theta x} + A_5 e^{kpcos\theta x} \right\} e^{jkpsin\theta y} e^{j\omega t} \quad (4.27)$$

where A_4 is the transmitted wave amplitude, and A_5 represents the nearfield wave amplitude. Equations (4.26) and (4.27) must satisfy the boundary conditions at the junction (x = 0) in order to evaluate the amplitudes A_1-A_5. The boundary conditions at the junction are:

$$K_t \,.\, (w_I - w_{II}) = -Q_{x_I} \,,$$

$$K_t \,.\, (w_I - w_{II}) = -Q_{x_{II}} \,,$$

$$K_r \cdot (w_I' - w_{II}') = M_{x_I} \ ,$$

$$K_r \cdot (w_I' - w_{II}') = M_{x_{II}} \ ,$$

where Q_x represents the shear force, M_x represents the bending moment. K_t and K_r are the translational and rotational stiffness of the coupling respectively. (') denotes a spatial derivative with respect to x coordinate.

The transmission coefficient τ_θ is the ratio of transmitted power to the incident power. It is defined as

$$\tau_\theta = \frac{|A_4|^2}{|A_1|^2} \ . \tag{4.28}$$

The assumption of the diffuse field leads to an averaging of the total incident and total transmitted powers over all the possible angles of incident θ. The diffuse field transmission coefficient may now be written as

$$\tau_d = \frac{\int_{-\pi/2}^{+\pi/2} |A_4|^2 \cos(\theta)\, d\theta}{\int_{-\pi/2}^{+\pi/2} |A_1|^2 \cos(\theta)\, d\theta} \ . \tag{4.29}$$

Equation (4.29) is evaluated numerically after the substitutions for A_4 and A_1.

Heckl [51] has interpreted the diffuse field transmission coefficient in terms of the coupling loss factor of a line junction, and found that

$$\eta_{12\infty} = \frac{C_g L \tau_d}{\pi \omega S_1} \ , \tag{4.30}$$

where C_g is the group velocity, S_1 is the area of the driven plate and L is the length of the junction. Equation (4.30) is used to calculate $\eta_{12\infty}$ in the frequency range 1-50 Hz. The result is displayed in figure (4.8).

4.5 Perturbation Analysis

The dimensions of the plate-plate system under consideration are selected such that the frequency response function will have about 15 resonant modes in the frequency band 1-50 Hz (centred at 25 Hz). These modes may be seen in the typical input power result of figure (4.2). This number of modes is considered to be adequate for the purpose of SEA calculations [52]. The dimensions and properties of the plates are given in table (4.1) below.

Length (mean)	Plate 1 (driven) Plate 2 (receiver)	2.75 m 2.65 m
Width	Plate 1, 2	1.5 m
Thickness	Plate 1, 2	3.0 E-3 m
Material	Plate 1, 2	Steel
Elasticity modulus	Plate 1, 2	1.95E+11 N/m^2
Density	Plate 1, 2	7700 Kg/m^3
Poisson's ratio	Plate 1, 2	0.28
Modal density	Plate 1 Plate 2	0.69 Mode/Hz 0.66 Mode/Hz
Coupling element stiffness	Translational (K_t) Rotational (K_r)	1.3E+4 N/m 1.3E+3 N.m/unit slope
Coupling dissipation loss factor (η_c)		0.15

Table (4.1)

A similar approach to that used for the coupled beams model (Chapter 2) is considered here: an SEA population model was constructed by perturbing the ratio of the length of the driven plate to the length of the receiver plate (l_1/l_2). The perturbations were introduced by employing the 'distribution sampling' application of the Monte-Carlo method. A sample of 32 elements of (l_1/l_2) was drawn from a normally distributed population of a known mean and standard deviation [44]. This sample was then fed to the mathematical model of the coupled plates. Injected power, transmitted power, total energies, and coupling loss factor were then predicted as described above (sections (4.2)-(4.5)). The predicted quantities formed ensembles of size of 32 elements.

To approximate the method of excitation that is required by SEA, the first plate (driven) is excited at 10 different positions. For each given force position the process of computation (of the quantities above) is carried out and the results are then averaged spatially over the selected force locations. The computations above were performed for given values of dissipation loss factors and modal densities, i.e., for given average modal overlap factor (M_{av}) values of the coupled plates. The process above was then repeated for different M_{av} values. Note that, M_{av} was increased by increasing the dissipation loss factors of the coupled plates. An attempt to increase M_{av} by increasing the modal densities was made difficult because of computation difficulties (arithmetic over-flow problems).

4.6 Results and Discussion

Mean and variance results for the coupling loss factor (η_{12}) and normalized power flow $\left\{ \begin{matrix} \bar{} \\ \underline{P_{12T}} \\ \bar{} \\ P_{in} \end{matrix} \right\}$ are obtained from the ensembles generated above. As mentioned earlier, the ensembles have the size of 32 observations at each given value of average modal overlap factor (M_{av}).

Figure (4.9) displays the mean of the coupling loss factor for different values of M_{av}. It shows that as M_{av} increases, the estimate of the mean coupling loss factor increases and approaches, asymptotically, the diffuse field estimate (the estimate from the coupled semi-infinite plates system). The mean of the normalized power flow, between the coupled plates, decreases as M_{av} increases as shown in figure (4.10). This is because of the high losses associated with the increased internal loss factors of the coupled plates. Modal energy ratio of a nominal coupled plates system is displayed

against M_{av} in figure (4.10.a). Figures (4.9) and (4.10) also show the 95 per cent confidence intervals for the estimated means for different M_{av} values. The interval decreases as M_{av} increases. The width of the interval demonstrates the effect of M_{av} on the sensitivity of predictions of the quantities above.

Figures (4.11) and (4.12) demonstrate the effect of M_{av} on the results of normalized variance of η_{12} and $\left\{\frac{\bar{P}_{12T}}{\bar{P}_{in}}\right\}$ respectively. They show that as M_{av} increases, the normalized variance decreases and exhibits very small values for M_{av} greater than unity. Note that the normalized variance of the coupling loss factor is much greater than that of the normalized power flow because both the power flow and the plates energy difference enter the equation of the coupling loss factor.

Figures (4.13) and (4.14) show the cumulative probability distributions of a given samples of η_{12} and $\left\{\frac{\bar{P}_{12T}}{\bar{P}_{in}}\right\}$ respectively. As noted before from the results of coupled beams model (Chapter 2), the distribution approaches that of the normal distribution as M_{av} increases and take the value of unity and greater.

4.6.1 The effect of force position on the predictions

As mentioned above, results for the mean and normalized variance of the coupling loss factor η_{12} and normalized power flow $\left\{\frac{\bar{P}_{12T}}{\bar{P}_{in}}\right\}$ were obtained as averages over an ensemble of similar (not identical) coupled plates systems and also over the randomly selected points of excitation. Although single point excitation has a special practical significance in the study of mechanical vibration of coupled structures, it is considered to be inadequate for the purpose of SEA as pointed out by Fahy [54]. For SEA analysis, all modes must be excited independently, whereas point excitation ensures that they are all coupled and not independent. The chosen number of ten points of excitation (in this work) was considered to be adequate [20] to simulate the statistical independence necessary for SEA.

The location of the point of excitation on the driven plate is found to have a considerable effect on the predictions of the values of the mean and the variance of the coupling loss factor and power flow of the coupled system. Relatively large values for the mean and variance of the above quantities are obtained when the excitation points are located near the coupling line. This may be attributed to the existence of the nearfield waves near the junction which contribute (locally) to the amount of energy transmitted across the junction and consequently to the value of the coupling loss factor. For this reason, points of excitations which produce biased results have not been considered. The selected points of excitation are located where there is no significant effect for the nearfield wave. The considered driving points are shown in figure (4.15). A typical distribution of nearfield amplitude along a line parallel to the x-axis of the driven plate can be seen in figure (4.16).

Computed results for the mean and the normalized variance of coupling loss factor of the coupled system which are obtained from a single point of excitation are displayed in figures (4.17) and (4.18) respectively. The point selected for the excitation is located near to the coupling line at a distance of 0.3 m (y_o = 0.6 m). Figure(4.17) shows, quite clearly, relatively large mean values for η_{12} at all different modal overlap conditions, in comparison with those obtained from the spatial averaging over many points of excitation. In addition the figure shows that the computed mean exceeds the diffuse field (SEA) estimate when the average modal overlap factor takes the value of one and greater. Figure (4.18) shows large values for the normalized variance of the coupling loss factor in comparison with the spatially averaged values.

Another demonstration for the effect of force position on the prediction of the mean of coupling loss factor can be seen in figures (4.19) and (4.20). The data shown in these figures were obtained as a result of exciting the first plate at adjacent points which are located along two perpendicular lines, (the lines intercept each other at the point x = 0.4 m, y_o = 0.45 m). The selected lines are parallel to the x and y axes. The data in figure (4.19) has an exponential like shape which results from the effect of the decaying nearfield near the coupling line, while the data in figure (4.20) has a sinusoidal like shape which results from the effect of the simple supports at y = 0 and y = b. Note that the data shown in figures (4.19) and (4.20) were computed for M_{av} value of 1.6.

For conclusion, by reference to the above discussions, we feel justified in assuming that the spatial averaging of the results over ten positions adequately satisfies the requirements for SEA.

4.6.2 The effect of modal count on the predictions

The modal count (N) of a vibrating subsystem is the number of modes of that subsystem that resonate in the frequency band Δf under consideration. It has a special importance in response prediction, when using SEA, as one of the energy storage parameters. It is often expressed in terms of the modal density n(f) so that

$$N = n(f) \, . \, \Delta f \quad .$$

Lyon [11], has explicitly indicated that the modal count represents one of the major parameters which produce the variance in response between the mean and any member of the population.

Whereas the modal overlap factor is independent of the choice of the analysis bandwidth, the number of resonant modes is approximately linearly proportional to the choice of the bandwidth. In the previous sections, we discussed the effect of modal overlap on the sensitivity of predictions of the coupling loss factor of a coupled plates system. This study is an attempt to isolate the influence of the number of resonant modes from the influence of the modal overlap factor. The investigation is carried out by computing the mean and normalized variance of the coupling loss factor of the coupled plates in different frequency bands. The bands were selected so that they contain different numbers of coupled resonant modes as shown in the modal pictures of input power spectra in figures (4.21)-(4.25). The computations were carried out for different modal overlap conditions and followed the approach described in section (4.5). Results for the mean and normalized variance of the coupling loss factor are plotted in figures (4.26) and (4.27) respectively. By noting the changes in the shapes of the curves a general conclusion may be drawn: that the number of modes, N, has a considerable effect on the sensitivity of prediction of the mean coupling loss factor. These figures also show that as the number of modes increases at a given value of modal overlap factor ($M_{av} > 1$), the estimate of coupling loss factor approaches that of the diffuse field.

Since it was not found possible to obtain an analytical estimate of the effect of N and M_{av} on the variance of the coupling loss factor, because of the extremely complex parametric dependance of the power flow expression, an empirical relationship was derived by combining the results for the normalized variance as a function of modal overlap factor in the different frequency bands. It was assumed that the relationship between the above three parameters has the form

$$\left\{\frac{s^2}{(\bar{r})^2}\right\} = \mathrm{Log}_{10}\, c' + a'\, \mathrm{Log}_{10}\,(M_{av}) + b'\, \mathrm{Log}_{10}\,(N) \qquad (4.31)$$

where $\left\{\frac{s^2}{(\bar{r})^2}\right\}$ is the normalized variance of coupling loss factor ; a', b', and c' are constants which were determined by plotting the different sets of data and performing best straight line fits. Note that s^2 is the variance and $\bar{r}$ is the mean value. This relationship is plotted in figure (4.28) and can be used to assess the uncertainty of the prediction of the coupling loss factor of the coupled plates model. It is not known how generally this form of relationship holds for other types of coupled systems, but this type of relationship may be constructed for other coupled system by following the approach above.

4.7 Pure Tone Analysis

Previous sections were concerned with the investigations of the sensitivity of the predictions of the coupling loss factor and power flow of the coupled plates system when the excitation was a simulated band of white noise and the averages were taken over a set of similar systems. In this section we considered the situation when the excitation is a pure tone (sinusoidal). Pure tone analysis has been carried out by Lyon [11] when he described the effect of this type of excitation on the coherence between modes in multi-modal response. It was found that it is possible to obtain what is called "Statistical response concentration" (the ratio of coherent rms response to the incoherent rms response) of significant value when many modes are coherently excited. Of course such a situation can arise when structures are excited by a pure tone. When the system excitation is broad band the statistical response concentration is not significant.

In this work a statistical calculation was carried out on pure tone results for the time averaged power flow between two coupled plates. Results for the normalized variance were obtained for the computed data in the frequency range 1-50 Hz. The coupled plates system had unperturbed (fixed) geometry and represented one realization from the set generated for the previous analysis (white noise excitation). Plate one (driven) had a length of 3 m, a width of 1.5 m, and a thickness of 3 mm. Plate two had a length of 2.65 m, a width of 1.5 m, and a thickness of 3 mm. Figure (4.29) shows a comparison between the computed (pure tone) normalized variance and that obtained from the previous analysis using white noise excitation. It is clear that the variance for the pure tone analysis is much higher than for band excitation for all modal overlap conditions. These results indicate that an unacceptably high uncertainty should be expected if broad band predictions are applied to systems under pure tone excitation.

4.8 Three Plates System

The mathematical model for two coupled plates is modified for the case of a three coupled plates system: the plates are coupled with each other by a similar line coupling and formed the configuration shown in figure (4.30). The properties and dimensions of the plates are given in table (4.2) below.

Length (mean)	Plate 1 (driven) Plate 2 Plate 3	2.75 m 2.75 m 2.65 m
Width	Plate 1, 2, 3	1.5 m
Thickness	Plate 1, 2, 3	3.0 E-3 m
Material	Plate 1, 2, 3	Steel
Elasticity modulus	Plate 1, 2, 3	1.95E+11 N/m^2
Density	Plate 1, 2, 3	7700 Kg/m^3
Modal density	Plate 1, plate 2 Plate 3	0.69 Mode/Hz 0.66 Mode/Hz
Poisson's ratio	Plate 1, 2, 3	0.28
Coupling element stiffness	Translational (K_t) Rotational (K_r)	1.3E+4 N/m 1.3E+3 N.m/unit slope
Coupling dissipation loss factor (η_c)		0.15

Table (4.2)

This analysis was performed in order to investigate the statistical properties of power flow between indirectly excited subsystems.

The coupled plates system is excited by a band limited random force similar to that of the previous model, applied to plate 1. A similar analysis to that of the two-plates system is carried out for the prediction of mean coupling loss factors η_{12} and η_{23}, and the predictions of normalized power flow through the coupling lines.

Figures (4.31) and (4.32) display the mean values of the coupling loss factors as well as the 95 per cent confidence intervals for the means at different values of average modal overlap factor (M_{av}) at junctions 1 and 2 respectively. Note that because

the modal overlap factors of the plates are almost similar, it was found convenient to calculate the average modal overlap factor of the coupled system (M_{av}) as

$$M_{av} = (M_1 M_2 M_3)^{1/3} ,$$

where M_1-M_3 represent the modal overlap factor for plates 1, 2, and 3 respectively. The figures above show that the coupling loss factors of the coupled system increase as M_{av} increases. Coupling loss factors of both junctions approach (asymptotically) the diffuse field estimate at $M_{av} \geq 1$. The figures also show that the confidence intervals of the means decrease as M_{av} increases. These results are similar to that for the two-plates system. Figure (4.33) shows a good agreement between the results obtained for both coupling loss factors η_{12} and η_{23}, although plate 1 is driven directly while plate 2 received an indirect excitation.

Figure (4.34) displays the results for the normalized variances of the coupling loss factors as functions of M_{av}. It shows that the normalized variance values decreases sharply as (M_{av}) increases and take relatively smaller values for $M_{av} \geq 1$. Figures (4.35) displays the mean values for the normalized power flow through junctions 1 and 2. The power flow decreases as M_{av} increases. Figure (4.36) shows the results for the normalized variances which also decrease as M_{av} increases. Cumulative probability distributions for samples of coupling loss factor and normalized power flow at the first junction are displayed in figures (4.37) and (4.38) for different M_{av} values. The distribution approaches normality as M_{av} increases and takes the values of unity and greater

4.9 Conclusions

From the analysis of coupled plates systems, the following general conclusions may be drawn:

(a) The travelling wave method overestimates the coupling loss factor of the coupled plates systems when the average modal overlap factor (M_{av}) is small (less than 1.0). This conclusion is similar to that drawn from the one dimensional model (coupled beams system).

(b) The sensitivities of the predictions of the coupling loss factor and the normalized power flow between the coupled plates are highly affected by the

degree of the modal overlap of the coupled system. High variances are reported for the above quantities at low values of M_{av} and vice-versa.

(c) The normalized variance calculations showed that the coupling loss factor is a highly sensitive quantity to the perturbations of the geometry of the coupled system than the normalized power flow.

(d) The excitation location has a great effect on the mean and the variance of the computed coupling loss factor. Points of excitations which are located near the coupling line produce high values for the mean and the variance. This is because of the existence of nearfield waves close to the coupling line.

(e) The number of resonant modes of the *coupled system* in the analysis frequency band has a considerable effect on the values of the mean and the normalized variance of the coupling loss factor. For a given M_{av} value ($M_{av} > 1$), the estimate of the coupling loss factor approaches that of the travelling wave method as the number of modes increases.

(f) Pure tone analysis of the power flow between two coupled plates showed an extremly high, frequency-dependent variance in comparison with those obtained from the frequency band averaged quantities.

(g) A good agreement was found between the values of the means and the variances of the coupling loss factors at both junctions of a three coupled plates system, irrespective of the way of excitation which applied across both junctions.

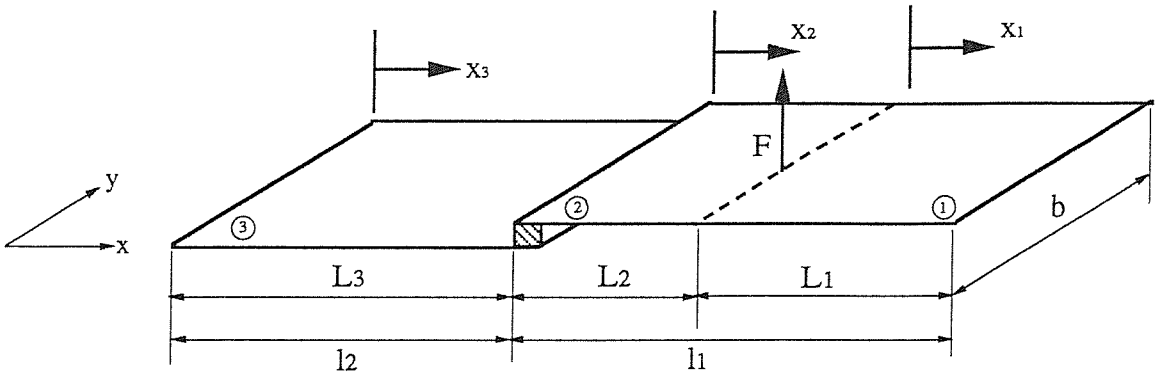

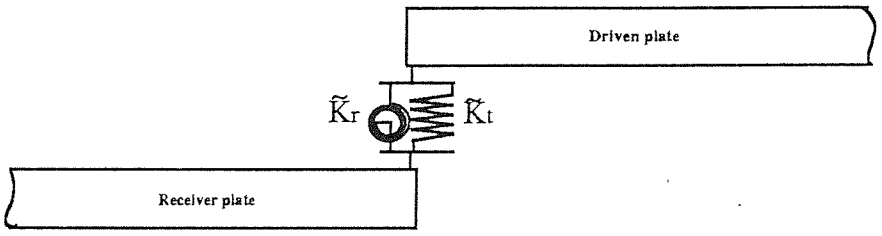

Figure : (4.1) Two Coupled plates system

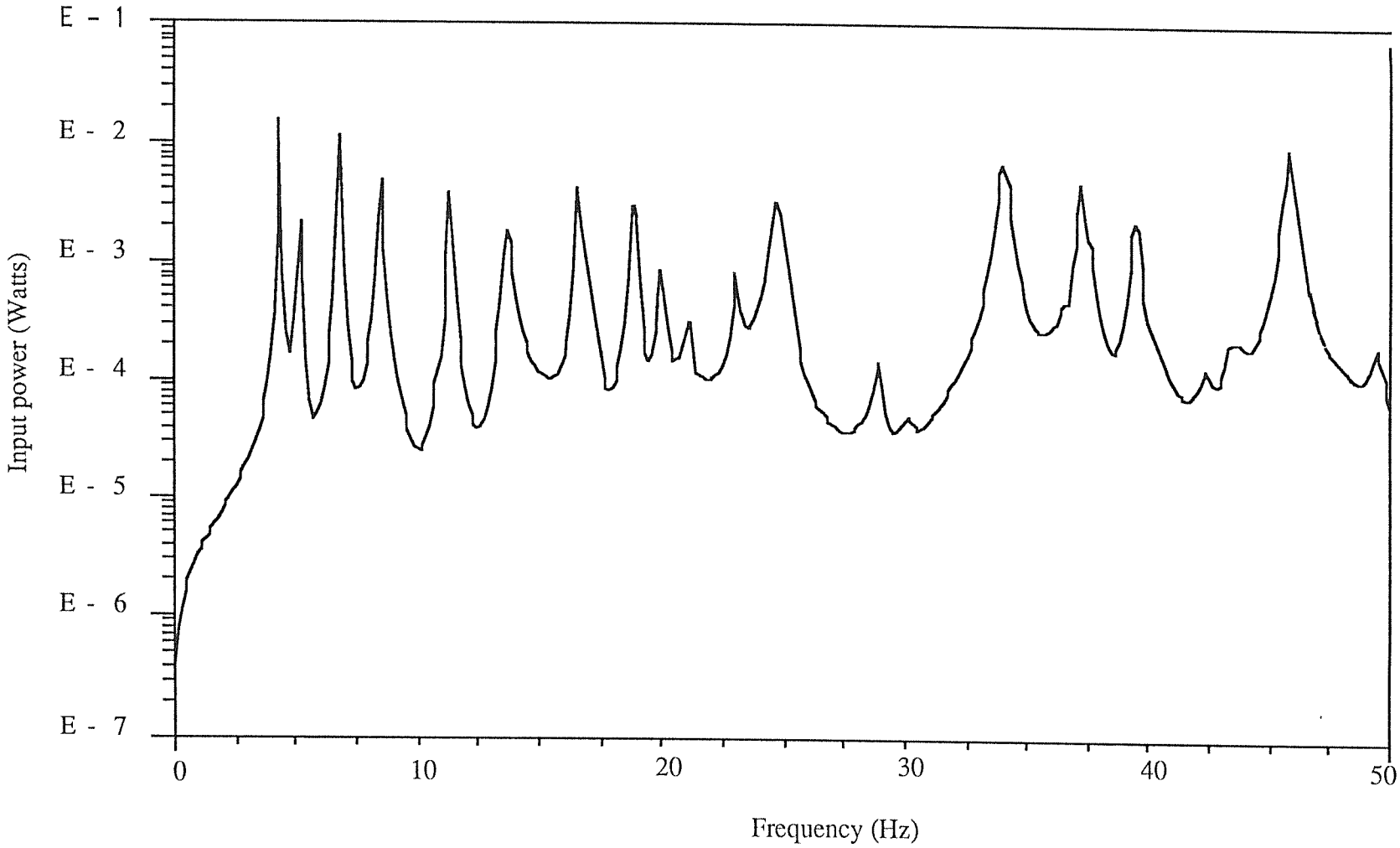

Figure (4.2) : Input power to a coupled plates system

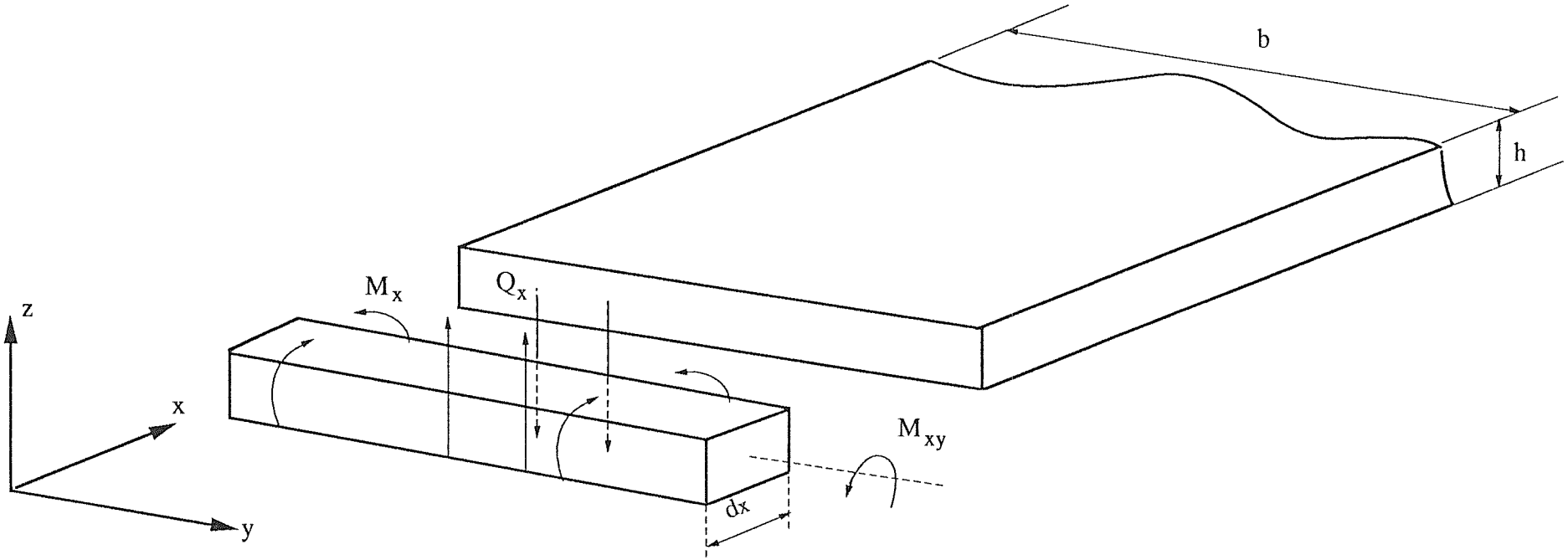

Figure (4.3) : shear forces and moments acting on a plate element.

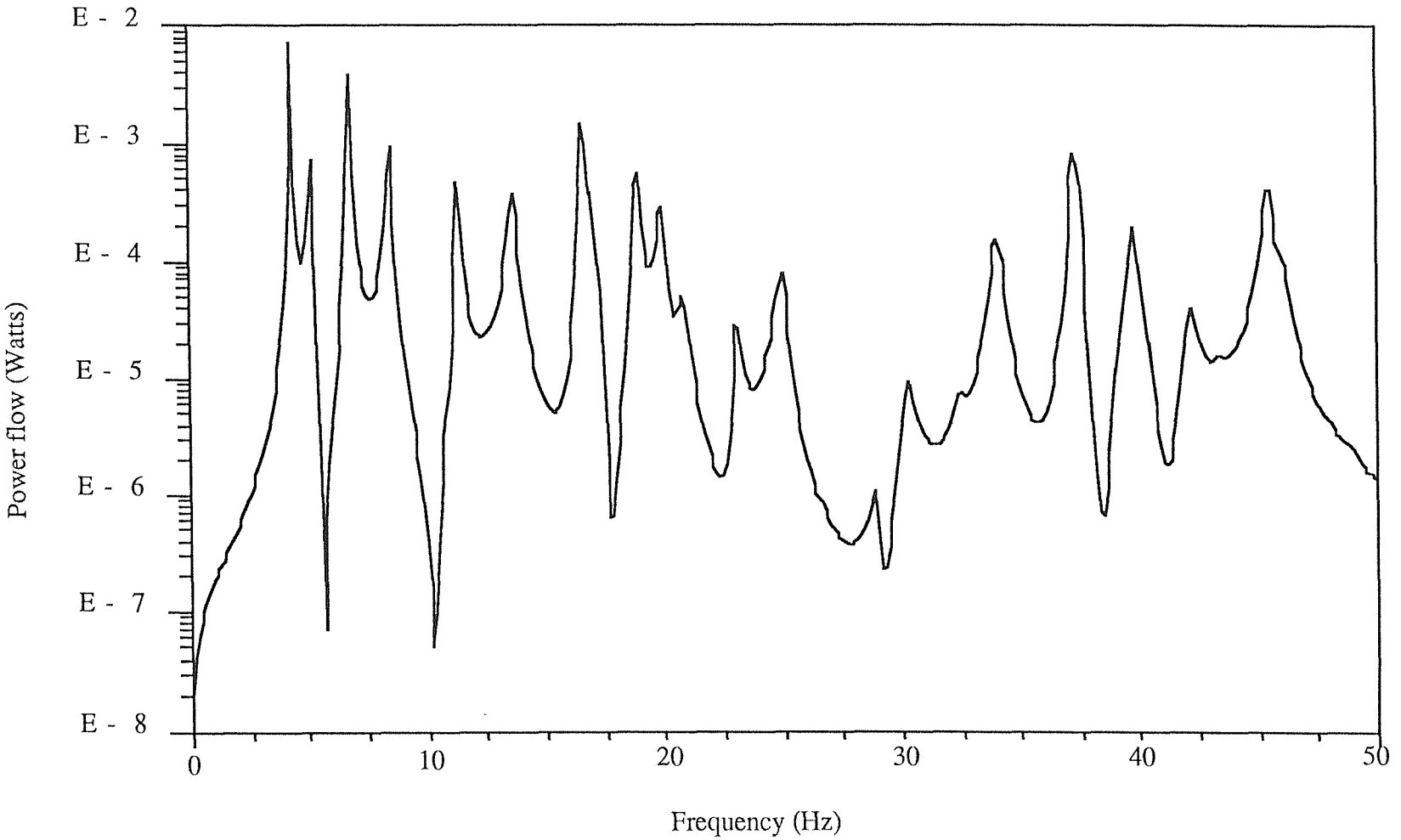

Figure (4.4) : The power flow between two coupled plates

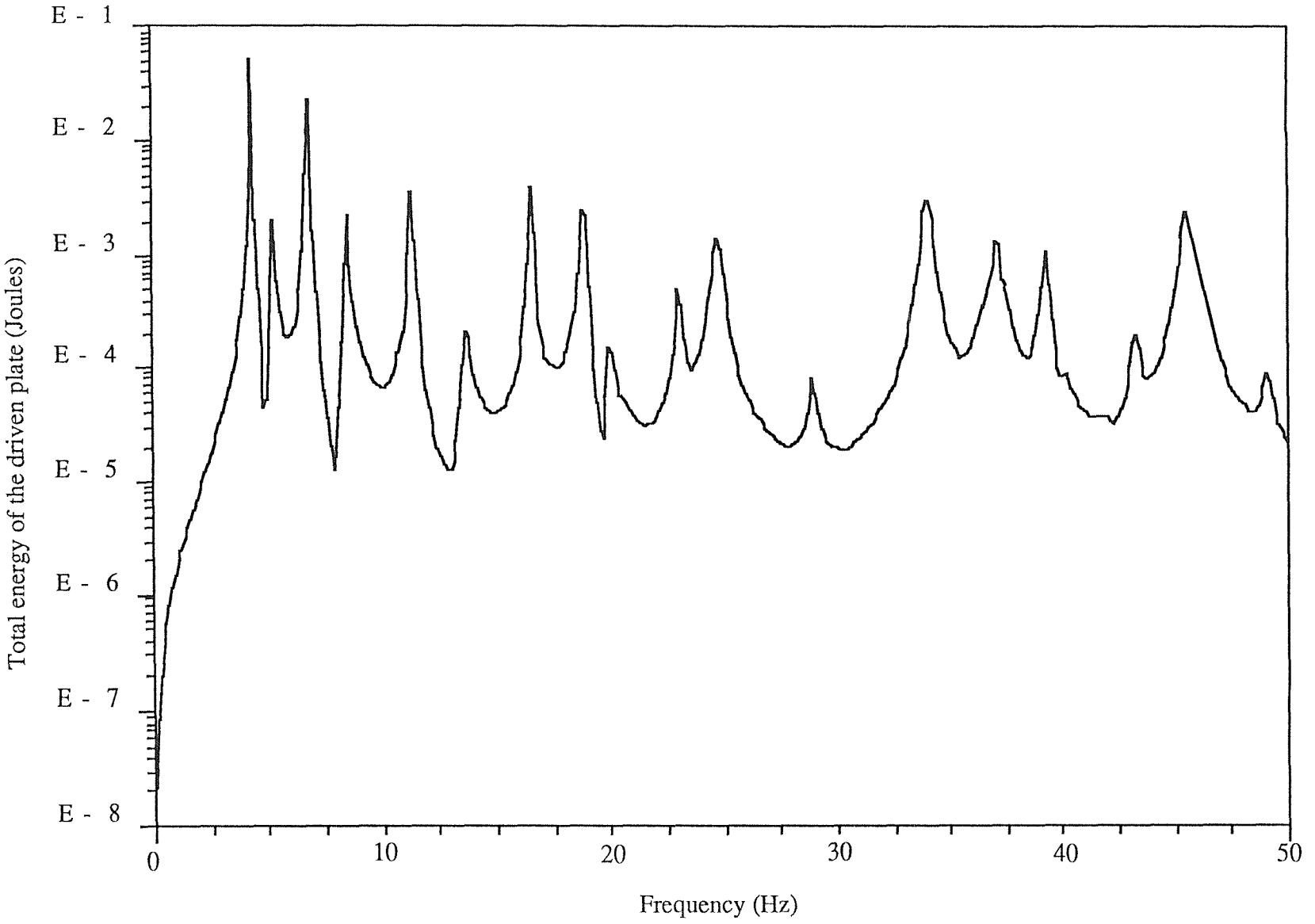

Figure (4.5.a) : Total energy of the driven plate of a coupled plates system

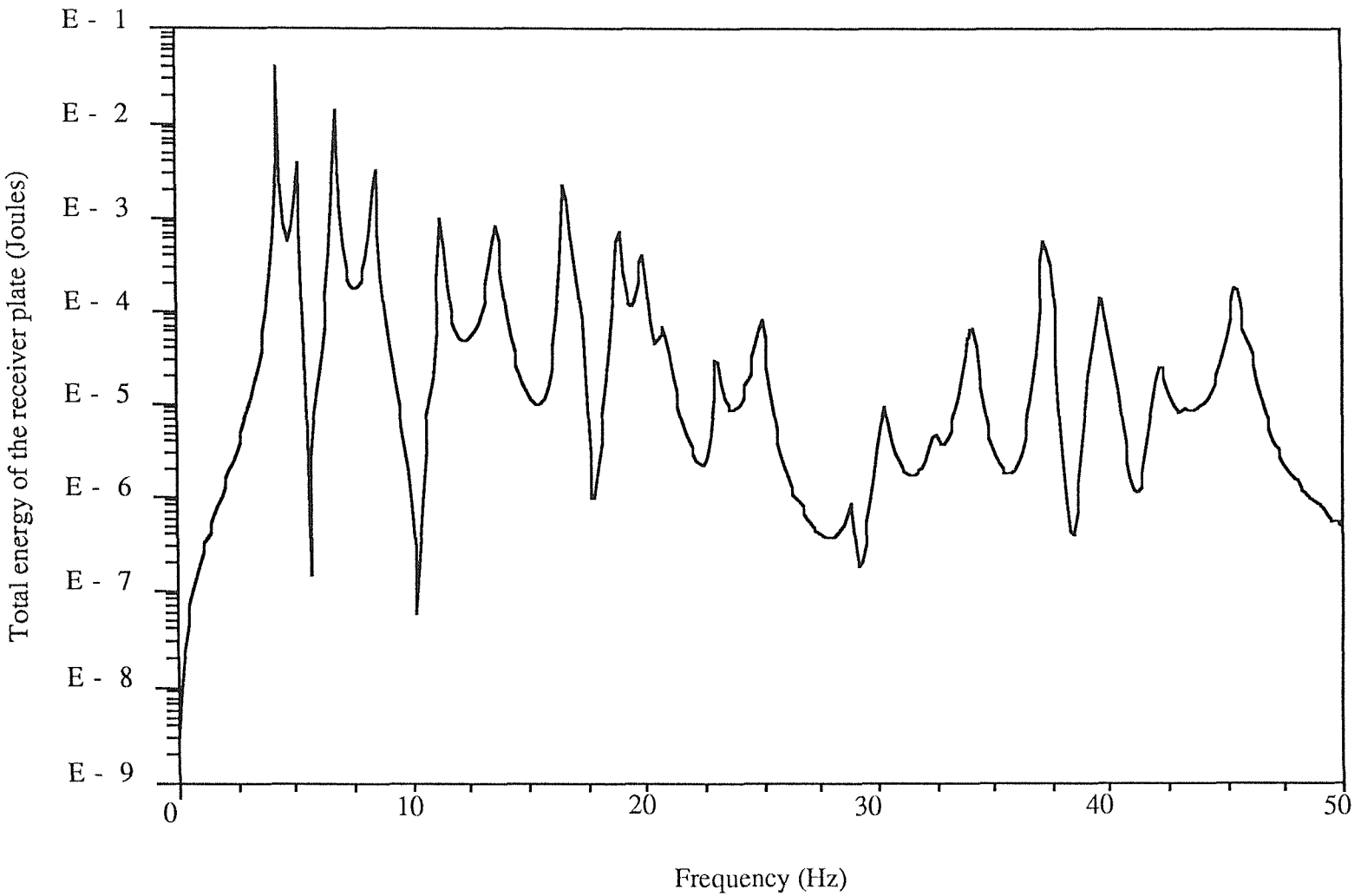

Figure (4.5.b) : Total energy of the receiver plate of a coupled plates system

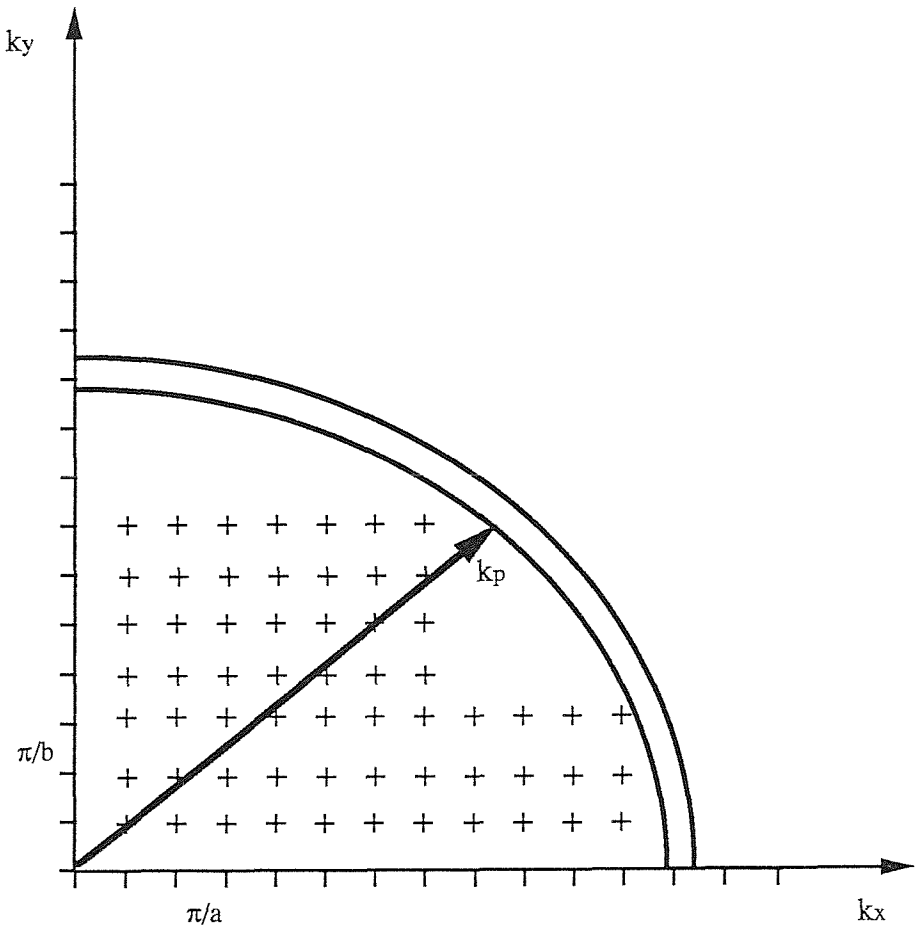

Figure (4.6) : Wave number diagram of a simply supported panel in flexure

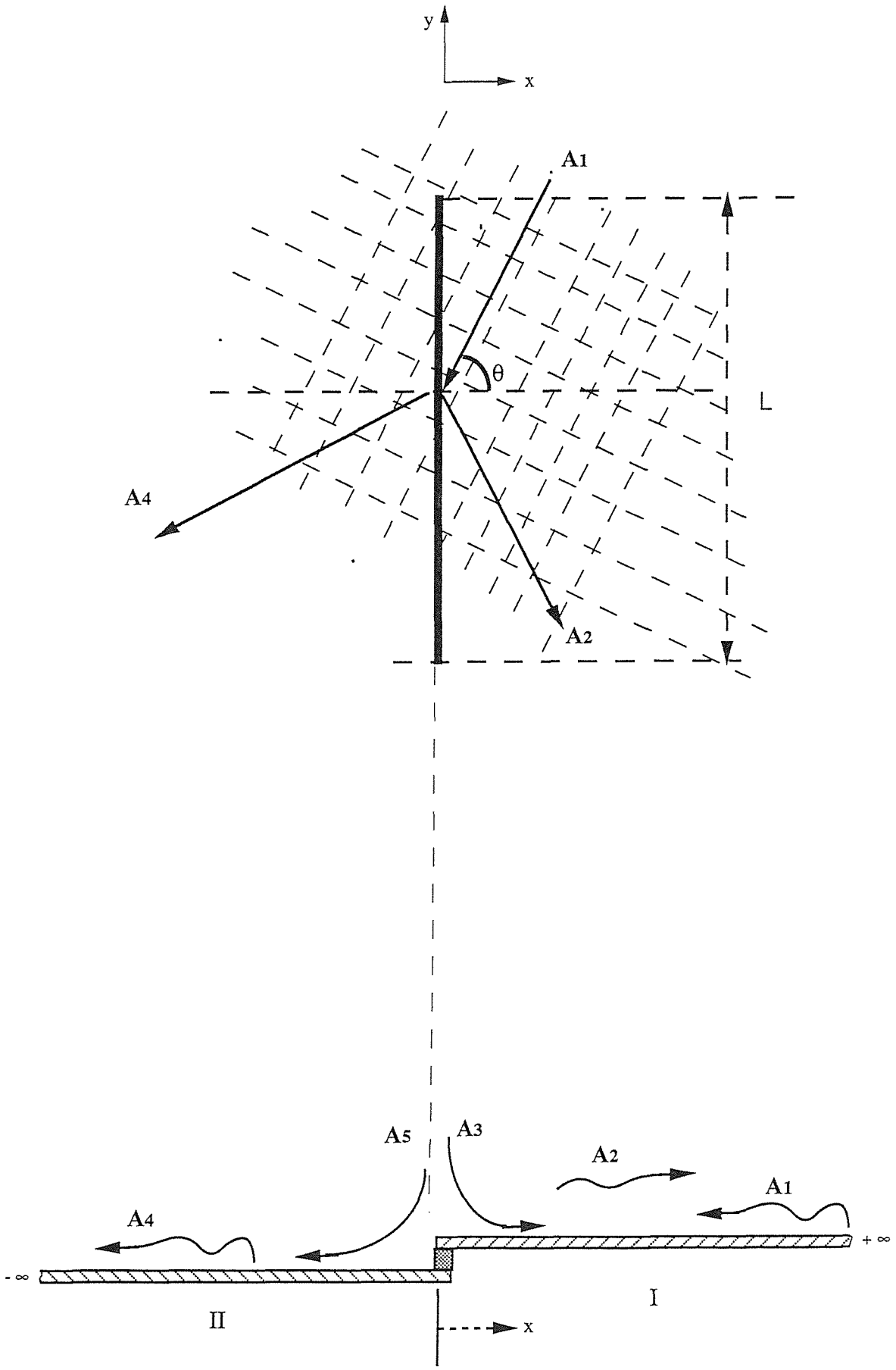

Figure (4.7) : Semi-infinite Coupled plates

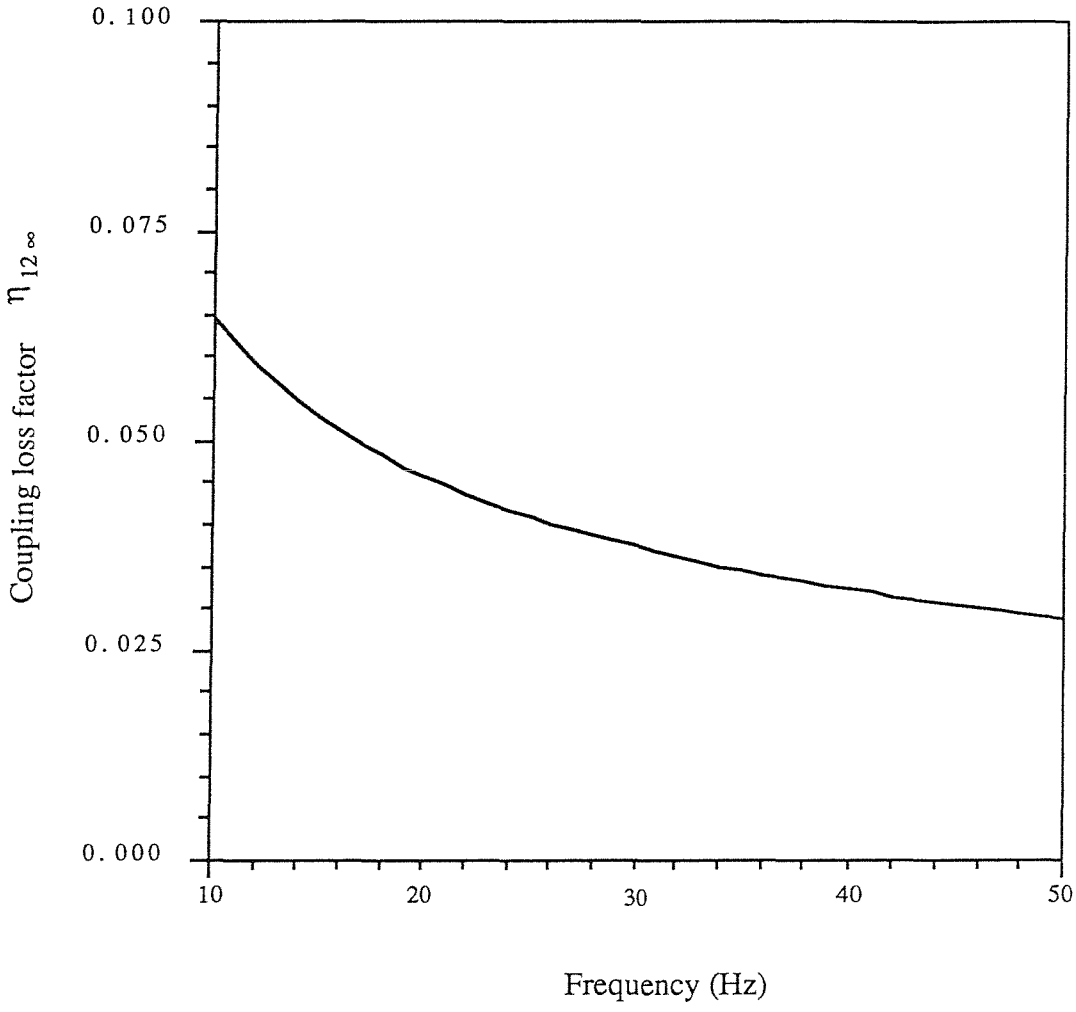

Figure (4.8) : Coupling loss factor of an infinite coupled plates system

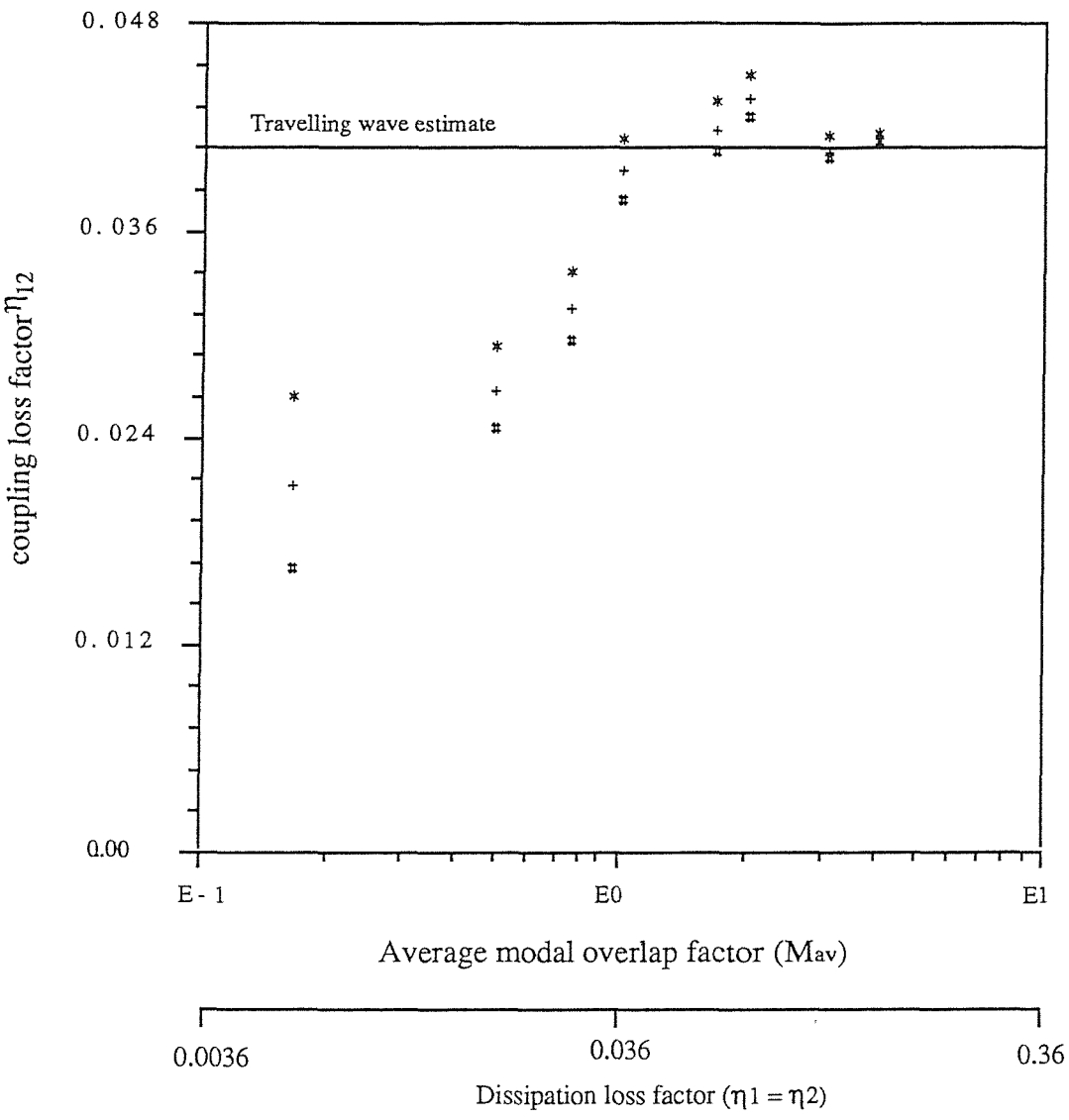

Figure (4.9) : The predicted coupling loss factor of coupled plates system.

+ Mean value, $\overset{*}{\underset{\#}{}}$ 95% confidence interval

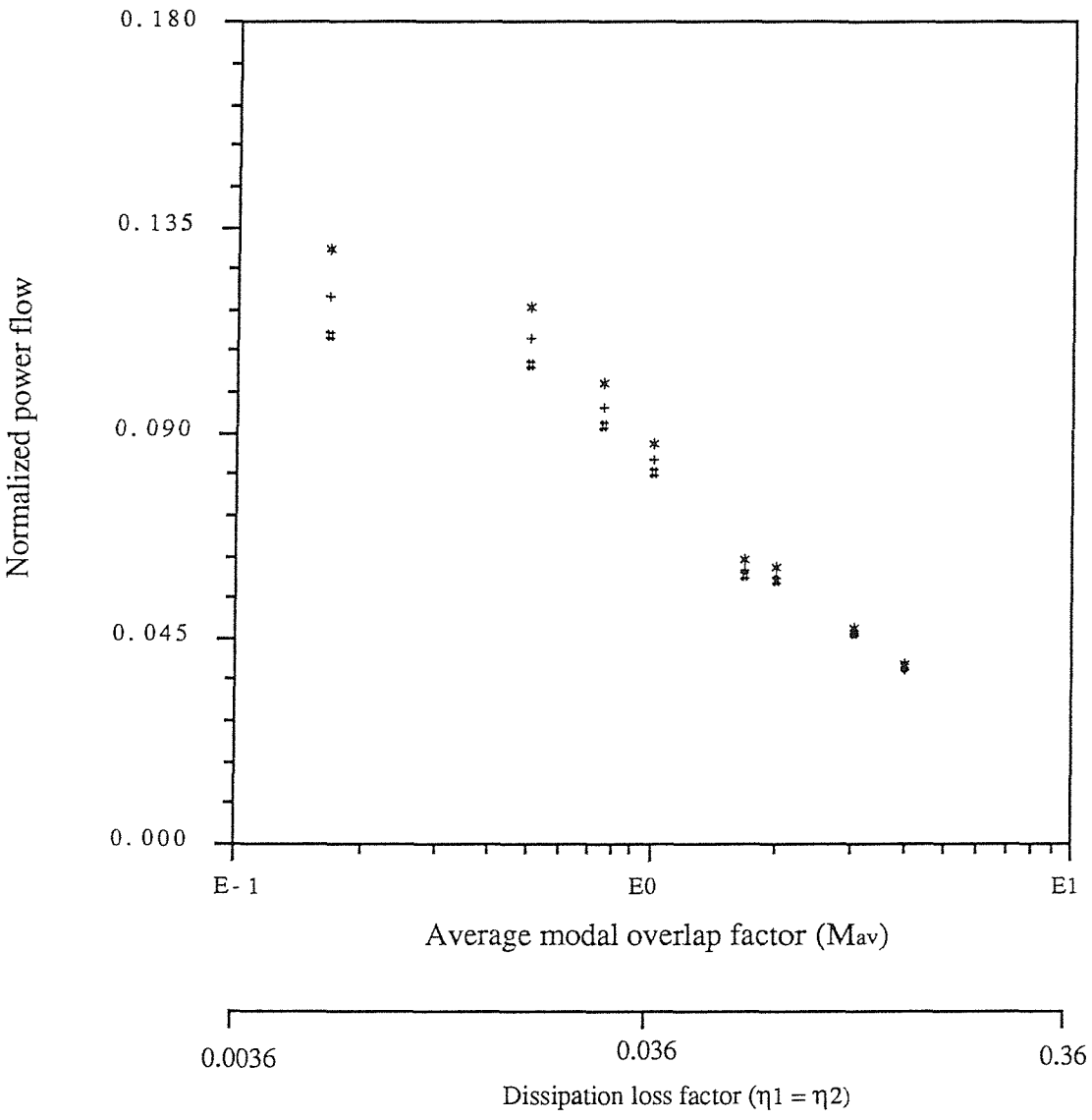

Figure (4.10) : Normalized power flow between two coupled plates.

+ Mean value, $\overset{*}{\#}$ 95% confidence interval.

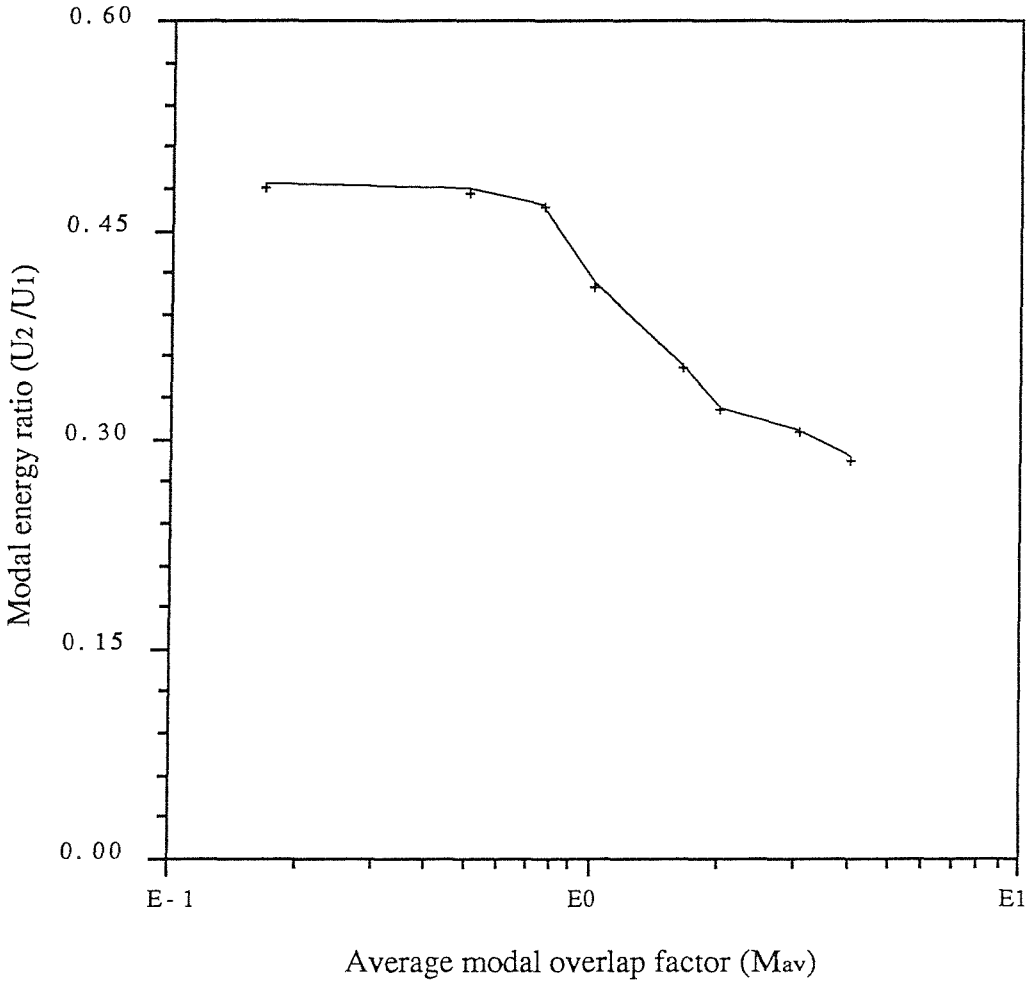

Figure (4.10.a) : Modal energy ratio of two coupled plates

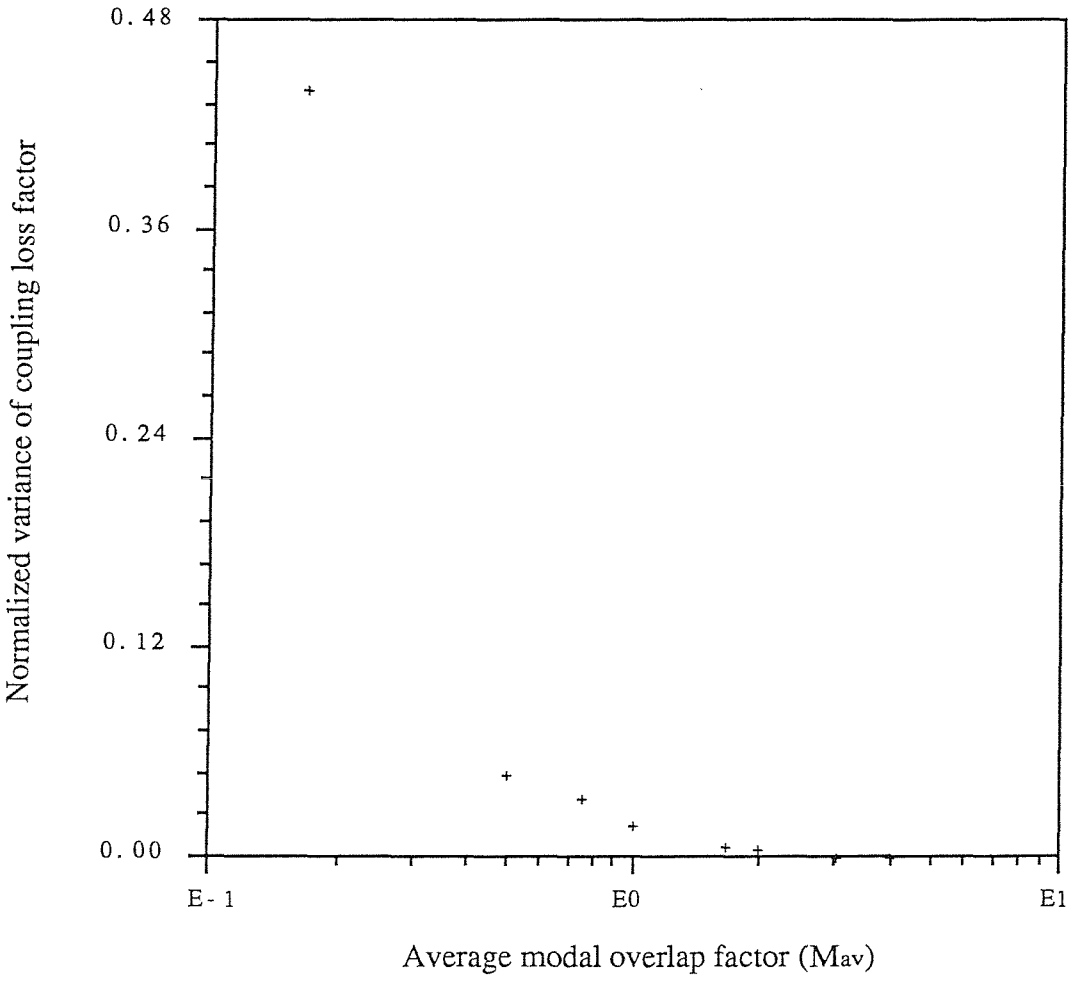

Figure (4.11) : The predicted normalized variance of coupling loss factor of coupled plates system.

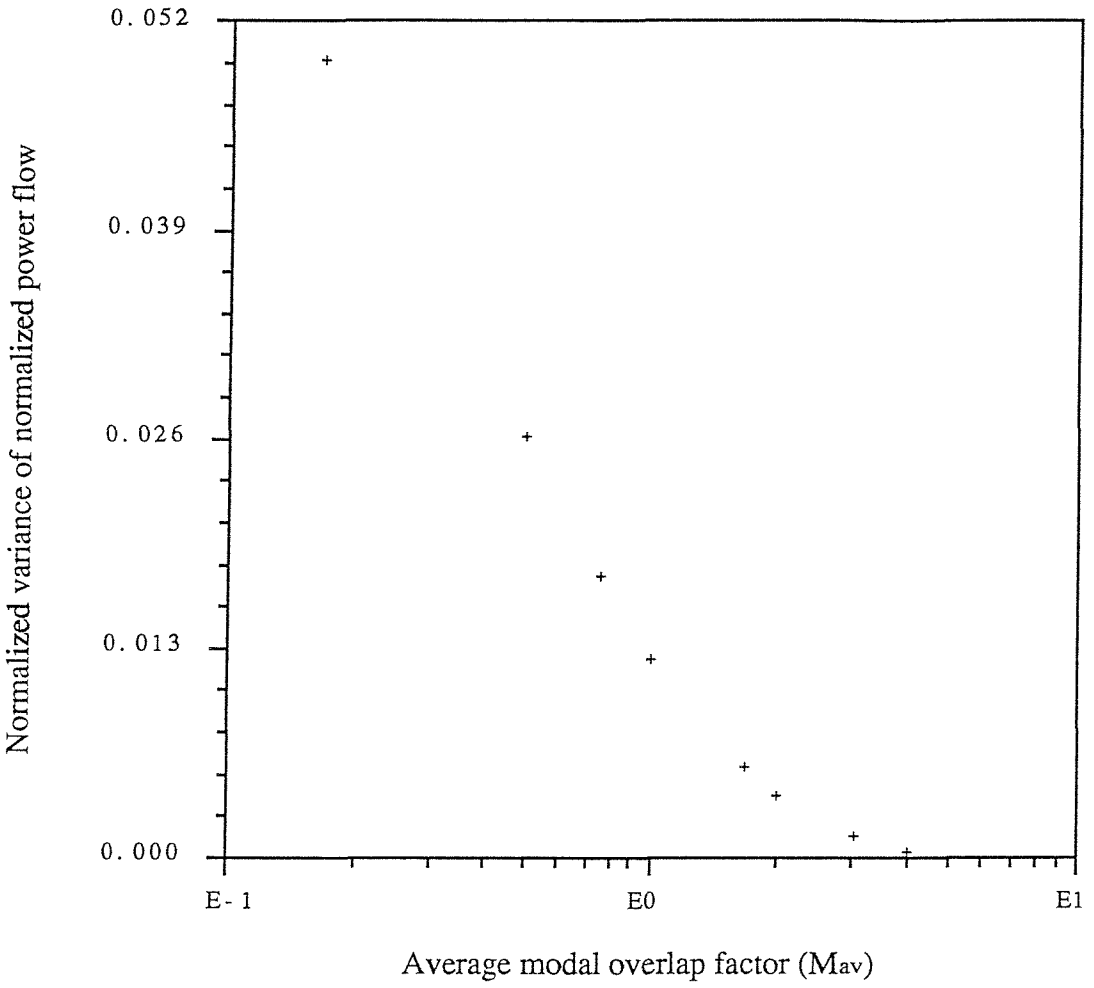

Figure (4.12) : Normalized variance of normalized power flow between two coupled plates.

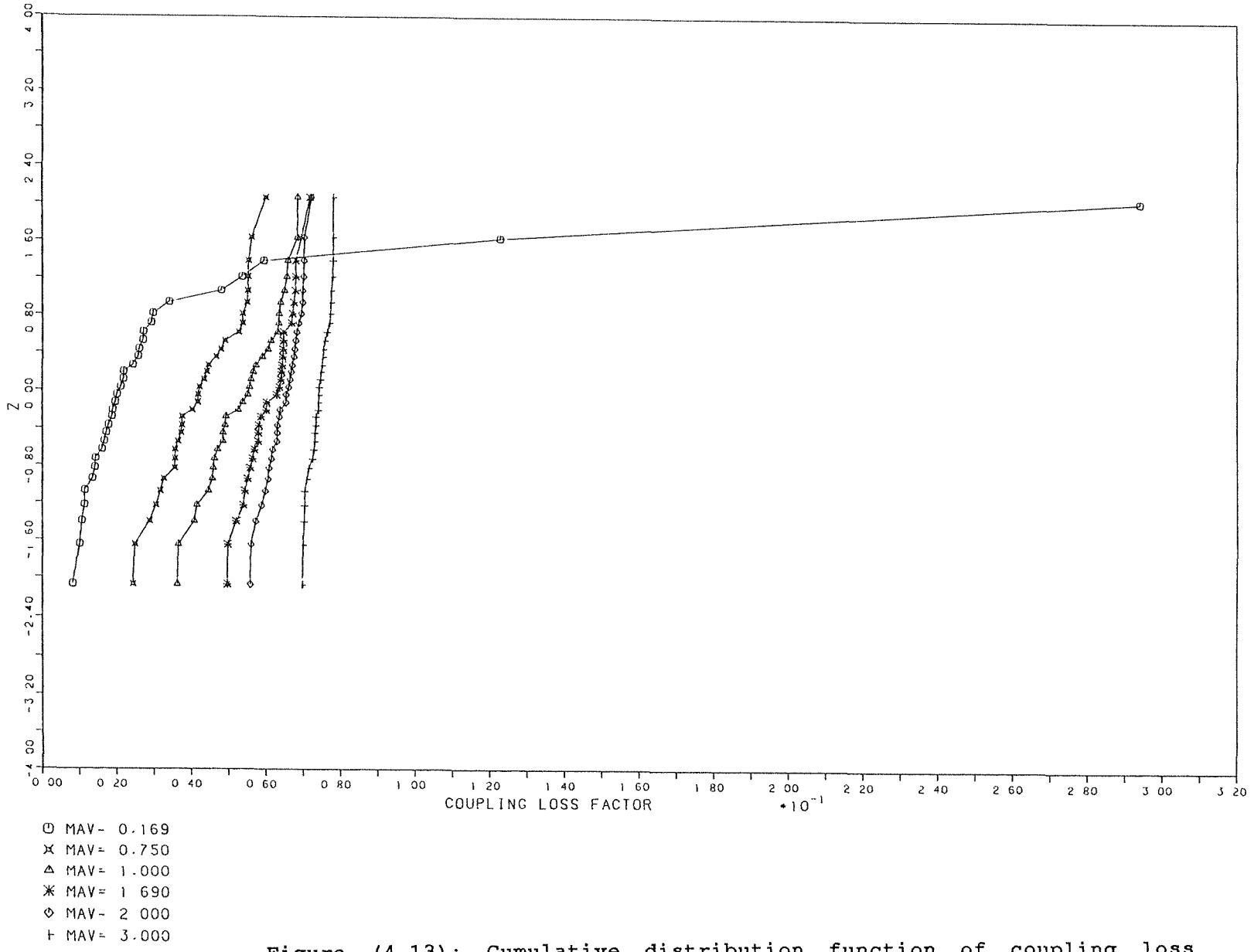

Figure (4.13): Cumulative distribution function of coupling loss factor of two coupled plates

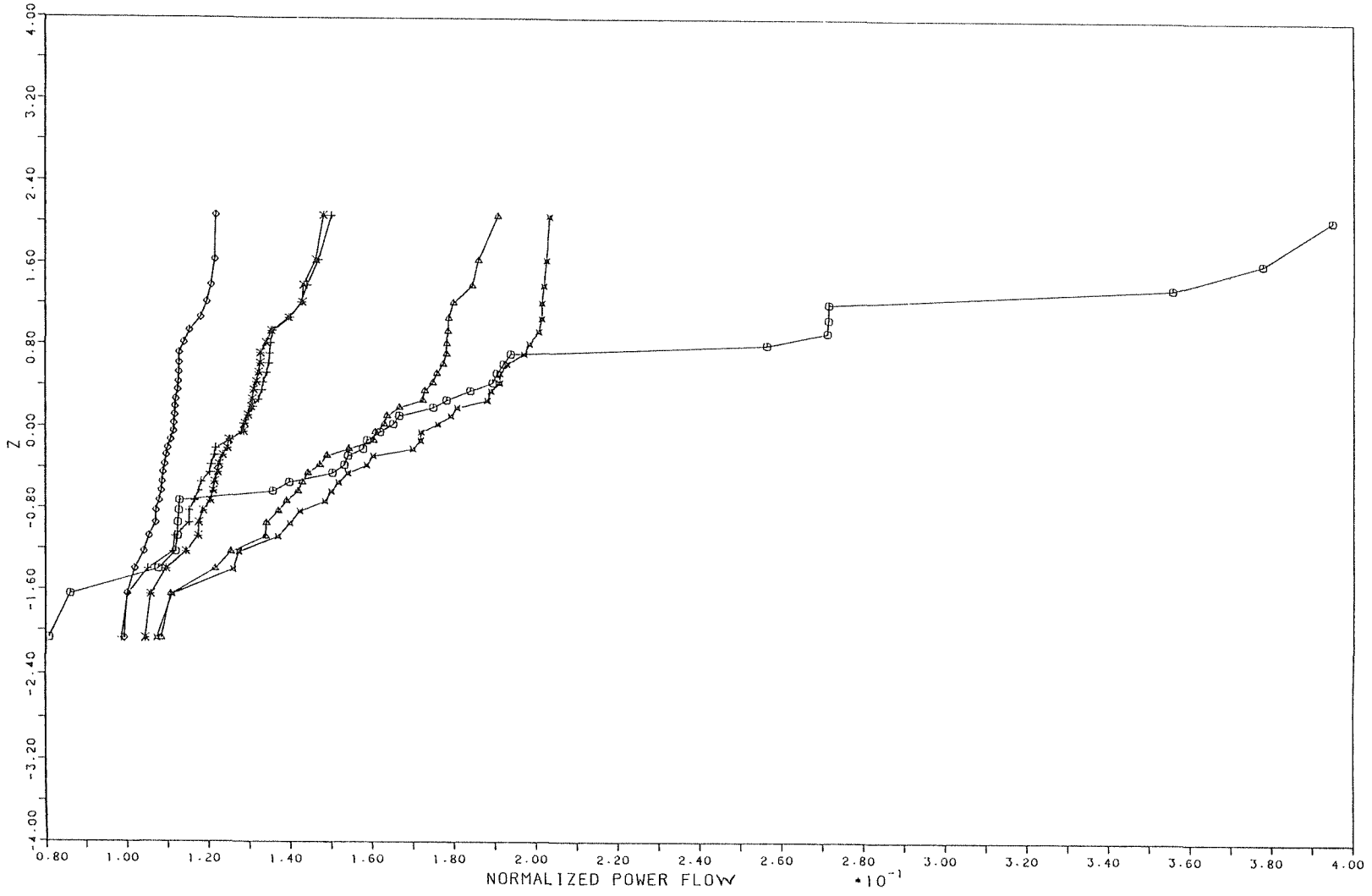

Figure (4.14): Cumulative distribution function of normalized power flow between two coupled plates

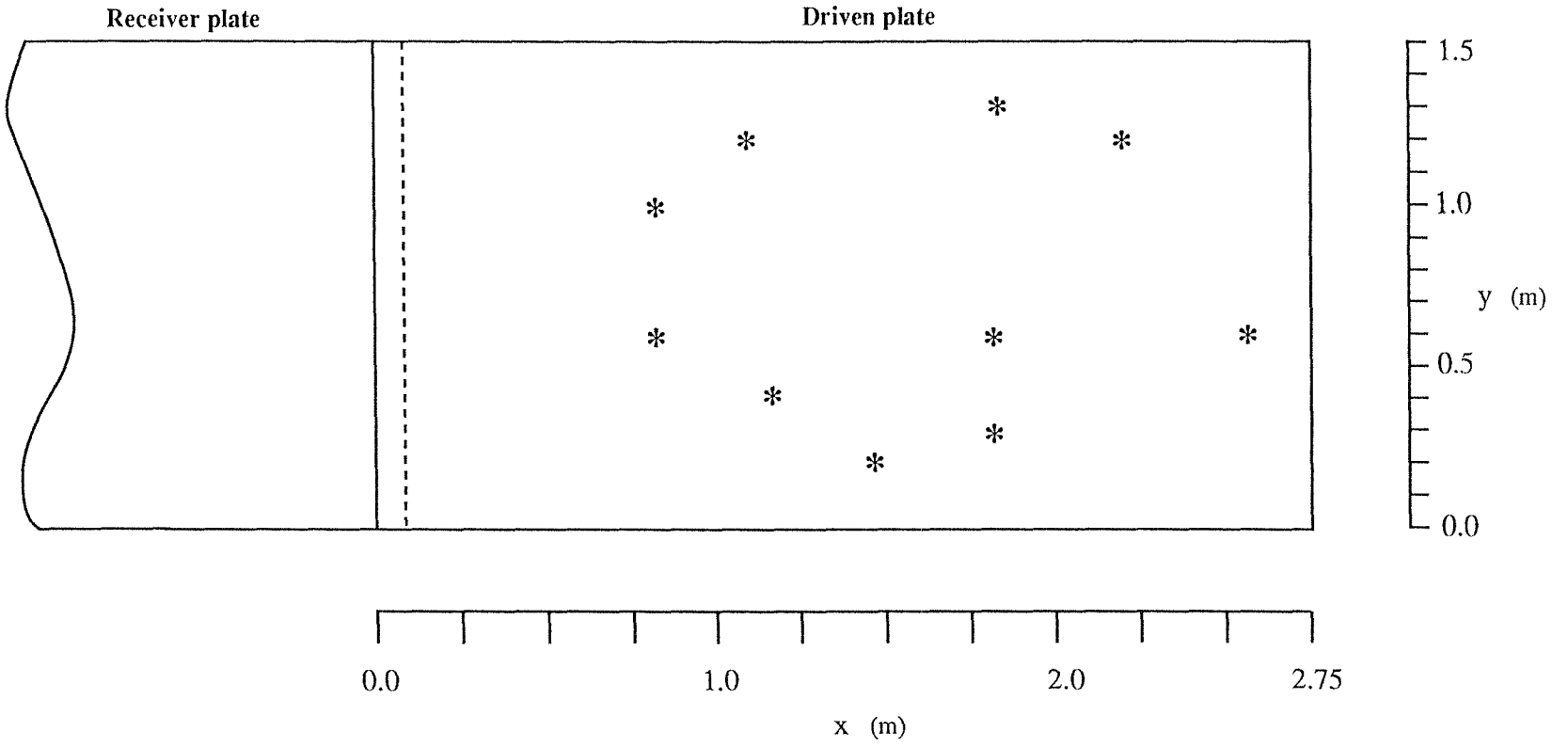

Figure (4.15) : The selected locations for the excitation of the coupled plates system

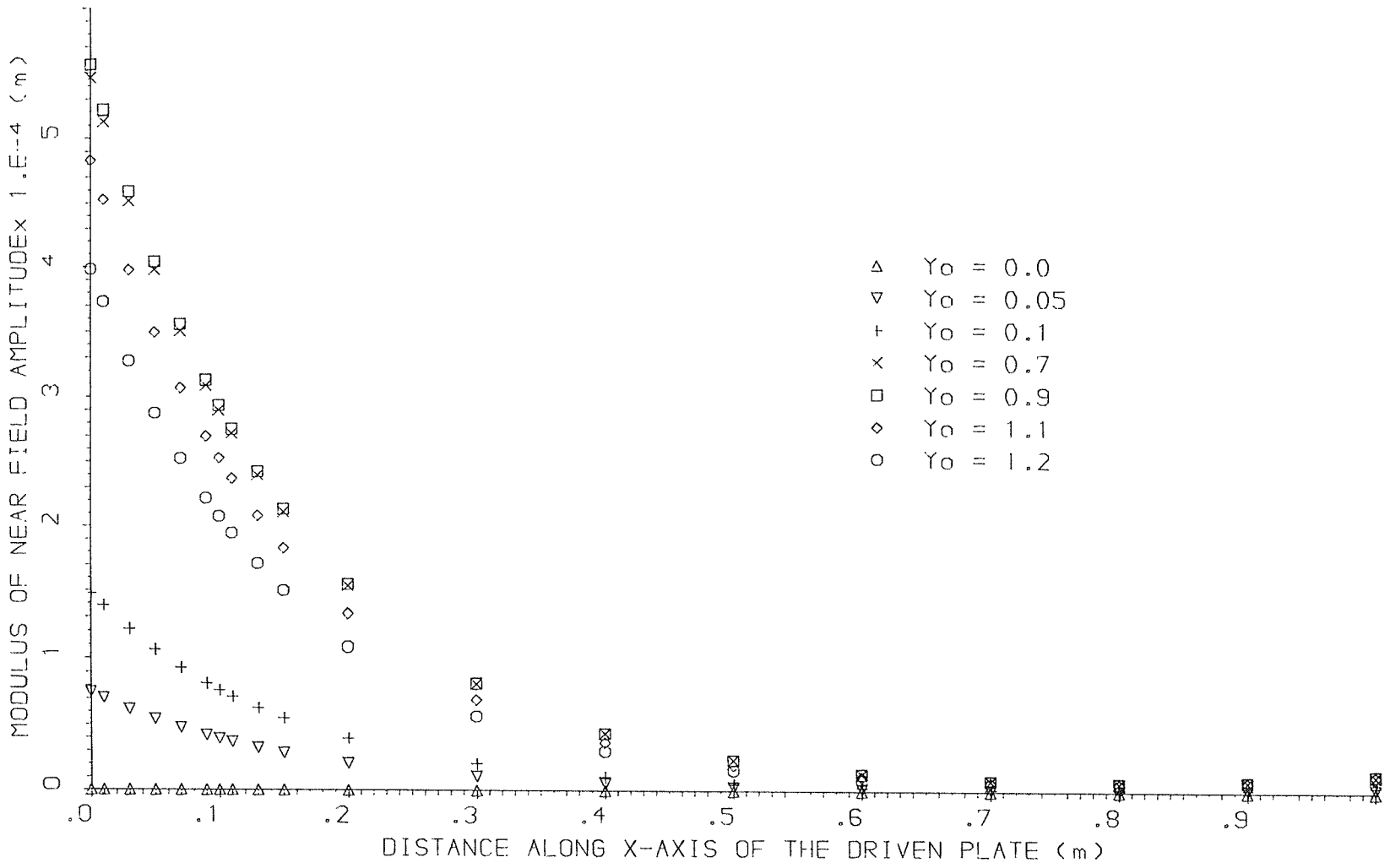

FIG.(4.16) NEAR FIELD AMPLITUDE DISTRIBUTION

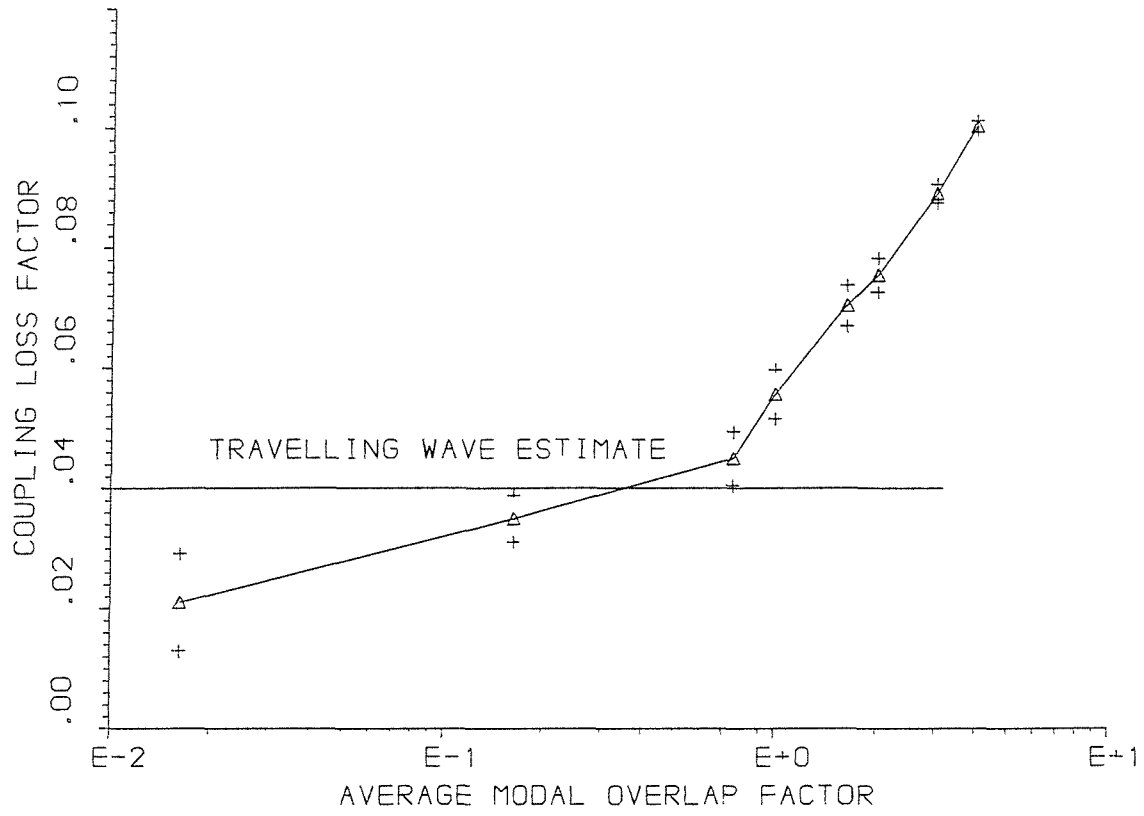

FIG. (4.17) COUPLING LOSS FACTOR (single point excitation)

△ MEAN VALUE, + 95% CONFIDENCE INTERVAL

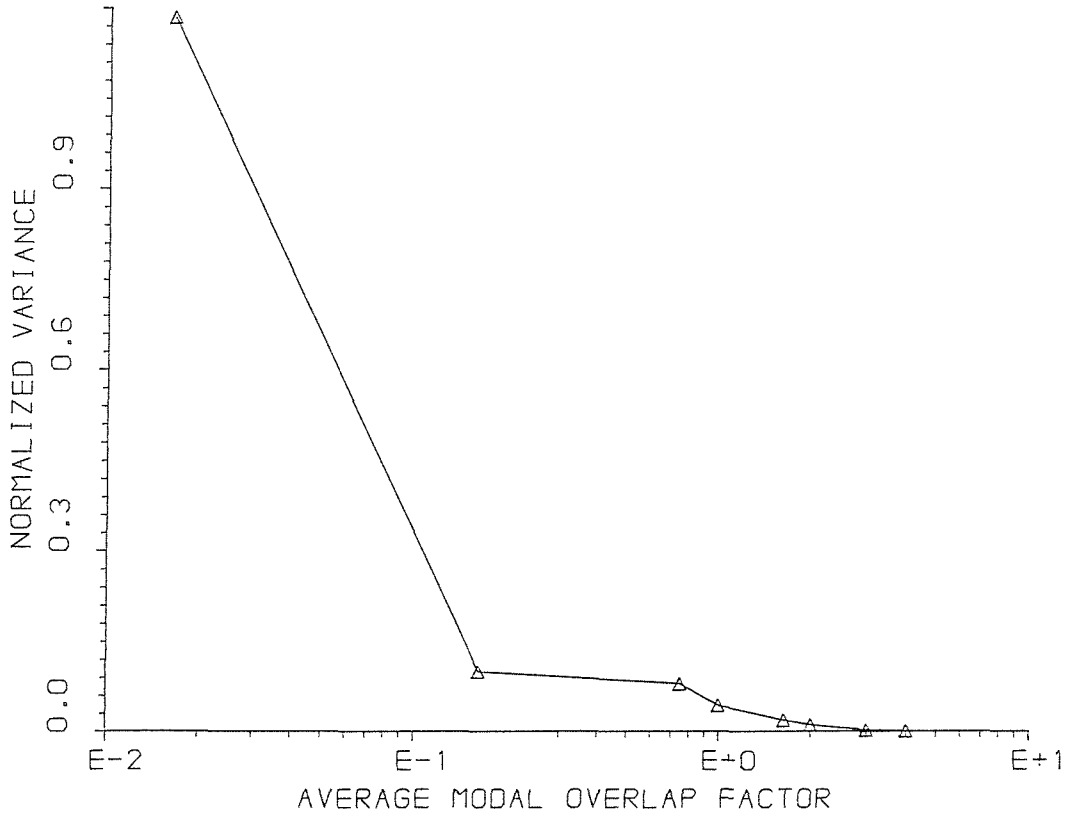

FIG. (4.18) NORMALIZED VARIANCE OF COUPLING LOSS FACTOR OF TWO COUPLED PLATES (single point excitation)

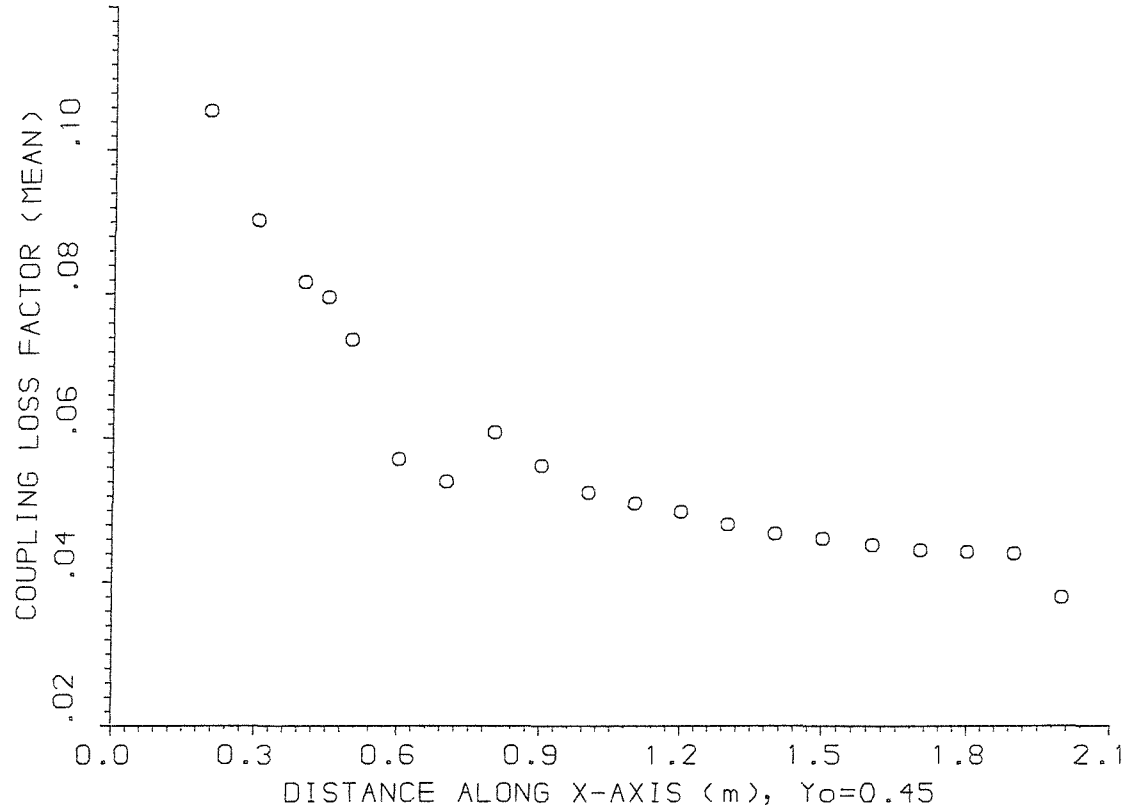

FIG.(4.19) DISTRIBUTION OF COUPLING LOSS FACTOR

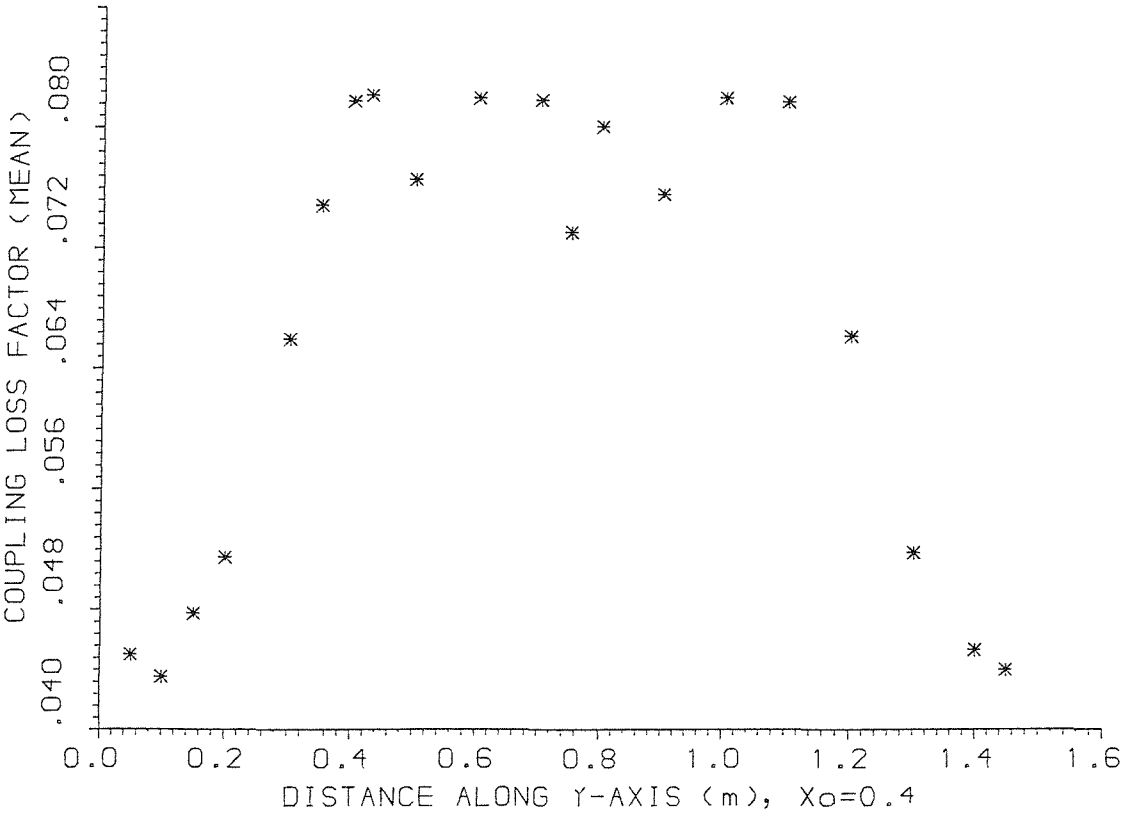

FIG.(4.20) DISTRIBUTION OF COUPLING LOSS FACTOR

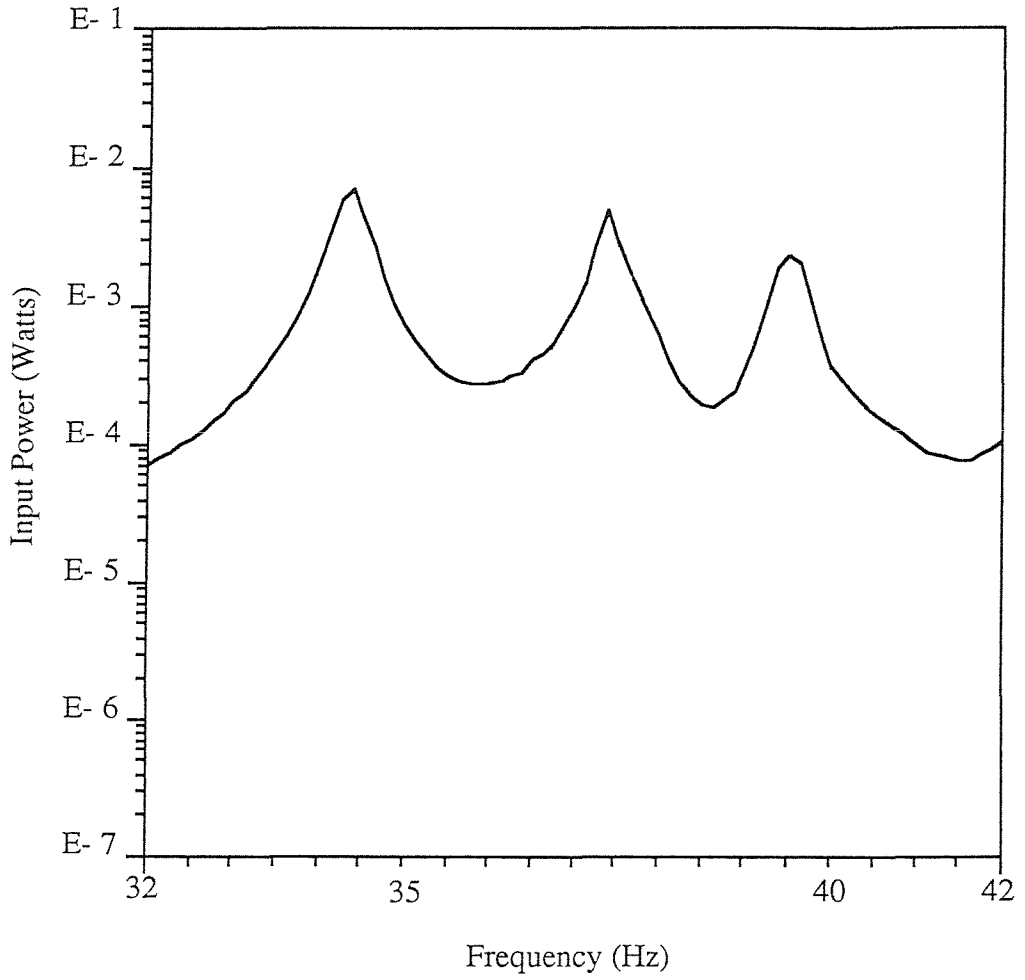

Figure (4.21) : Input power to a two coupled plates system in the frequency range 32-42 Hz

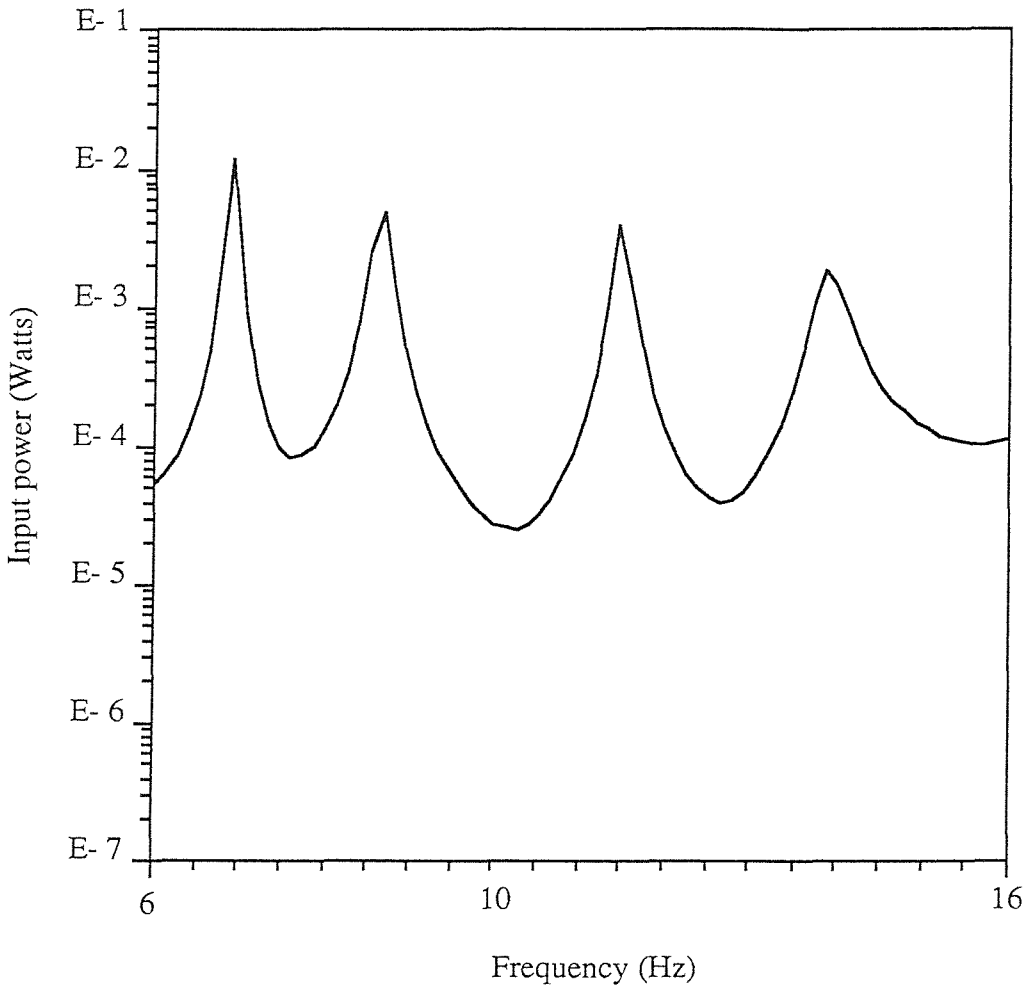

Figure (4.22) : Input power to a two coupled plates system in the frequency range 6-16 Hz

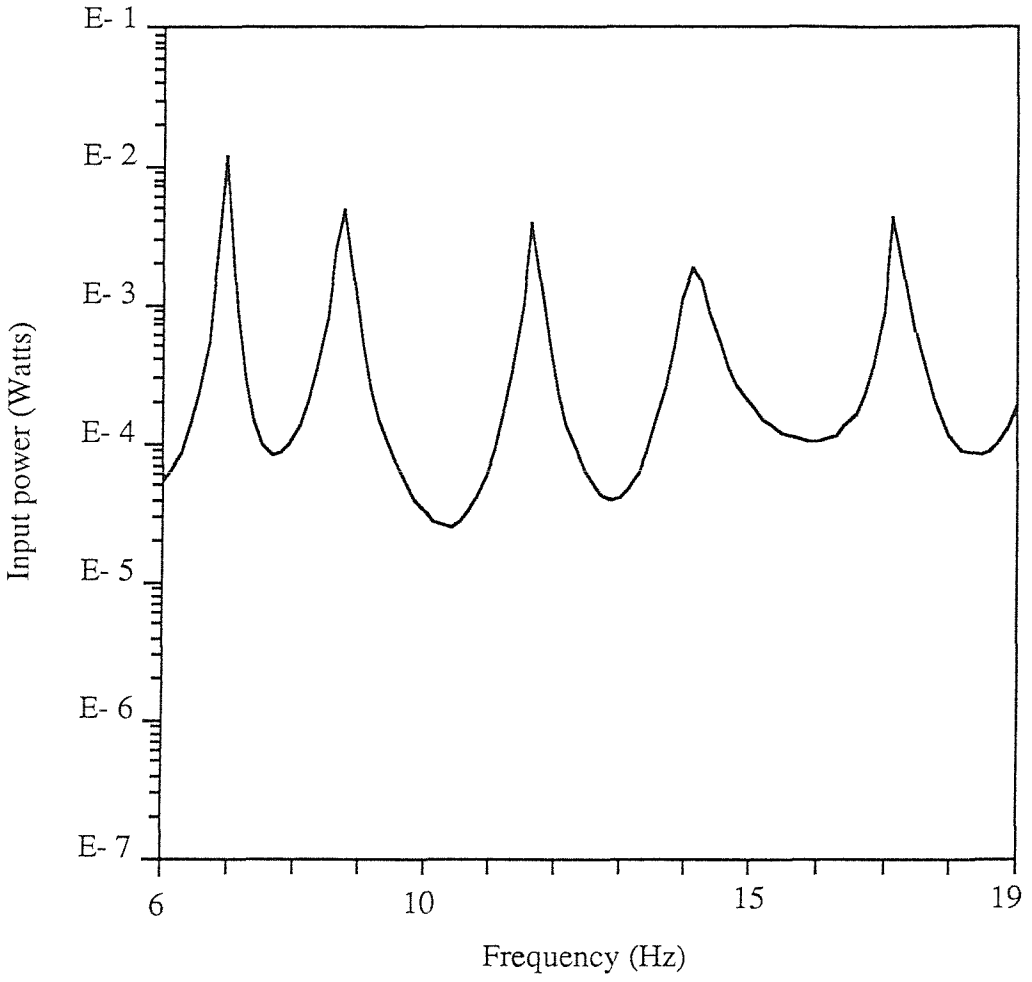

Figure (4.23) : Input power to a two coupled plates system in the frequency range 6-19 Hz

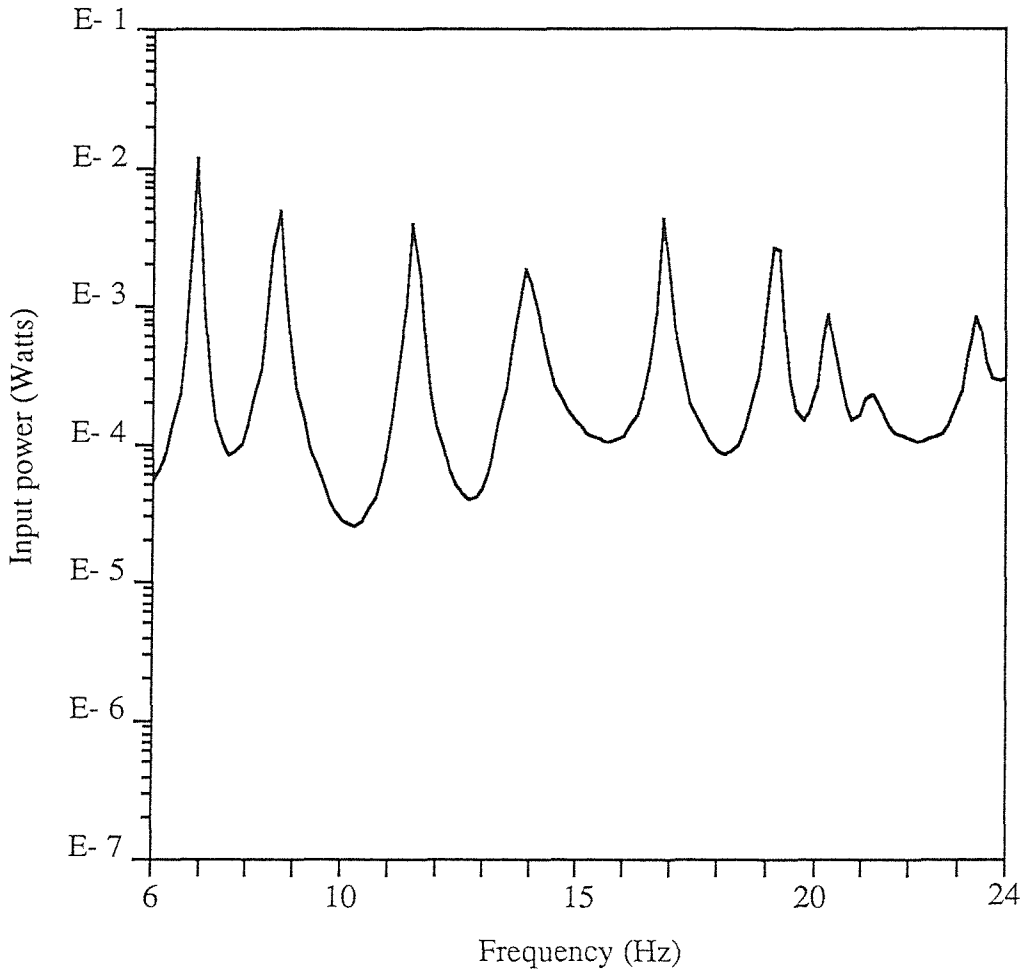

Figure (4.24) : Input power to a two coupled plates system in the frequency range 6-24 Hz

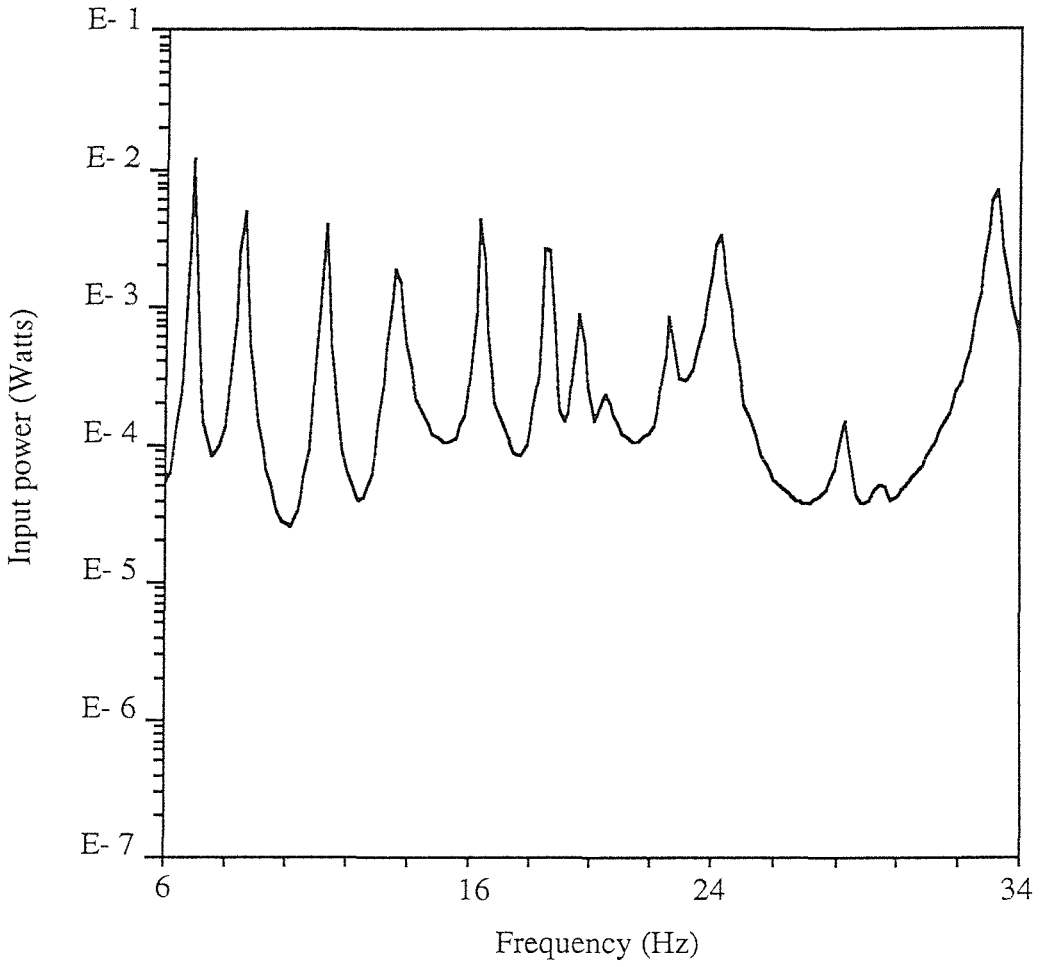

Figure (4.25) : Input power to a two coupled plates system in the frequency range 6-34 Hz

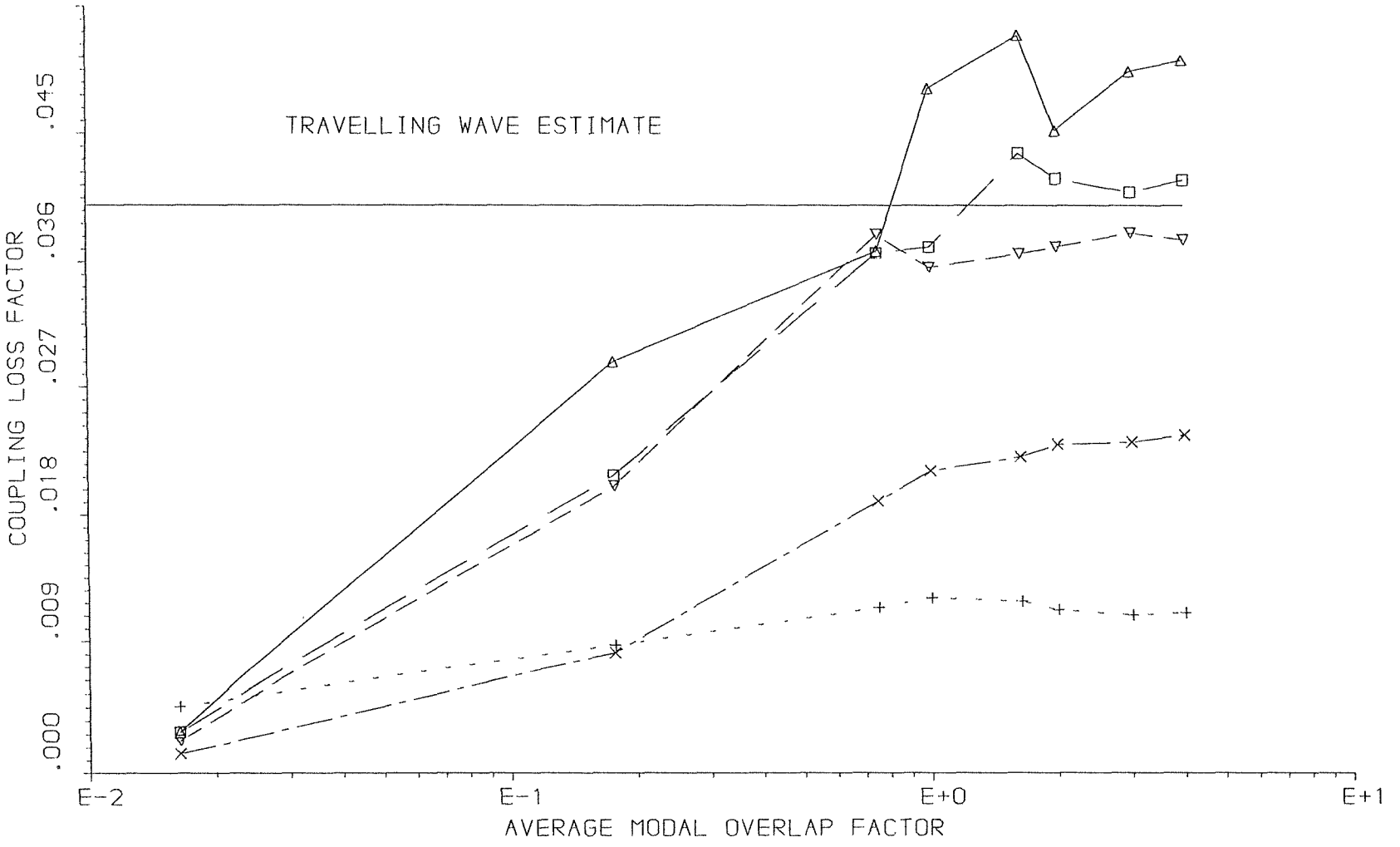

FIG. (4.26) COUPLING LOSS FACTOR IN DIFFERENT FREQUENCY BANDS
+ N=3, × N=4, ▽ N=5, □ N=8, △ N=11, (N IS NO. OF MODES)

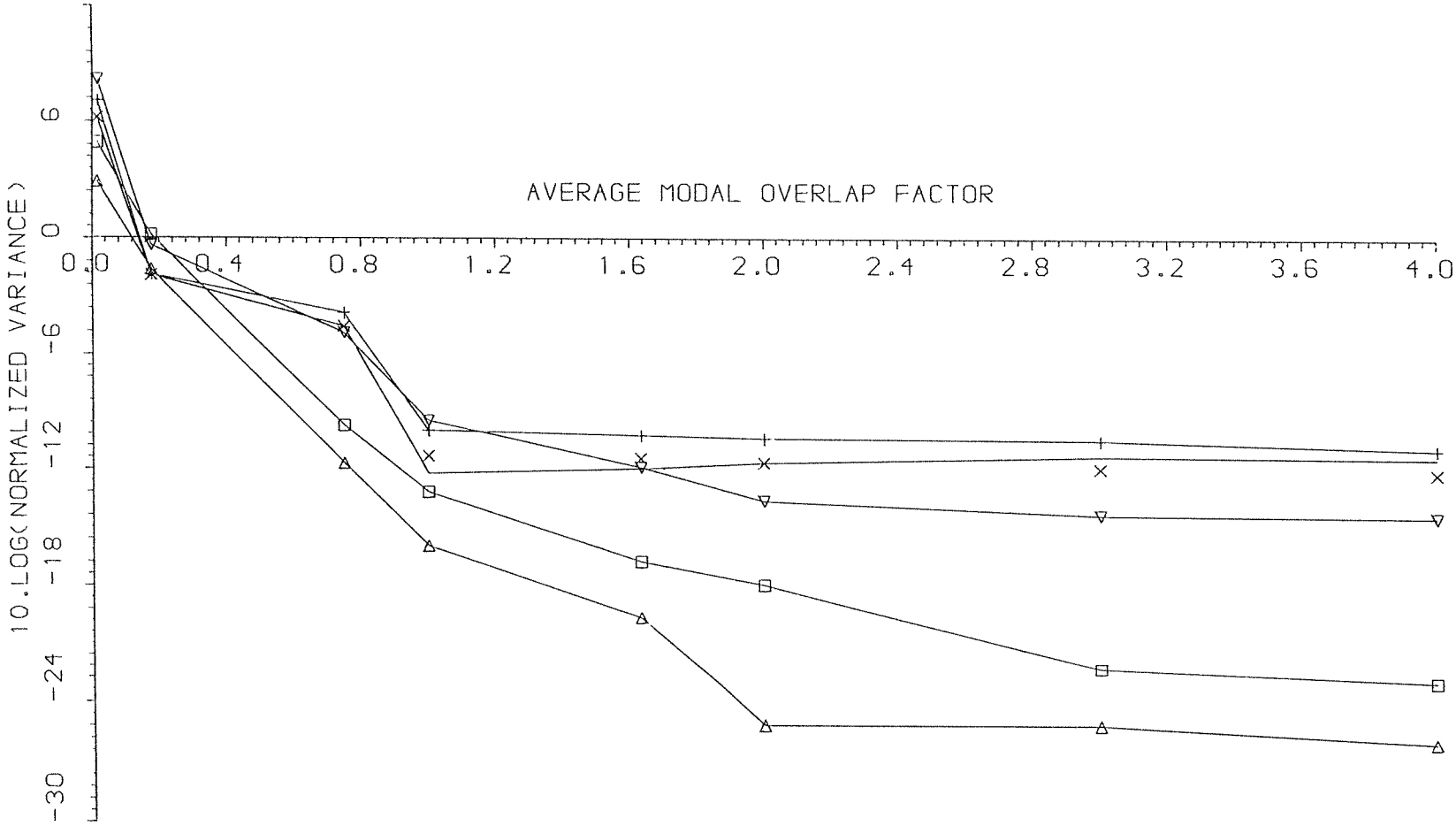

FIG. (4.27) NORMALIZED VARIANCE OF COUPLING LOSS FACTOR
IN DIFFERENT FREQUENCY BANDS

+ N=3, × N=4, ▽ N=5, □ N=8, △ N=11

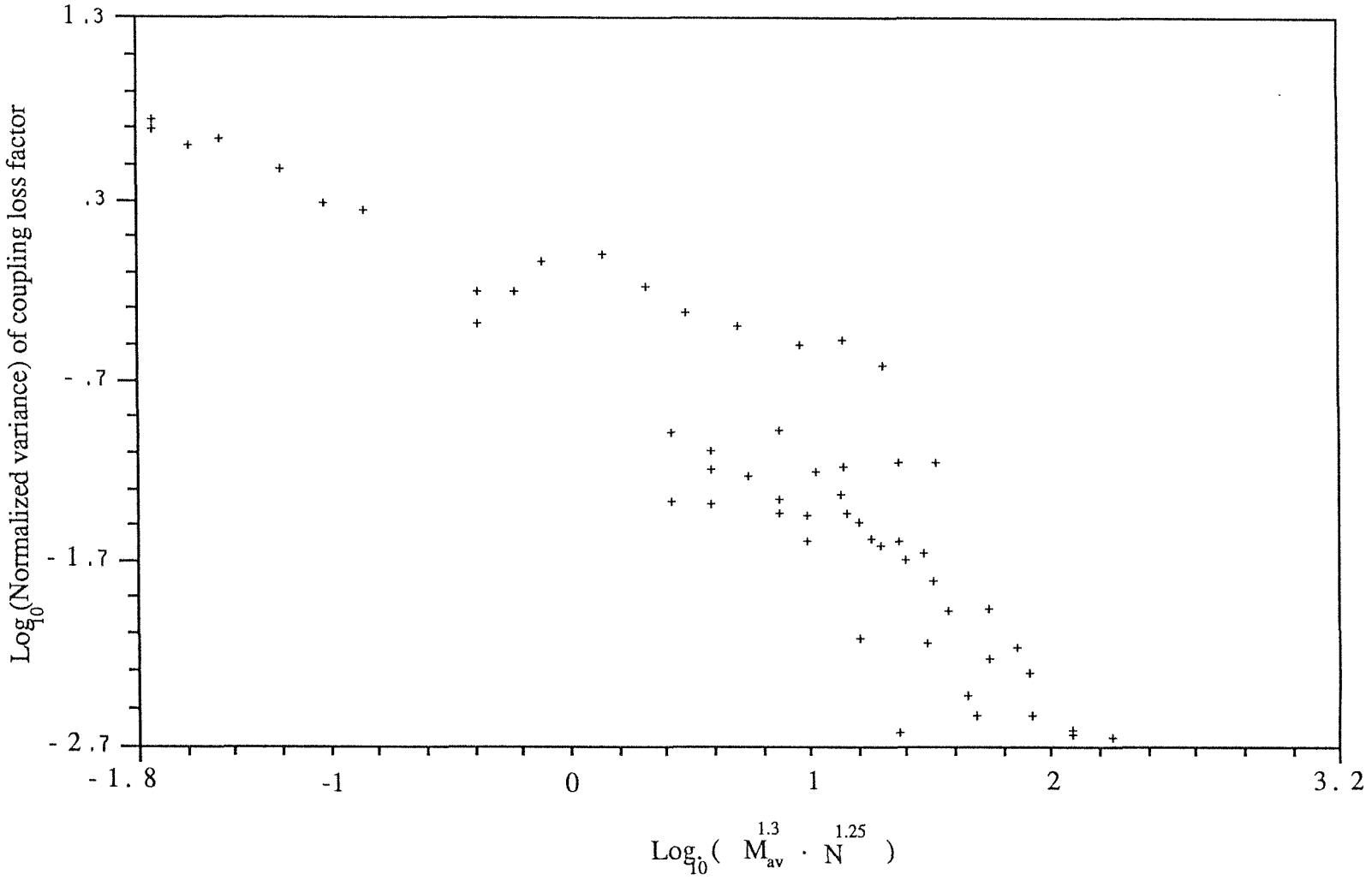

Figure (4.28) : A semi-empirical relationship between the normalized variance of the coupling loss factor, number of resonant modes, and the average modal overlap facor of coupled plates system

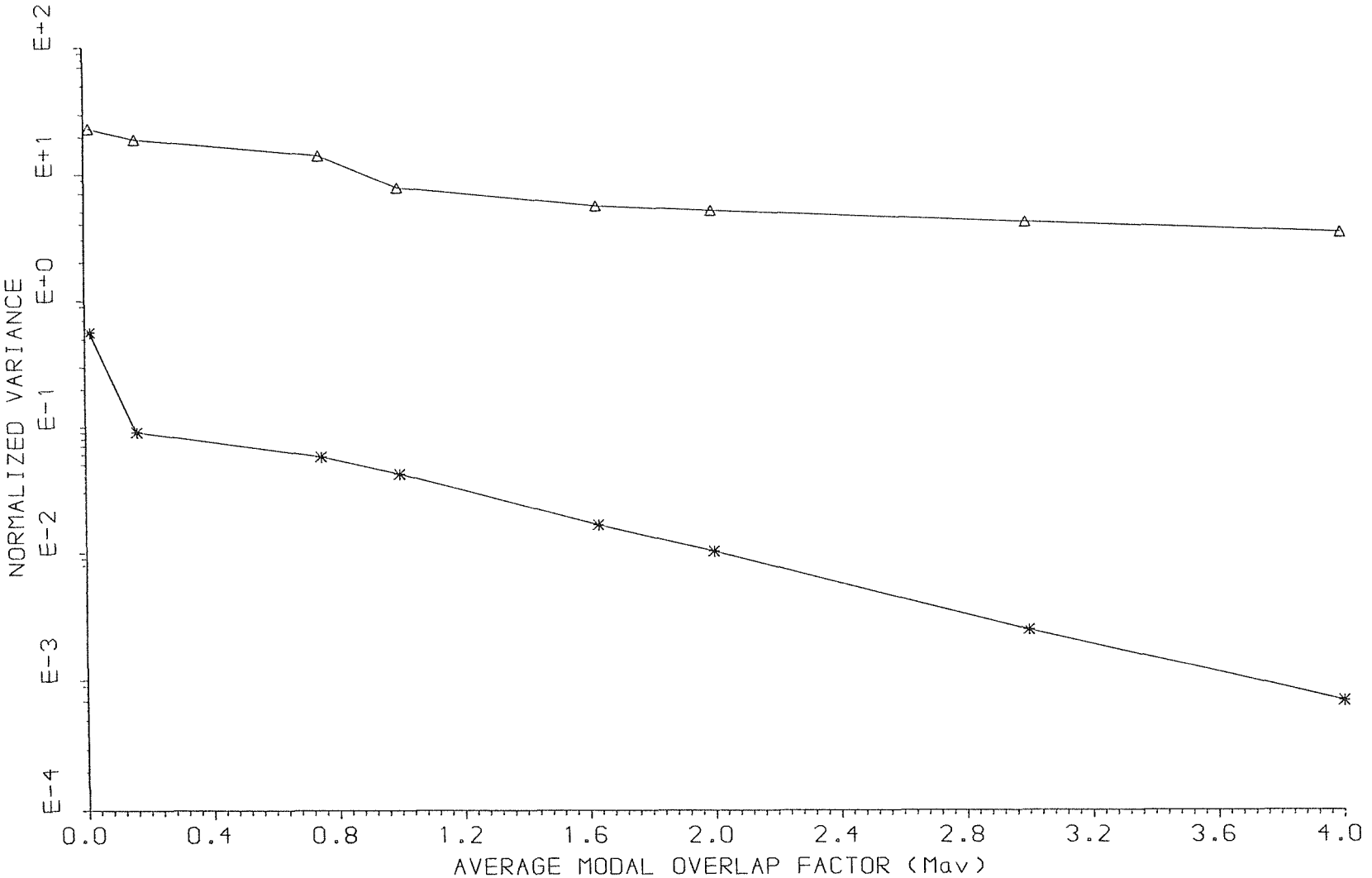

FIG. (4.29) A COMPARISON BETWEEN PURE TONE AND FREQUENCY-AVERAGE VALUES OF NORMALIZED VARIANCE OF POWER FLOW

△ PURE TONE, * FREQUENCY-AVERAGE

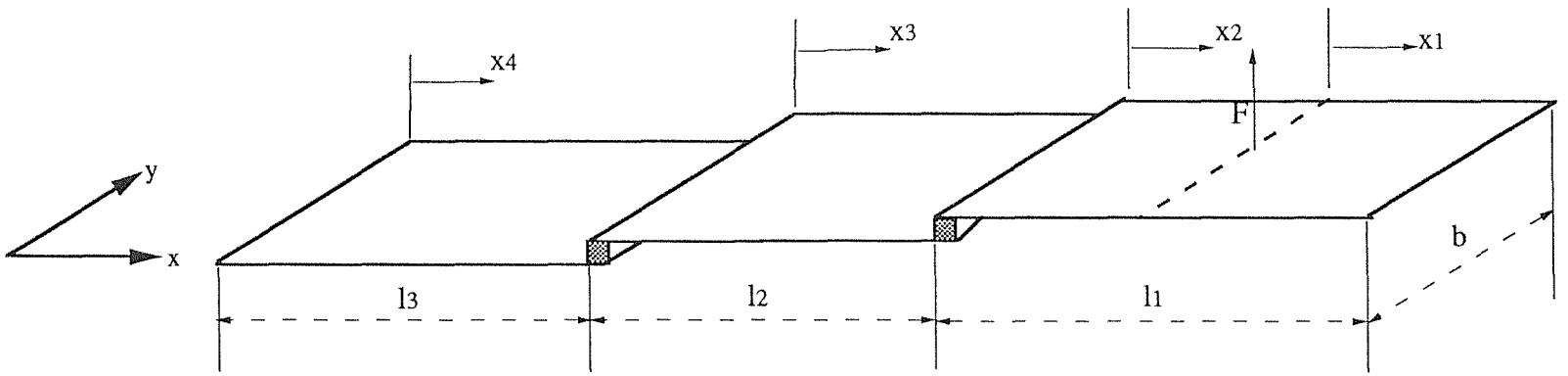

Figure (4.30) Three Coupled Plates System

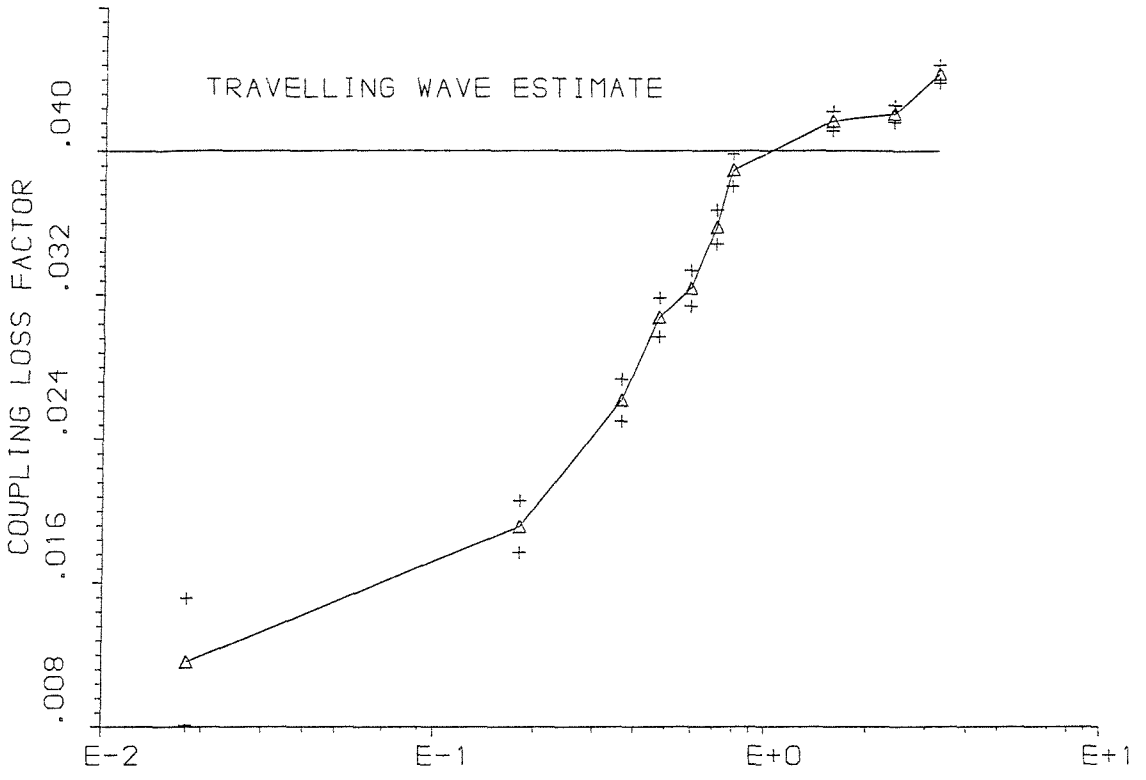

FIG. (4.31) COUPLING LOSS FACTOR (JUNCTION 1)

△ MEAN VALUE, + 95% CONFIDENCE INTERVAL

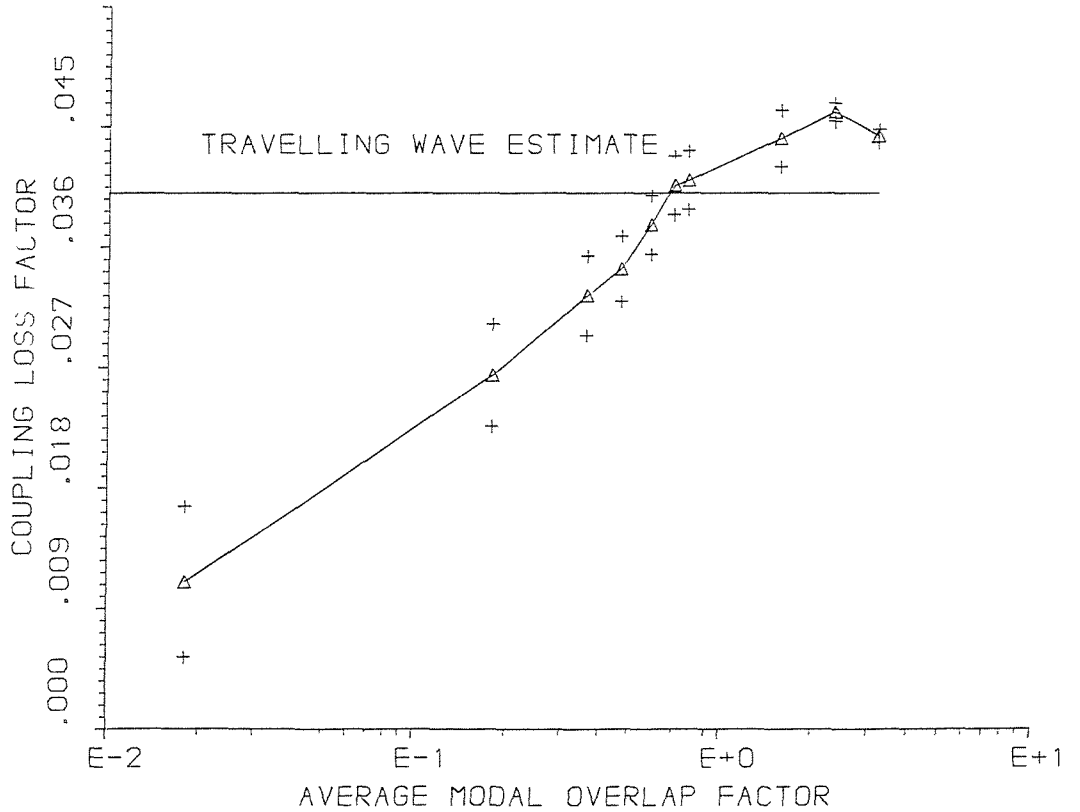

FIG. (4.32) COUPLING LOSS FACTOR (JUNCTION 2)

△ MEAN VALUE, + 95% CONFIDENCE INTERVAL

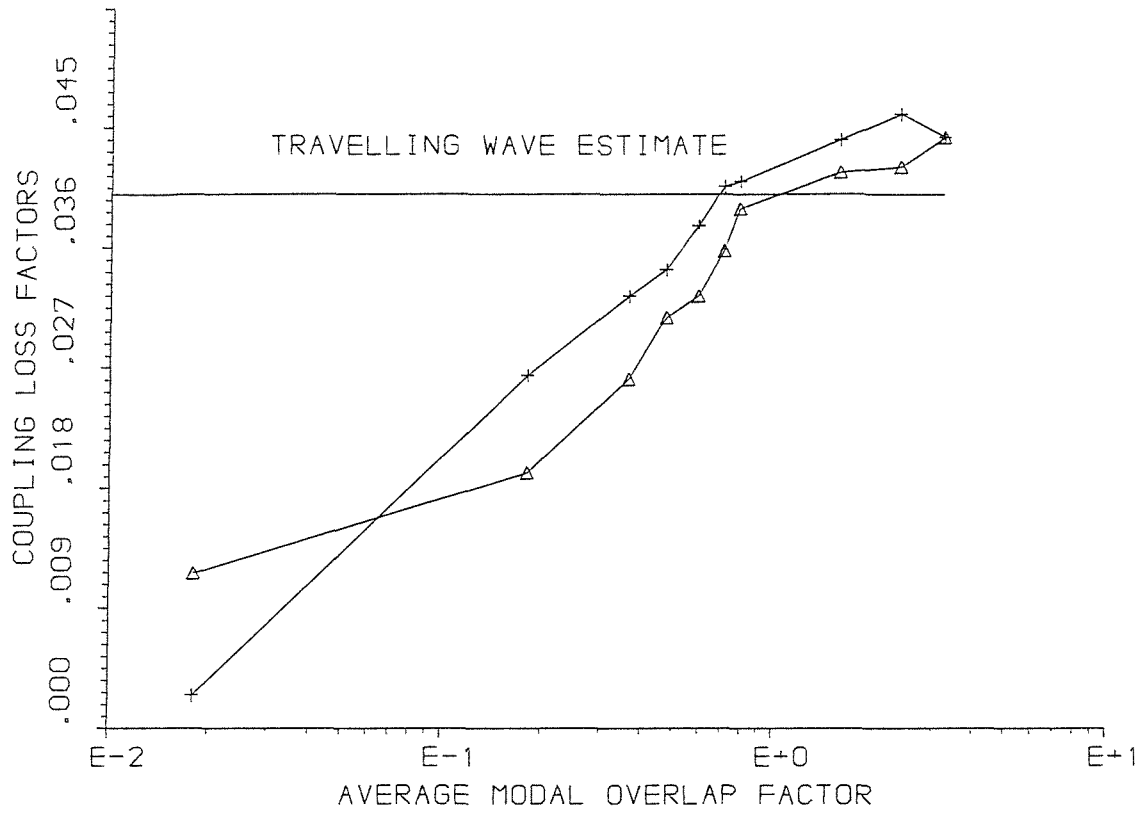

FIG. (4.33) COUPLING LOSS FACTORS OF 3 COUPLED PLATES.

△ JUNCTION 1, + JUNCTION 2

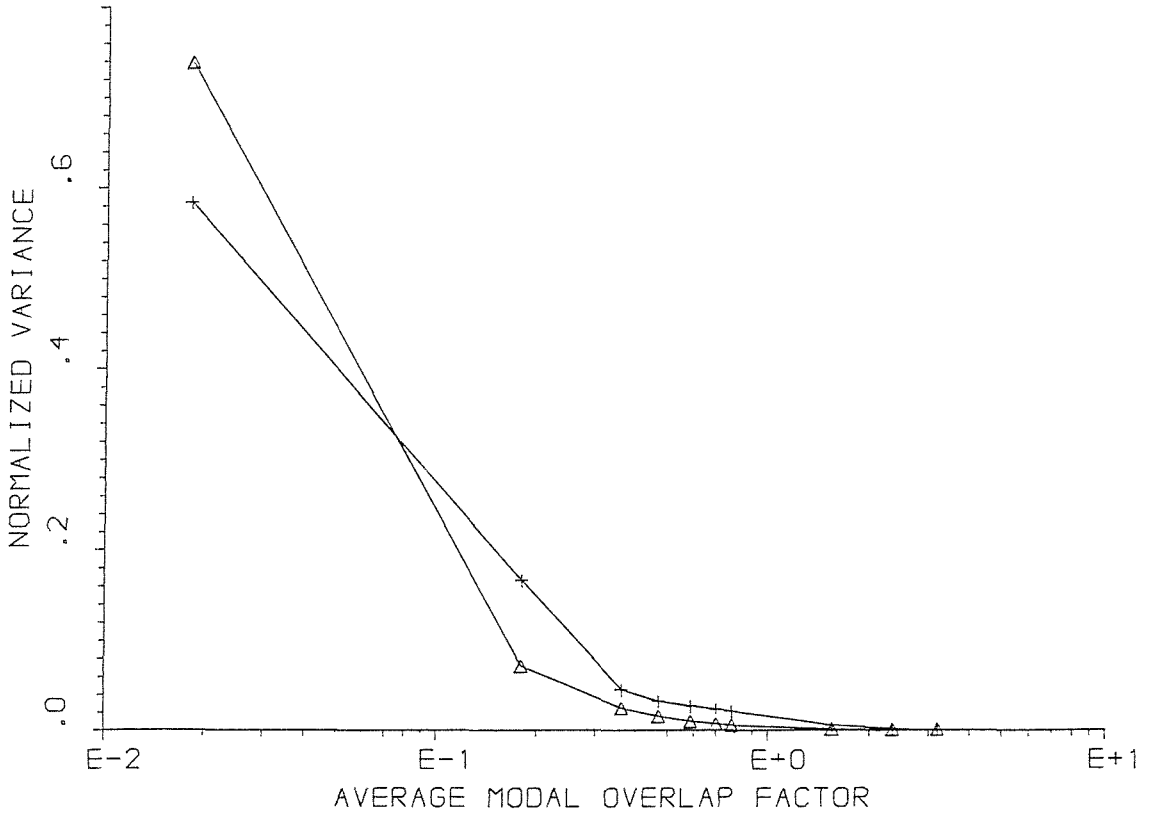

FIG. (4.34) NORMALIZED VARIANCE OF COUPLING LOSS FACTORS

△ JUNCTION 1, + JUNCTION 2

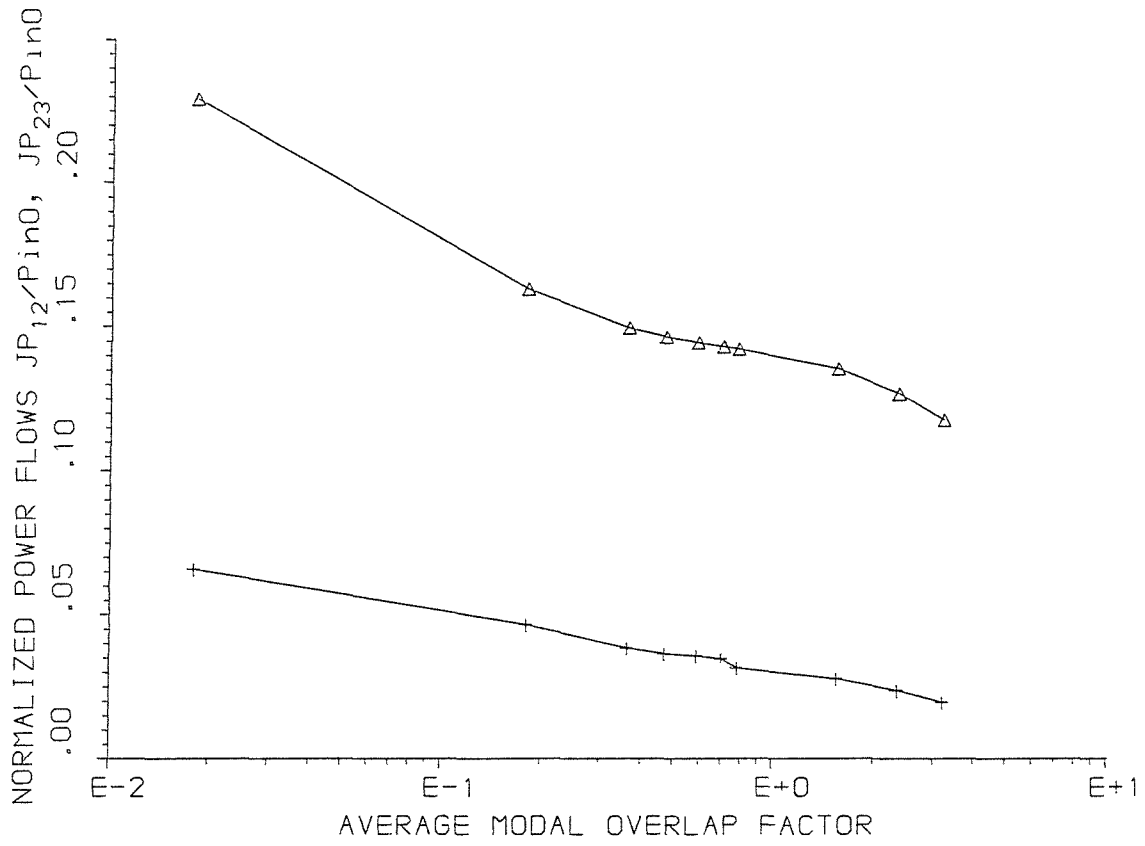

FIG. (4.35) NORMALIZED POWER FLOW OF 3 COUPLED PLATES.

△ JUNCTION 1, + JUNCTION 2

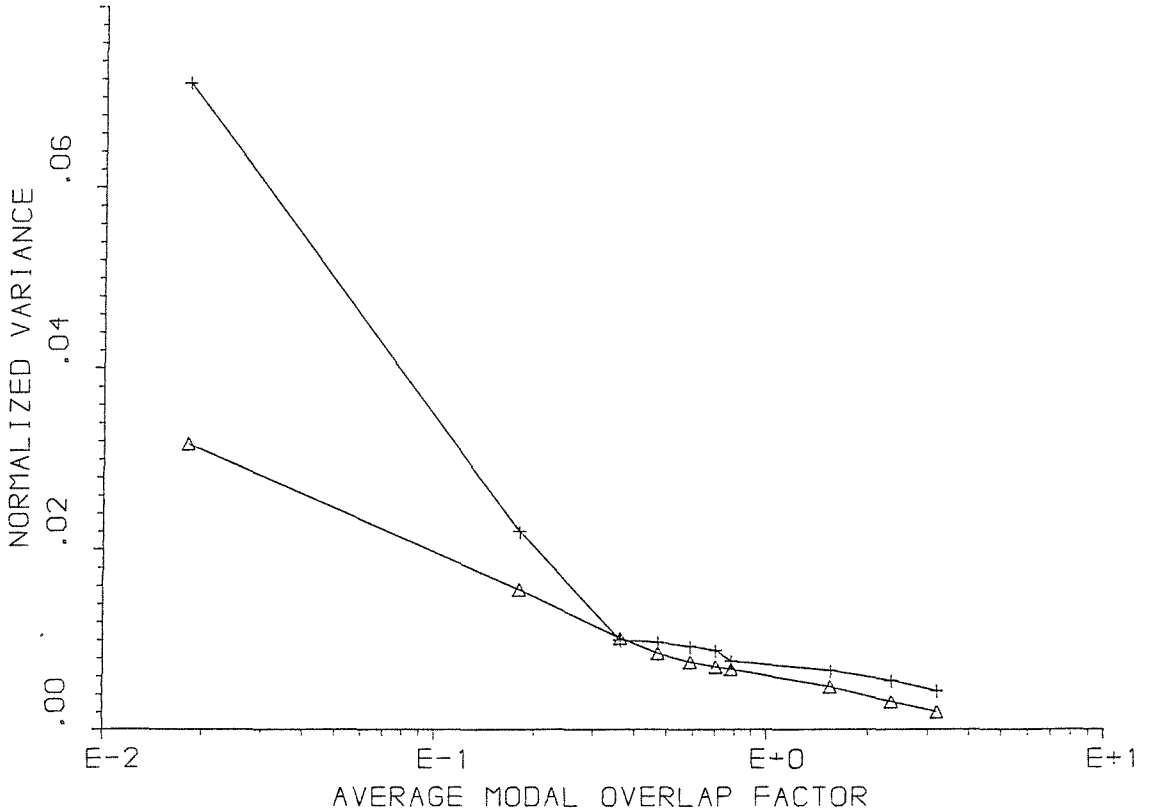

FIG.(4.36) NORMALIZED VARIANCE OF NORMALIZED POWER FLOWS

△ JUNCTION 1, + JUNCTION 2

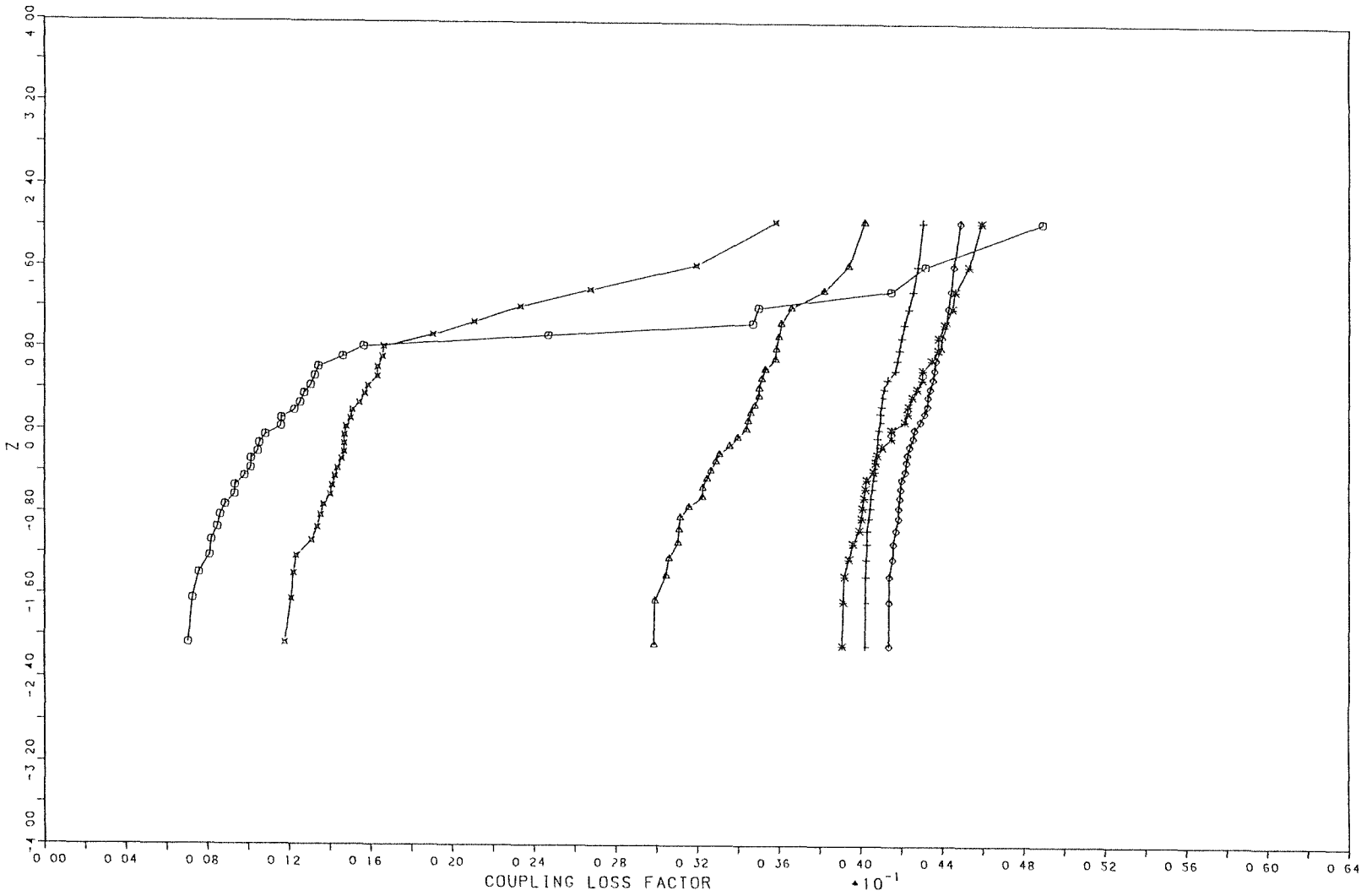

Figure (4.37): Cumulative distribution function of coupling loss factor of the first junction of a three coupled plates system

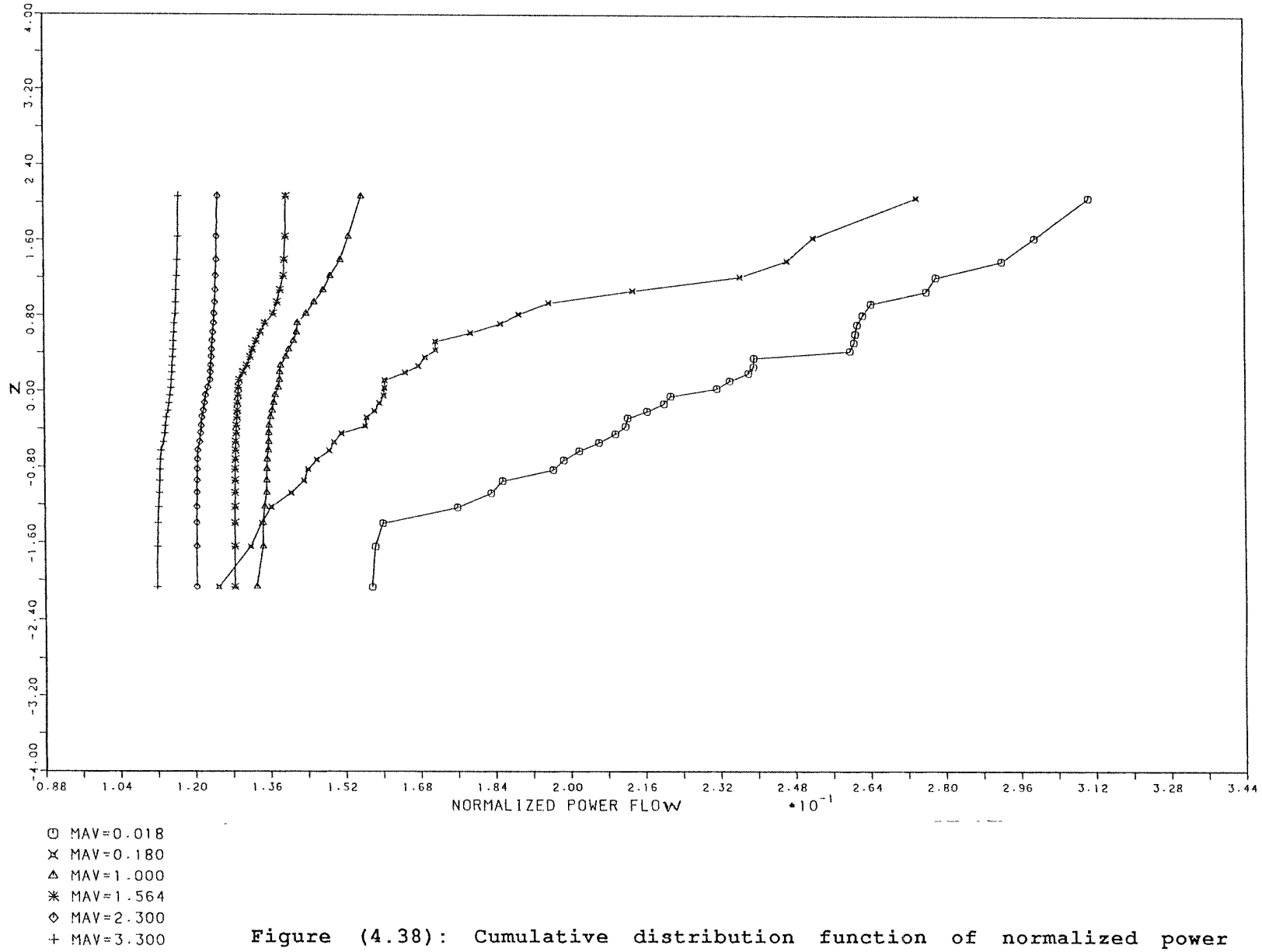

Figure (4.38): Cumulative distribution function of normalized power flow, across the first junction, of a three coupled plates system

CHAPTER 5

POWER FLOW BETWEEN COUPLED RODS

5.1 Introduction

In the previous chapters , various cases of coupled multi-mode systems were analysed. The main objective was to investigate the uncertainty of predictions which are associated with the employment of Statistical Energy Analysis. One of the conclusions which resulted from those investigations was that the widely used wave transmission analysis overestimates the mean of the coupling loss factor (η_{12}) when the modal overlap is low. No physical explanation was given for this observation because the expression for the coupling loss factor contains three elements (variables) which depend on a very complicated fashion of subsystem and coupling parameters. These variables are the power flow and the modal energies of the coupled subsystems.

Previous chapters have also shown that the coupling loss factor, as defined by the ratio of power flow to modal energy difference, is much more sensitive to small perturbations of subsystem geometry under conditions of low modal overlap than the power flow between the subsystems. It might be argued that, in practice, this sensitivity of coupling loss factor is irrelevant, because what really matters is the vibrational energy of the individual subsystems which are determined by actual power flows. This may be true for theoretical predictions of system response, but it has serious implications for the reliability of experimental determinations of coupling loss factors by inversion of the matrix relating injected powers to subsystem energies. Such tests are constrained by the considerations of cost and time to be carried out on only one or two physical systems, which do not necessarily possess the nominal physical parameters attributed to the class of system investigated (e.g. one car body structure selected arbitrarily from a very large set of nominally identical replicas).

In this chapter it is intended to examine, in detail, the power flow equation of two coupled subsystems and to study the influences of the various subsystems parameters on the energy sharing process. In order not to obscure the physics by structural complexity, we treat the coupling between two rods in longitudinal vibration.

Two different systems of coupled rods are investigated in this chapter. These are:

(a) A case of coupling between two rods in which the lengths of both rods are allowed to increase in order to vary the modal overlap.

(b) A case of coupling between two rods in which the length of the receiver rod is allowed to increase while keeping a fixed, relatively small, value for the modal overlap factor of the directly driven rod.

For both cases, results for the power flow and the coupling loss factor are presented.

5.2 Coupled Rods System: Theoretical Model and Assumptions

The mechanical system considered in this chapter is shown in figure (5.1). It consists of two steel rods vibrating longitudinally and coupled together at the ends $x_1 = L_1$ and $x_2 = 0$. The other ends of the rods are assumed to be free. Rod 1 has a cross-sectional area of 0.01 m^2 while rod 2 has a cross sectional area of 0.06 m^2. The length of rod 2 is assumed to be 0.65 times the length of rod 1. Rod 1 is forced with a point harmonic force ($\tilde{F} = F_0 e^{j\omega t}$) as shown. This particular coupled system was chosen because a solution exists for a rod in longitudinal vibration, and as a result, an exact closed-form solution for the quantities of interest may be found. An internal dissipation loss factor of 0.001 is assumed for both rods.

The equation of longitudinal free vibration of a rod is given by

$$\tilde{Y}\frac{\partial^2\tilde{u}(x,t)}{\partial x^2} = \rho\frac{\partial^2\tilde{u}(x,t)}{\partial t^2}\ , \qquad (5.1)$$

where $\tilde{u}$ is the longitudinal displacement of the rod, $\tilde{Y} = Y(1 + j\eta)$ is the complex Young's modulus, η is the loss factor and ρ is the density. The solution for this equation can be written, for rod 1 and rod 2 respectively, as

$$\tilde{u}_1(x_1,t) = (\tilde{A}_1 e^{jkx_1} + \tilde{A}_2 e^{-jkx_1})\, e^{j\omega t}\ , \qquad (5.2)$$

$$\tilde{u}_2(x_2,t) = (\tilde{A}_3 e^{jkx_2} + \tilde{A}_4 e^{-jkx_2})\, e^{j\omega t} \ , \qquad (5.3)$$

where $\tilde{A}_2$ and $\tilde{A}_1$ are the incident and the reflected (at the junction) wave amplitudes respectively which travel in rod 1. $\tilde{A}_4$ and $\tilde{A}_3$ represent the transmitted and the reflected (at the far end of rod 2) wave amplitudes respectively. $\tilde{k} = \tilde{k}_1 = \tilde{k}_2$ is the complex wave number of the motion which is given by

$$\tilde{k} = k\{1 - j(\eta/2)\}$$

In order to find the amplitudes of the different waves which are present, equations (5.2) and (5.3) must satisfy the boundary conditions at the junction and at the free ends of the coupled rods system. These boundary conditions are

(a) At the junction ($x_1 = L_1$, $x_2 = 0$),

$$\tilde{u}_1 = \tilde{u}_2 \ ,$$

and

$$\tilde{F}_{s1} = \tilde{F}_{s2} \ ,$$

where $\tilde{F}_{s1}$ and $\tilde{F}_{s2}$ are the normal stress forces on the cross section areas S_1 and S_2 respectively, which are given by

$$\tilde{F}_{s1} = S_1 \tilde{Y} \frac{\partial \tilde{u}_1}{\partial x_1} \ ,$$

and

$$\tilde{F}_{s2} = S_2 \tilde{Y} \frac{\partial \tilde{u}_2}{\partial x_2} \ .$$

(b) At the free end of rod 1 ($x_1 = 0$),

$$\tilde{F} + S_1 \tilde{Y} \frac{\partial \tilde{u}_1}{\partial x_1} = 0 \ .$$

(c) At the free end of rod 2 ($x_2 = L_2$),

$$S_2 \tilde{Y} \frac{\partial \tilde{u}_2}{\partial x_2} = 0 \ .$$

Substitution of equations (5.2) and (5.3) into the boundary conditions gives the following expressions for the complex wave amplitudes $\tilde{A}_1$ - $\tilde{A}_4$:

$$\tilde{A}_1 = \frac{F_o \mu_2}{j S_1 \tilde{Y} \tilde{k} (\mu_1 - \mu_2)} \ , \qquad (5.4.a)$$

$$\tilde{A}_2 = \frac{F_o \mu_1}{j S_1 \tilde{Y} \tilde{k} (\mu_1 - \mu_2)} \ , \qquad (5.4.b)$$

$$\tilde{A}_3 = \frac{F_o e^{-2jkL_2}}{j S_1 \tilde{Y} \tilde{k} (\mu_1 - \mu_2)} \ , \qquad (5.4.c)$$

and

$$\tilde{A}_4 = \frac{F_o}{j S_1 \tilde{Y} \tilde{k} (\mu_1 - \mu_2)} \ , \qquad (5.4.d)$$

where μ_1 and μ_2 are given by

$$\mu_1 = \frac{S_1 \mu_2 e^{jkL_1} - S_2 e^{-2jkL_2} + S_2}{S_1 e^{-jkL_1}} \ .$$

$$\mu_2 = \frac{(S_1 + S_2) e^{-2jkL_2} - (S_2 - S_1)}{2 S_1 e^{jkL_1}} \ ,$$

5.3 Calculation of Input Power

The time averaged input power to the coupled rods system is given by

$$\bar{P}_{in} = 1/2\ |\tilde{F}|^2\ Re\{\tilde{H}_o\}\ , \qquad (5.5)$$

where $\tilde{H}_o$ is the driving point mobility of the coupled system (at $x_1 = 0$), which is given by,

$$\tilde{H}_o = j\omega(\tilde{A}_1 + \tilde{A}_2)\ .$$

Substitution for the amplitudes $\tilde{A}_1$ and $\tilde{A}_2$ from equations (5.4.a) and (5.4.b) produces the following expressions for the time averaged injected power, i.e.,

$$\bar{P}_{in} = 1/2\ |F_o|^2\ Re\left\{\frac{\omega(\mu_1+\mu_2)}{S_1\ \tilde{Y}\ \tilde{k}\ (\mu_1-\mu_2)}\right\} \qquad (5.6)$$

where μ_1 and μ_2 are given above.

The time averaged input power may also be written as,

$$\bar{P}_{in} = 1/2\ |\tilde{V}_o|^2\ Re\{\tilde{Z}_o\}\ ,$$

where $\tilde{Z}_o$ is the driving point impedance of the coupled system (at $x_1 = 0$), and $\tilde{V}_o$ is the velocity at the same point. If we write $\tilde{Z}_o$ in terms of its resistive and reactive parts as

$$\tilde{Z}_o = R_o + jI_o\ ,$$

then

$$\bar{P}_{in} = \frac{1}{2}|F_o|^2\left[\frac{R_o}{(R_o^2+I_o^2)}\right] \qquad (5.7)$$

5.4 Calculation of Power Flow

The time-average power flow from rod 1 to rod 2 across the junction is given by

$$\bar{P}_{12} = 1/2\ \mathrm{Re}\{\tilde{F}_c\ .\ \tilde{V}_c^*\}\ , \qquad (5.8)$$

where $\tilde{F}_c$ and $\tilde{V}_c$ are the force and the velocity at the junction ($x_2 = L_2$) respectively . They are given by

$$\tilde{F}_c(x_2) = \tilde{F}_{s2}(x_2,t) = S_2\,\tilde{Y}\,\frac{\partial \tilde{u}_2}{\partial x_2}\ ,$$

$$= j\tilde{k}\,S_2\tilde{Y}(\tilde{A}_3 - \tilde{A}_4)\ ,$$

and

$$\tilde{V}_c(x_2) = j\omega(\tilde{A}_3 + \tilde{A}_4)\ .$$

The substitution for the amplitudes $\tilde{A}_3$ and $\tilde{A}_4$ from (5.4.c) and (5.4.d) produces the following expression for the time averaged power flow between the rods, i.e.,

$$\bar{P}_{12} = \frac{1}{2}|F_o|^2\left\{\frac{S_2}{S_1^2}\right\}\mathrm{Re}\left\{\omega\left(\frac{e^{-2jkL_2}-1}{j(\mu_1-\mu_2)}\right)\left(\frac{e^{-2jkL_2}+1}{j\tilde{k}\tilde{Y}(\mu_1-\mu_2)}\right)^*\right\}\ . \qquad (5.9)$$

The time averaged power flow between the coupled rods may also be written in the alternative form

$$\bar{P}_{12} = 1/2\ |\tilde{V}_c|^2\ \mathrm{Re}\{\tilde{Z}_2\}\ , \qquad (5.10)$$

where $\tilde{Z}_2$ is the impedance of the receiver rod at the coupling point which is given by

$$\tilde{Z}_2 = (j/\omega)\ \tilde{Y}\ S_2\ \tilde{k}\ \tan(\tilde{k}L_2).$$

$\tilde{V}_c$ can be written in terms of the velocity of the driven uncoupled rod at $x_1 = L_1$ as

$$\tilde{V}_c = \tilde{V}_1 - \frac{\tilde{F}_c}{\tilde{Z}_1}\ , \qquad (5.11)$$

where $\tilde{Z}_1$ is the impedance of the directly driven rod at the attachment point which is given by

$$\tilde{Z}_1 = (-j/\omega)\ \tilde{Y}\ S_1\ \tilde{k}\ \tan(\tilde{k}L_1).$$

$\tilde{F}_c$ can be written as

$$\tilde{F}_c = \tilde{Z}_2\,\tilde{V}_c\ . \qquad (5.12)$$

By combining equations (5.10) and (5.11) one finds [57] that the attachment point vibrates with the velocity

$$\tilde{V}_c = \frac{\tilde{V}_1}{1+(\tilde{Z}_2/\tilde{Z}_1)}\ . \qquad (5.13)$$

In view of equation (5.10), the time averaged energy that the receiver rod extracts from the driven rod is found to obey

$$\bar{P}_{12} = 1/2 \frac{\mathrm{Re}\{\tilde{Z}_2\}\ |\tilde{V}_1|^2}{|1+(\tilde{Z}_2/\tilde{Z}_1)|^2} \ . \qquad (5.14)$$

If we write $\tilde{Z}_1$ and $\tilde{Z}_2$ as

$$\tilde{Z}_1 = R_1 + jI_1 \ ,$$

and

$$\tilde{Z}_2 = R_2 + jI_2 \ ,$$

where R and I represent the resistive part and the reactive part of the impedance respectively, then equation (5.14) can now be written as

$$\bar{P}_{12} = \frac{1}{2}\left[\frac{R_2 |\tilde{V}_1|^2 (R_1^2+I_1^2)}{(R_1+R_2)^2 + (I_1+I_2)^2} \right] . \qquad (5.15)$$

$\tilde{V}_1$ can be written in terms of the impedance of rod 1 as

$$\tilde{V}_1 = \frac{\tilde{F}}{\tilde{Z}_1 \cos(\tilde{k}\ L_1)} .$$

Under the assumption of low damping, we can write $|\tilde{V}_1|^2$ in the following approximate form

$$|\tilde{V}_1|^2 = \frac{|F_0|^2}{(R_1^2+I_1^2)\left[\cos^2(kL_1)+\zeta^2 k^2 L_1^2 \sin^2(kL_1)\right]} \ ,$$

where $\zeta = \eta/2$, is the damping coefficient. Equation (5.15) can now be written as

$$\bar{P}_{12} = \frac{1}{2}\left[\frac{R_2}{(R_1+R_2)^2 + (I_1+I_2)^2} \right] \frac{|F_0|^2}{\left[\cos^2(kL_1)+\zeta^2 k^2 L_1^2 \sin^2(kL_1)\right]} \; .$$

(5.16)

Equation (5.16) is a general expression for the calculation of power flow between any two subsystems coupled at a point.

The other form of interest, for the power flow expression, is that of the ratio between the time-average power flow and the time-average input power. Using equations (5.7) and (5.16), the normalized power flow can be written as

$$\frac{\bar{P}_{12}}{\bar{P}_{in}} = \frac{R_2 |F_0|^2 (R_0^2+I_0^2)}{R_0\left[(R_1+R_2)^2 + (I_1+I_2)^2\right]\left[\cos^2(kL_1)+\zeta^2 k^2 L_1^2 \sin^2(kL_1)\right]}$$

(5.17)

Equation (5.17) is considered in the parametric study of the effects of the individual components of the impedances on the behaviour of the quantity $\frac{\bar{P}_{12}}{\bar{P}_{in}}$ in different modal overlap conditions. An analysis for expressing the time averaged quantities of input power and power flow in terms of the direct and the transfer impedances of the uncoupled rods is shown in Appendix IV. This form has not been considered in the investigations because it is rather complicated compared with the form of equation (5.17).

5.5 Calculation of Total Energies

The time-averaged total energy of each coupled rod is calculated as twice the time averaged kinetic energy. It is written for the individual rods as

$$\bar{E}_1 = \frac{1}{2}\omega^2 \int_{L_1} m'_1 |\tilde{u}_1|^2 \, dx_1 \ , \tag{5.18}$$

$$\bar{E}_2 = \frac{1}{2}\omega^2 \int_{L_2} m'_2 |\tilde{u}_2|^2 \, dx_2 \ , \tag{5.19}$$

where m'_1 and m'_2 are the mass per unit length of rod 1 and rod 2 respectively. The substitution for the different wave amplitudes from equations (5.4) will produce the following expressions for the total time-averaged energies, i.e.,

$$\bar{E}_1 = 1/2\ \omega^2 m'_1 \int_{L_1} \left| \frac{F_0\mu_2 e^{jkx_1} + F_0\mu_1 e^{-jkx_1}}{jS_1\tilde{Y}\tilde{k}(\mu_1-\mu_2)} \right|^2 dx_1 \ , \tag{5.20}$$

$$\bar{E}_2 = 1/2\ \omega^2 m'_2 \int_{L_2} \left| \frac{F_0 e^{-2jkL_2}.e^{jkx_2} + F_0 e^{-jkx_2}}{jS_1\tilde{Y}\tilde{k}(\mu_1-\mu_2)} \right|^2 dx_2 \ . \tag{5.21}$$

5.6 Semi-infinite Undamped Coupled Rods

The system analyzed in this section consists of two semi-infinite, lossless rods coupled at their ends as shown in figure (5.2). The cross section areas and the material properties are similar to those of the previously described finite system. The object of the present analysis is to obtain estimates for the power flow and the coupling loss factor, using the travelling wave method [2], and compare them with those obtained for the finite system.

Consider an incident longitudinal wave travelling in rod 1 from the left. At the junction (x = 0), transmitted and reflected waves are generated. The displacement responses of rod 1 and rod 2 can be written as

$$u_1(x,t) = (A_i e^{-jkx} + A_r e^{jkx})\, e^{j\omega t} \ , \qquad (5.22)$$

$$u_2(x,t) = A_t e^{-jkx}\, e^{j\omega t} \ , \qquad (5.23)$$

where A_i is the amplitude of the incident wave, A_r is the reflected wave amplitude, and A_t represents the transmitted wave amplitude. Equation (5.22) and (5.23) satisfy the boundary conditions at the coupling point, (x_1=0). These boundary conditions are

(a). $u_1 = u_2$,

(b). $F_{s1} = F_{s2}$, (5.24)

The substitution of equations (5.22) and (5.23) into the boundary conditions gives the following expressions for the transmitted and reflected wave amplitudes in terms of the incident wave amplitude, i.e.,

$$A_t = \frac{2A_i}{1+(S_2/S_1)} \ , \qquad (5.25)$$

and

$$A_r = \frac{A_i(1-(S_2/S_1))}{1+(S_2/S_1)} \ . \qquad (5.26)$$

The time-averaged incident power in rod 1 and the time-averaged transmitted power from rod 1 to rod 2 can be written respectively as,

$$\bar{P}_{in\infty} = \frac{1}{2}(\rho\, S_1\, \omega^2\, C_1 A_i^2) \ , \qquad (5.27)$$

and

$$\bar{P}_{12\infty} = \frac{1}{2}(\rho S_2 \omega^2 C_l \hat{A}_i^2) \quad , \tag{5.28}$$

where C_l is the longitudinal wave speed. An expression for the normalized power flow can now be obtained, after the substitution for the wave amplitudes, as

$$\frac{\bar{P}_{12\infty}}{\bar{P}_{in\infty}} = \frac{4}{\{\sqrt{(S_1/S_2)}+\sqrt{(S_2/S_1)}\}^2} \quad . \tag{5.29}$$

The ratio above represents the transmission coefficient τ_∞ of the coupled rods. Using the assumption that the energy transmitted across the junction is small so that the reflected wave has nearly the same energy as the incident wave, then the total time averaged vibrational energy of rod 1 of length L_1 is given by

$$\bar{E}_1 = \rho S_1 \omega^2 \hat{A}_i^2 L_1 \quad . \tag{5.30}$$

By definition, coupling loss factor $\eta_{12\infty}$ is written as

$$\eta_{12\infty} = \frac{\bar{P}_{12\infty}}{\bar{E}_1 \omega} \tag{5.31}$$

Substitution of equations (5.28) and (5.30) into (5.31) gives the following expression for the travelling wave estimate of coupling loss factor

$$\eta_{12\infty} = \frac{1}{2}\frac{C_l \tau_\infty}{\omega L_1} \tag{5.32}$$

5.7 Results and discussions

From the analysis of the finite coupled rods system described in the previous sections, the time averaged quantities of input power, power flow, and total energies, were computed at intervals of 1 Hz in the 1/3 octave frequency band centred at 5000 Hz. The results were obtained for a range of values of average modal overlap factor ($M_{av} = \sqrt{M_1 M_2}$) of the coupled rods system. Typical spectra for the input power and the power flow are shown in figures (5.3)-(5.7) and (5.8)-(5.12) respectively. It should be noted that the different M_{av} values were obtained by varying the lengths of the coupled rods, (i.e., by assuming different modal density values, $n(f) = 2L/C_g$), but keeping a fixed length ratio (L_2/L_1) value of 0.65. The internal loss factors of the rods(η_1 and η_2) had a fixed value of 0.001.

Band quantities for $\bar{P}_{in}$, $\bar{P}_{12}$, $\bar{E}_1$ and $\bar{E}_2$ were obtained by integrating their spectra over the above mentioned frequency range. Figure (5.13) displays the frequency averaged values of input power to the coupled system, against average modal overlap factor. The figure shows that the input power has an almost constant value, independent of the average modal overlap. This result is consistent with that of Scharton [61].

Figure (5.14) displays the computed band values of normalized power flow between the finite coupled rods against average modal overlap factor. This figure shows that the power flow decreases with the length of the coupled rods. The reason for this is the increase in the energy absorbed by the directly driven rod as the length of the latter increases.

The coupling loss factor (η_{12}) is evaluated on the basis of SEA hypothesis (see equation (2.34)) using the calculated band values of $\bar{P}_{12}$, $\bar{E}_1$ and $\bar{E}_2$ above, at different M_{av} values. The results are plotted in figure (5.15) together with the frequency averaged estimates of $\eta_{12\infty}$ obtained from the travelling wave method (equation (5.32)). The value of η_{12} for the finite coupled system falls well below the travelling wave estimate when M_{av} is small (less than 1.0). η_{12} approaches the estimate of the infinite system when M_{av} takes the value of unity and greater. This result supports those previously obtained for coupled beams and coupled plates systems. An explanation for the coupling loss factor behaviour, presented in the figure above, is given in the subsequent section.

Concerning the power flow between the coupled rods, the quantity $\bar{P}_{12}/|\tilde{V}_1|^2$ (see equation 5.15) is considered first for the purpose of presenting the effects of the individual components of the impedances of the uncoupled rods on the spectrum of the power flow. The reasons for the consideration of this particular quantity are first, that its peaks have almost the same order of magnitude as the resistive parts and the reactive parts of the impedances; and second, the spectrum of this quantity exhibits these peaks at the same frequencies as the absolute power flow ($\bar{P}_{12}$). The spectrum of ($\bar{P}_{12}/|\tilde{V}_1|^2$) is plotted in figures (5.16) and (5.17) for M_{av} value of 0.008 and a length ratio (L_2/L_1) of 0.65. The figures also display the real parts and the moduli of the imaginary parts of the impedances of the uncoupled rods respectively. These figures show that the maximum power flow occurs at the natural frequencies of the coupled system as proved by figure (5.18) which shows that the reactive part of the driving point impedance of the coupled system (I_o) vanishes at these frequencies.

From the results presented in figures (5.16) and (5.17), a general conclusion can be drawn that maximum power flow between the coupled rods can be obtained when the sum of the reactive parts of the impedances of the uncoupled rods (I_1+I_2) is zero. This can be seen clearly, in figure (5.17), at the frequencies which correspond to the first, second and the fourth peaks of ($\bar{P}_{12}/|\tilde{V}_1|^2$). But there are special, rare cases which do not correspond to this condition. The third peak of ($\bar{P}_{12}/|\tilde{V}_1|^2$) corresponds to the case when both uncoupled rods are close to anti-resonance. The sensitivity of this behaviour is indicated in figure (5.19). This figure is produced after the perturbation of the length ratio (L_2/L_1) to be 0.64 instead of 0.65. It shows that all peaks of power flow correspond to the condition of zero sum of (I_1+I_2). The observation above is consistent with condition given in reference [57] that maximum power flow can be achieved when the impedances of the uncoupled rods are complex conjugates.

Note that the peaks in the resistive parts of the impedances correspond to the anti-resonances of the uncoupled rods, while the dips of the moduli of the reactive parts correspond to the resonance frequencies of the uncoupled rods.

5.8 Short-long Rods System

As noted previously, the power flow between two coupled rods of equal loss factors decreases as the lengths of the rods increase. The reason for this is the increase in the dissipated energy of the directly driven rod which consequently reduces the amount of energy transfered to the other rod. In this section, an attempt is made to eliminate the influence of the length of the driven rod on the power flow as follows. The length of the driven rod is kept fixed such that a constant value of 0.01 is assumed for the modal overlap factor (M_1) of this rod, while different values of modal overlap factor (M_2) of the receiver rod are assumed (by assuming different length values). For each value of M_2, the band value of normalized power flow $\frac{\bar{P}_{12}}{\bar{P}_{in}}$ is computed and can be seen in figure (5.20). This figure shows the behaviour that as the modal overlap factor of the long rod (M_2) increases, $\frac{\bar{P}_{12}}{\bar{P}_{in}}$ increases, which is unlike the results previously obtained from the long-long rods system. This figure shows that as M_2 increases and takes the value of 1.0 and greater the normalized power flow exhibits a fixed value which is independent of any further increase in M_2.

Figure (5.21) displays the results for the coupling loss factor (η_{12}) of the short-long rods system at the different M_2 values. The curve of this figure shows a similar trend to that of the coupled long-short beams system (described in Chapter 2): as M_2 increases η_{12} increases and approaches asymptotically the travelling wave estimate (equation (5.32)). To explain this behaviour of coupling loss factor and that shown in figure (5.15) of the previous model, the results of normalized power flow shown in figures (5.14) and (5.20) are used as follows. The ratio $\frac{\bar{P}_{12}}{\bar{P}_{in}}$ may written as

$$\frac{\bar{P}_{12}}{\bar{P}_{in}} = \gamma = \frac{\eta_2 \omega \bar{E}_2}{\eta_1 \omega \bar{E}_1 + \eta_2 \omega \bar{E}_2} \quad . \tag{5.33}$$

As it was assumed that $\eta_1 = \eta_2 = \eta$, then

$$\frac{\bar{E}_1}{\bar{E}_2} = \frac{1}{\gamma} - 1 = \frac{1-\gamma}{\gamma} \quad . \tag{5.34}$$

The substitution of equation (5.34) in SEA relationship (equation (2.34)) gives the following expression for the coupling loss factor in terms of normalized power flow (γ)

$$\eta_{12} = \frac{\gamma\eta}{1-\gamma-(n_1/n_2)\gamma} \quad . \tag{5.35}$$

For the two cases of coupled rods (long-long and short-long), equation (5.35) can be studied as follows.

(a) Short -long rods system.

(i) In the region where the modal overlap factor of the long rod (M_2) is small; i.e., $n_1(\omega) \approx n_2(\omega)$, equation (5.35) may written as

$$\eta_{12} \approx \frac{\gamma\eta}{1-2\gamma} \quad , \tag{5.35.a}$$

which shows that η_{12} is only a function of normalized power flow (for a constant value of dissipation loss factors). This produces the small values of η_{12} compared with the estimate of the travelling wave method shown in figure (5.21).

(ii) When M_2 is large enough compared with the constant value of M_1; i.e., $n_1(\omega) \ll n_2(\omega)$, equation (5.35) may written as

$$\eta_{12} \approx \frac{\gamma\eta}{1-\gamma} \quad . \tag{5.35.b}$$

As γ increases in this region and takes approximately a constant value at high modal overlap (see figure (5.20), η_{12} increases and behaves in a similar fashion.

(b) Long-long rods system.

As it was assumed for this case that the length ratio (L_2/L_1) equals 0.65, then equation (2.35) can be written as

$$\eta_{12} \approx \frac{\gamma\eta}{1\text{-}2.5\gamma} \quad . \qquad (5.35.c)$$

Equation (5.35.c) can be studied in a similar way as described above to explain the fall of the value of coupling loss factor from the estimate of the travelling wave method at low modal overlap and the agreement between the two estimates at high modal overlap.

In order to investigate the influences of the individual parts of the impedances of the rods on the specific behaviour of the power flow shown in figure (5.20), The spectra of the normalized power flow $\frac{\bar{P}_{12}}{\bar{P}_{in}}$ are evaluated in the frequency band of interest and displayed in figures (5.22) through (5.26) for M_2 values of 0.02, 0.1, 0.5, 1.0 and 1.5 respectively and for a fixed M_1 value of 0.01. The figures show that the normalized power flow has its maximum values at the resonance frequencies of the receiver rod and the peaks have the same level throughout the frequency range of interest. As M_2 increases (i.e., the length of the receiver rod increases), the maximum values of $\frac{\bar{P}_{12}}{\bar{P}_{in}}$ are hardly change, but the minimum values increase considerably, and the spectrum exhibits many peaks because of the increase in the modal density of the receiver rod: consequently, the frequency integral increases. A further increase in the modal overlap of the receiver rod (M_2) smooths out the spectrum of the normalized power flow and the latter become independent of frequency at higher M_2 values as can be seen in figures (5.25) and (5.26) for M_2 values of 1.0 and 1.5 respectively. The smooth spectrum of $\frac{\bar{P}_{12}}{\bar{P}_{in}}$ gives an indication that the system is behaving like an infinite system.

Figures (5.27) - (5.29) display a comparison between the spectra of the real parts (R_1 R_2, and R_o) of the impedances of the uncoupled rods and those of the

coupled system for the different M_2 values above. These figures show that as M_2 increases, the maxima of the spectra of R_2 decrease while the minima increase. When M_2 takes a value which is greater than 1.0 (see figure (5.29)), R_2 exhibits a fixed value which is independent of frequency. R_0 behaves in a similar way to R_2 but its spectrum is not flat at higher M_2 values. The smooth spectrum of R_0 (at high M_2) exhibits peaks at the resonance frequencies of the directly driven rod.

Figures (5.30)-(5.32) display a comparison between the imaginary parts (I_1, I_2 and I_0) of the impedances for the same values of M_1 and M_2 mentioned above. They show that as M_2 increases and takes large values, I_2 decreases and takes negligible values at all frequencies in the frequency range of interest.

From the results above, we can say that the resistive part of the impedance of the receiver rod (R_2) is a dominant parameter in controlling the behaviour of the frequency averaged value of $\frac{\bar{P}_{12}}{\bar{P}_{in}}$ (shown in figure (5.20)) at different M_2 values. This is supported by the following investigation of the effect of modal overlap factor of the receiver rod on the behaviour of R_2. The latter can be written as,

$$R_2 = \mathrm{Re}\{\tilde{Z}_2\} = \mathrm{Re}\left\{ (j/\omega)\, \tilde{Y}\, S_2\, \tilde{k} \tan(\tilde{k}L_2) \right\} \quad . \qquad (5.36)$$

If we write $\tilde{k}$ and $\tilde{Y}$ as

$$\tilde{k} = k_2(1-j\zeta) \ ,$$

and

$$\tilde{Y}_2 = Y_2(1+j2\zeta) \ .$$

As the damping is assumed to be very low ($\zeta \ll 1$), then R_2 can be expressed approximately as

$$R_2 = \frac{S_2 Y}{C_1}\left[\frac{(1+\zeta^2)\sinh(\zeta kL_2)\cosh(\zeta kL_2)}{\left\{\cos(kL_2)\cosh(\zeta kL_2)\right\}^2 + \left\{\sin(kL_2)\sinh(\zeta kL_2)\right\}^2} \right] ,$$

or, in terms of the modal overlap factor of the receiver rod (M_2) as:

$$R_2 = \frac{S_2 Y}{C_1}\left[\frac{(1+\zeta^2)\sinh\left(\frac{M_2\pi}{2}\right)\cosh\left(\frac{M_2\pi}{2}\right)}{\left\{\cos(kL_2)\cosh\left(\frac{M_2\pi}{2}\right)\right\}^2 + \left\{\sin(kL_2)\sinh\left(\frac{M_2\pi}{2}\right)\right\}^2}\right] . \quad (5.37)$$

Equation (5.37) can be studied as follows.

(i) When the modal overlap factor of the receiver rod is large enough ($M_2 > 1$), then

$$\sinh\left(\frac{M_2\pi}{2}\right) \approx \cosh\left(\frac{M_2\pi}{2}\right),$$

and therefore R_2 may be written approximately as

$$R_2 \approx \frac{S_2 Y}{C_1} , \quad (5.38)$$

which is simply represents the characteristic impedance of an infinite rod. This takes a constant value for given properties and dimensions of the rod. This result explain the asymptotic behaviour of the integral of normalized power (figure(5.20)), at high modal overlap.

(ii) When M_2 takes small values ($M_2 \ll 1$), then $\sinh\left(\frac{M_2\pi}{2}\right)$ will be very small quantity and very close to $\left(\frac{M_2\pi}{2}\right)$, and $\cosh\left(\frac{M_2\pi}{2}\right)$ will approach the value of unity. Therefore R_2 can be written in the following approximate form as

$$R_2 = \frac{S_2 Y}{C_1}\left[\frac{\left(\frac{M_2\pi}{2}\right)}{\cos^2(kL_2)+\left(\frac{M_2\pi}{2}\right)^2\sin^2(kL_2)}\right] , \quad (5.39)$$

which produces a relatively small value in the integral sense (the integral of R_2 spectra at different M_2 values is displayed in Figure (5.33)). This result clearly explains the

fall of the integral of the normalized power flow $\left(\frac{\bar{P}_{12}}{\bar{P}_{in}}\right)$ below the asymptotic level, at low modal overlap as shown in figure (5.20). Equation (5.39) shows that R_2 has its maximum value when $\cos(kL_2) = 0$ and $\sin(kL_2) = 1$. In this case, R_2 may be written approximately as

$$R_2 \approx \frac{2S_2Y}{\pi M_2 C_l} \quad . \tag{5.40}$$

It is invesely proportional to M_2, which explains the decrease in the values of the maxima of R_2 as M_2 increases (see Figures (5.27)-(5.29)). On the other hand, R_2 has its minimum value when $\cos(kL_2) = 1$ and $\sin(kL_2) = 0$. In this case R_2 can be written as

$$R_2 \approx \frac{\pi S_2 Y M_2}{2C_l} \, . \tag{5.41}$$

The latter form explains the increase in the minima of R_2 as M_2 increases, as shown in figures (5.27-5.29).

5.9 Conclusions

From the analysis of coupled rods system, we can draw the following main conclusions:

(a) The travelling wave method overestimates the coupling loss factor of the coupled rods system at low modal overlap. As soon as one of the rods, or both of them, enjoys high modal overlap condition, the estimate of coupling loss factor approaches the travelling wave estimate asymptotically. This conclusion supports those obtained from previous models of coupled beams and coupled plates systems.

(b) When two long rods are coupled together the power flow between them decreases as the modal overlap factor of the directly driven rod increases. This is because of the increase in the energy absorbed by the rod as its length increases.

(c) For a fixed, small, value of modal overlap for the directly driven rod, the normalized power flow increases as the modal overlap factor of the receiver rod (M_2) increases. The frequency averaged value takes an almost fixed value as M_2 takes the value of 1.0 or greater.

(d) The parametric study of power flow equation of coupled rods systems has shown that, maximum power flow generally correspond to the condition when the sum of the reactive parts of the uncoupled rods vanishes. This condition has a high probability of occurrence but it is not guaranteed for all peaks of power flow in the frequency band of interest. This study has also shown (for a case of short-long rods system) that the real part of the impedance of the receiver rod is a dominant parameter. It controls the integral of normalized power flow in all modal overlap conditions. The computed results of R_2 explained the asymptotic fixed value of power flow at high modal overlap and also explained the fall of the estimate of the power flow below that of the power flow of the infinite system at low modal overlap.

(e) An explanation for the behaviour of coupling loss factor of coupled rods in different modal overlap conditions was obtained. This explanation was based on the well understood results of normalized power flow between the coupled rods.

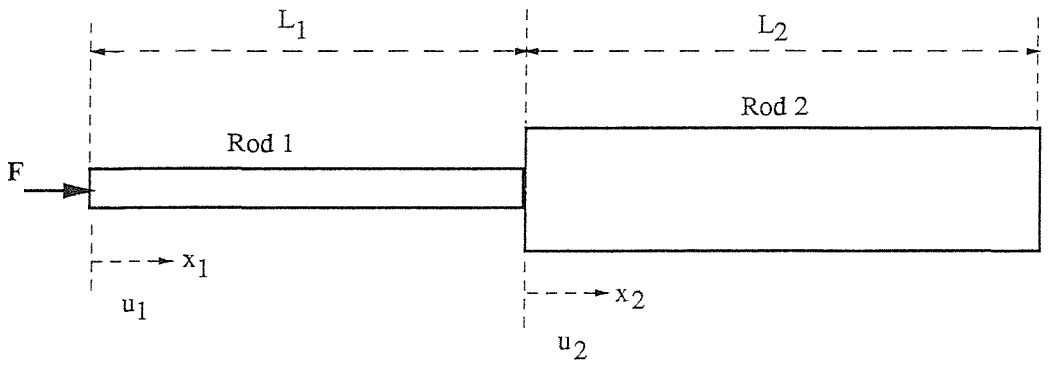

Figure (5.1.a)

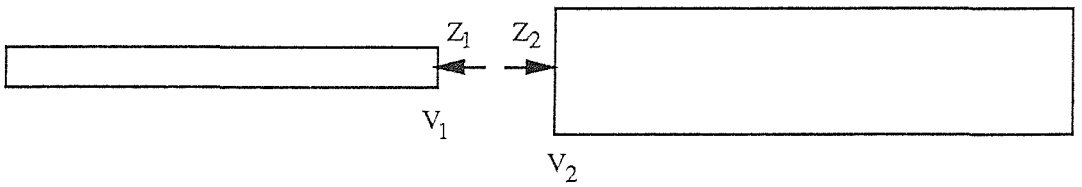

Figure (5.1.b)

Figure (5.1) : Coupled rods system

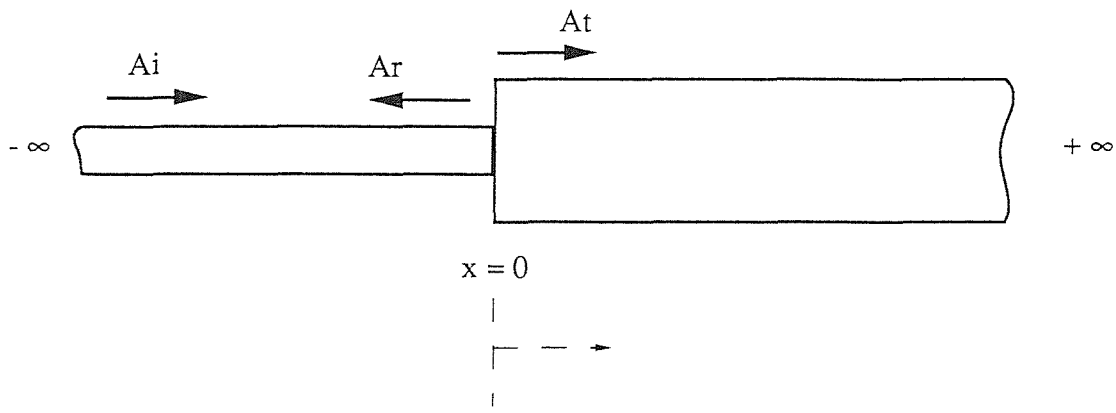

Figure (5.2) : Semi-infinite Coupled rods system

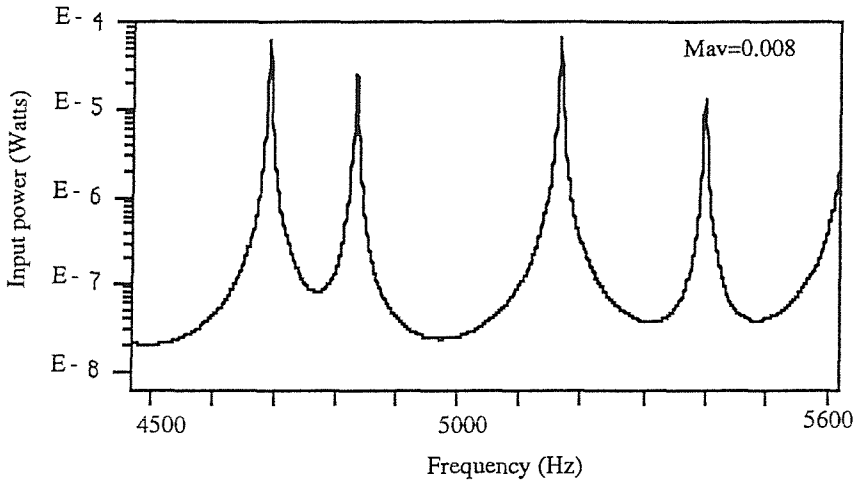

Figure (5.3) : Input power to a two coupled rods system

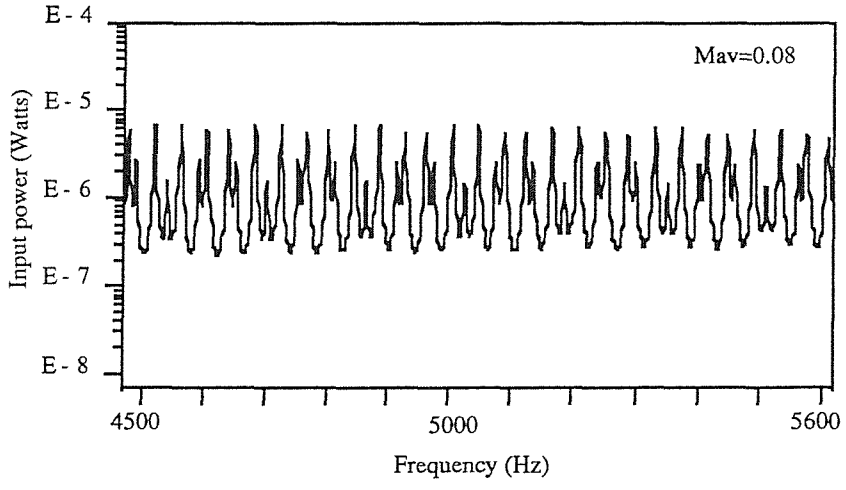

Figure (5.4) : Input power to a two coupled rods system

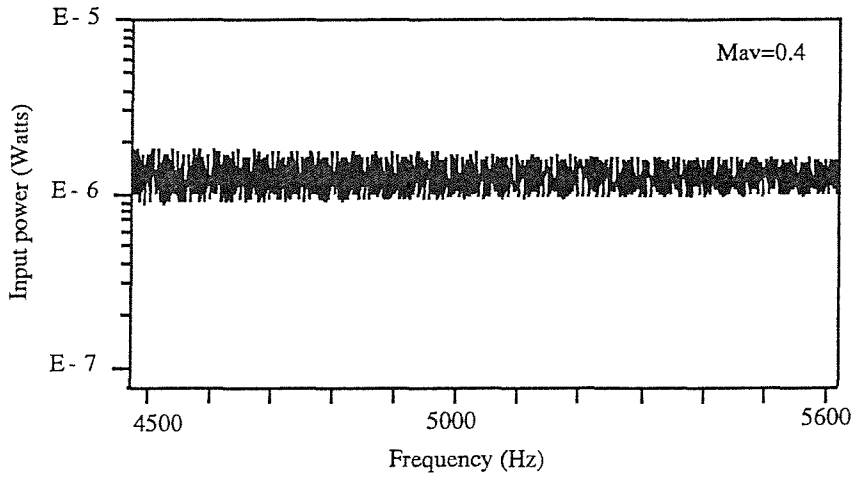

Figure (5.5): Input power to a two coupled rods system

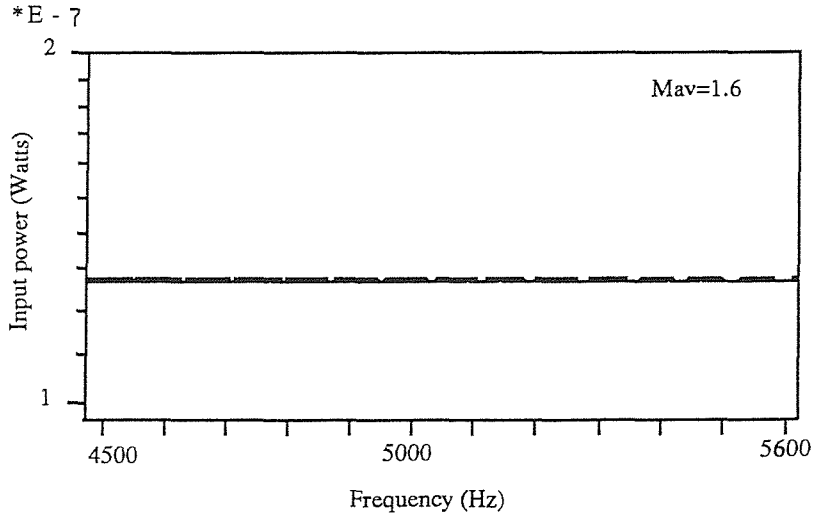

Figure (5.6): Input power to a two coupled rods system

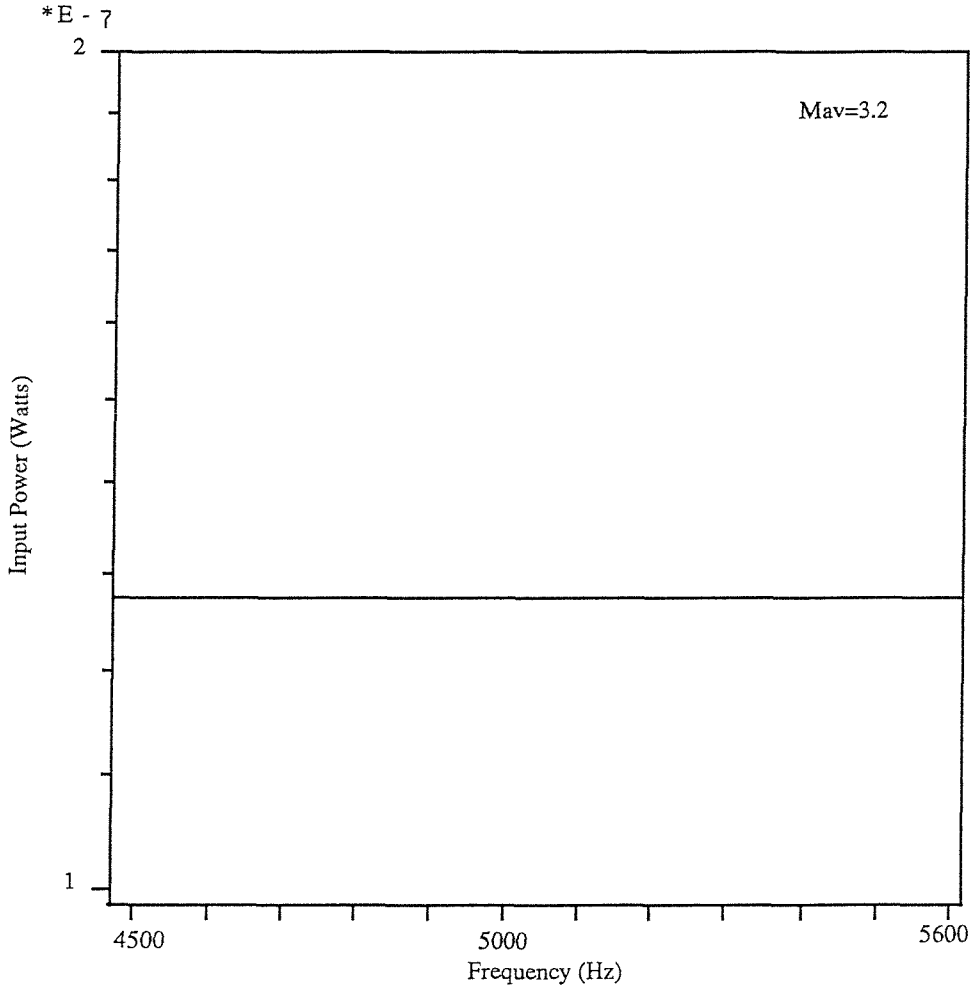

Figure (5.7): Input power to a two coupled rods system

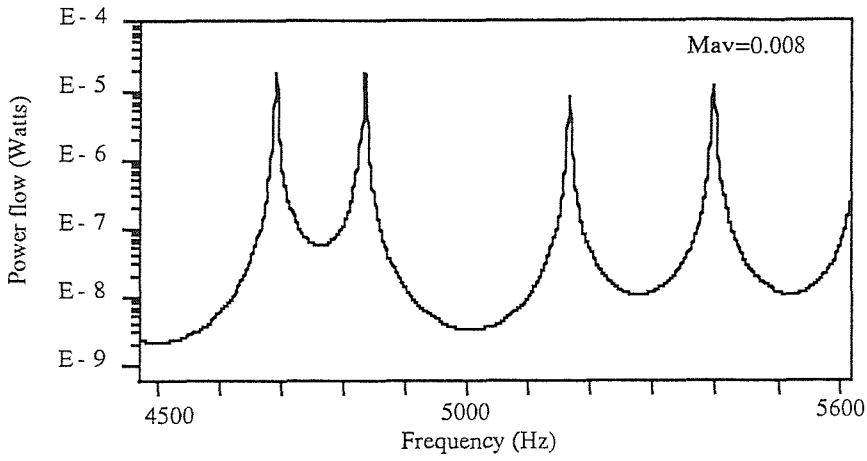

Figure (5.8) : Power flow between two coupled rods

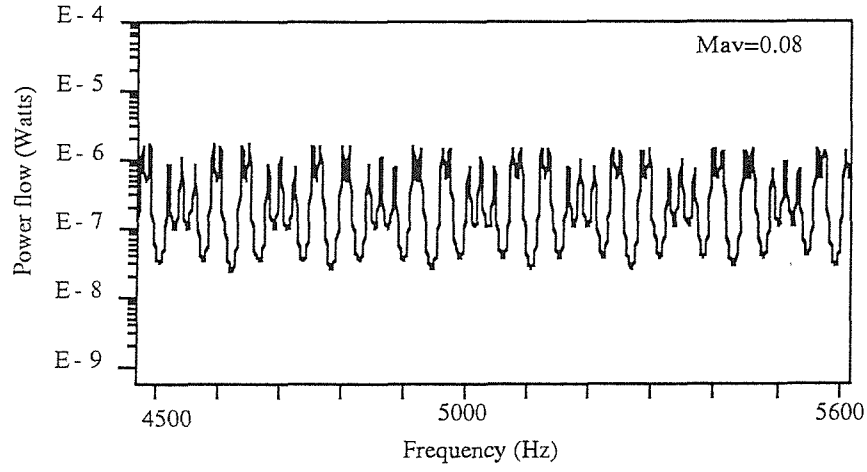

Figure (5.9) : Power flow between two coupled rods

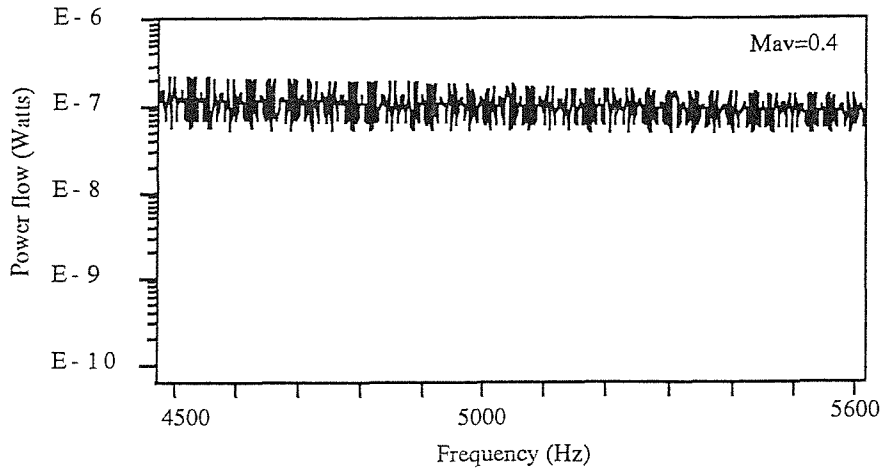

Figure (5.10): Power flow between two coupled rods

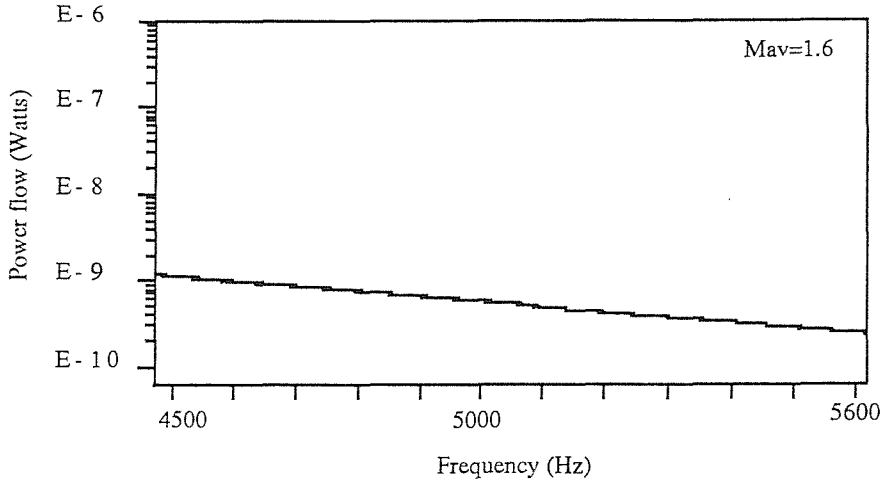

Figure (5.11): Power flow between two coupled rods

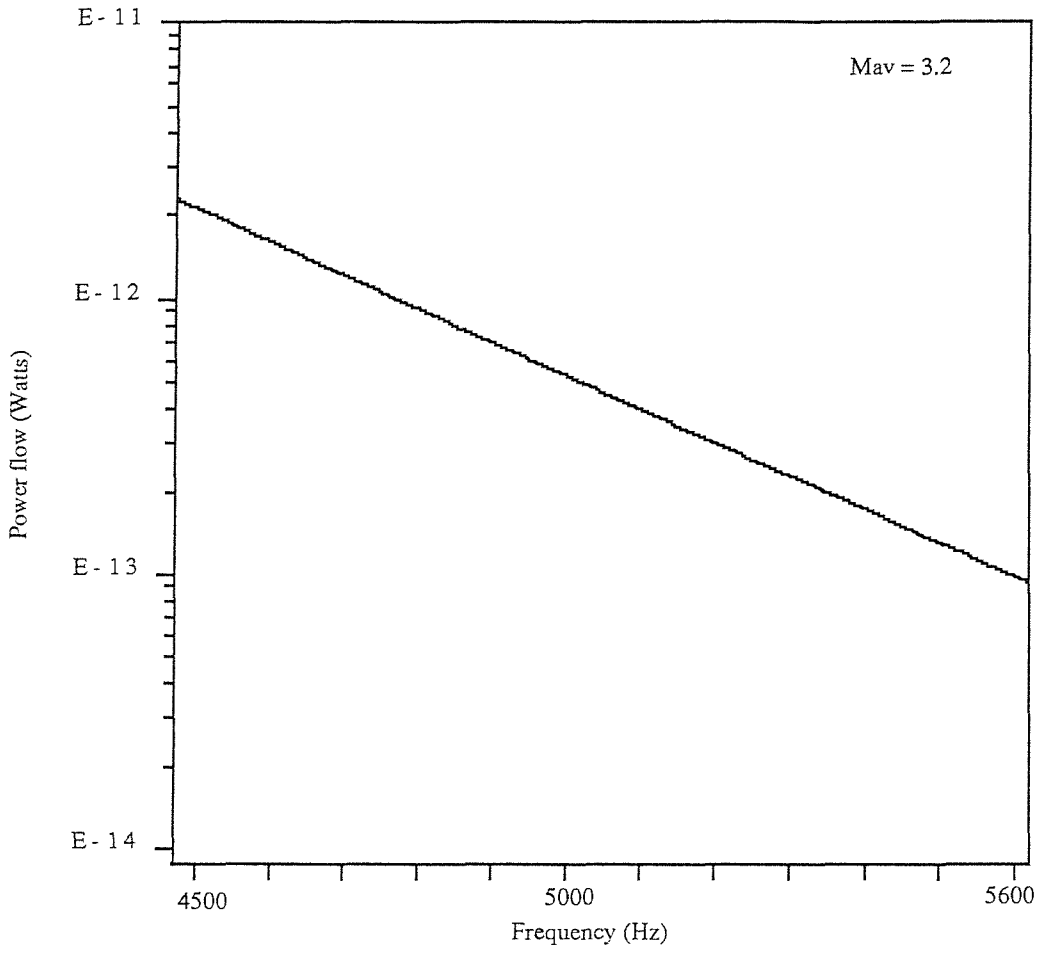

Figure (5.12): Power flow between two coupled rods

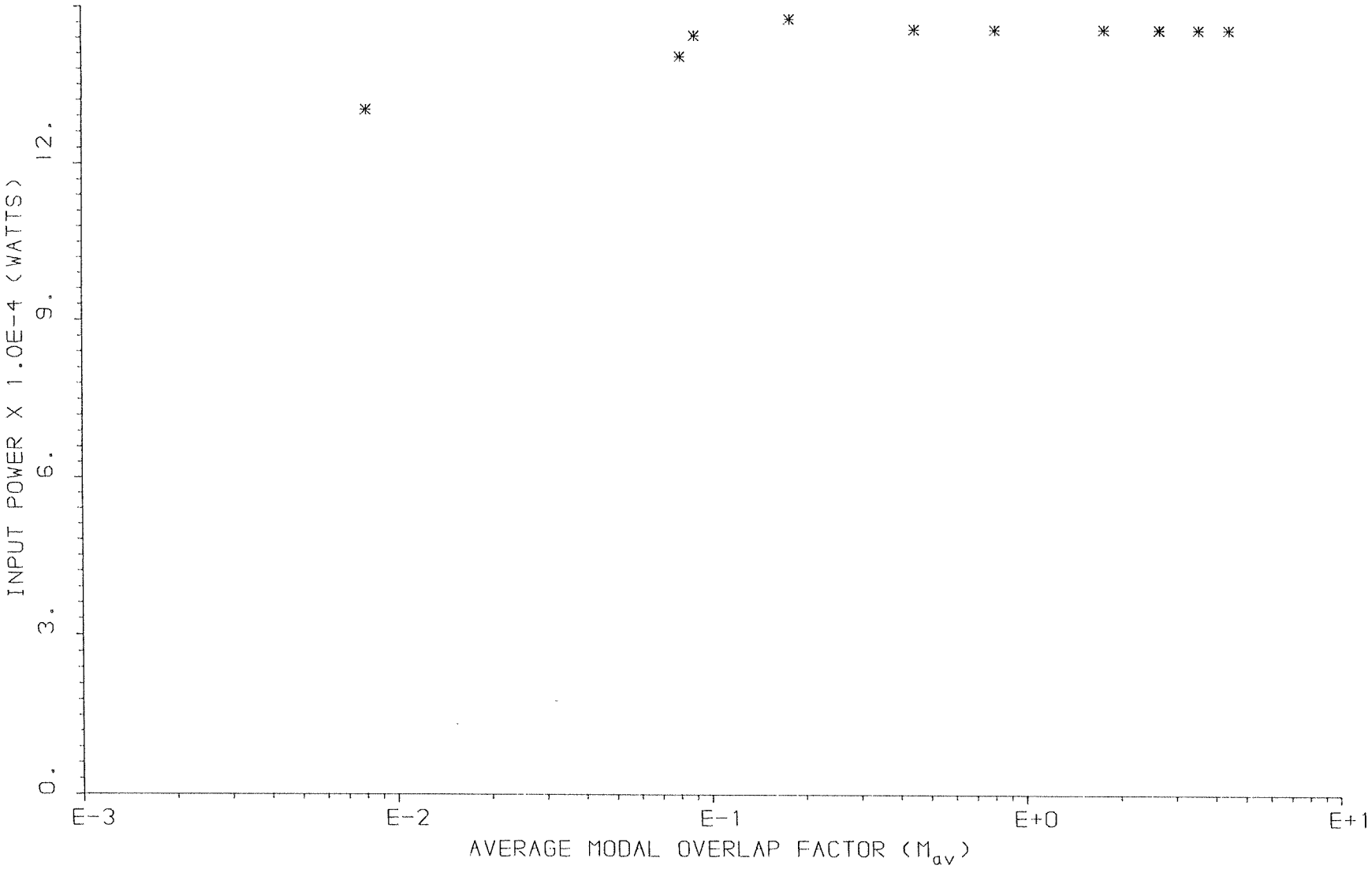

FIG. (5.13) INJECTED POWER TO A COUPLED RODS SYSTEM

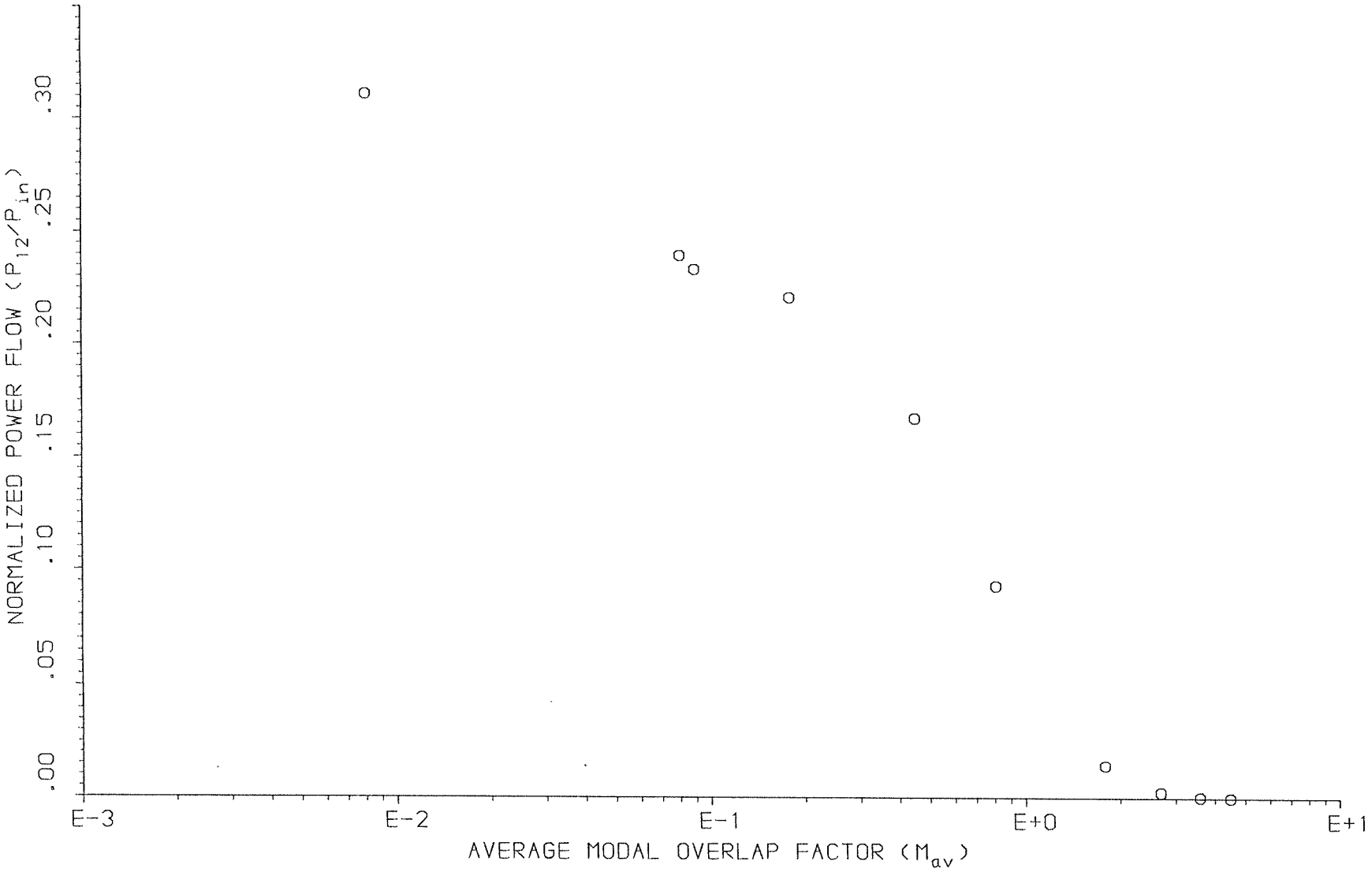

FIG. (5.14) POWER FLOW BETWEEN COUPLED RODS

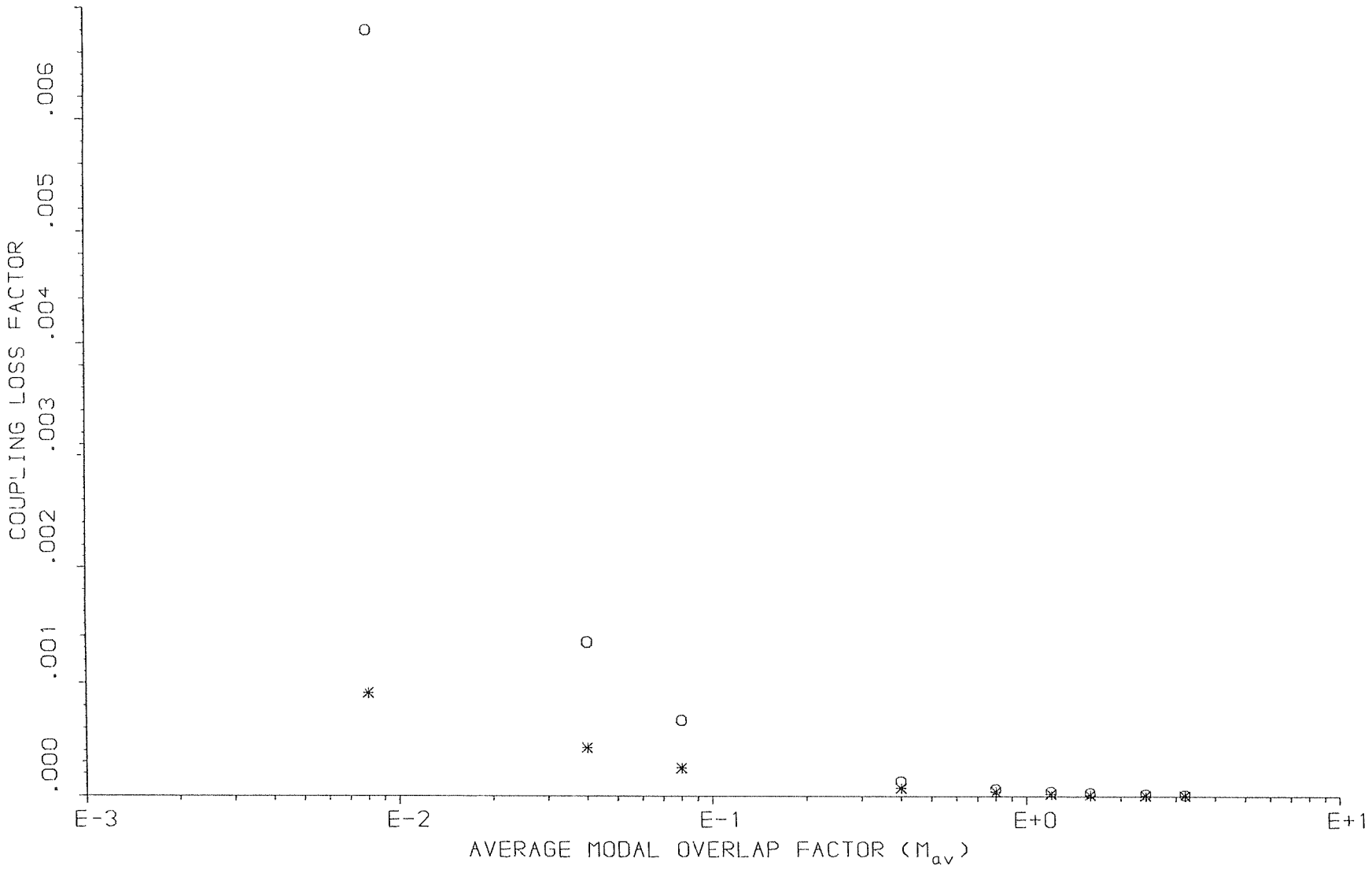

FIG. (5.15.a) COUPLING LOSS FACTOR OF COUPLED RODS SYSTEM
*FINITE SYSTEM ESTIMATE, o TRAVELLING WAVE ESTIMATE

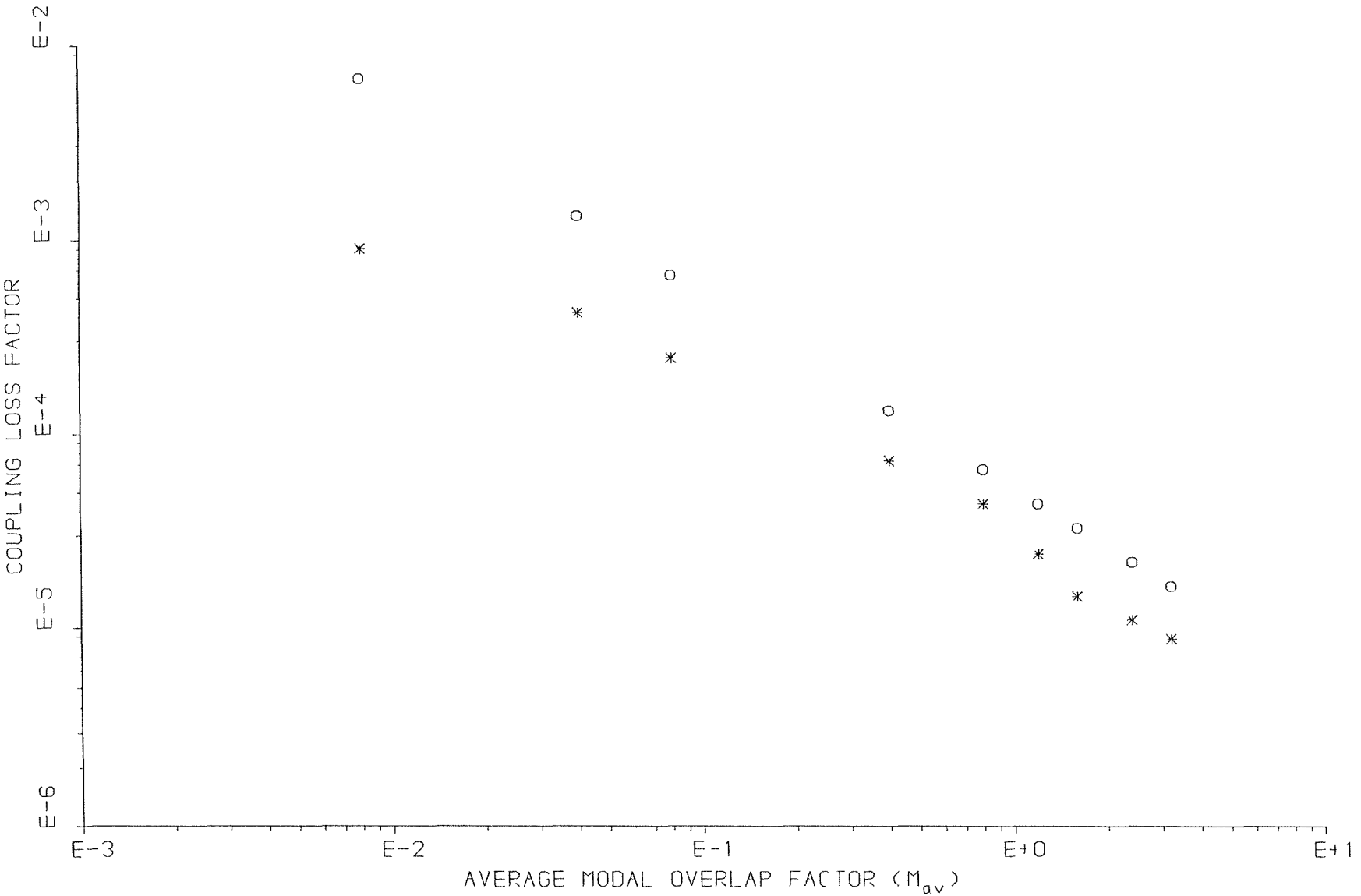

FIG. (5.15.b) COUPLING LOSS FACTOR OF COUPLED RODS SYSTEM
*FINITE SYSTEM ESTIMATE, o TRAVELLING WAVE ESTIMATE

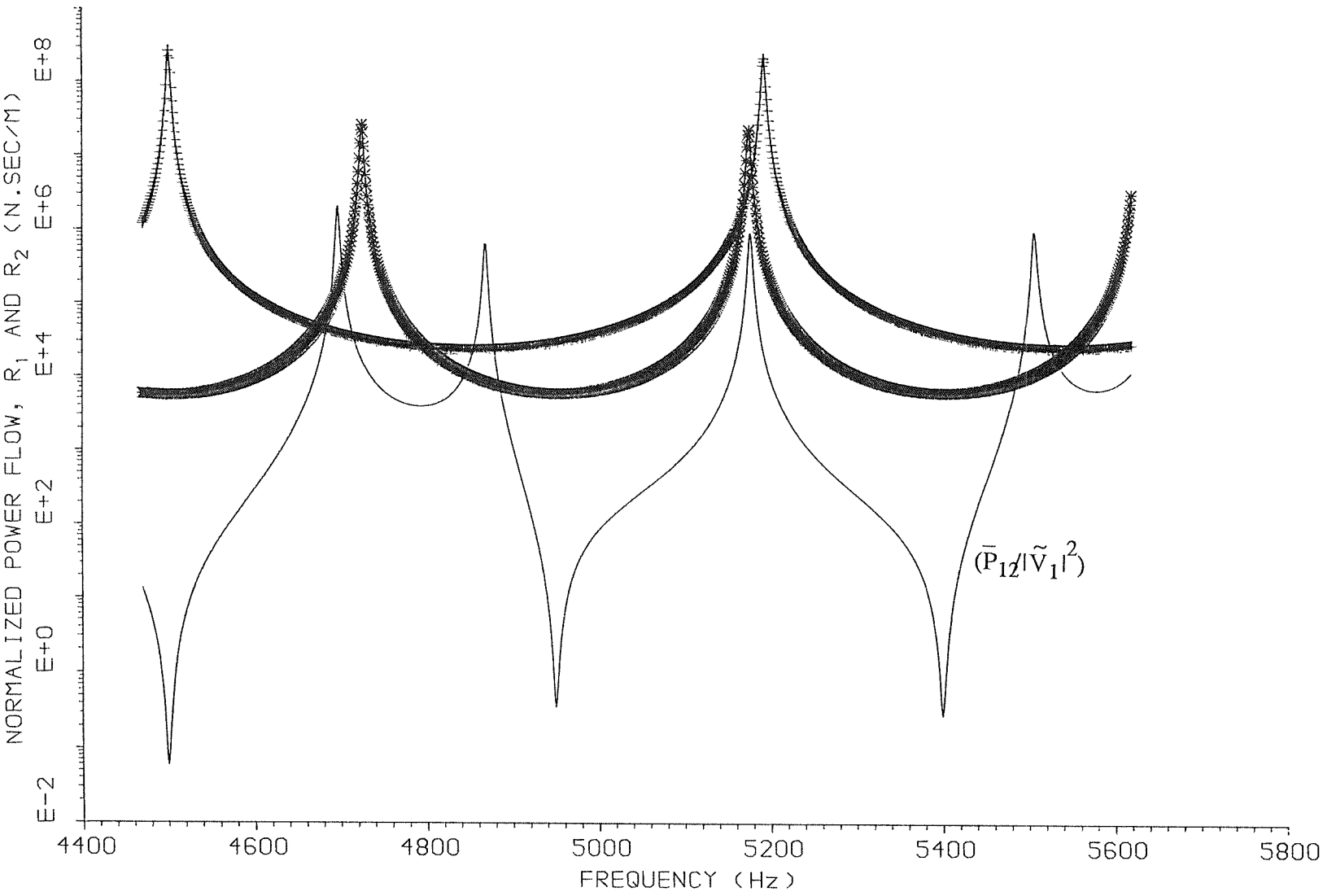

FIG.(5.16) NORMALIZED POWER FLOW AND THE REAL PARTS OF Z1 AND Z2
—— POWER FLOW, ---*--- Real(Z1), ---+--- Real(Z2)

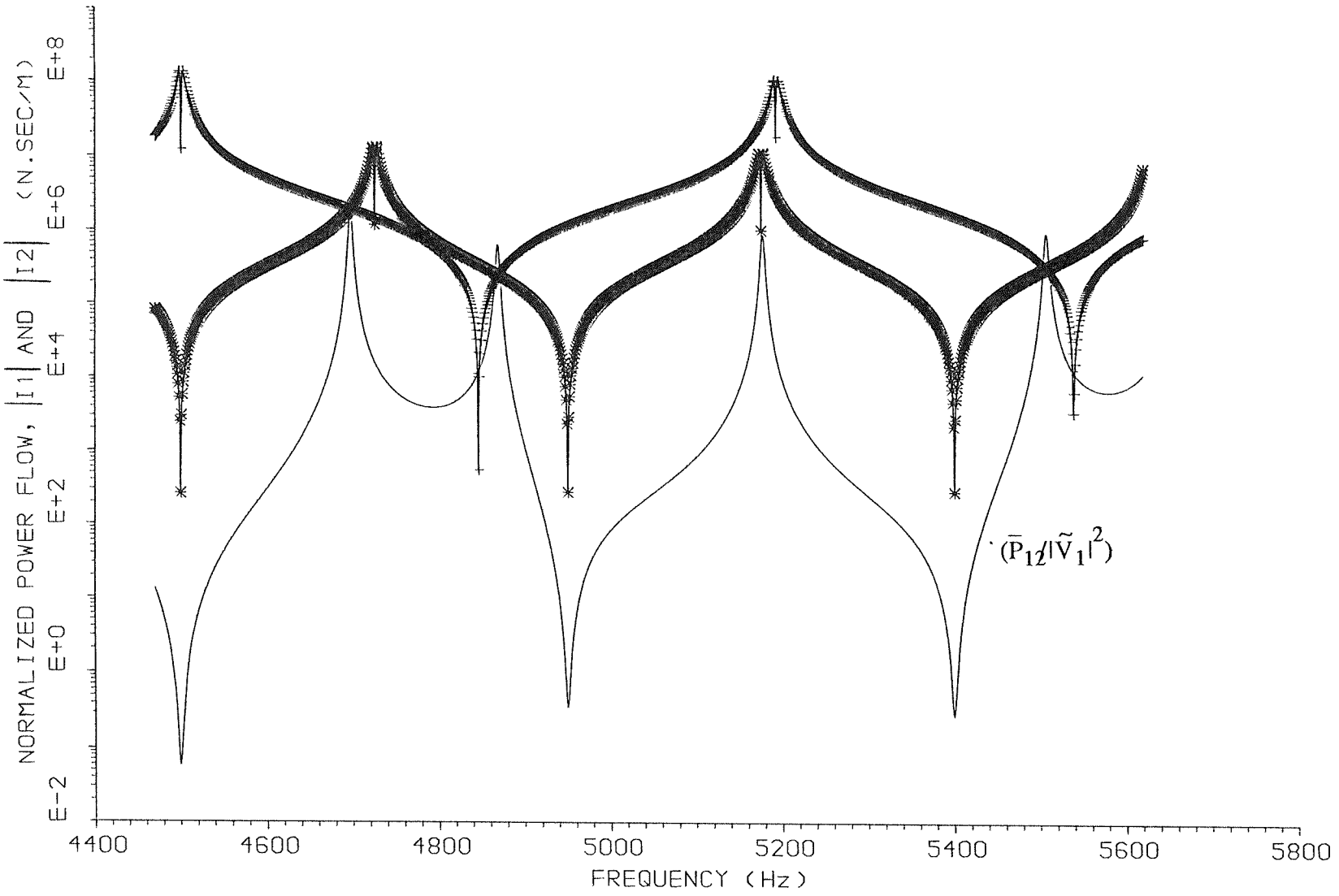

FIG.(5.17) NORMALIZED POWER FLOW AND THE MODULI OF Imag. Z1 AND Z2
— POWER FLOW, ---*--- |I1|, ---+--- |I2|

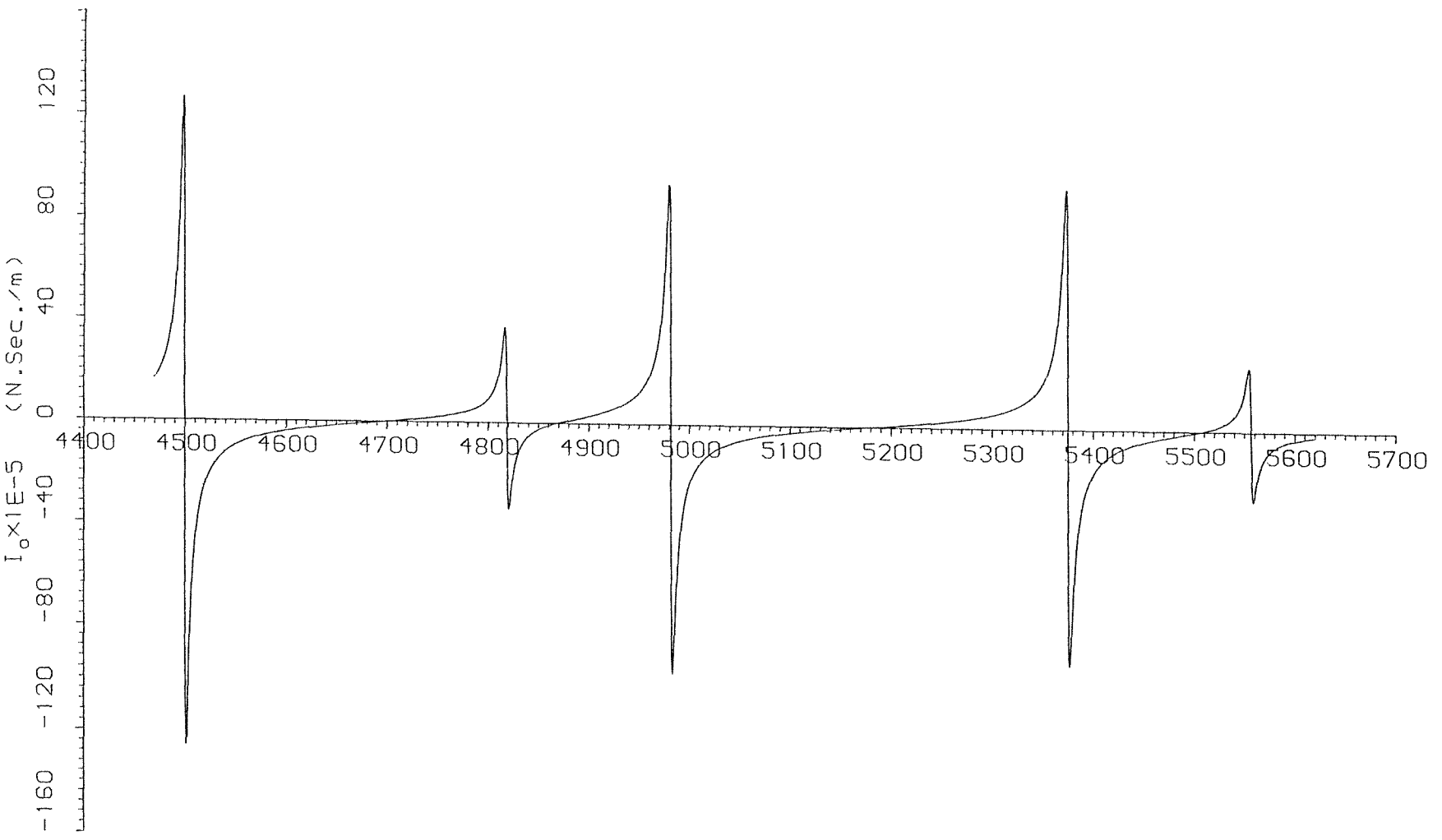

FIG.(5.18):THE IMAGINARY PART (I_o) OF DRIVING POINT IMPEDANCE OF COUPLED RODS SYSTEM

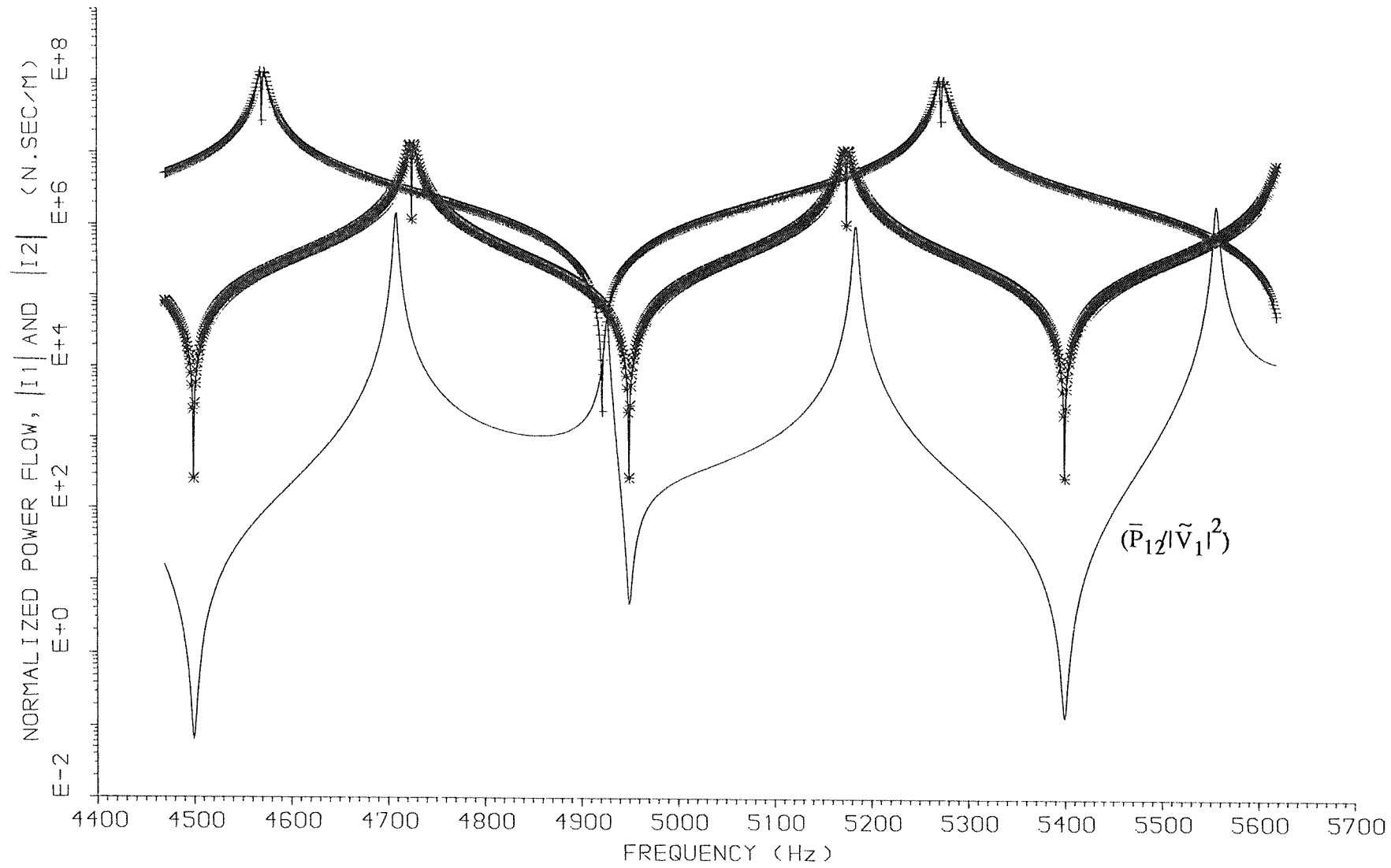

FIG.(5.19) NORMALIZED POWER FLOW AND THE MODULI OF Imag. Z1 AND Z2
—— POWER FLOW, ---*--- |I1| , ---+--- |I2|,(L2/L1=0.64)

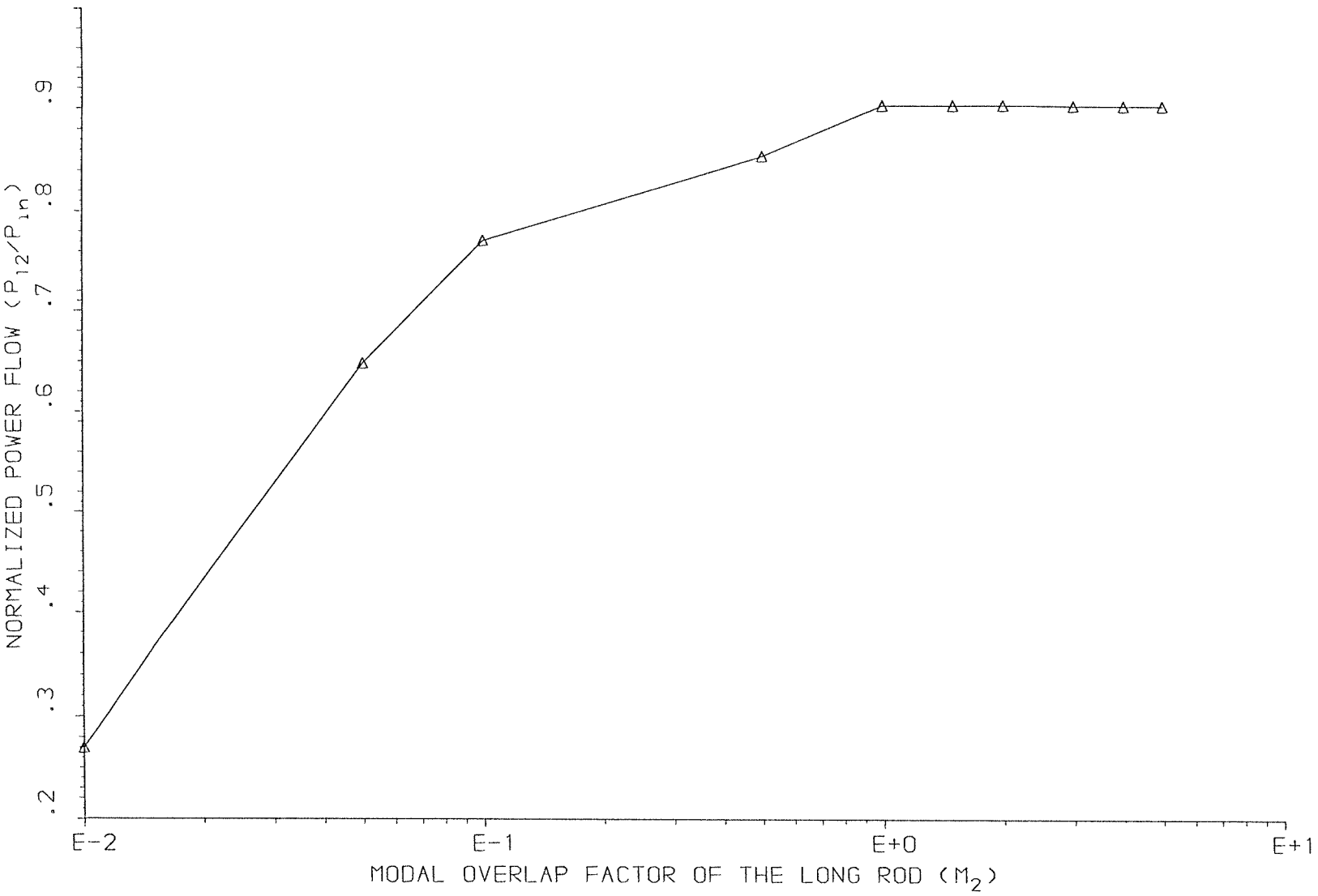

FIG.(5.20) NORMALIZED POWER FLOW OF SHORT-LONG RODS SYSTEM, M1=0.01

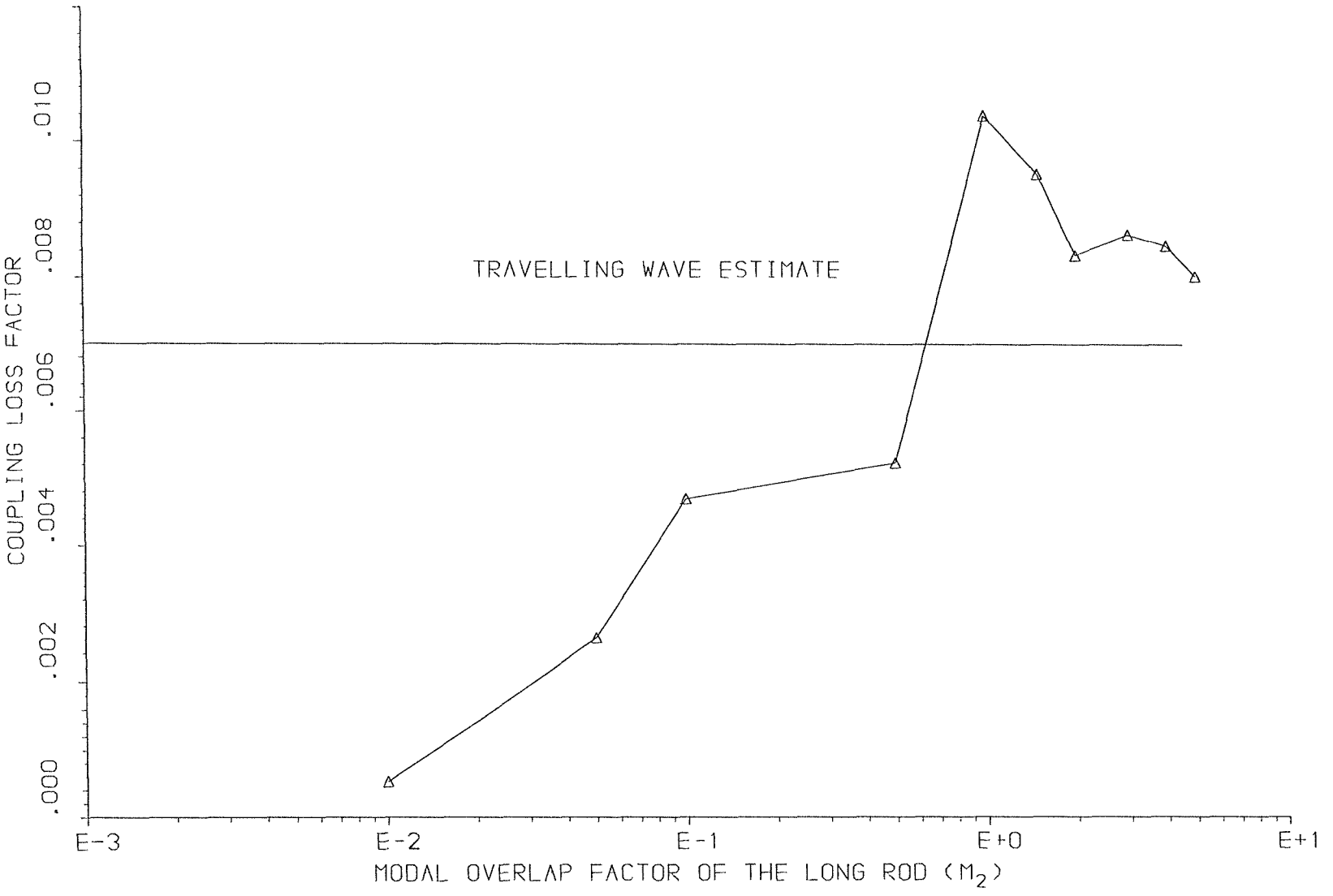

FIG.(5.21) COUPLING LOSS FACTOR OF SHORT-LONG RODS SYSTEM, M1=0.01

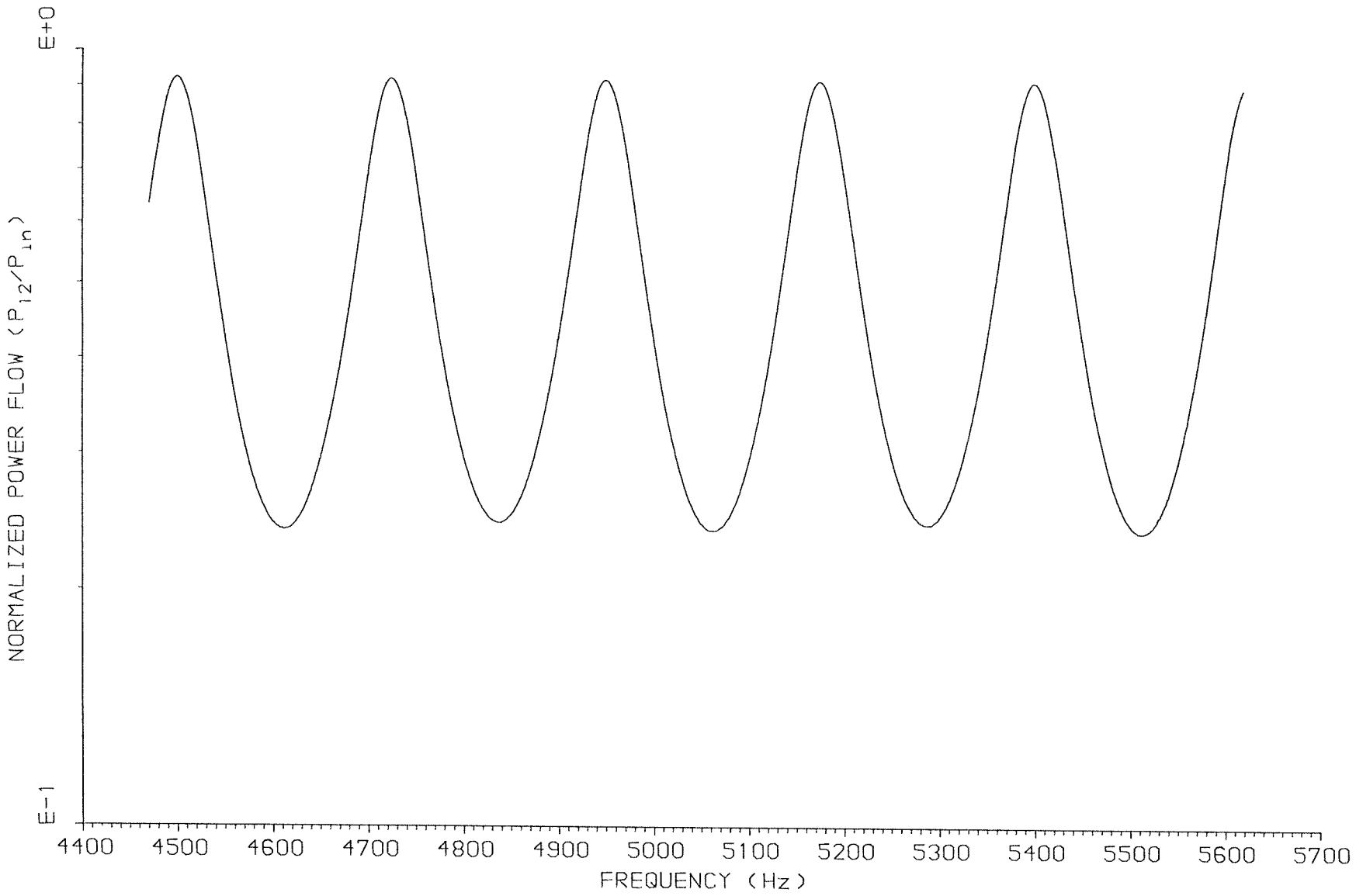

FIG.(5.22) NORMALIZED POWER FLOW BETWEEN TWO COUPLED RODS
M_1=0.01, M_2=0.02

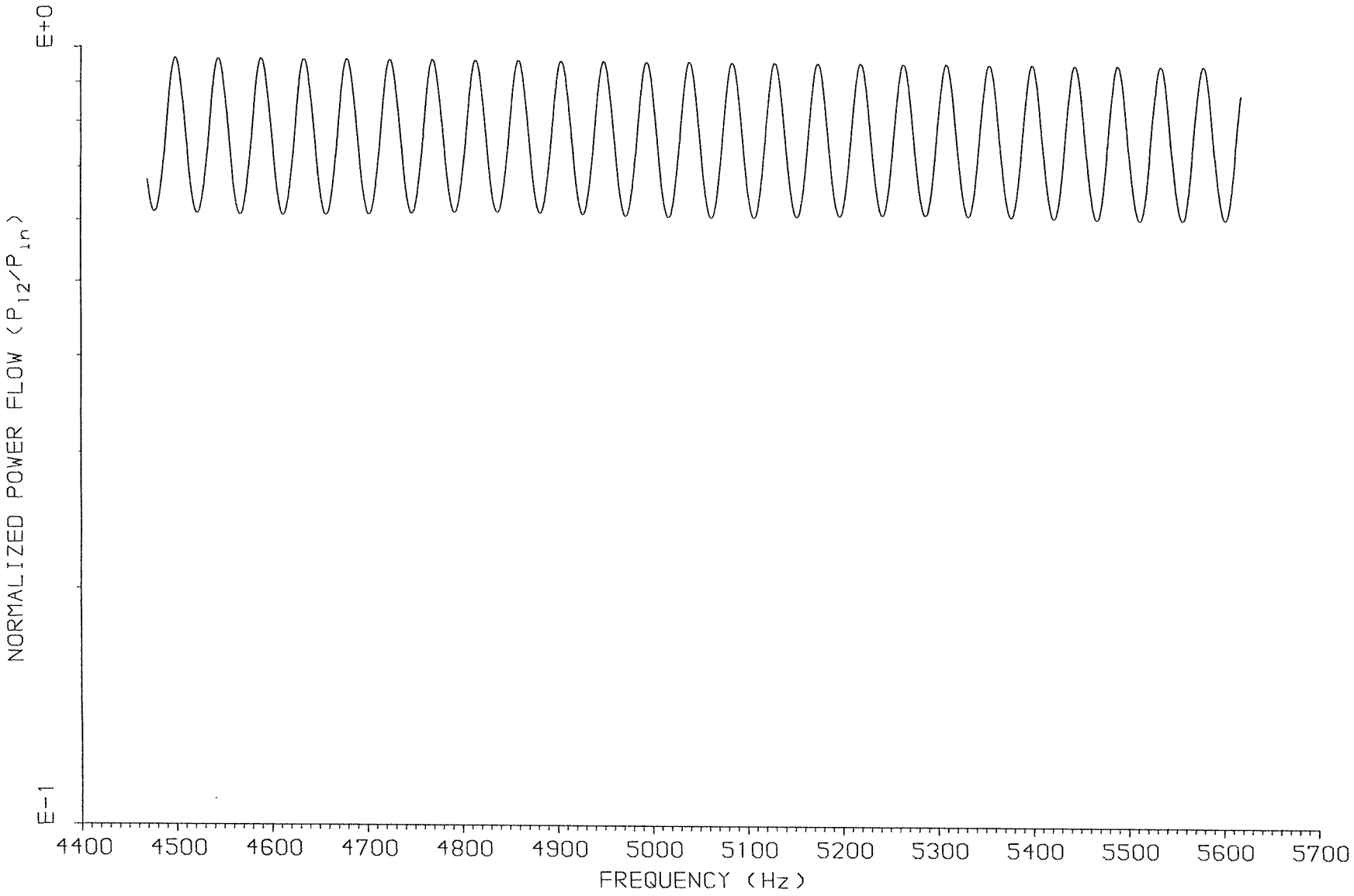

FIG.(5.23) NORMALIZED POWER FLOW BETWEEN TWO COUPLED RODS
M_1=0.01, M_2=0.1

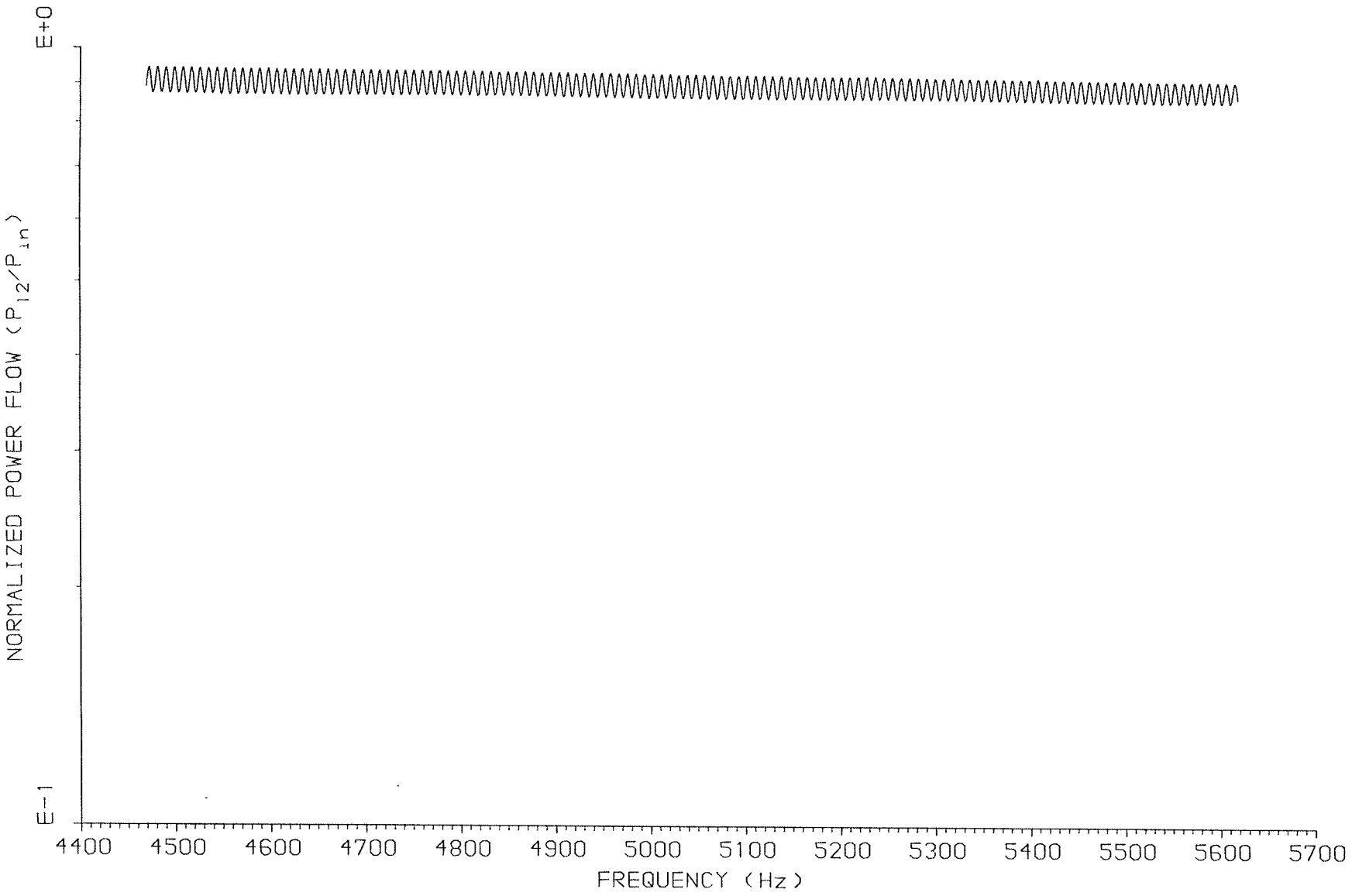

FIG.(5.24) NORMALIZED POWER FLOW BETWEEN TWO COUPLED RODS
M_1=0.01, M_2=0.5

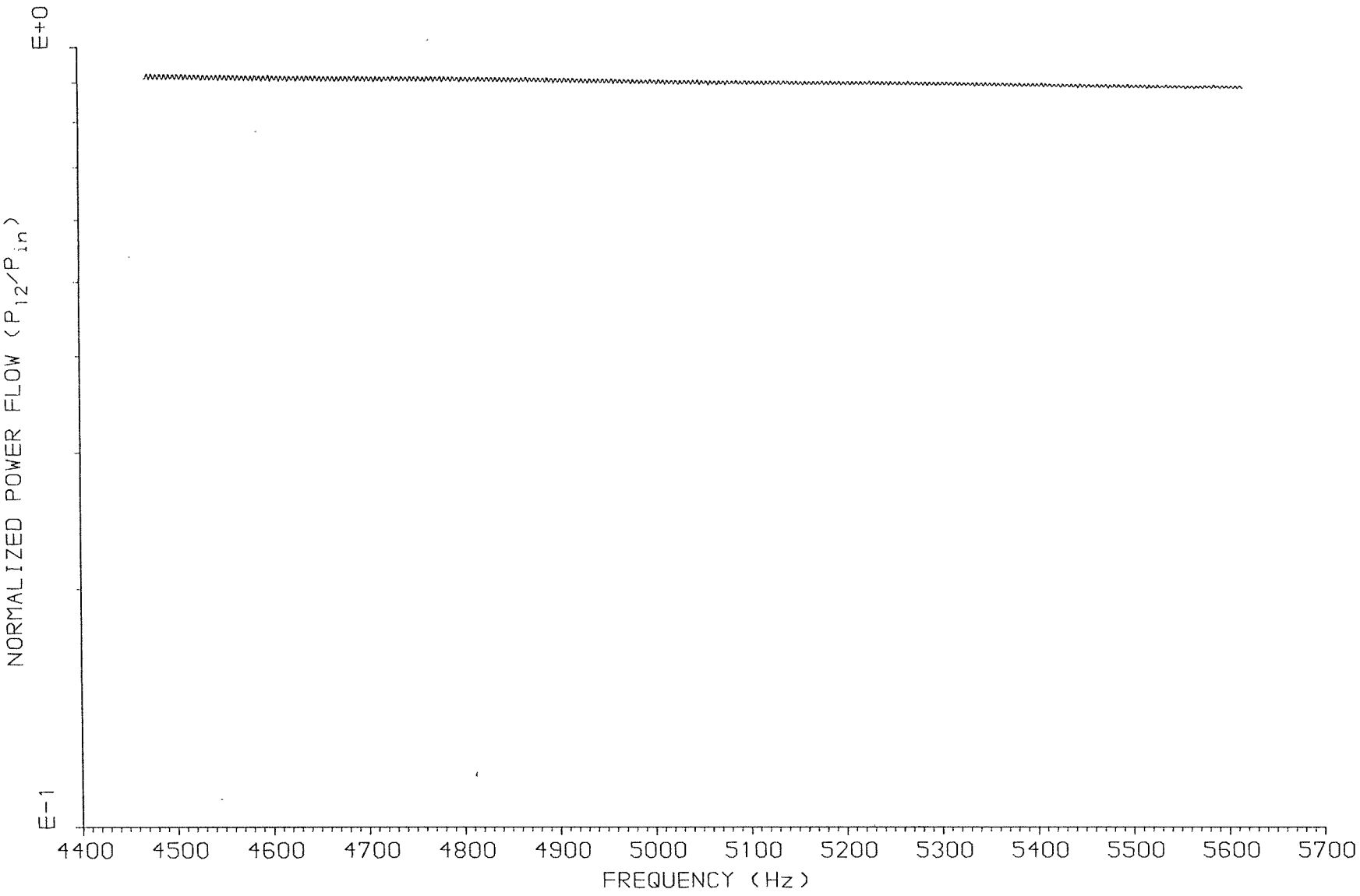

FIG.(5.25) NORMALIZED POWER FLOW BETWEEN TWO COUPLED RODS
M_1=0.01, M_2=1.0

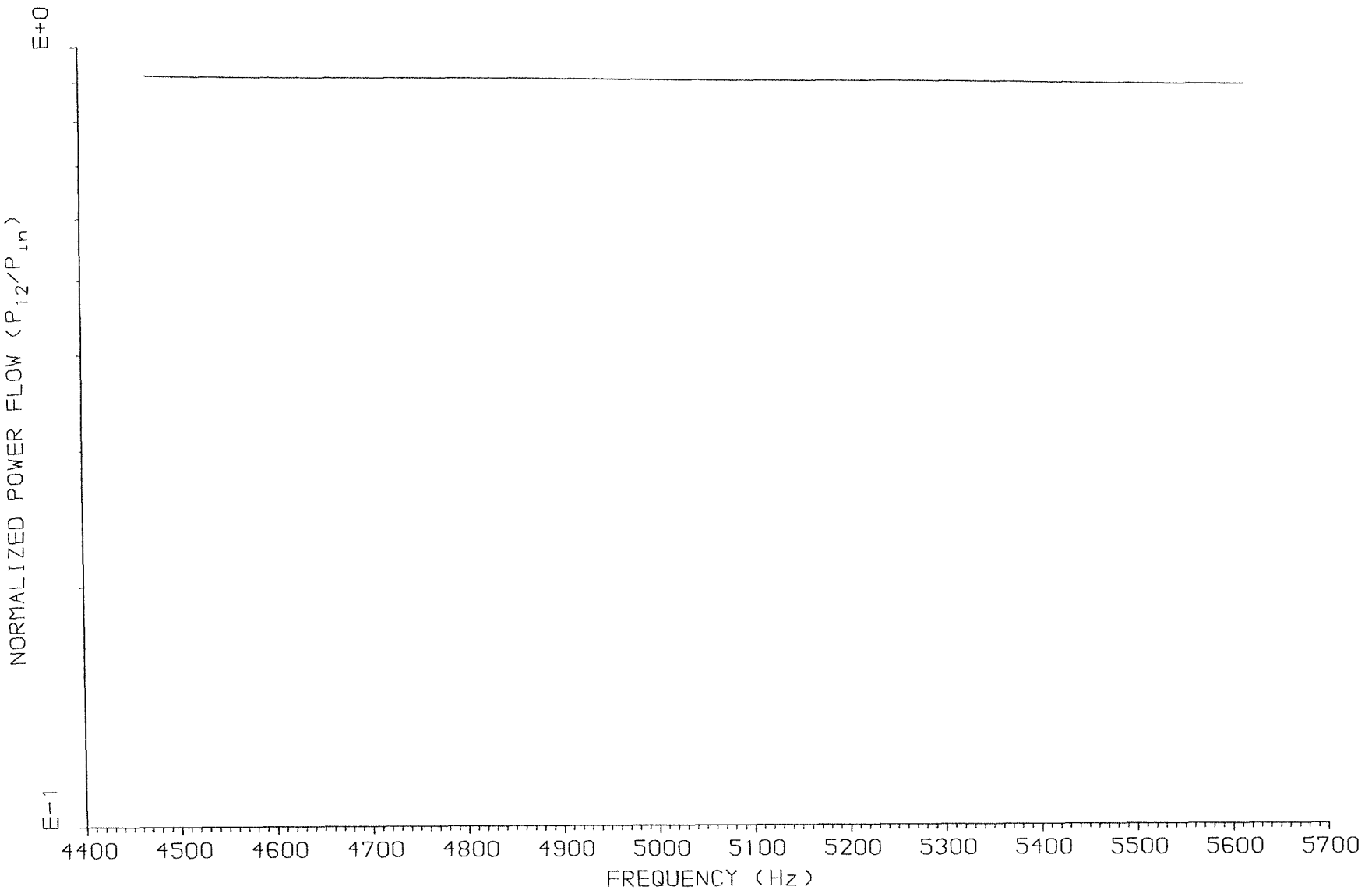

FIG.(5.26) NORMALIZED POWER FLOW BETWEEN TWO COUPLED RODS
M_1=0.01, M_2=1.5

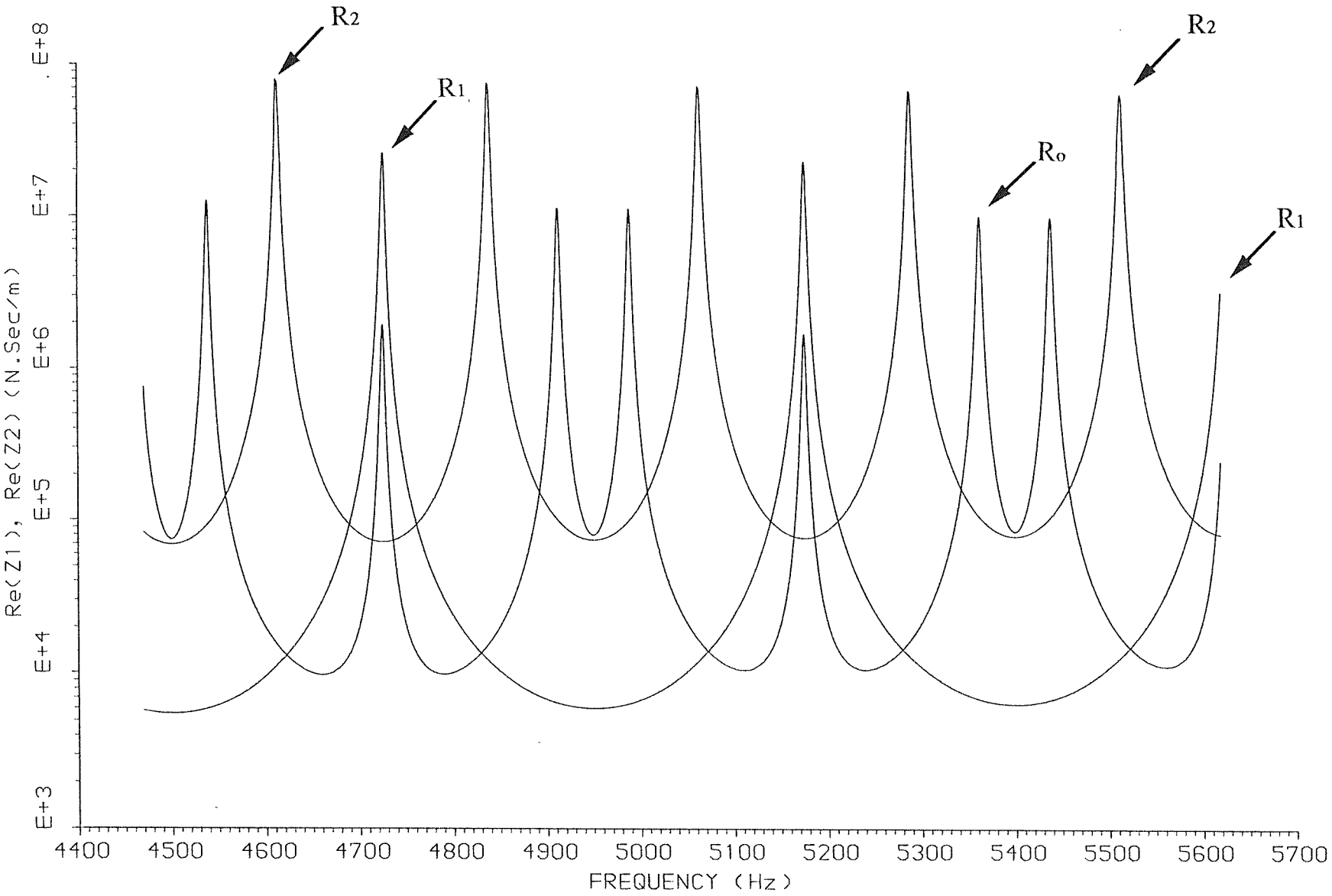

FIG.(5.27) THE REAL PARTS OF THE IMPEDANCES OF COUPLED RODS SYSTEM
$M_1=0.01$, $M_2=0.02$

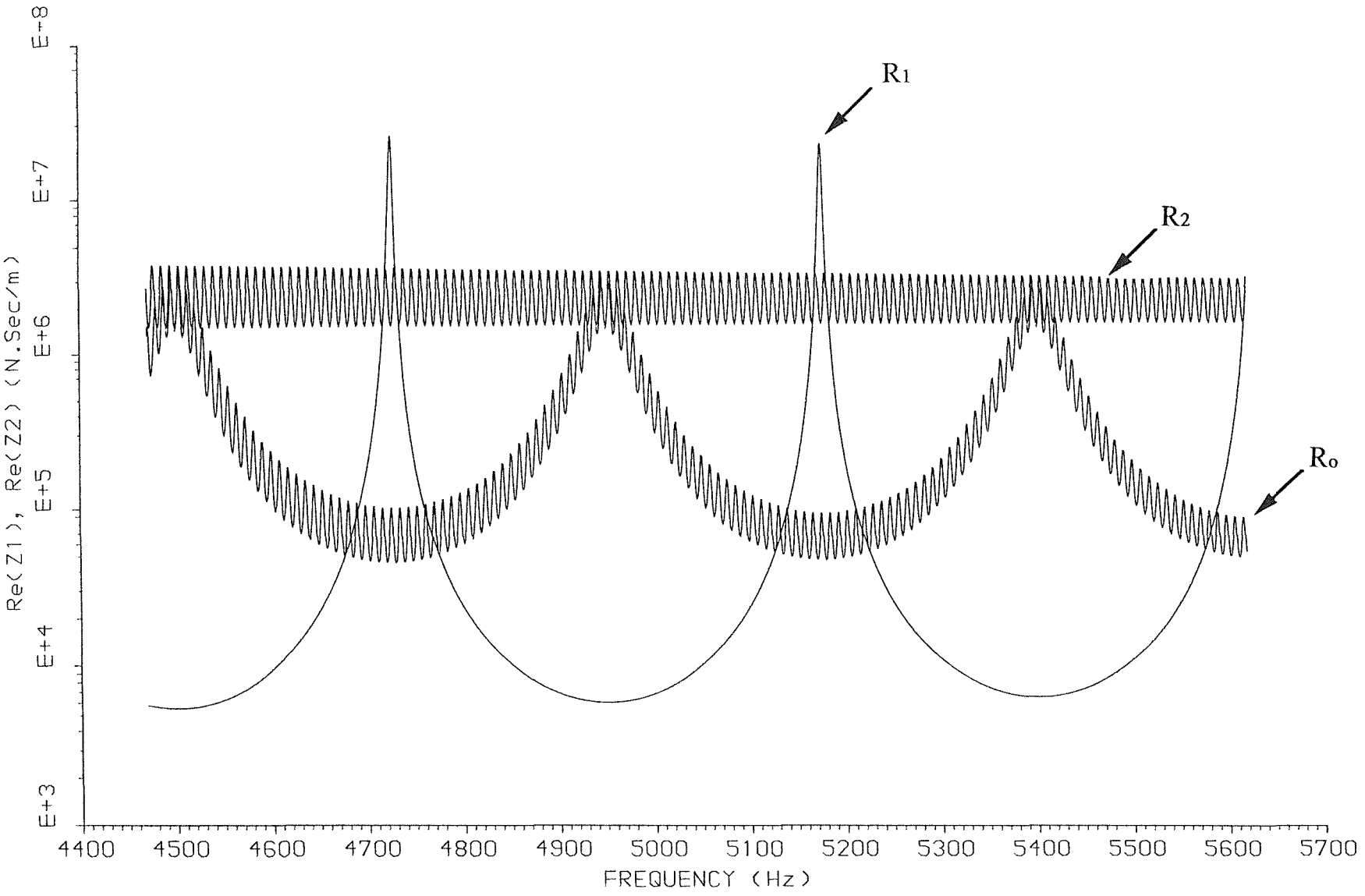

FIG.(5.28) THE REAL PARTS OF THE IMPEDANCES OF COUPLED RODS SYSTEM
M_1=0.01, M_2=0.5

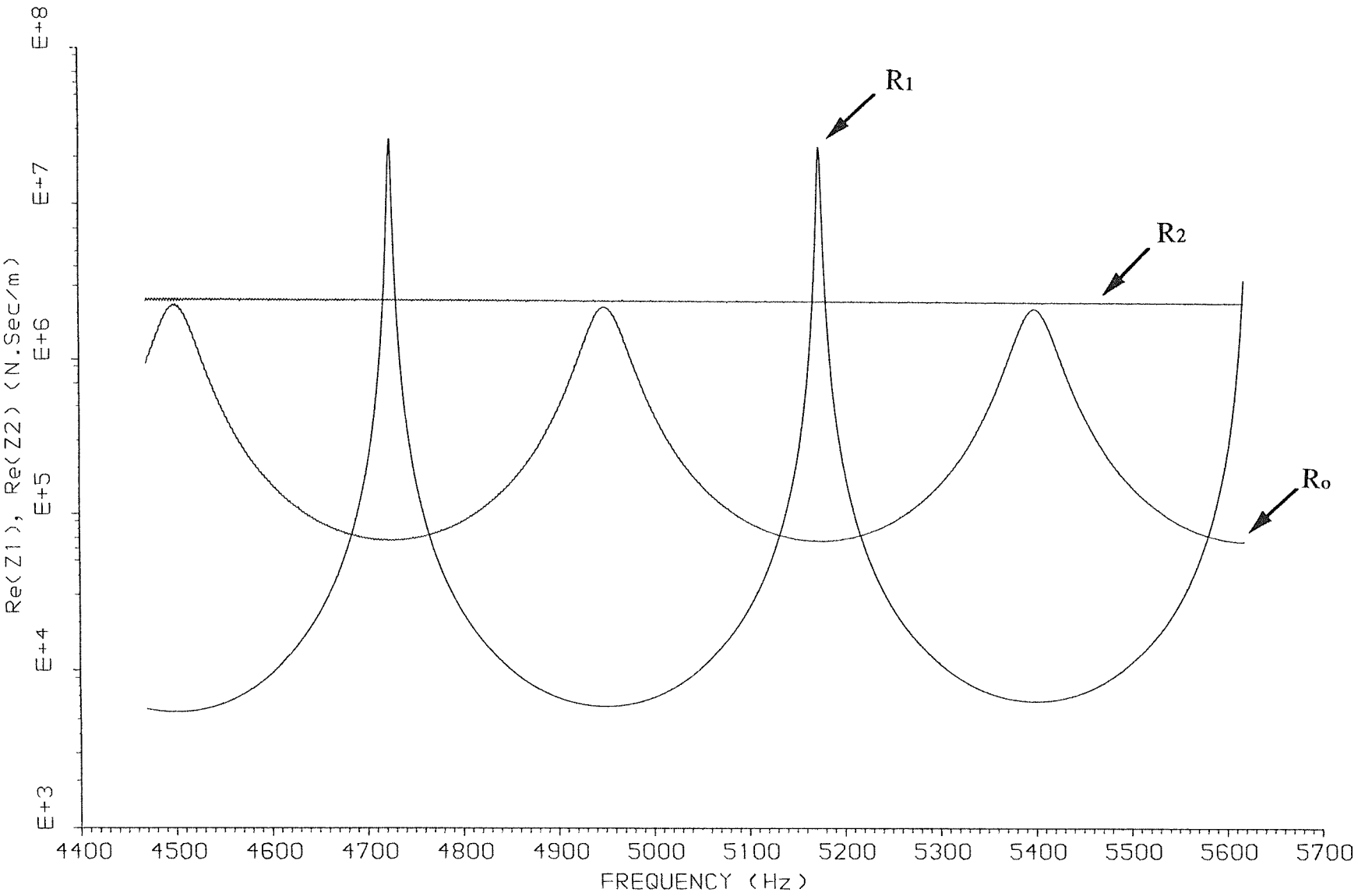

FIG.(5.29) THE REAL PARTS OF THE IMPEDANCIES OF COUPLED RODS SYSTEM
M_1=0.01, M_2=1.5

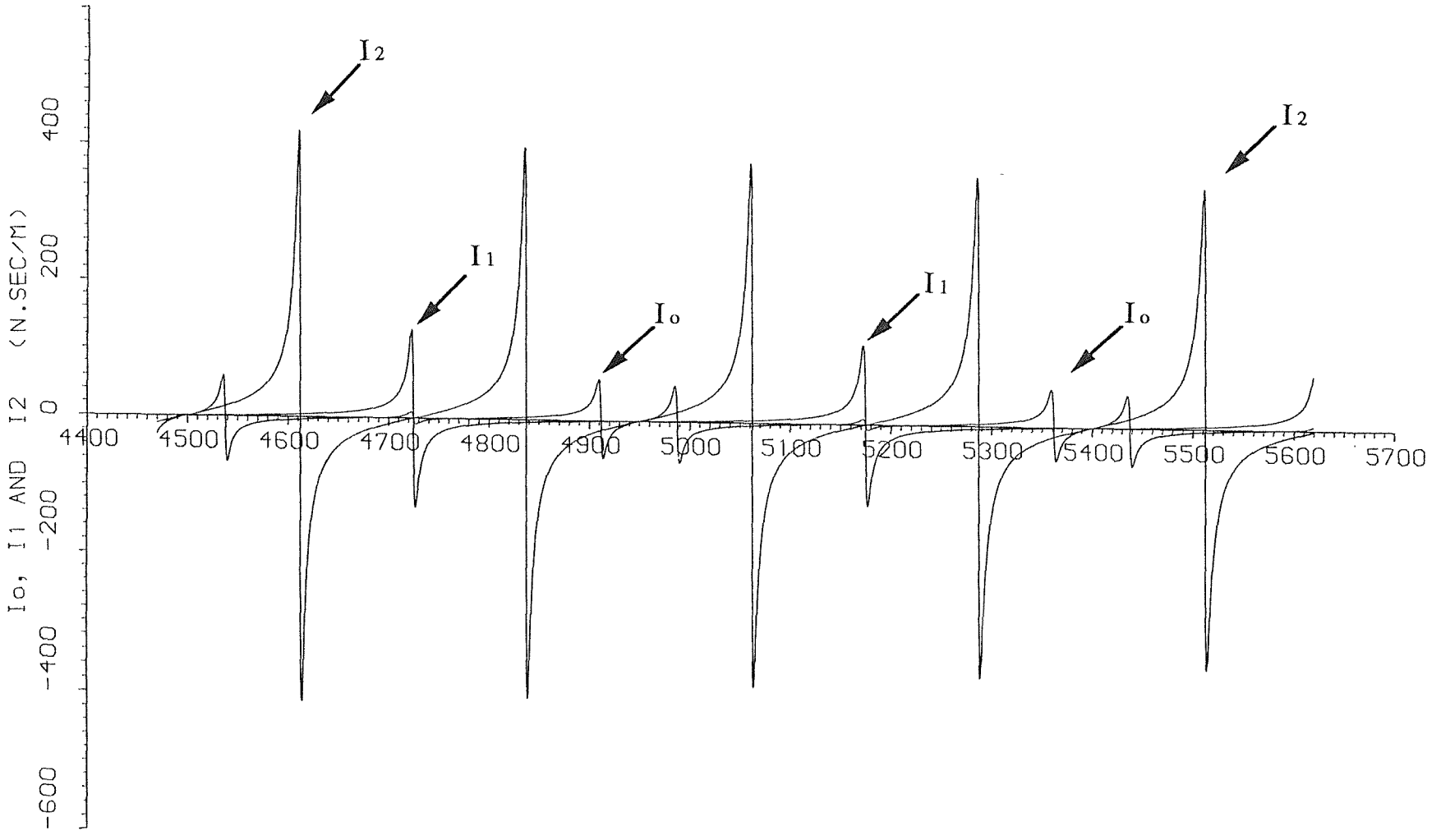

FIG.(5.30) COMPARISON BETWEEN THE IMAGINARY PARTS OF THE IMPEDANCES
M_1=0.01, M_2=0.02

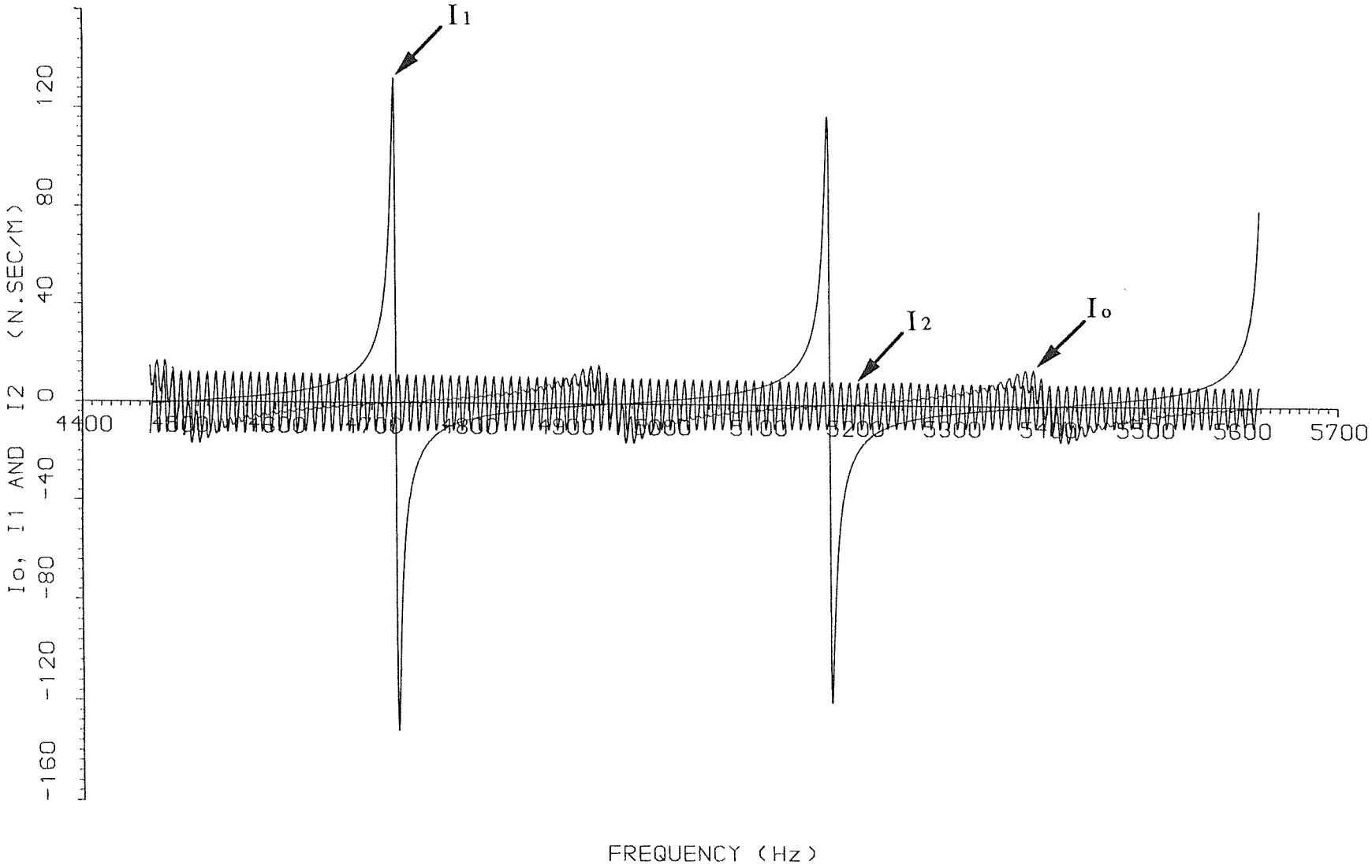

FIG.(5.31) COMPARISON BETWEEN THE IMAGINARY PARTS OF THE IMPEDANCES
M_1=0.01, M_2=0.5

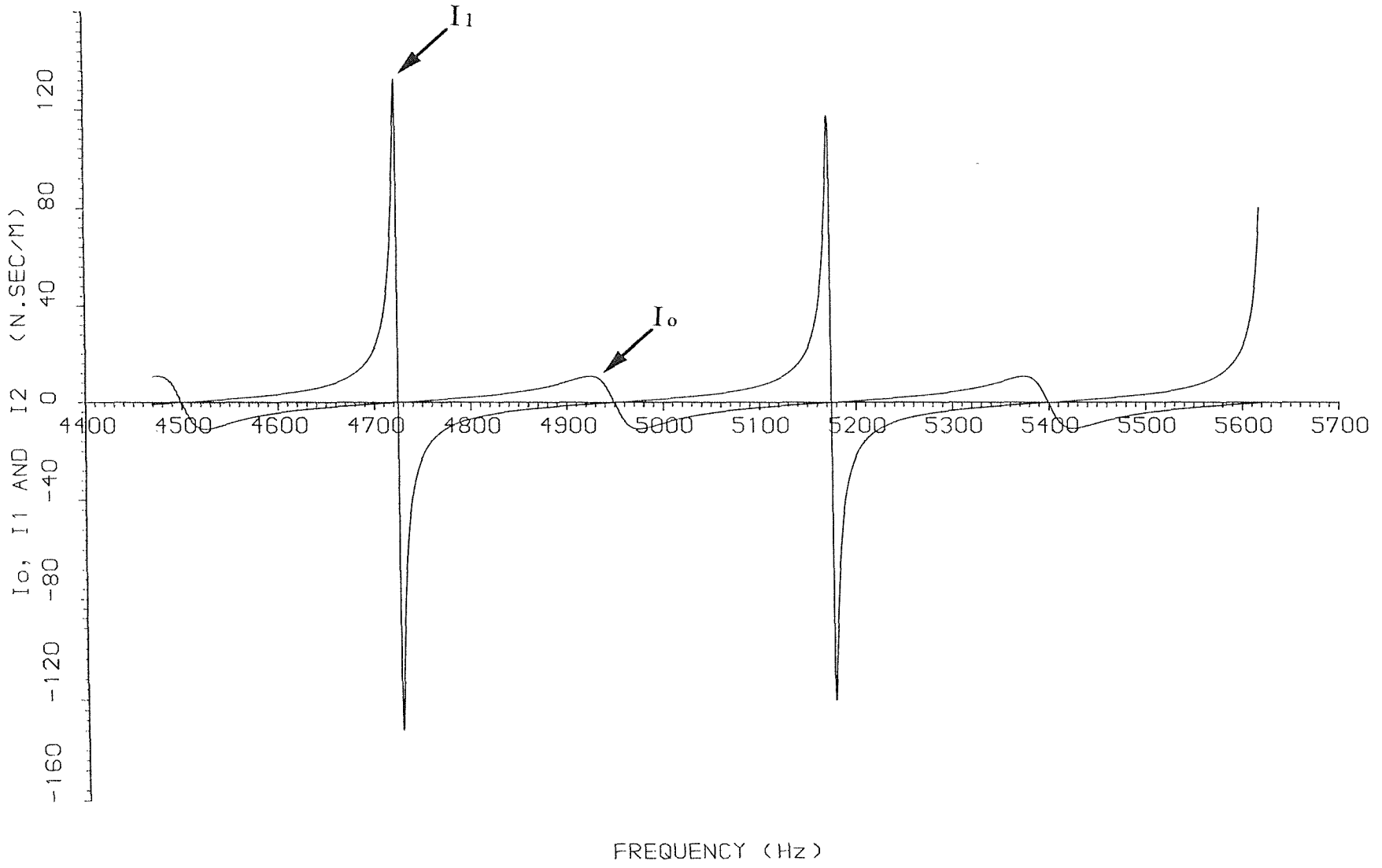

FIG.(5.32) COMPARISON BETWEEN THE IMAGINARY PARTS OF THE IMPEDANCES
M_1=0.01, M_2=1.5

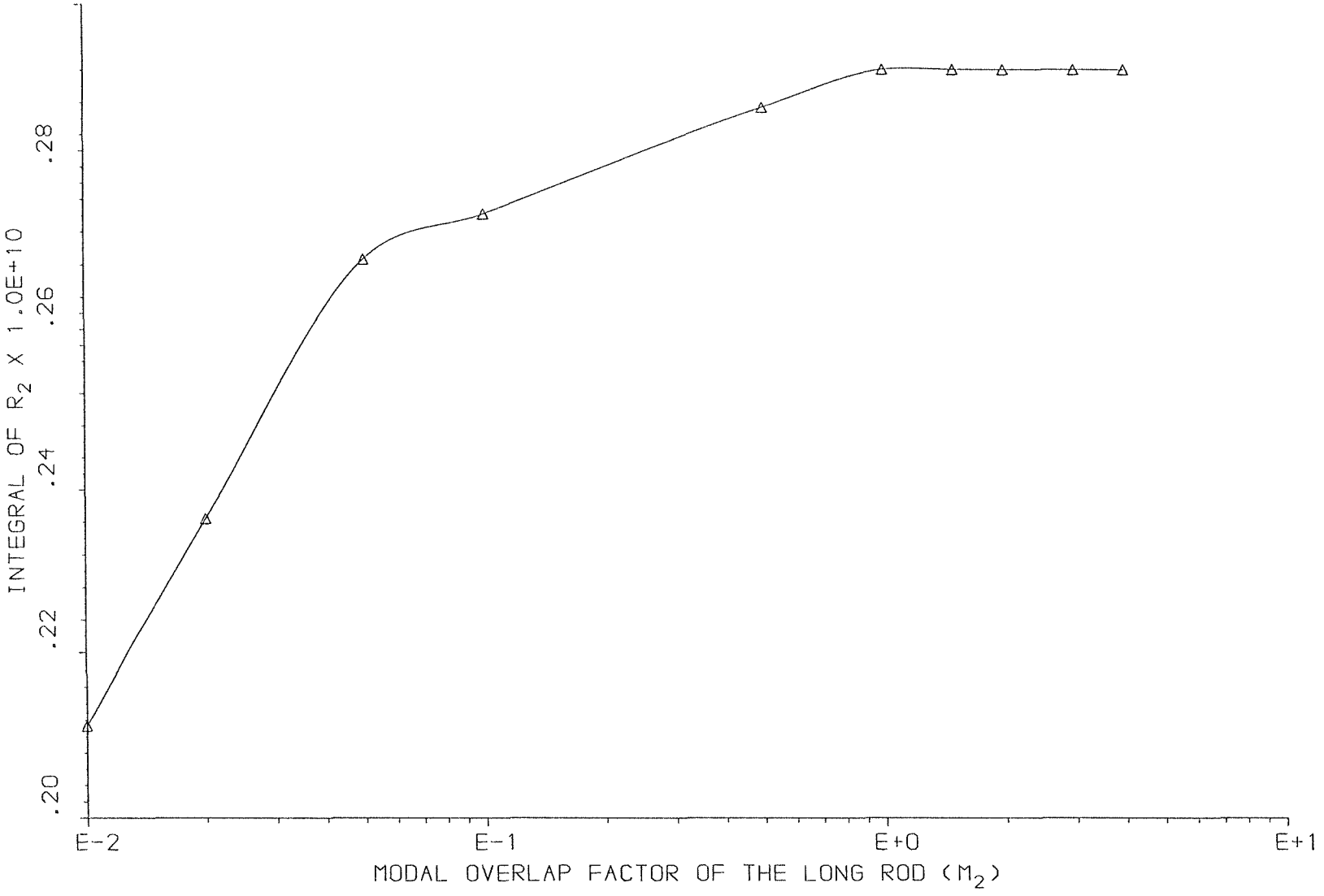

FIG.(5.33) FREQUENCY INTEGRATED VALUE OF R_2 OF SHORT-LONG RODS SYSTEM, M_1=0.01

CHAPTER 6

POWER FLOW BETWEEN A VIBRATING PANEL AND FLUID IN A CAVITY

6.1 Introduction

In the previous chapters, cases of coupling between multi-modal, one-dimensional and two-dimensional vibrating systems were analyzed by using exact solutions to the equations of motions of those systems. The coupling loss factor was evaluated on the basis of the SEA hypothesis, and the sensitivity of the calculations of this factor and the power flow between the coupled subsystems was investigated by means of statistical population models. This chapter is concerned with a case of coupling between a two-dimensional structural system (panel) and a three-dimensional acoustical system (enclosed fluid). This case is investigated by using the result of the coupled oscillator theory.

The first application of coupled oscillator, energy flow theory to randomly vibrating mechanical systems of engineering interest was that of Lyon and Maidanik in 1962 [1]. They demonstrated the proportionality of power flow between two linearly, conservatively, coupled oscillators to the difference between the time average (uncoupled) energies of the oscillators, when subjected to statistically independent random forces. They applied the analysis to the interaction between the acoustic modes of a room and one flexible wall, but did not fully explore the details of this problem. They treat the acoustic field as diffuse, and therefore do not work out in detail the case when a typical dimension-acoustic wave length ratio is not large and when the diffuse field assumption is unacceptable.

Newland [5] was the first to present a power flow analysis which enabled estimates to be made of errors involved in the use of approximations such as those

made by Lyon and Maidanik in their *ad hoc* linearisation. This perturbation method also allowed certain statistics of the power flow process to be evaluated.

Fahy [30,31] used the above mentioned theory as a tool to analyze the vibration of thin shell structures by random sound generated in a closed volume of fluid contained by the structures. The analysis has been carried out by means of numerical and statistical methods for the internal acousto-structural modal coupling factors and the corresponding modal average radiation efficiency. Results have been compared with that for a diffuse sound field [29]. It is found that the response of containing structures was the same as that for a diffuse acoustic field above a frequency (known as the lower limiting frequency), determined by the geometry, the speed of sound of the fluid, and the material properties of the structures. Below this frequency, the response falls below the diffuse field value. It is also found experimentally [30] that the introduction of irregularity into the geometry of the enclosure volume affects the coupling only at those frequencies below the lower limiting frequency.

The coupled system analyzed in this chapter consists of a thin, simply supported panel and a contiguous fluid in a rectangular box. The main body of the analysis in this chapter is a sequel to those of references [1] and [30]. The main object is to investigate the sensitivity of the computed radiation efficiency of the panel to small variations in the details of the geometry of the coupled system by following a similar approach to that of previous chapters.

Results for the mean and variance of radiation efficiency are obtained and studied with respect to other acousto-structural parameters of interest, such as modal overlap factor and number of coupled mode pairs.

6.2 Coupling between structure and fluid volume; basic theory

The basis of the following analysis is the coupled oscillator theory [1]. The differential equations of forced motion of two coupled sets of oscillators representing structural modes and acoustic modes are written (for coupled mode pairs) as

$$\ddot{S}_m + \beta_m \dot{S}_m + \omega_m^2 S_m + \left(\sum_r B_{rm}\, \dot{q}_r\right) = F_m \ , \qquad (6.1.a)$$

$$\ddot{q}_r + \beta_r \dot{q}_r + \omega_r^2 q_r - \left(\sum_m B_{mr}\, \dot{S}_m\right) = G_r \quad , \qquad (6.1.b)$$

where

$$S_m = \sqrt{\varepsilon_m}\; S_m' \quad ,$$

and

$$q_r = \sqrt{\frac{\rho\, V\, \varepsilon_r}{MC_o^2}} \;\cdot\; q_r' \;\cdot$$

S_m' is the generalized coordinate of the displacement of the structure normal to its surface, and q_r' is the generalized coordinate of the acoustic velocity potential of the fluid. ρ is the density of the fluid in the acoustic space, V represents the volume of the space, M is the total mass of the structure, and C_o is the speed of sound in the fluid. ε_m and ε_r are normalizing constants for the structural mode and the acoustic mode respectively which are given by

$$\varepsilon_m = M^{-1} \int_S \phi_m^2(\underline{x}) \cdot m''(\underline{x})\, d\underline{x} \quad ,$$

and

$$\varepsilon_r = V^{-1} \int_V \varphi_r^2(\underline{r})\, d\underline{r} \quad ,$$

where $\phi_m(\underline{x})$ is the displacement eigenfunction of structural mode m, and $\varphi_r(\underline{r})$ is the velocity potential eigenfunction of acoustic mode r: $\underline{x}$ and $\underline{r}$ denote position vectors of points on structure and fluid respectively. B_{rm} is the acousto-structural coupling factor, $m''(\underline{x})$ is the mass density, ω_m and ω_r represent the natural radian frequencies of

structural mode m and acoustic mode r, respectively. β_m and β_r are the half-power bandwidths of modes m and r, respectively. F_m and G_r represent the generalized forces on mode m and mode r respectively. If the coupling terms $(\sum_r B_{rm}\dot{q}_r)$ and $(\sum_m B_{mr}\dot{S}_m)$ are incorporated into the forcing terms, equations (6.1.a) and (6.1.b) become,

$$\ddot{S}_m + \beta_m\dot{S}_m + \omega_m^2 S_m + B_{rm}\dot{q}_r = F_m - \sum_{k\neq r} B_{km}\dot{q}_k = F_m' \quad , \qquad (6.2.a)$$

$$\ddot{q}_r + \beta_r\dot{q}_r + \omega_r^2 q_r - B_{mr}\dot{S}_m = G_r + \sum_{n\neq m} B_{nr}\dot{S}_n = G_r' \quad . \qquad (6.2.b)$$

With the assumption, which is not easily justified, that F_m' and G_r' are independent and white, equations (6.2) now represent the coupled motion of only two oscillators in which Lyon and Maidanik write the power flow per unit mass from the m^{th} mode to the r^{th} mode as

$$j_{mr} = g_{mr}\ (\theta_m - \theta_r) \quad , \qquad (6.3)$$

where θ_m and θ_r are the average, uncoupled, energies per unit mass of the oscillators subjected to inputs F_m' and G_r'. With further assumption that the parameters (B_{rm}/β_r) and (B_{rm}/β_m) are very small (a weak coupling is involved), the coupling constant g_{mr} is then derived as

$$g_{mr} = \frac{B_{mr}^2\,(\beta_m\omega_r^2 + \beta_r\omega_m^2)}{(\omega_m^2 - \omega_r^2) + (\beta_m + \beta_r)\,(\beta_m\omega_r^2 + \beta_r\omega_m^2)} \quad , \qquad (6.4)$$

where

$$B_{mr} = \left\{ \frac{C_o^2 \ \rho}{V \ \varepsilon_r \ \varepsilon_m \ M} \right\}^{1/2} \int_S \varphi_r(\underline{x}) \ \phi_m(\underline{x}) \ d\underline{x} \qquad (6.5)$$

The important feature of equation (6.4) is the strong sensitivity of the denominator to the difference between the structural and acoustic modes natural frequencies, ω_m and ω_r which enable the following first order approximations [30]

$$g_{mr} \approx B_{mr}^2 \ (\beta_m + \beta_r)^{-1} \quad : \ | \omega_m - \omega_r | < 1/2 \ (\beta_m + \beta_r) \qquad (6.6.a)$$

$$\approx 0 \quad : \ | \omega_m - \omega_r | > 1/2 \ (\beta_m + \beta_r) \qquad (6.6.b)$$

The conditions of equations (6.6) modified those which appeared in reference [1]. The original conditions virtually excluded any power flow with practical damping values, whereas the present conditions restrict significant power flow to modes of which the difference in natural frequencies is less than the sum of half their half power bandwidths. The conditions of equation (6.6) are considered in the analysis of the present work as a criterion to separate the significant acousto-structural mode pairs which are referred to as having 'proximate modal coupling'.

6.3 Panel-Box system

The coupled system analyzed consists of a thin, steel, elastic, rectangular, simply supported panel of a uniform thickness and density. The panel forms one complete wall of an otherwise rigid rectangular box containing air with dimensions of 0.82 m × 0.65 m × 3mm. The box had the dimensions of 0.82 m × 0.65m × 0.60 m. The configuration of the system is shown in figure (6.1). The coupled multi-mode subsystems are represented by the panel and the fluid in the box.

The eigenfunctions of the structural displacement and the acoustic velocity potential are given by

$$\phi_m(x,y) = \sin(\frac{m\pi x}{a}) \sin(\frac{n\pi y}{b}) \qquad (6.7)$$

$$\varphi_r(x,y,z) = \cos(\frac{p\pi x}{a}) \cos(\frac{q\pi y}{b}) \cos(\frac{r\pi z}{c}) \qquad (6.8)$$

where m and n are the structural mode order. p, q, and r represent the acoustic mode order. a and b are the panel dimensions and a,b,c are the box dimensions. The substitution of these eigenfunctions into equation (6.5) for B_{mr} gives

$$B_{mr} = \left\{ \frac{C_o^2 \ \rho}{V \ \varepsilon_r \ \varepsilon_m \ M} \right\}^{1/2} (-1)^r \left[\frac{ma}{p^2\pi} \left\{ \frac{(-1)^{m+p}-1}{1-(m/p)^2} \right\} \right] \left[\frac{nb}{q^2\pi} \left\{ \frac{(-1)^{n+q}-1}{1-(n/q)^2} \right\} \right]$$

: $m \neq p$, $n \neq q$

$= 0$: (m+p) even or (n+q) even

(6.9)

The natural frequencies of acoustic mode ω_r and structural mode ω_m are calculated as

$$\omega_r = k_r \ C_o \quad , \qquad (6.10)$$

$$\omega_m = k_p \ C_b \quad , \qquad (6.11)$$

where k_r is the acoustic wave number corresponding to the acoustic mode order p,q,r which is given by

$$k_r = \sqrt{(p\pi/a)^2 + (q\pi/b)^2 + (r\pi/c)^2} \quad .$$

k_p is the flexural wave number of the panel corresponding to the structural mode order m,n and it is given by

$$k_p = \sqrt{(m\pi/a)^2 + (n\pi/b)^2} \quad .$$

C_b is the flexural wave speed which is given by

$$C_b^2 = \frac{B}{\rho_s h} \left\{ (m\pi/a)^2 + (n\pi/b)^2 \right\} \quad ,$$

where B is the flexural rigidity of the panel, ρ_s is the density of the panel, and h is the thickness. Note that because the flexural waves are dispersive, there is a unique frequency for every uniform elastic panel at which free waves travel with the same speed C_b as sound waves in the adjacent fluid. This frequency is called the critical frequency (f_c) and is given by

$$f_c = \frac{C_o^2}{1.8\ h\ C_l}$$

The critical frequency for the steel panel (3 mm thick) of the present model is about 4100 Hz.

The power flow between the sound field and the panel is most simply expressed in terms of the average radiation resistance (R_{rad}) of the panel. For a directly excited fluid (indirectly excited panel), the ratio of space averaged mean square vibration acceleration to space averaged mean square pressure, for multi-mode coupling, is written as [1]

$$\frac{S_a(\omega)}{S_p(\omega)} = \frac{2\pi^2 C_o n_s(\omega)}{M \rho} \left[\frac{R_{rad}}{R_{rad} + R_{mech}}\right] , \qquad (6.12)$$

where $S_a(\omega)$ is the spectral density of panel acceleration, $S_p(\omega)$ is the spectral density of acoustic pressure, $n_s(\omega)$ is the modal density of the panel, and $R_{mech} = \beta_m \cdot M$, is the mechanical resistance. The radiation resistance (R_{rad}) is given by

$$R_{rad} = (M/N_s) \sum_{m\ r} g_{m\,r} \qquad , \qquad (6.13)$$

where N_s is the average number of structural modes in the frequency band of interest. Equation (6.13) is based on the assumption that each structural mode in the frequency band $\Delta\omega$ is coupled to all acoustic modes that exist in that frequency band.

The coupling loss factor between a structure and a sound field is most simply expressed by the average radiation resistance of the structure (R_{rad}) interacting with an infinite space (diffuse sound field). It is written as [11]

$$\eta_{sa} = \frac{R_{rad}}{\omega M} .$$

The coupling from the acoustical space to the structure can be found from

$$\eta_{as} = \eta_{sa} (N_s/N_a) ,$$

where N_a is the average number of acoustic modes in the frequency band of interest.

Fahy [30] has established the concept of the 'Lower Limiting Frequency', the frequency below which the simplified results of radiation resistance to a diffuse field may be in error. However, above this frequency the estimate of (R_{rad}) obtained from mode-mode coupling (equation (6.13)) was found to be in a good agreement with the diffuse field estimate. The lower limiting frequency has been estimated for the present

case of coupling (Panel-Box system) and found to be corresponding fairly closely to the value of frequency for which the average number of mode pairs, having maximum proximate coupling, pairs falls below one or two. This value can be obtained from the following equation

$$\frac{2\pi^2 \, h^2 \, C_o^2}{3(\beta_r + \beta_m)(a+b)(abc)} = (f/f_c) \, \mathrm{Sin}^{-1}(\sqrt{f/f_c}) \, \Delta\omega \qquad (6.14)$$

The equation above is evaluated for the value of f, (using the dimensions of the coupled system described above),.and is found to be about 1100 Hz.

6.4 Perturbation Analysis

As mentioned earlier, the main objective of this study is to investigate the sensitivity of the computed radiation efficiency to the small alterations of the dimensions of the coupled panel-box system.

A similar approach to those of previous chapters is followed here: a statistical population model is created by employing the distribution sampling application of the Monte Carlo method. The thickness (h) of the panel is perturbed in the range of 10% of the mean value assumed above. The thickness sample, which contains 20 elements, is drawn from a normally distributed population of a known mean and standard deviation. For each thickness element in the perturbed set, the radiation efficiency is calculated as follows:

(a) Calculation of all possible natural frequencies of the panel modes (ω_m) and the acoustic modes (ω_r) in the frequency band of interest using equations (6.10) and (6.11).

(b) Assuming a value for the parameter ($\beta_r + \beta_m$) which is the sum of the half-power bandwidths (modal damping coefficients) of structural and acoustic modes. Note that $\beta_m = \omega_m \eta_m$, and $\beta_r = \omega_r \eta_r$. Where η_m and η_r represent the dissipation loss factors of the structural and acoustic modes respectively.

(c) Selection of all acoustic modes having natural frequencies sufficiently close to each natural frequency of the panel mode and obeying the frequency proximity condition of equation (6.6.a) in the frequency band of the analysis.

(d) Calculation of the modal coupling factor (B_{mr}), using equation (6.9) for each mode pair that was located in step (c) above.

(e) Calculation of the coupling constant (g_{mr}) for each mode pair according to equation (6.4) above.

(f) Calculation of radiation resistance (R_{rad}), using equation (6.13) and the radiation efficiency of the panel, in the given frequency band of interest, which is given by

$$\sigma = \frac{R_{rad}}{\rho . C_o \; a.b} \; .$$

Steps (a)-(f) above are carried out for all the thickness values in the generated set. The computed radiation efficiencies form an ensemble of twenty observations. That is, for the given (assumed) value of the parameter ($\beta_r + \beta_m$). The computation above are then repeated for different ($\beta_r + \beta_m$) values and also in different 1/3 octave frequency bands. The results are plotted in figures (6.2)-(6.8). From these results, mean and variance values are obtained and plotted in figures (6.11) and (6.12).

6.5 Results and Discussion

Figures (6.2)-(6.8) display the populations of computed radiation efficiency (associated with the panel thickness perturbations) of the Panel-Box system in different 1/3 octave frequency bands (centred at 500-6300 Hz) and also for a range of values of the parameter ($\beta_r + \beta_m$). Each curve on these figures is obtained for a given value of panel thickness in the generated, normally distributed, set of thicknesses, i.e., each curve displays the radiation efficiency for one realization in the ensemble of the similar (not identical) coupled systems. The figures show quite clearly that the higher the value of the parameter ($\beta_r + \beta_m$), the less the fluctuations of the estimate of the radiation efficiency (σ). This result is attributed to the fact that the number of coupled acousto-structural mode pairs (N_{rm}) is a linear function of the parameter ($\beta_r + \beta_m$) in a given

frequency band : as $(\beta_r + \beta_m)$ increases, the number of mode pairs contributing to the power flow process increases and hence the sensitivity of the computed estimate of the radiation efficiency about the mean value decreases. The linear relationship between N_{rm} and $(\beta_r + \beta_m)$ is demonstrated in figure (6.9) for one realization (h = 3 mm), in one 1/3 octave frequency band centred at 5000 Hz and for different acoustic cavity volumes. Note that, at low frequency bands (small Δf), this relationship is no longer linear because of the lack of the number of contributing mode pairs. However, it is also affected by the size of the acoustic cavity.

Figures (6.2)-(6.8) also demonstrate the effect of the frequency bandwidth on the sensitivity of the computed estimate of σ. For a given value of $(\beta_r + \beta_m)$, the fluctuation of the computed value about the mean tends to diminish as the frequency increases. Obviously, this is because of the rapid increase in the number of acoustic modes that are coupled to each structural mode in the frequency band of interest.

From above, we can conclude that the figures (6.2)-(6.8) demonstrate the mixed effects of the average modal overlap factor (M_{av}) of the coupled system and the average number of acousto-structural mode pairs (N_{rm}) on the sensitivity of the computed radiation efficiency of the panel to the small variations in the geometry of the coupled system. The scale of M_{av} shown in the above figures represents the mean values which are calculated at the different 1/3 octave frequency bands. Note that M_{av} is given by

$$M_{av} = \sqrt{M_a M_s}$$

where $M_a = \beta_r n_a(\omega)$ is the modal overlap factor of the acoustic enclosure and $M_s = \beta_m n_s(\omega)$ is the modal overlap of the panel. $n_a(\omega)$ and $n_s(\omega)$ are the modal densities of the fluid and the panel respectively which are given by

$$n_a(\omega) = \frac{V\omega^2}{2\pi^2 C_o^3} + \frac{S\omega}{8\pi C_o^2} \ ,$$

$$n_s(\omega) = \frac{A_p}{4\pi} . \sqrt{\rho h / B} \ ,$$

where S is the total area of the acoustic enclosure. Figure (6.10) shows a comparison between the modal densities of the coupled subsystems, as functions of frequency and the size (height (c)) of the acoustic enclosure.

The results obtained above are confirmed by the calculation of the normalized variance (variance/mean^2) of the panel radiation efficiency. Figures (6.11) and (6.12) display the normalized variance against the centre frequency of the band of the analysis and against the parameter ($\beta_r + \beta_m$) respectively. Figure (6.11) shows that the normalized variance decreases as the centre frequency of the band of the analysis increases, that is for a given value of the parameter ($\beta_r + \beta_m$). More reduction in the value of the normalized variance can be noted at higher values of ($\beta_r + \beta_m$). On the other hand, figure (6.12) shows the strong influence of the parameter ($\beta_r + \beta_m$) on the results of normalized variance at different 1/3 octave frequency bands. Also a rapid decrease can be noted for higher frequency bands. In other words, from close examination of the results of these two figures we are able to distinguish between the strong influences of the average modal overlap factor and the average number of coupled mode pairs on the sensitivity of the computation of radiation efficiency to the proposed perturbations of the coupled system.

As the modal density of the flat plate ($n_s(f)$) is independent of frequency and the modal density of the acoustic enclosure ($n_a(f)$) is a strong function of frequency (see figure (6.10)), the effect of $n_a(f)$ on the computed radiation efficiency is also investigated. This analysis was carried out by assuming three different box height values (c = 0.15, c = 0.30, and c = 0.60) and a fixed thickness value (h = 3 mm) for the mathematical model of the coupled system. The radiation efficiency was then computed according to the assumed height values and at different 1/3 octave frequency bands. The results are displayed in figures (6.13)-(6.16) for ($\beta_r + \beta_m$) values of 25, 40, 100, and 300 respectively. These figures show that the higher the frequency and (or) the higher the values of damping coefficients ($\beta_r + \beta_m$), the less the effect of changing the acoustic field modal density on the sensitivity of the results of radiation efficiency. High variations of σ are noted in the low frequency region which is due to the small number of contributing mode pairs (N_{rm}) in that region.

The sensitivity of the computed radiation efficiency to the perturbations of panel thickness may also be noted from the shapes of cumulative probability distribution curves. These curves are constructed from the computed populations of σ in 1/3 octave frequency bands centred at 4000 Hz and 5000 Hz as shown in figures (6.17) and (6.18) respectively. Figure (6.17) shows the distributions for different

values of average modal overlap factor while figure (6.18) shows the distributions for different ($\beta_r + \beta_m$) values. Both figures show similar results to those of previous chapters (coupled beams and coupled plates models): the distribution of σ approaches the normality as the parameter ($\beta_r + \beta_m$) (i.e the modal overlap factor) increases.

6.6 Conclusions

From the numerical investigations of the coupling between structure and acoustic field, the following conclusions can be drawn.

(a) The sensitivity of the computed estimate of radiation efficiency of the panel (due to a random sound in the contained fluid) to the perturbations of the panel thickness is highly affected by the value of the sum of the half-power bandwidths of the panel and acoustic modes ($\beta_r + \beta_m$). The variance has the tendency to decrease as ($\beta_r + \beta_m$) increases. For a given 1/3 octave frequency bandwidth, this result can be considered as a pure effect for the average modal overlap factor of the coupled system.

(b) The variance of the computed populations of radiation efficiency is highly sensitive to the frequency bandwidth of the analysis. It decreases as the centre frequency of the 1/3 octave band increases. This is attributed to the fact that the number of coupled acousto-structural mode pairs which contribute to the power flow between the subsystems increases.

(c) The sensitivity of the results of radiation efficiency to the changes in the modal density of the acoustic enclosure tends to diminish as the average modal overlap factor increases.

(d) The statistical distribution of the computed radiation efficiency approaches (approximately) that of the normal distribution as the parameter ($\beta_r + \beta_m$) increases, i.e., as the average modal overlap factor increases. This result supports those obtained from the previous cases of coupling between one dimensional and two dimensional systems.

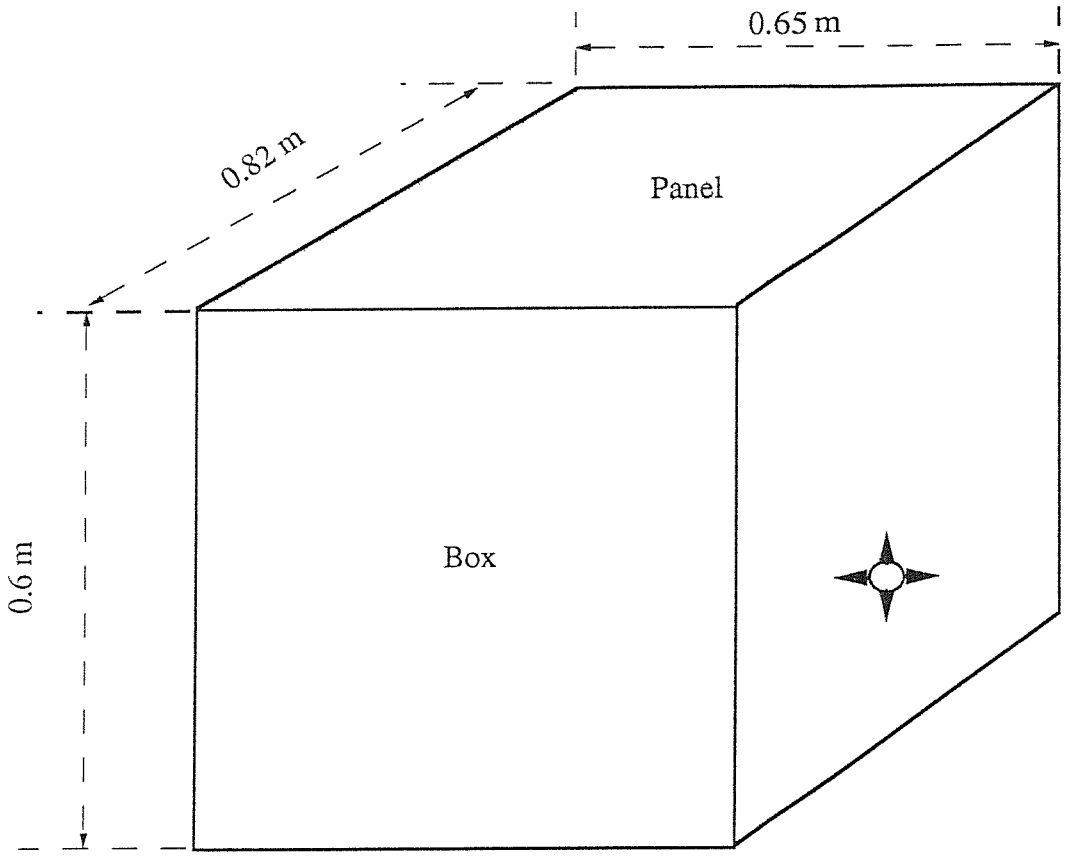

Figure (6.1) : Panel-Box model

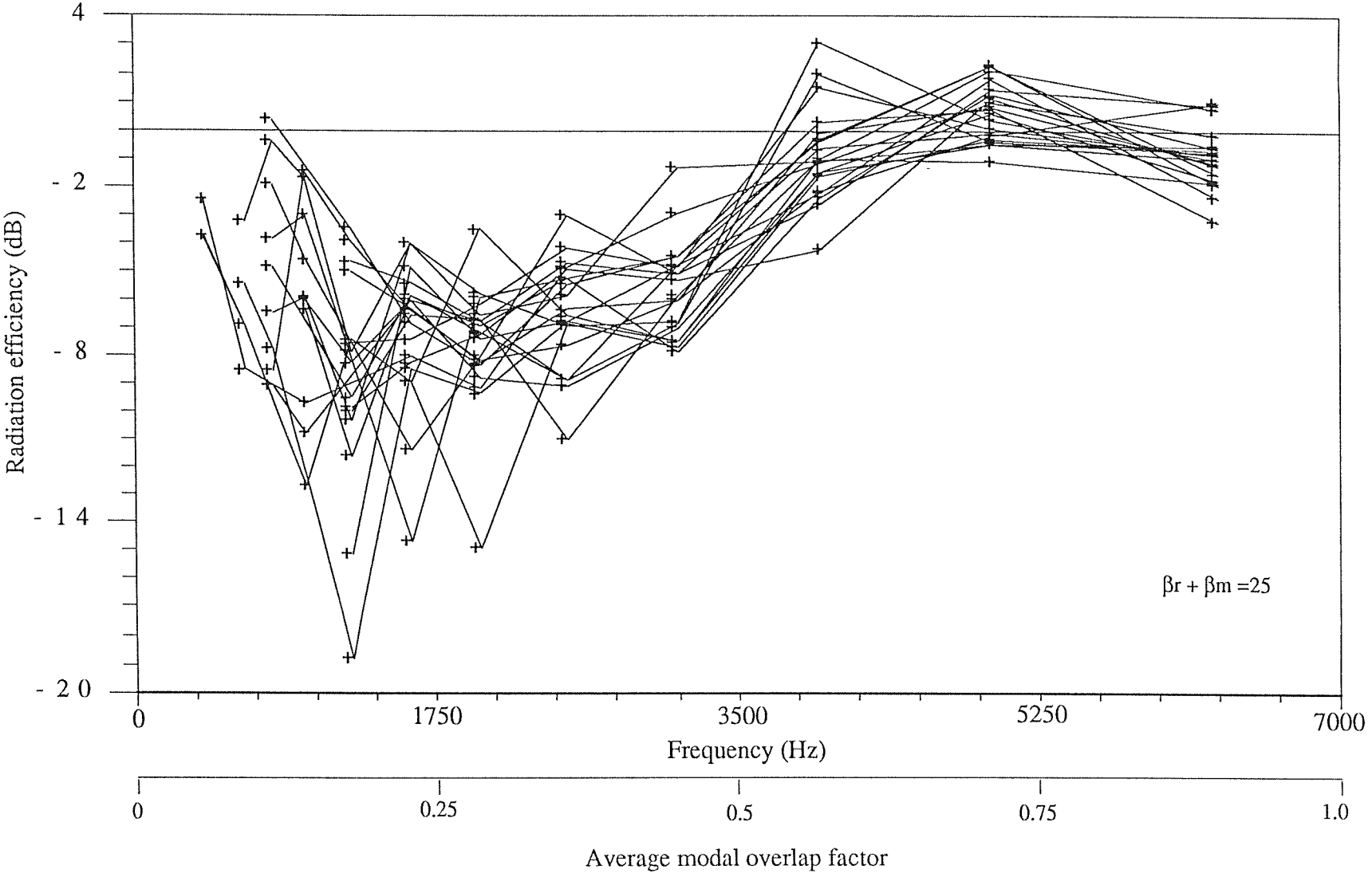

Figure (6.2) : The population of radiation efficiency of a simply supported panel

(1/3 octave band averages)

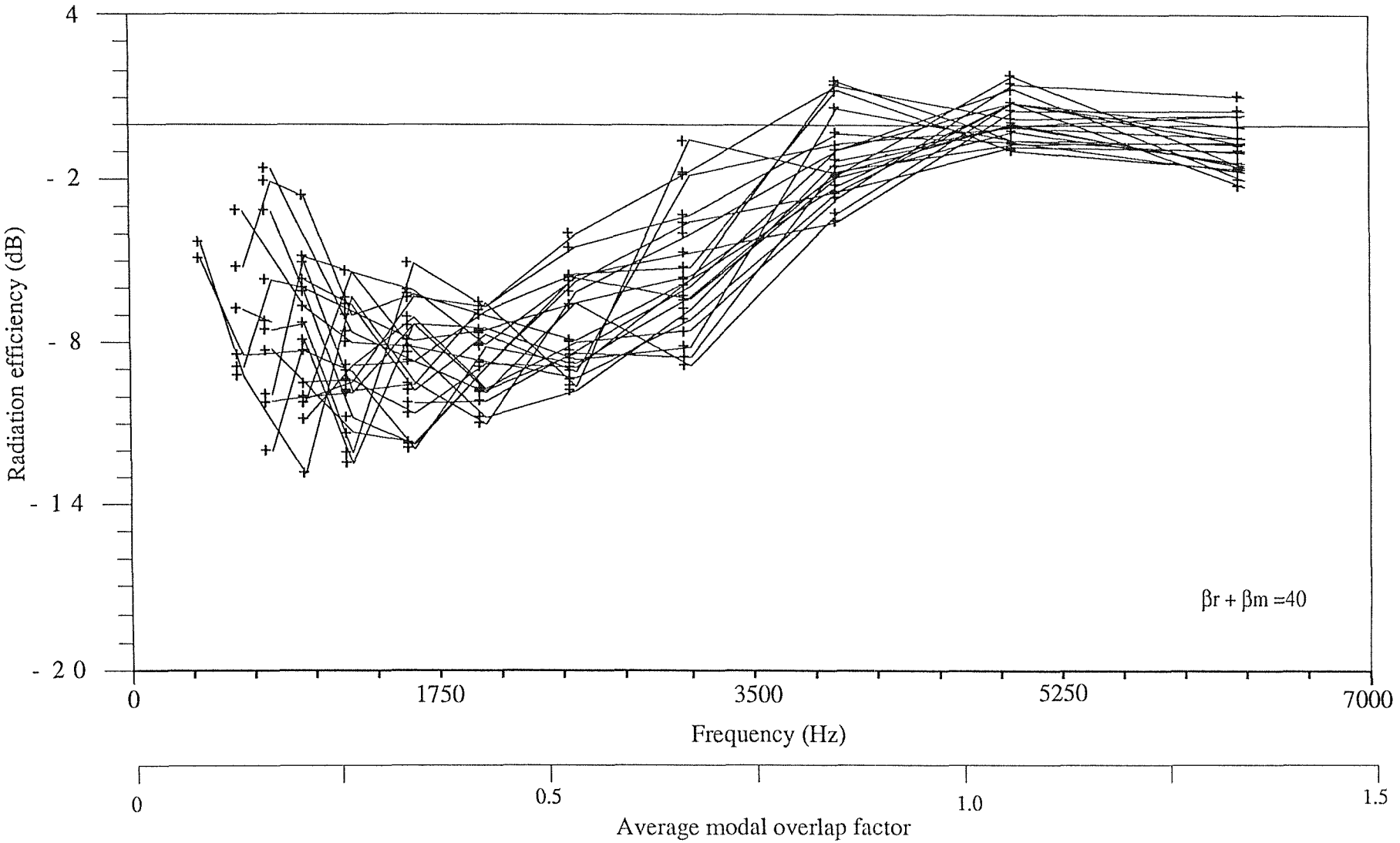

Figure (6.3) : The population of radiation efficiency of a simply supported panel (1/3 octave band averages)

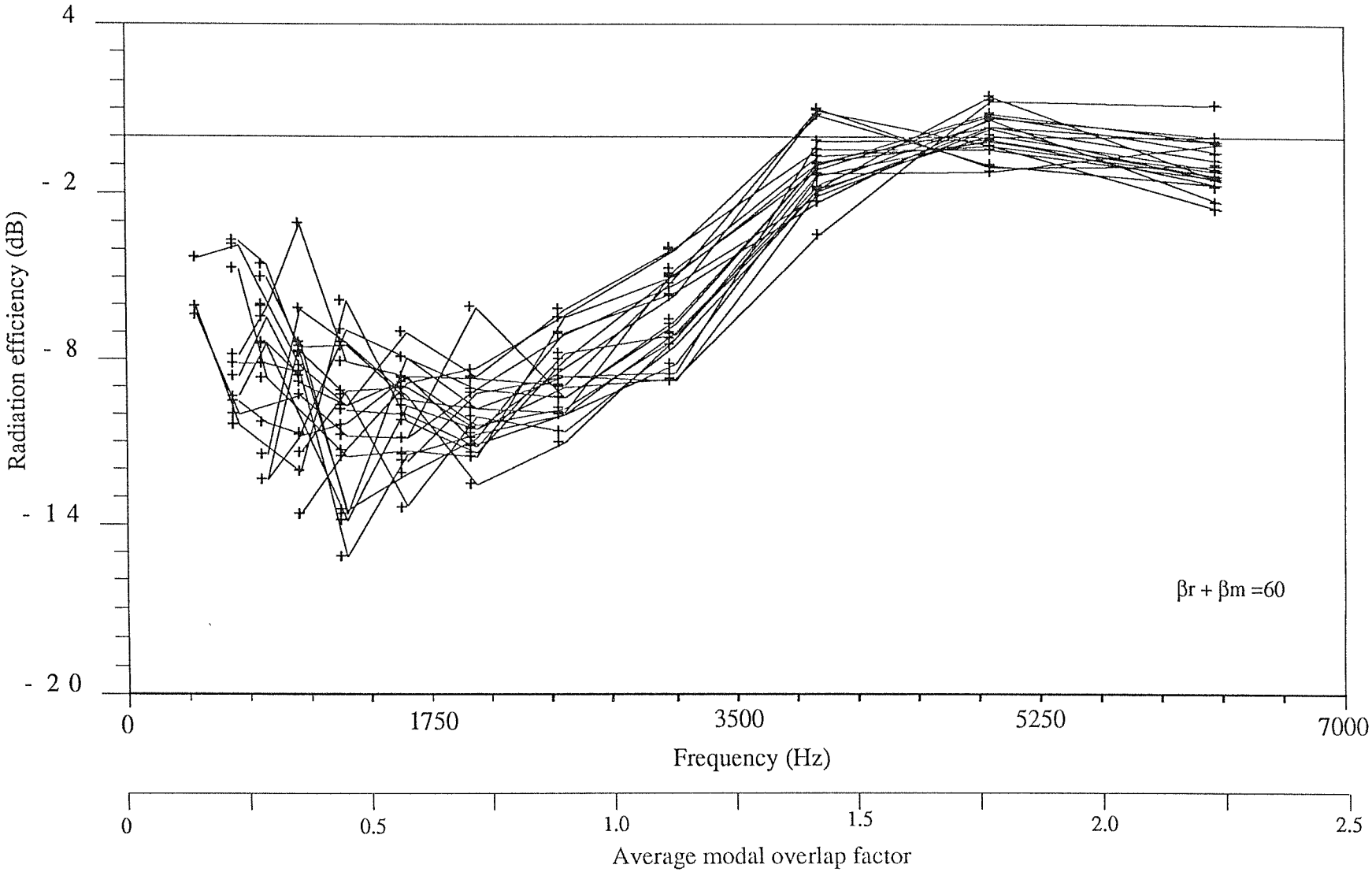

Figure (6.4) : The population of radiation effeciency of a simply supported panel (1/3 octave band averages)

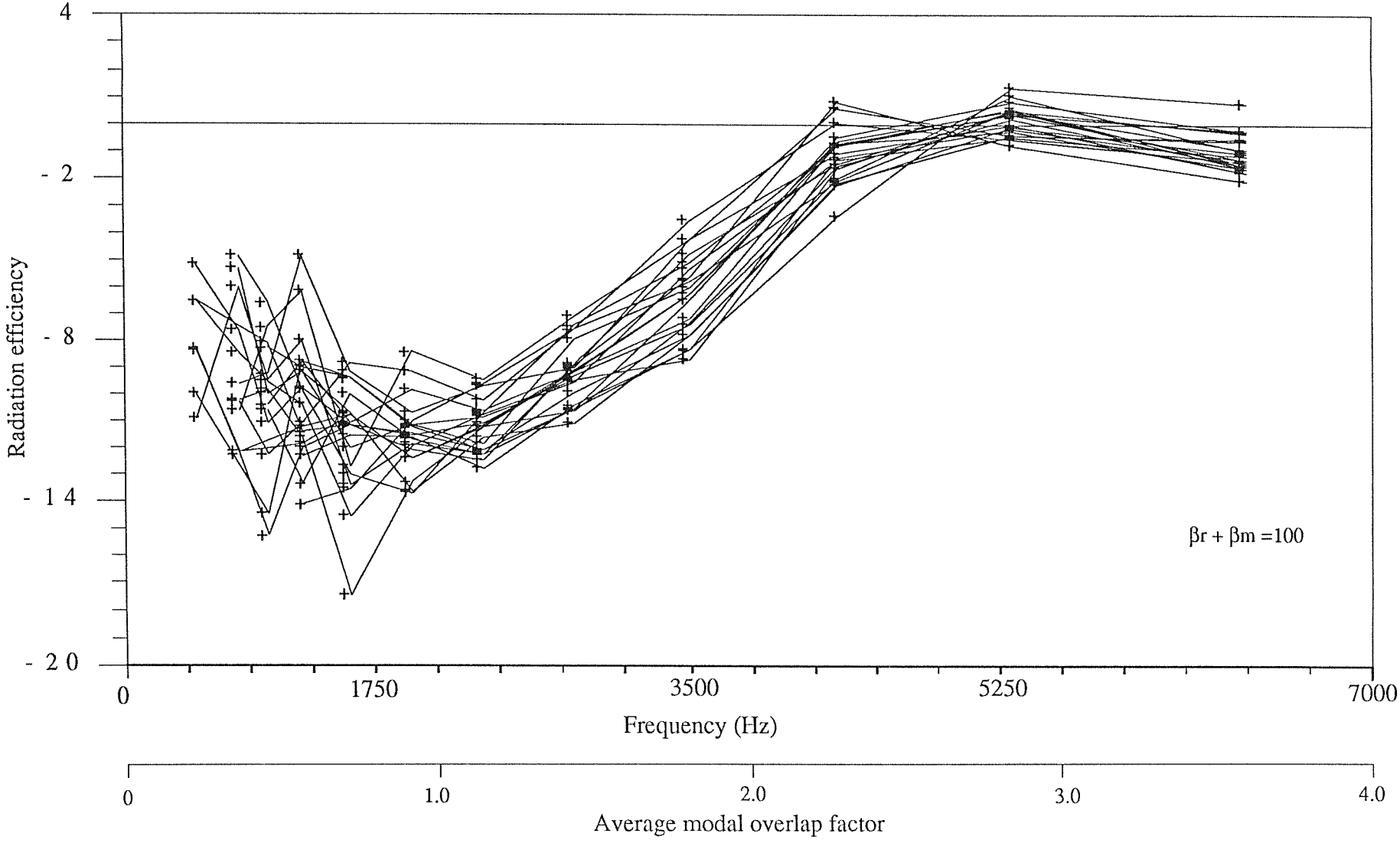

Figure (6.5) : The population of radiation efficiency of a simply supported panel (1/3 octave band averages)

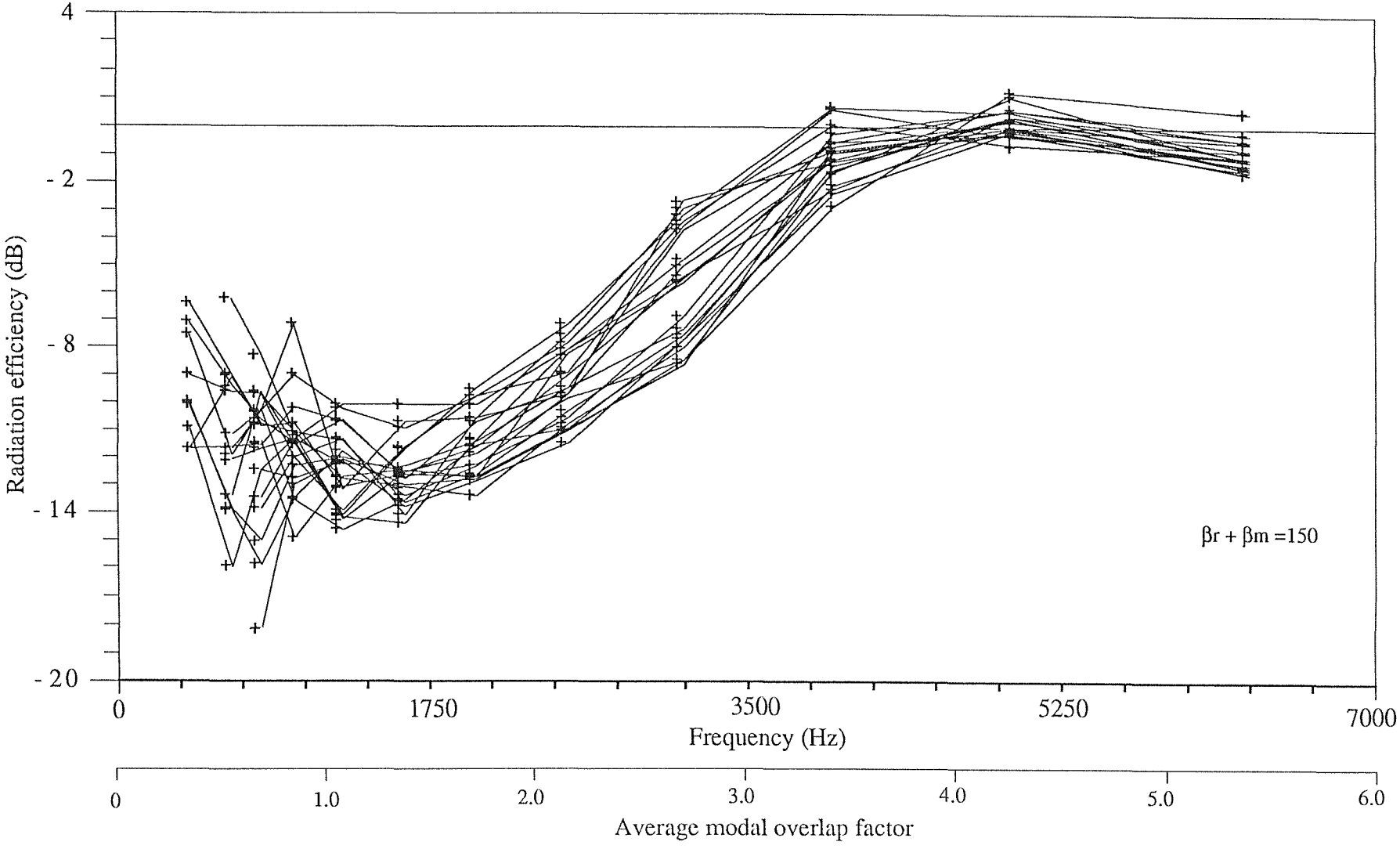

Figure (6.6) : The population of radiation efficiency of a simply supported panel (1/3 octave band averages)

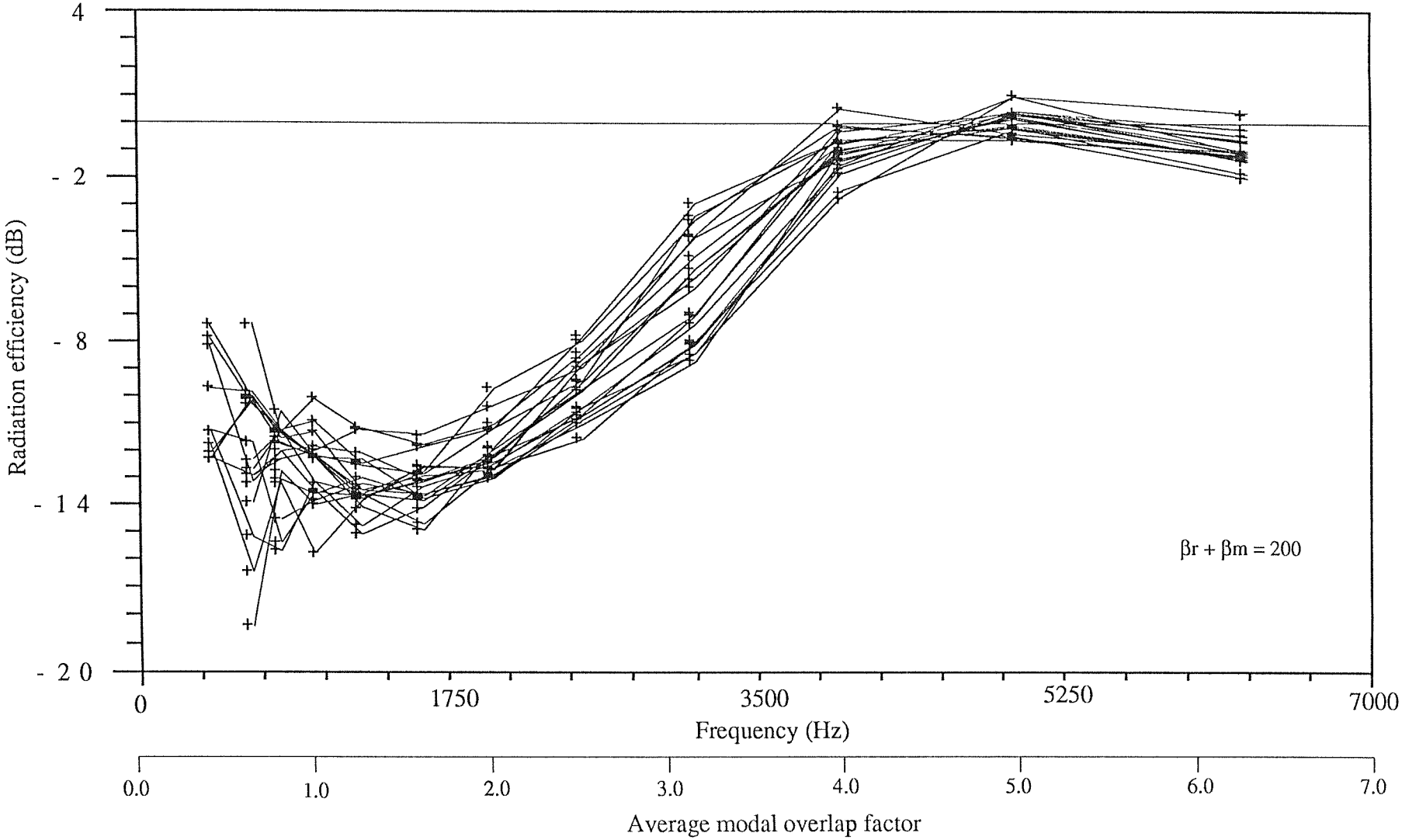

Figure (6.7) : The population of radiation efficiency of a simply supported panel (1/3 octave band averages)

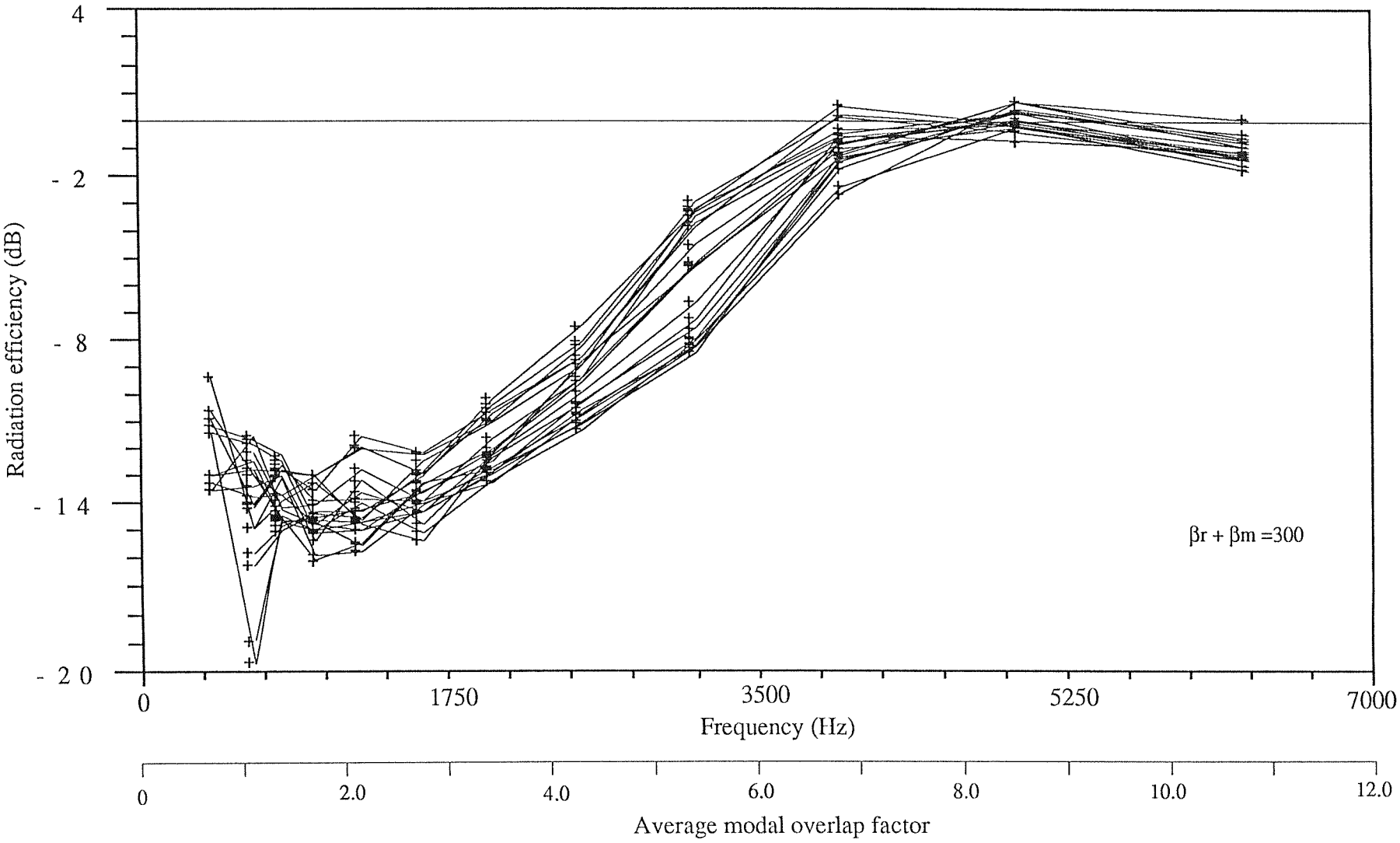

Figure (6.8) : The population of radiation efficiency of a simply supported panel (1/3 octave band averages)

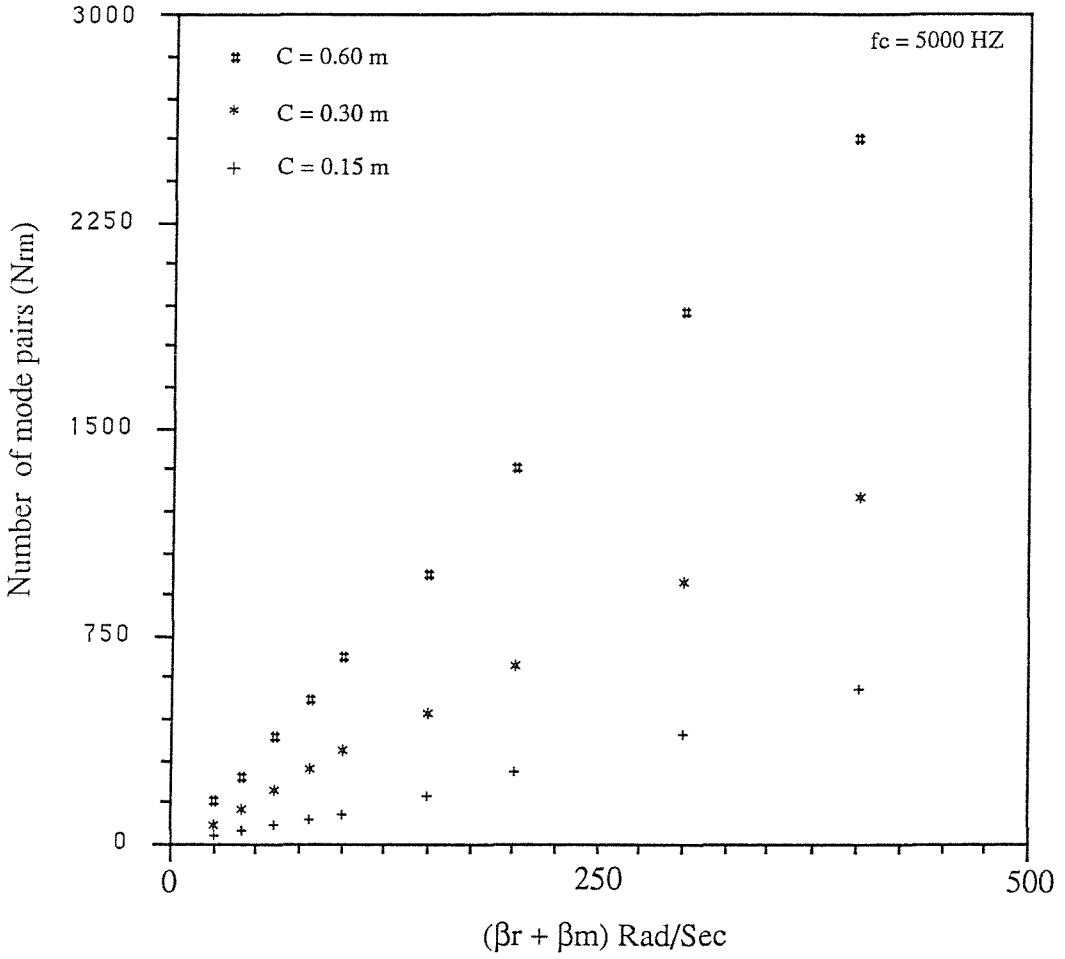

Figure (6.9) : The computed number of acousto-structural mode pairs in a 1/3 octave frequency band centred at 5000 Hz

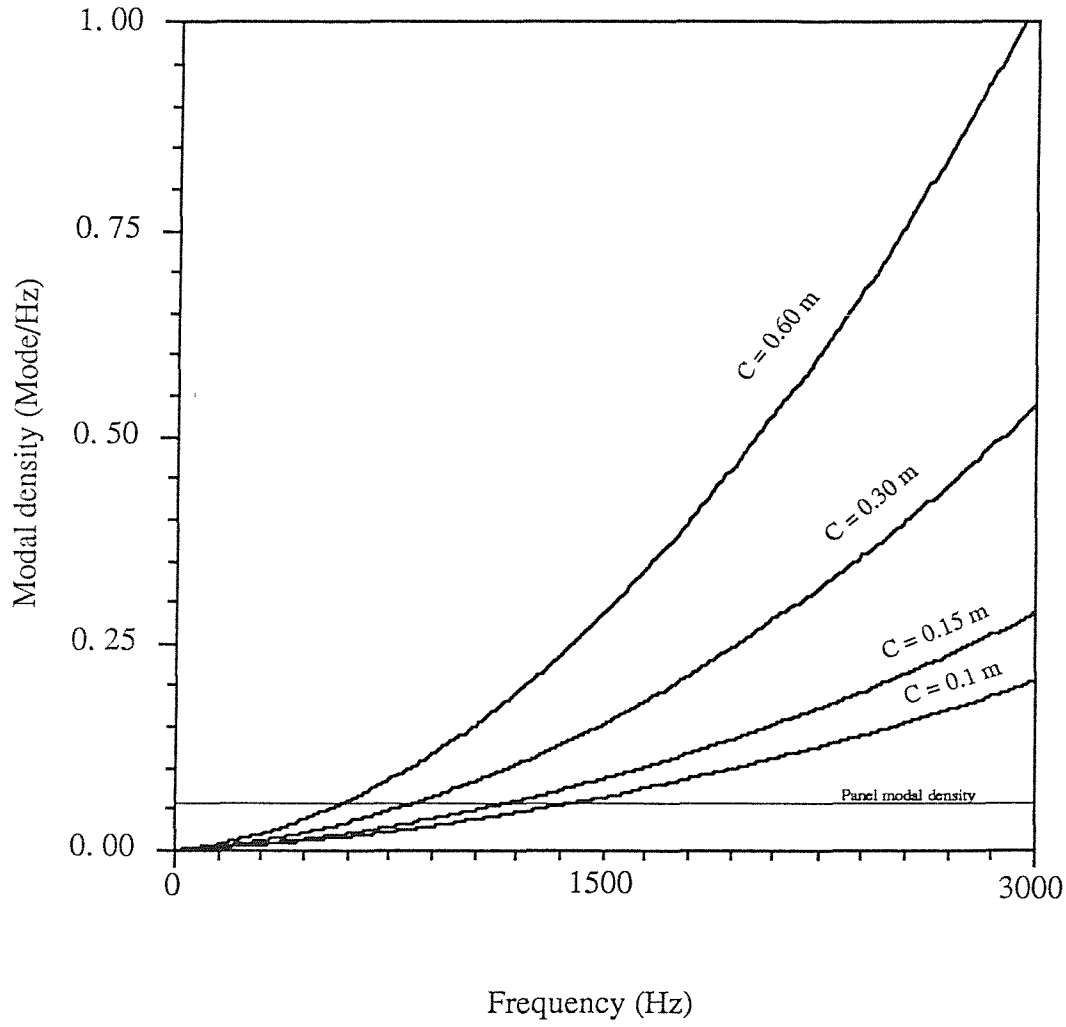

Figure (6.10) : The modal densities of 3mm panel and the acoustic cavity (different depths) of the panel-box system

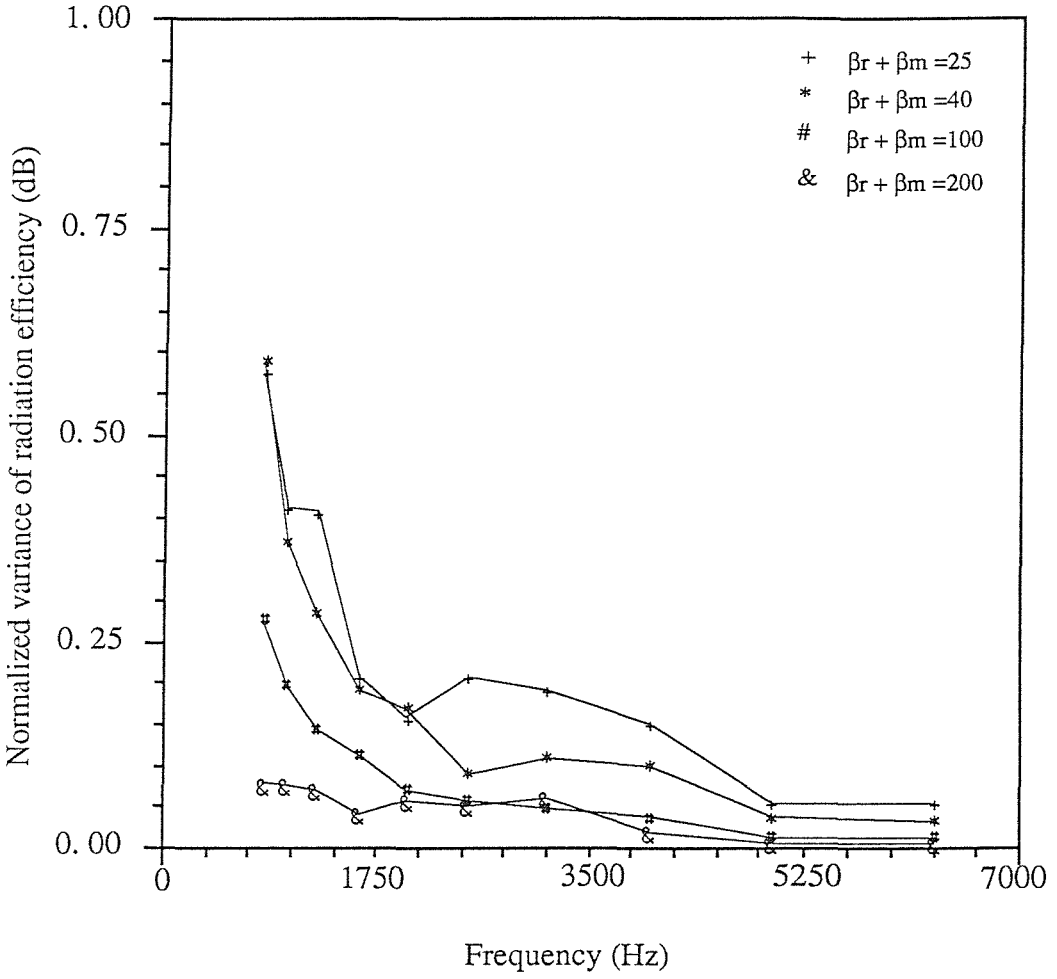

Figure (6.11) : The normalized variance of the radiation efficiency of the panel (1/3 octave band averages)

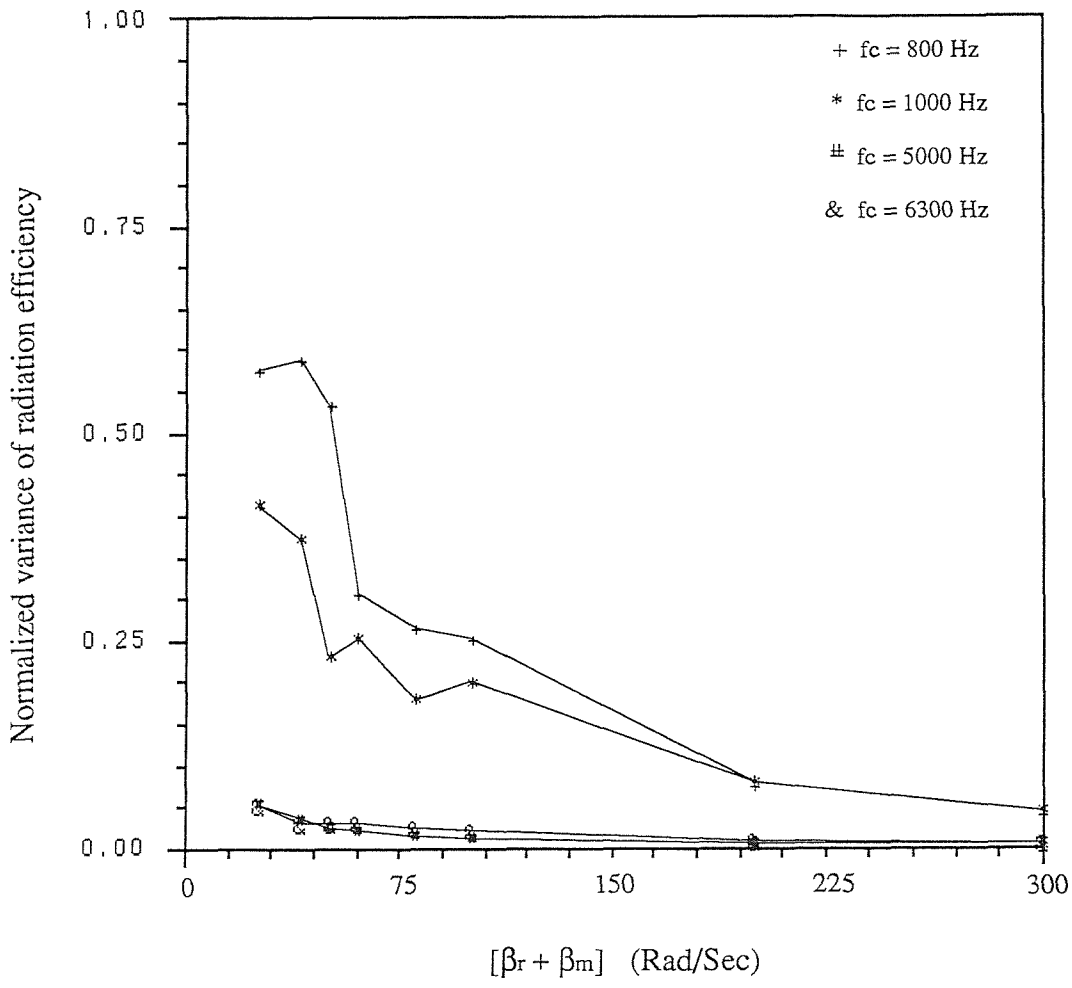

Figure (6.12) : The normalized variance of the radiation efficiency of the panel in different 1/3 octave frequency bands, (fc is the centre frequency of the band).

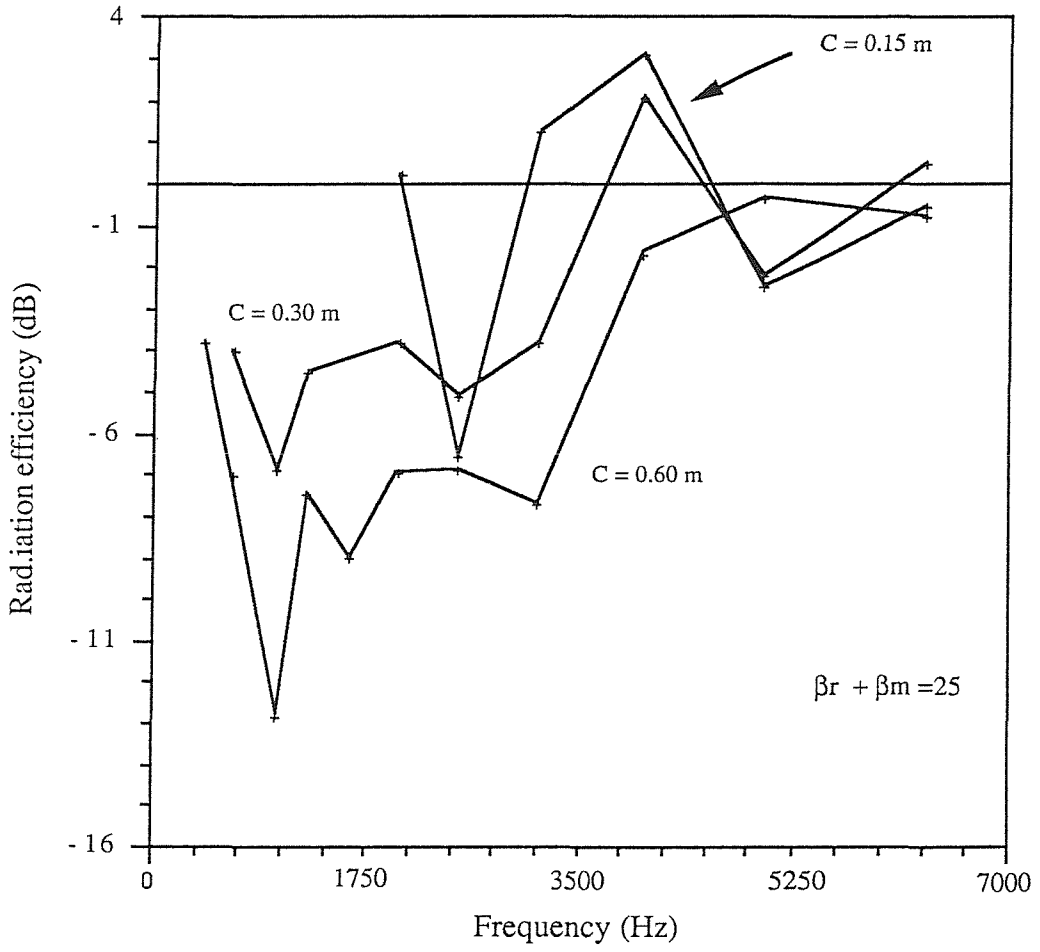

Figure (6.13) : Radiation efficiency of 3 mm panel (1/3 octave band averages)

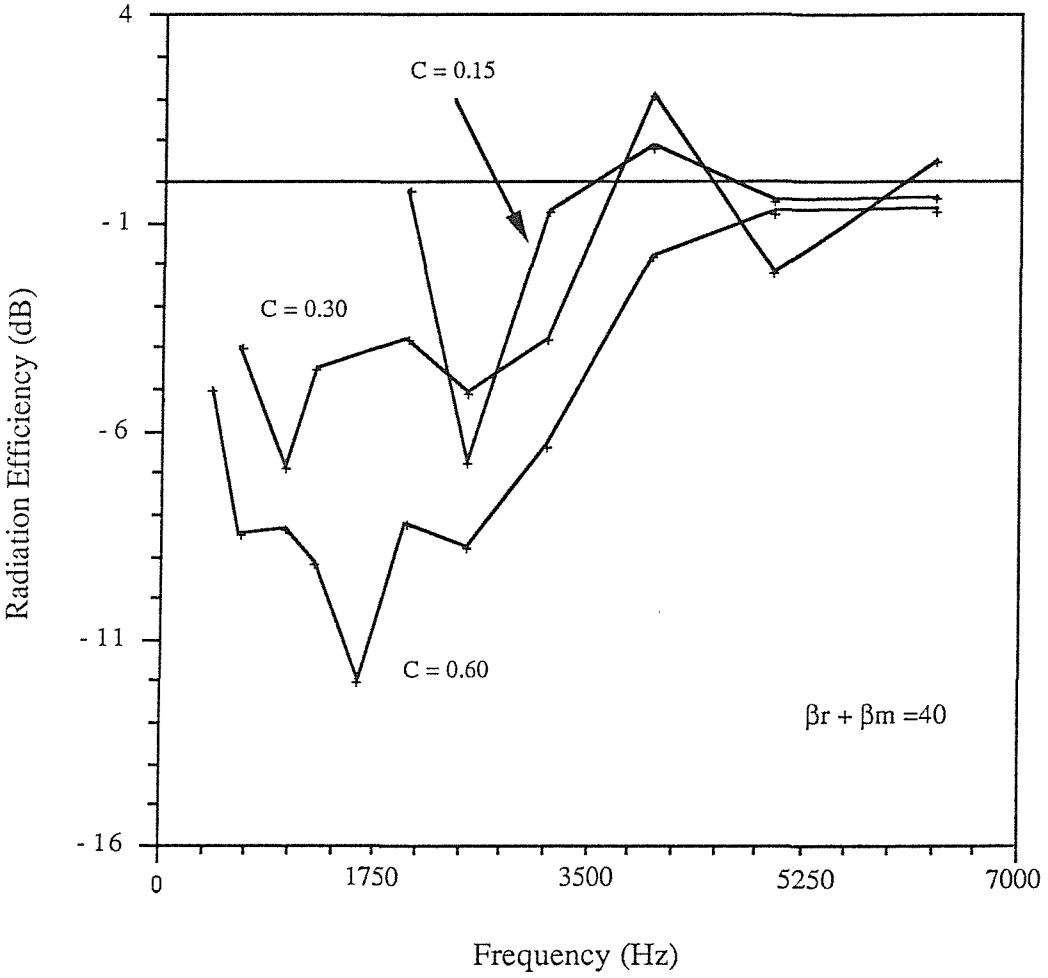

Figure (6.14) : Radiation efficiency of 3 mm panel (1/3 octave band averages)

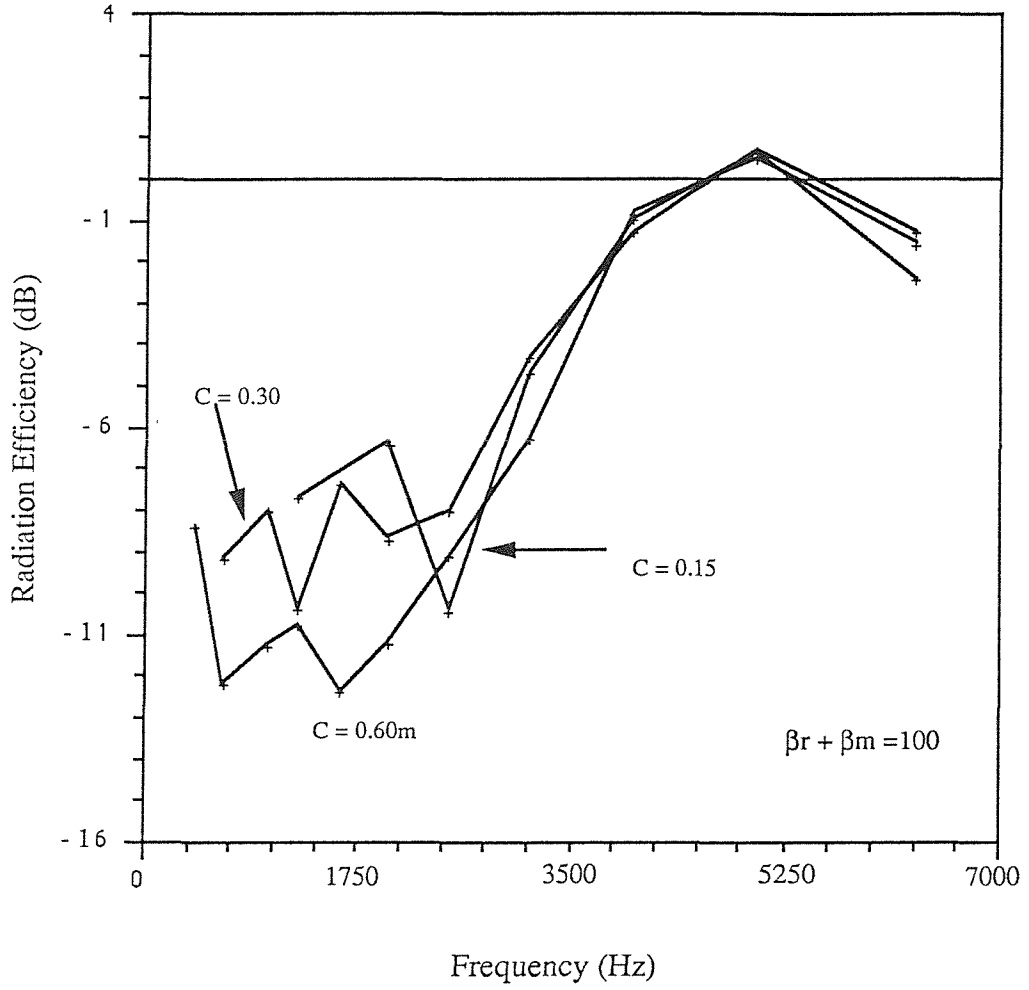

Figure (6.15) : Radiation efficiency of 3 mm panel (1/3 octave band averages)

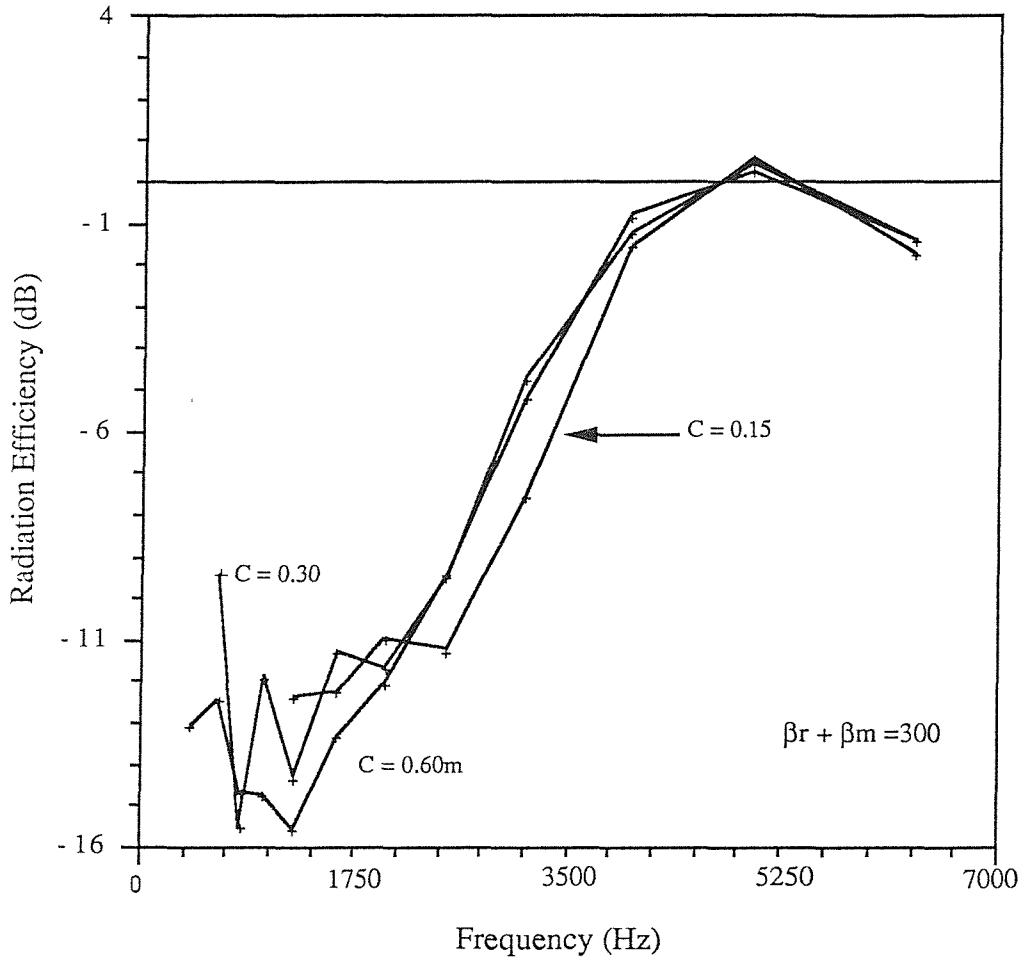

Figure (6.16) : Radiation efficiency of 3 mm panel (1/3 octave band averages)

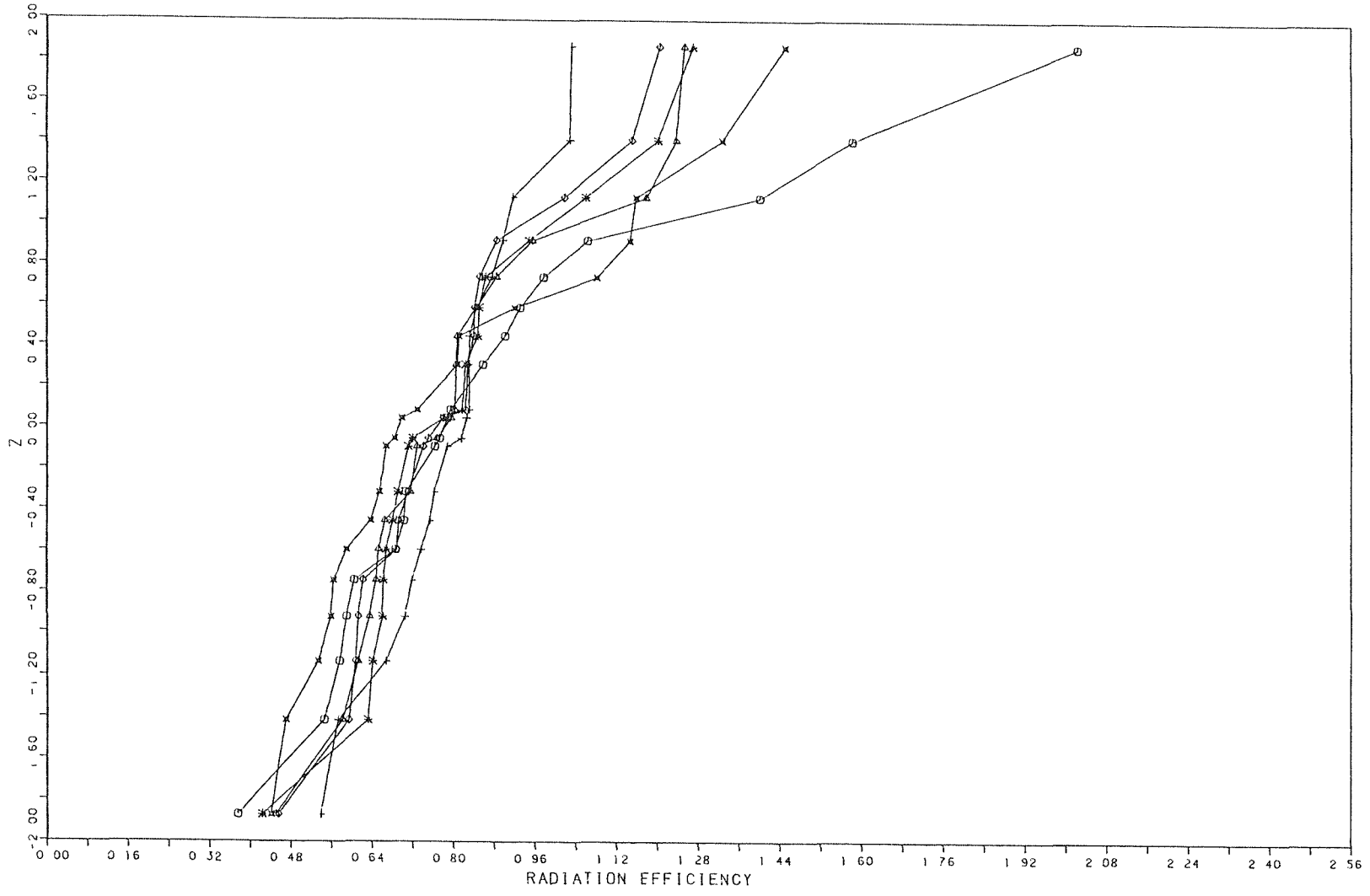

Figure (6.17): Cumulative distribution function of radiation efficiency of simply supported panel in a 1/3 octave band centred at 4000 Hz

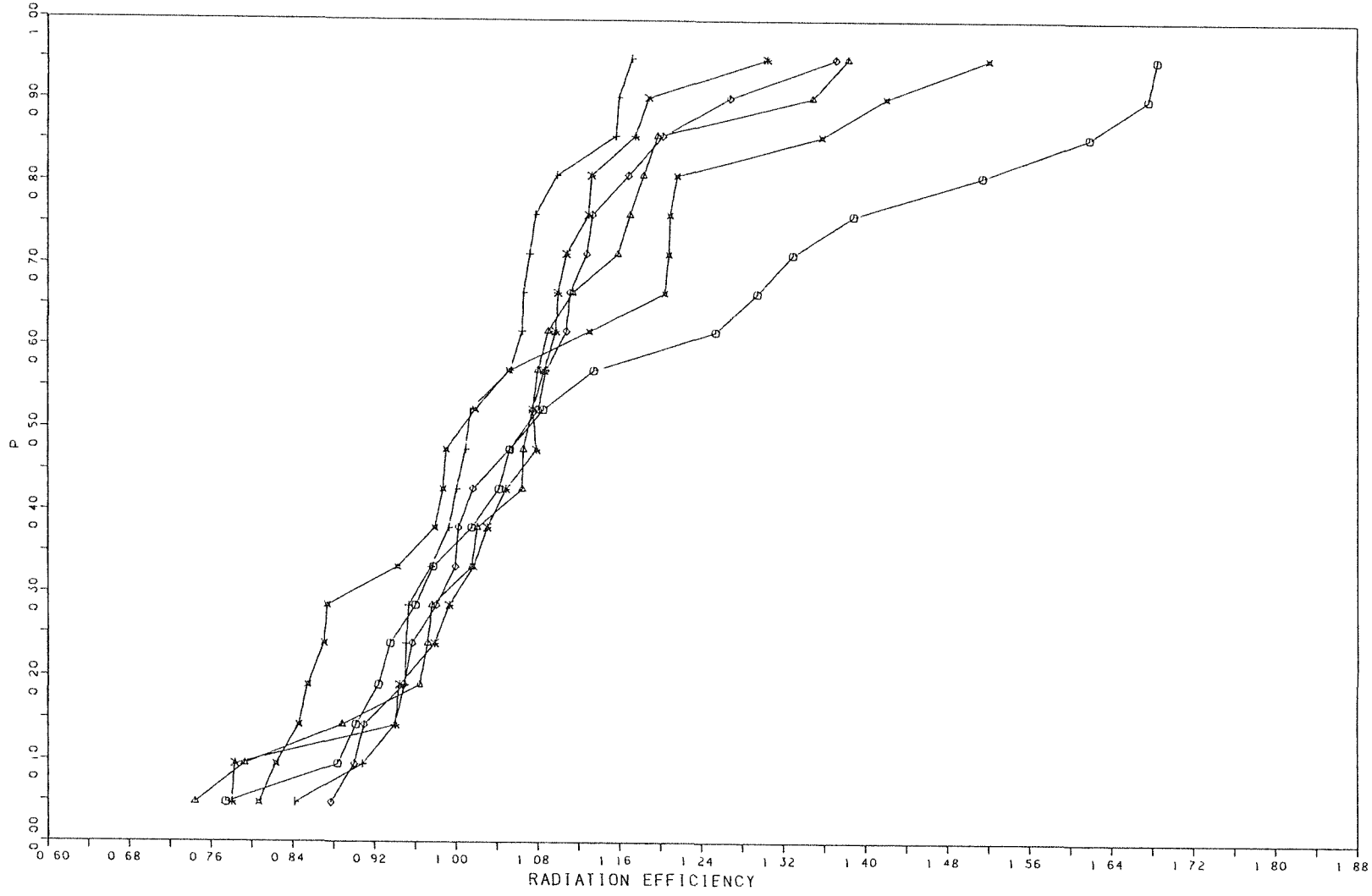

Figure (6.18): Cumulative distribution function of radiation efficiency of simply supported panel in a 1/3 octave band centred at 5000 Hz

CHAPTER 7

INVESTIGATION OF POWER FLOW BETWEEN COUPLED PLATES

7.1 Introduction

This chapter of the thesis deals with the experimental investigation of energy transfer between two coupled plates as a result of the excitation of one of them by a random force. Energy ratio was chosen as the measured quantity rather than the absolute power flow across the coupling element because of the practical difficulties associated with the measurements of the latter quantity.

The plates were thin aluminium, weakly clamped along the edges by a wooden frame. Ensembles of energy ratio were created from the measurements on a perturbed system of coupled plates. The natural frequencies and the mode shapes of the coupled plates were altered by placing a small mass on the surface of the undriven plate. The aim of this work was to investigate the sensitivity of the measurement of energy ratio of the coupled plates to small variations in the structural details of the system under test. The results were obtained in different frequency bands. Mean and normalized variance values were obtained from the measured ensembles of energy ratio. Also cumulative probability distributions were constructed for the different ensembles and studied with respect to other structural parameters. Results for the power flow and the coupling loss factor were inferred from the measurments of energy ratio of the coupled plates.

7.2 Test Rig and Instrumentations

The test rig used for the measurements of the energy ratio and the internal loss factor of the coupled system was composed of a thin, aluminium, rectangular flat plate having a thickness of 3.25 mm and a surface area of (0.865×0.556) m^2. The plate was divided, along its breadth, into two nominally identical plates by a hollow steel bar having a cross sectional area of (0.025×0.025) m^2 and a thickness of 3 mm. The steel bar was fixed

tightly to the plate by five light screws. A diagram is shown in figure (7.1). The fitted steel bar acts as a coupling element between the plates It reflects some of the incident energy and allows the rest to be transmitted across it. The coupled plates were supported along the edges by a wooden frame which acts as a weakly clamped boundary. The test rig was placed on a rigid wooden table.

The instrumentation used in the measurements is shown in table (7.1) below. The equipment was connected according to the schematic diagram shown in figure (7.2)

Item	Description	Quantity
1. Accelerometer	B&K 4375	2
2. Charge amplifier	B&K 2535	2
3. Force transducer	B&K 8200	1
4. Electrodynamic exciter	Pyeling 101	1
5. Noise generator	B&K 1405	1
6. Power amplifier	H&H 25	1
7. Spectrometer	B&K 2112	1
8. Oscilloscope	Telequipment DM64	1
9. 2-channel signal analyzer	Solartron 1200	1

Table (7.1)

7.3 Measurements

7.3.1 Internal loss factor measurements

The *in situ* internal loss factors of the plates were measured on the original plate with the steel bar detached. The power injection method [20] was employed in the measurements.

If one injects power in steady state in a certain frequency band the total power (P_{in}) is the sum of the power flows into the various modes of the band. In this case the steady state injected power may be written in terms of modal loss factors as follows [55]

$$P_{in} = \sum_{i=1}^{N} \omega_i U_i \eta_i \ , \qquad (7.1)$$

where U_i is the modal energy , η_i is the modal loss factor, and ω_i is the natural frequency of the mode "i". N is the number of resonant modes that exist in the frequency band of interest. The right-hand side of equation (7.1) suggests that one can define the band average value of internal loss factor as follows

$$\sum_{i=1}^{N} \omega_i U_i \eta_i = E\, \bar{\eta}_i \omega \ , \qquad (7.2)$$

where E is the total stored energy of the plate and $\bar{\eta}_i$ is the average modal dissipation loss factor. Use of equation (7.2) allows equation (7.1) to be written as

$$\bar{\eta}_i = \frac{P_{in}}{\omega E} \ . \qquad (7.3)$$

Equation (7.3) has been proposed by Fahy [55] as a definition for the average loss factor. Note that this expression holds only under the circumstances when the total stored energy in

the plate is equally distributed among the modes in the frequency band of interest. Equation (7.3) was used in the measurements of the *in situ* average internal loss factor of the plate.

The input power to the plate was measured using the instrumentation set-up shown in figure (7.3). The plate was driven at a point by the mini-shaker. The shaker was driven by a band of white noise via the power amplifier. The force transducer and an accelerometer were placed in axis at the driving point to acquire, simultaneously, the applied force and the resulting response at that point. These signals were fed, after the charge amplifications, to the 1200 Solartron signal analyzer. Fahy [56] has shown that a short calculation leads to a more direct method of measurement. He suggested that the injected power may be written as

$$P_{in} = -\frac{1}{2\pi}\int_{f_1}^{f_2} \frac{\mathrm{Im}(G_{fa}(f))}{f}\, df \qquad (7.4)$$

where P_{in} is the mean power input within the frequency band (f_1, f_2), $G_{fa}(f)$ is the one-sided cross spectral density of force and acceleration, f denotes the centre frequency of the band in Hz and Im( ) implies "the imaginary part of". This method by-passes the acceleration integration step and it was especially convenient in the present experiments because of the post-processing capabilities of the digital analyzer. The imaginary part of the cross spectral density was obtained and then integrated between the two specified frequencies. The results were then substituted in equation (7.4) to give the power input to the plate in the selected frequency band of interest.

The total vibrational energy (E) stored in the plate in a frequency band centred at ω is related to the space averaged mean-squared velocity over the plate $\langle V^2 \rangle$ by the equation

$$E = M \langle V^2 \rangle \ , \qquad (7.5)$$

where M is the mass of the plate. A number of twelve different locations were selected over the plate surface to acquire the acceleration levels. Mean squared velocities were then obtained after the integration of the acquired signals. The results were then averaged over

the selected positions and substituted in equation (7.5) to give the total stored energy in the plate under test.

Results for injected power and total energy were then used in equation (7.3) to obtain the average modal internal loss factor of the plate.

The measurements were carried out in three selected frequency bands of the widths 2000, 500, and 100 Hz centred at 4000, 500, and 400 Hz respectively. Typical mean squared velocity spectra are shown in figures (7.4), (7.5), and (7.6) for the above frequency bands respectively. Figures(7.7)-(7.11) show some of the typical results for transfer functions and cross spectra which have been obtained from the measurements. Reasonable values for the average internal loss factor were obtained in the above mentioned frequency bands. They were; 0.02, 0.04, and 0.05 respectively.

7.3.2 Energy ratio measurement

Using the set-up for instrumentation shown in figure (7.1), the total stored vibrational energy of the coupled plates was measured as follows. The power was injected in the coupled plates system by the mini-shaker. The shaker was attached to the system at a point located on the source plate (see figure (7.1). It was driven by a band of white noise via the power amplifier. The response (acceleration) of the coupled plates was measured at a point on each coupled plate simultaneously. The acquired acceleration levels were fed, after the charge amplifications, to the band pass filters. The filtered accelerations were then monitored on two analogue voltmeters.

The above process of measurements was carried out for twenty response positions on each plate in a given frequency band. The results were then averaged over the different selected positions.

The total energies of the coupled plates were then calculated, after the calibrations of acceleration signals, using equation (7.5). Results for energy ratio E_2/E_1 were obtained in four 1/3 octave bands centred at 400, 500, 630, and 800 Hz and two octave bands centred at 500 and 400 Hz.

7.4 Perturbation Analysis

A set of similar (not identical) systems of coupled plates was simulated, experimentally, by perturbing the natural frequencies and mode shapes of the coupled plates system under test. This was achieved by adding a small, lumped, mass of 0.202 Kg to the total mass of the coupled plates system. The set of simulated coupled systems was then generated by moving the added mass to different selected locations on the coupled plates system. Sixteen locations for the mass were selected, successively, on the surface of the receiver plate. At each given location for the mass, the procedure of measurements of $\bar{E}_2/\bar{E}_1$ was carried out as described in section (7.3) above. This means that the simulated set of coupled plates systems had sixteen elements.

The purpose of this experimental analysis was to investigate the sensitivity of the measured quantity ($\bar{E}_2/\bar{E}_1$) to small changes in the details of the dynamics of the coupled plates. The experiments were conducted at the different frequency bands (mentioned in the previous section). These frequency bands were chosen such that there were different numbers of interacting resonant modes for the vibrating coupled plates system. The aim of conducting the experiments in different frequency bands is to study the effect of the modal overlap factor and the modal count on the sensitivity of the energy exchange process of the coupled plates system.

Mean and normalized variance results were obtained from the measured ensembles of ($\bar{E}_2/\bar{E}_1$) in the different frequency bands (i.e., at different modal overlap conditions). The results are tabulated in table (7.2) below. The normalized power flow $\left[\frac{\bar{P}_{12}}{\bar{P}_{in}}\right]$ from plate 1 to plate 2 and the coupling loss factor (η_{12}) were inferred from the measured ensembles of ($\bar{E}_2/\bar{E}_1$) using the following relationships.

$$\frac{\bar{P}_{12}}{\bar{P}_{in}} = \frac{\eta_2\,\omega\,\bar{E}_2}{\eta_1\,\omega\,\bar{E}_1+\eta_2\,\omega\,\bar{E}_2} .$$

As $\eta_1 = \eta_2 = \eta$, $\frac{\bar{P}_{12}}{\bar{P}_{in}}$ can now be written as

$$\frac{\bar{P}_{12}}{\bar{P}_{in}} = \frac{(\bar{E}_2/\bar{E}_1)}{1 + (\bar{E}_2/\bar{E}_1)} . \qquad (7.6)$$

Similarly, the coupling loss factor is written as

$$\eta_{12} = \frac{\eta\ \omega \bar{E}_2}{\omega\ n_1 \left\{ (\bar{E}_1/n_1) - (\bar{E}_2/n_2) \right\}} .$$

where $n_1 = n_2 = n$, are the modal densities of the plates. η_{12} can now be written in terms of $(\bar{E}_2/\bar{E}_1)$ as

$$\eta_{12} = \frac{\eta\ (\bar{E}_2/\bar{E}_1)}{1 - (\bar{E}_2/\bar{E}_1)} . \qquad (7.7)$$

Cumulative probability distributions for $(\bar{E}_2/\bar{E}_1)$, $\frac{\bar{P}_{12}}{\bar{P}_{in}}$, and (η_{12}) are shown in figures (7.12)-(7.14) respectively, for the selected different frequency bands.

7.5 Discussion of Results

Table (7.2) displays the results of the mean and the normalized variance of the measured energy ratio $(\bar{E}_2/\bar{E}_1)$ at the different selected frequency bands. The tabulated results demonstrate the combined influences of the average modal overlap factor (M_{av}) and the analysis bandwidth on the sensitivity of the measurements. Unfortunately, because of

the small number of data acquired, we are not able to separate the effects of the above different parameters. The results show that the normalized variance of $(\bar{E}_2/\bar{E}_1)$ has the tendency to decrease as the bandwidth increases. This may be attributed to the increase in the number of contributing modes (N) of the coupled system in the selected frequency band of interest. In other words, this means that the measurement of energy ratio tends to become insensitive to the small alterations (introduced by the mass addition) of the dynamics of the coupled plates system as the number of modes increases in the frequency band of interest.

The results in table (7.2) also show that the average modal overlap factor has a similar effect on the sensitivity of the measurements as that of the number of modes. The normalized variance has the tendency to decrease as M_{av} increases. This can be clearly noted from the comparison between the results obtained at the 400 Hz 1/3 octave band and the 4000 Hz octave band.

Centre frequency (Hz)	M_{av}	Mean of $(\bar{E}_2/\bar{E}_1)$	Normalized variance of $(\bar{E}_2/\bar{E}_1)$	Number of modes (N)
400 (1/3)	0.4749	0.51191	0.047306	4
500 (1/3)	0.5936	0.41474	0.028975	6
630 (1/3)	0.7480	0.11725	5.5749E-3	7
800 (1/3)	0.7530	0.39515	0.014281	9
500 (1/1)	0.4797	0.3062524	4.47625E-3	16
4000 (1/1)	2.420	0.16238	4.47625E-3	32

Table (7.2)

These results support those obtained from the theoretical predictions of the coupled plates system (Chapter 4).

Figure (7.12) confirms the results described above. It displays the cumulative probability distributions of $(\bar{E}_2/\bar{E}_1)$ at different frequency bands. It should be noted here that because of the small size of the samples of $(\bar{E}_2/\bar{E}_1)$ (sixteen elements) the constructed distributions can only define the general trend and the central part of the data but not the extreme values. The figure shows that as the bandwidth increases, the distribution of $(\bar{E}_2/\bar{E}_1)$ approaches the normality (the shape of a straight line) at which the probability of obtaining an estimate for energy ratio which is close to the mean is high. The cumulative probability distributions of $\frac{\bar{P}_{12}}{\bar{P}_{in}}$ and η_{12}, (displayed in figures (7.13) and (7.14) respectively), show similar trends to that of $(\bar{E}_2/\bar{E}_1)$ in the different frequency bands. They also show that the normalized power flow is less sensitive to the perturbations of the dynamics of the coupled system than the coupling loss factor. The latter result supports those obtained from the theoretical calculations (described in the previous chapters).

Peculiar results for the mean, normalized variance, and cumulative probability distribution were reported in the 1/3 octave frequency band centred at 630 Hz (see table 7.2 and figures (7.12)-(7.14)). Relatively small values for the mean and normalized variance were obtained in comparison with the values obtained at the adjacent frequency bands (centered at 500 and 800 Hz) which contain an almost similar number of resonant modes. Also, the cumulative probability distribution had almost the shape of normal distribution unlike the distributions at the adjacent bands which had similar average modal overlap factor values. The reason for low mean values of energy ratio, normalized power flow, and coupling loss factor may be attributed to the relatively low response of the wooden frame, surrounding the plates, at this particular frequency band which consequently reduce the total energy transmitted between the panels. The acceleration of the wooden frame can be shown in figure (7.15). No explanation has been found for the relatively low variance value and the normal distribution of $(\bar{E}_2/\bar{E}_1)$ in this frequency band because of the lack of time needed for further tests.

7.6 Conclusions

From the results of experimental work described in this chapter, the following conclusions can be drawn.

(a) The normalized variance across the ensemble of the measured energy ratio of two coupled plates, generated from the perturbations of the dynamics of the system, has the tendency to decrease as the average modal overlap factor increases. This result supports the theoretical calculations previously obtained.

(b) The normalized variance of energy ratio has the tendency to decrease as the number of modes increases in the measurement frequency band of interest.

(c) The cumulative probability distribution of the measured ($\bar{E}_2/\bar{E}_1$) approaches the normality as the frequency bandwidth increases. This conclusion supports the theoretical results obtained previously.

(d) Surprisingly, small variance values and approximately normal distributions were observed for the energy ratio, the normalized power flow and the coupling loss factor in the 1/3 octave frequency band centred at 630 Hz, compared with the results obtained in the adjacent frequency bands which contain an almost similar number of modes and at which the coupled system enjoys similar condition of modal overlap. Therefore, further tests need to be done to investigate the vibration of the particular system in this particular frequency band.

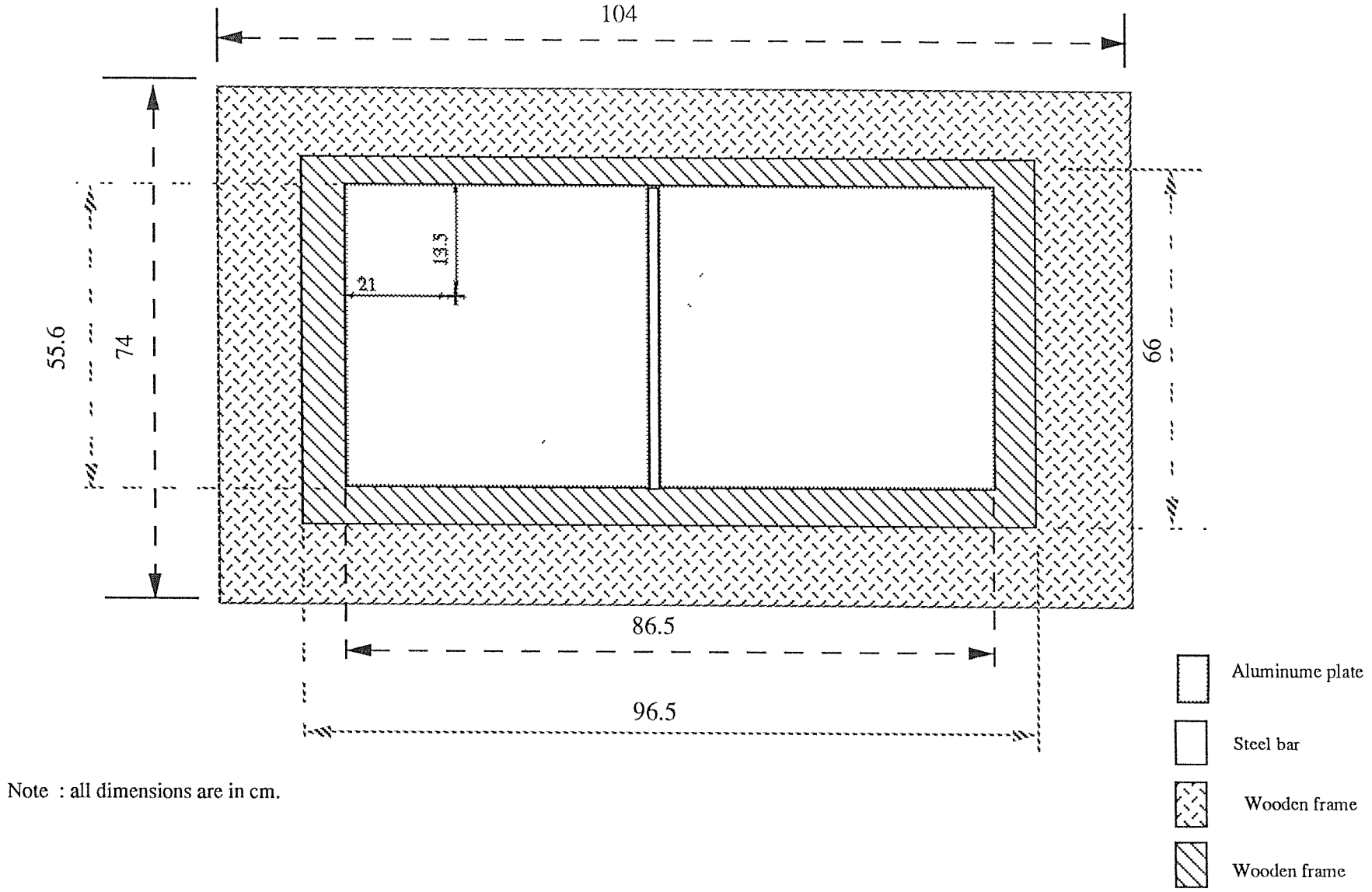

Note : all dimensions are in cm.

Fig (7.1): Test rig

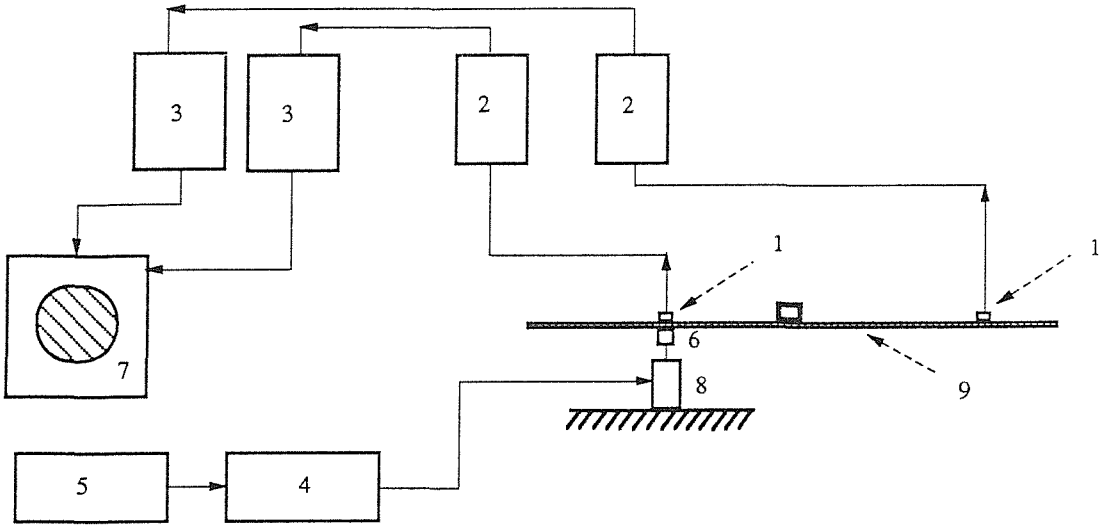

1-Accelerometer
2-Charge amplifier
3-Spectrometer
4-Power amplifier
5-Signal generator
6-Force transducer
7-Signal analyzer
8-Electrodynamic exciter
9-Test rig

Figure (7.2)

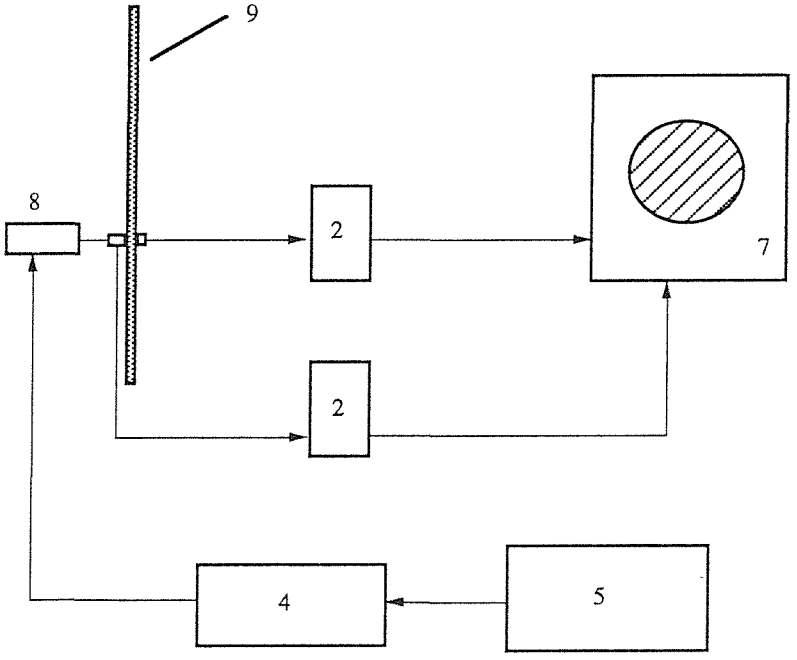

Figure (7.3)

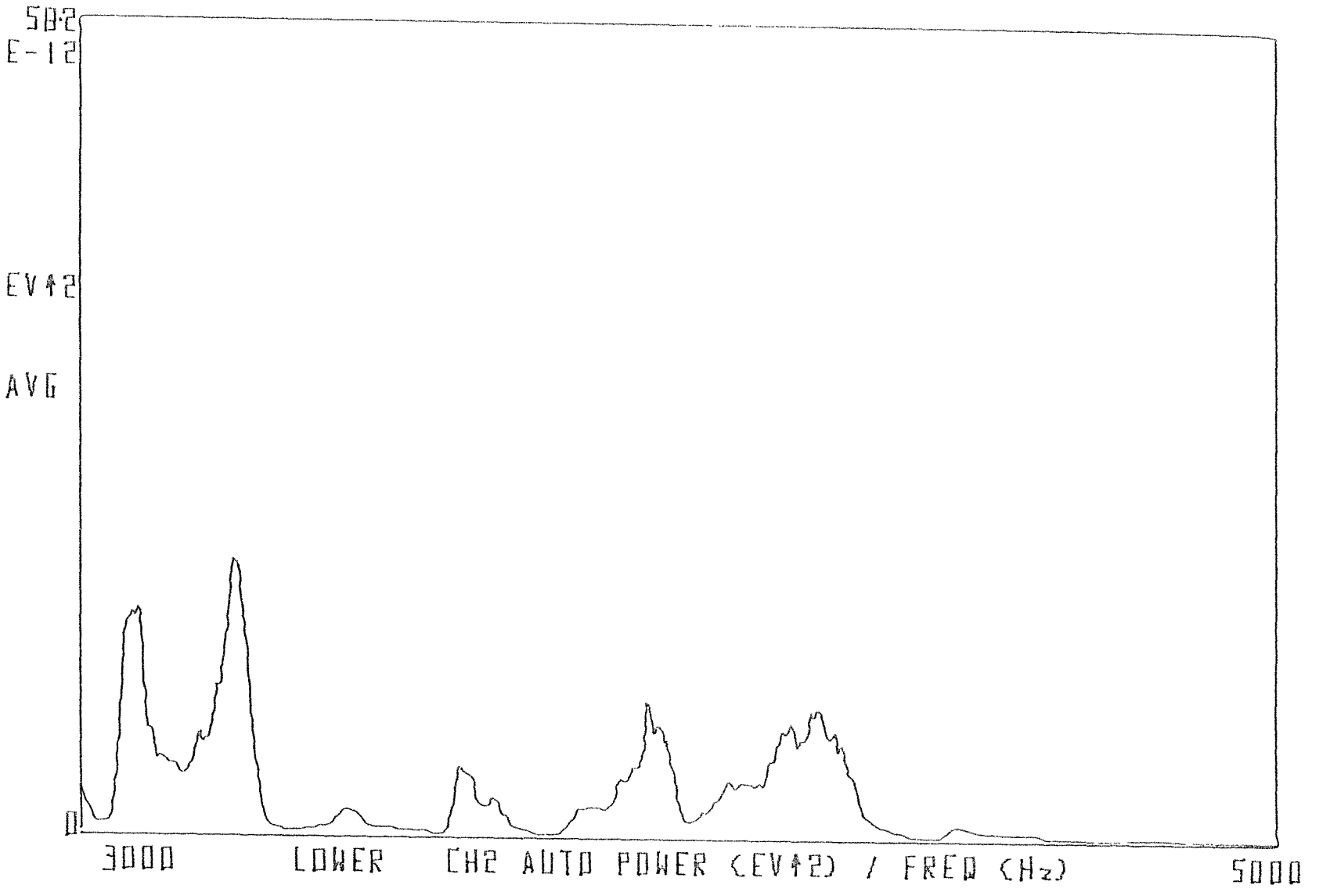

Figure (7.4): Auto power spectrum of the plate velocity in the frequency range 3000-5000 Hz.

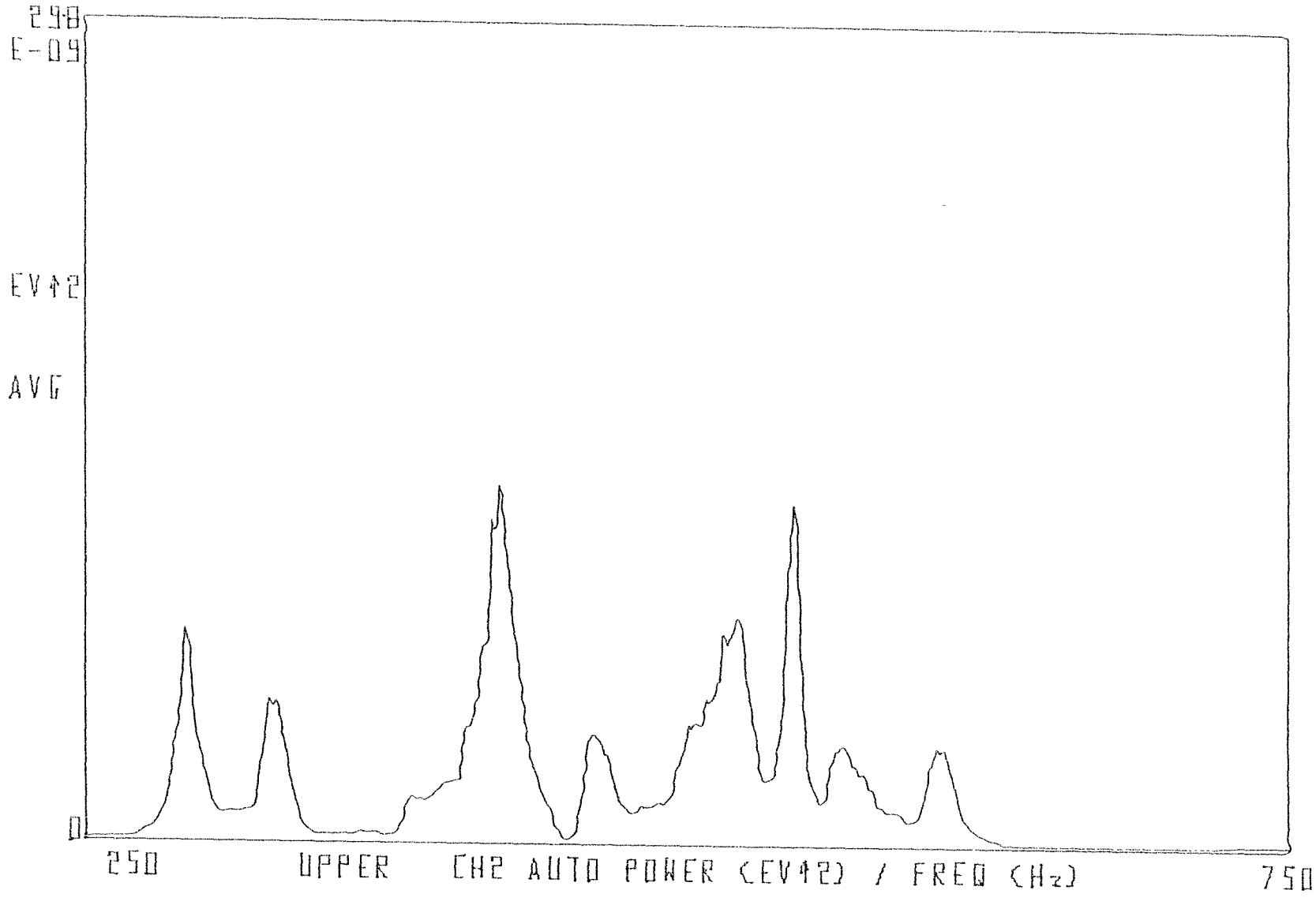

Figure (7.5): Auto power spectrum of the plate velocity in the frequency range 250-750 Hz.

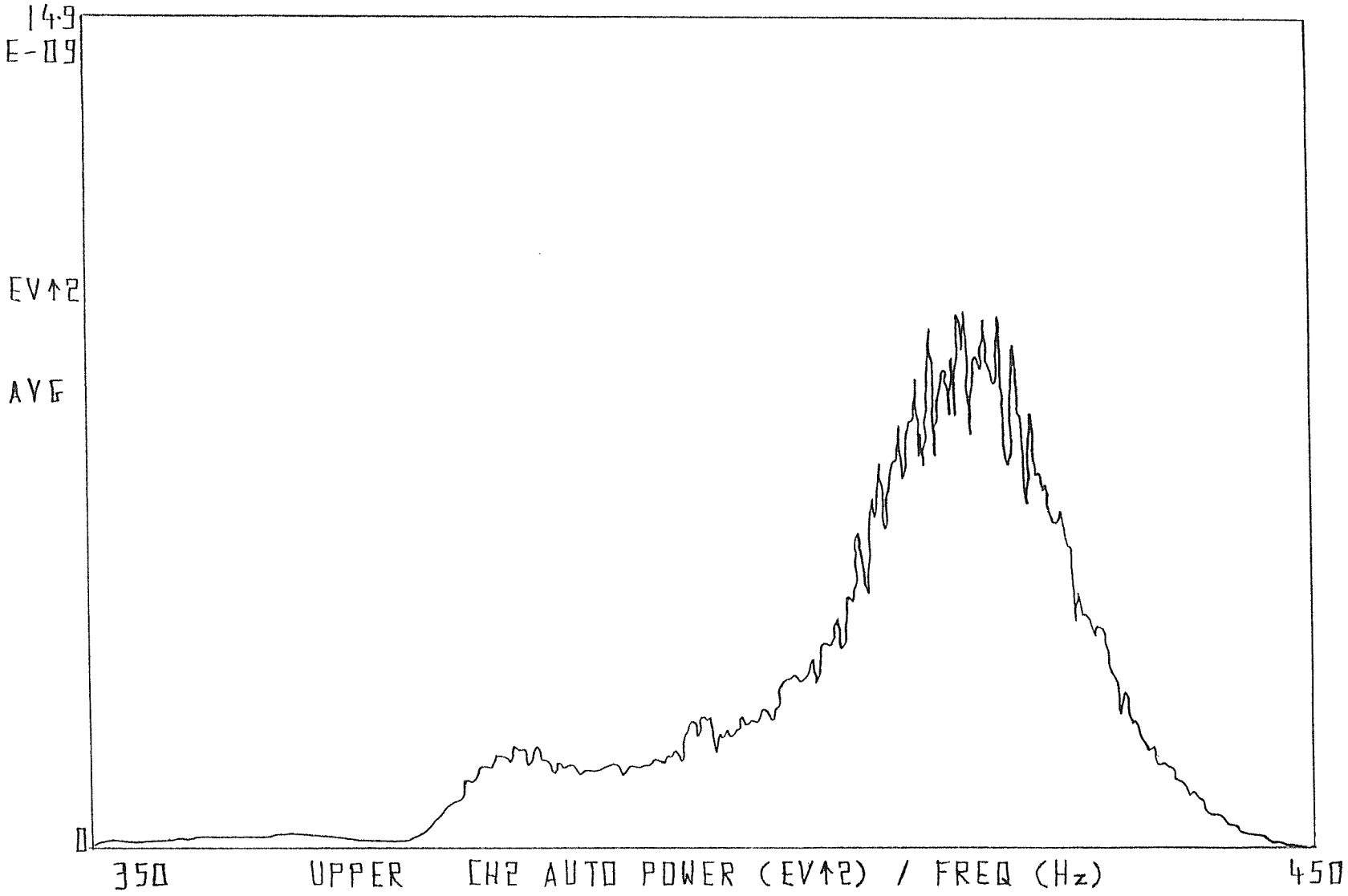

Figure (7.6): Auto power spectrum of the plate velocity in the frequency range 350-450 Hz.

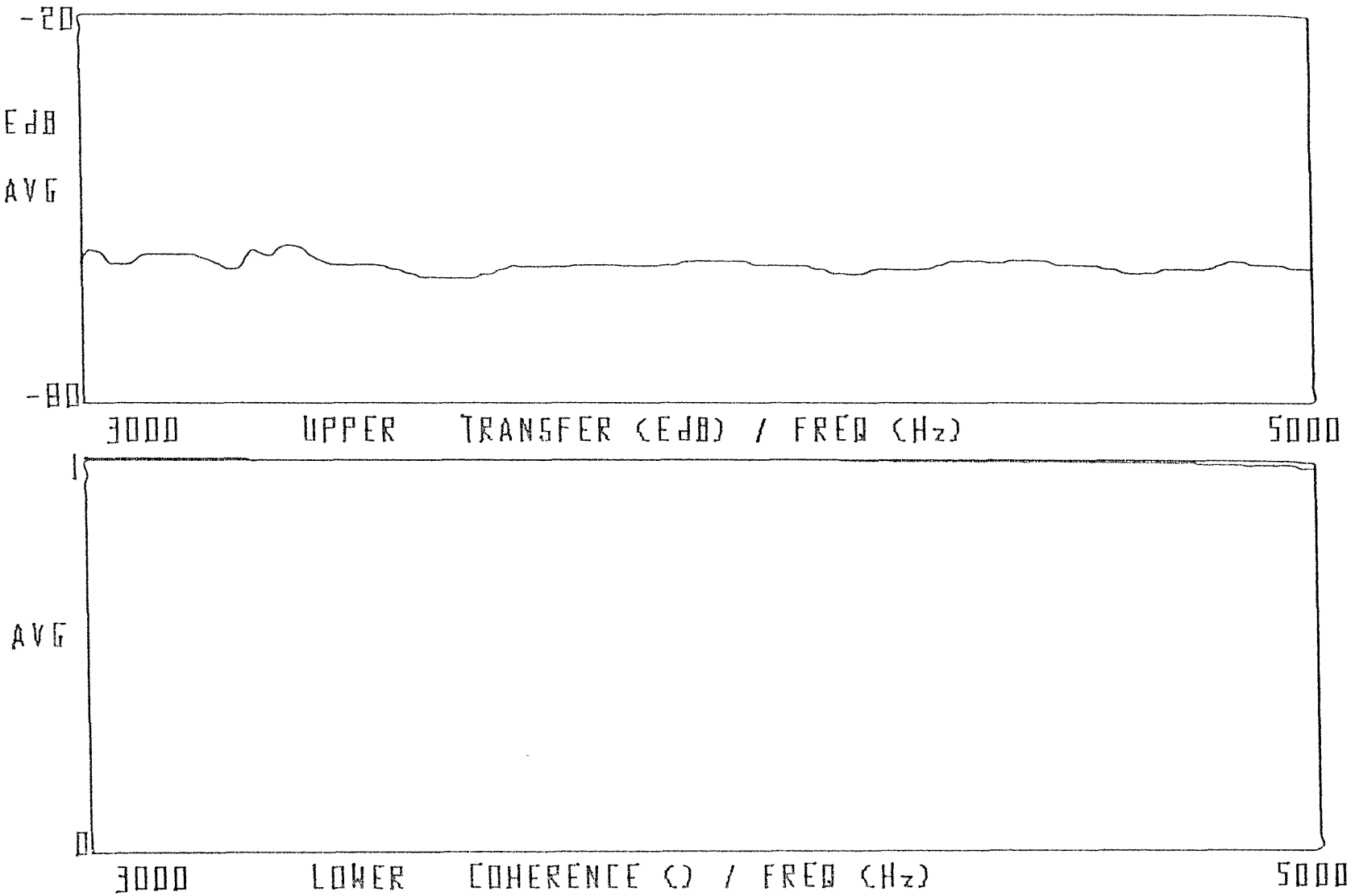

Figure (7.7): The transfer function and the coherence function between the force signal and the velocity signal at the driving point of the plate in the frequency range 3000-5000 Hz.

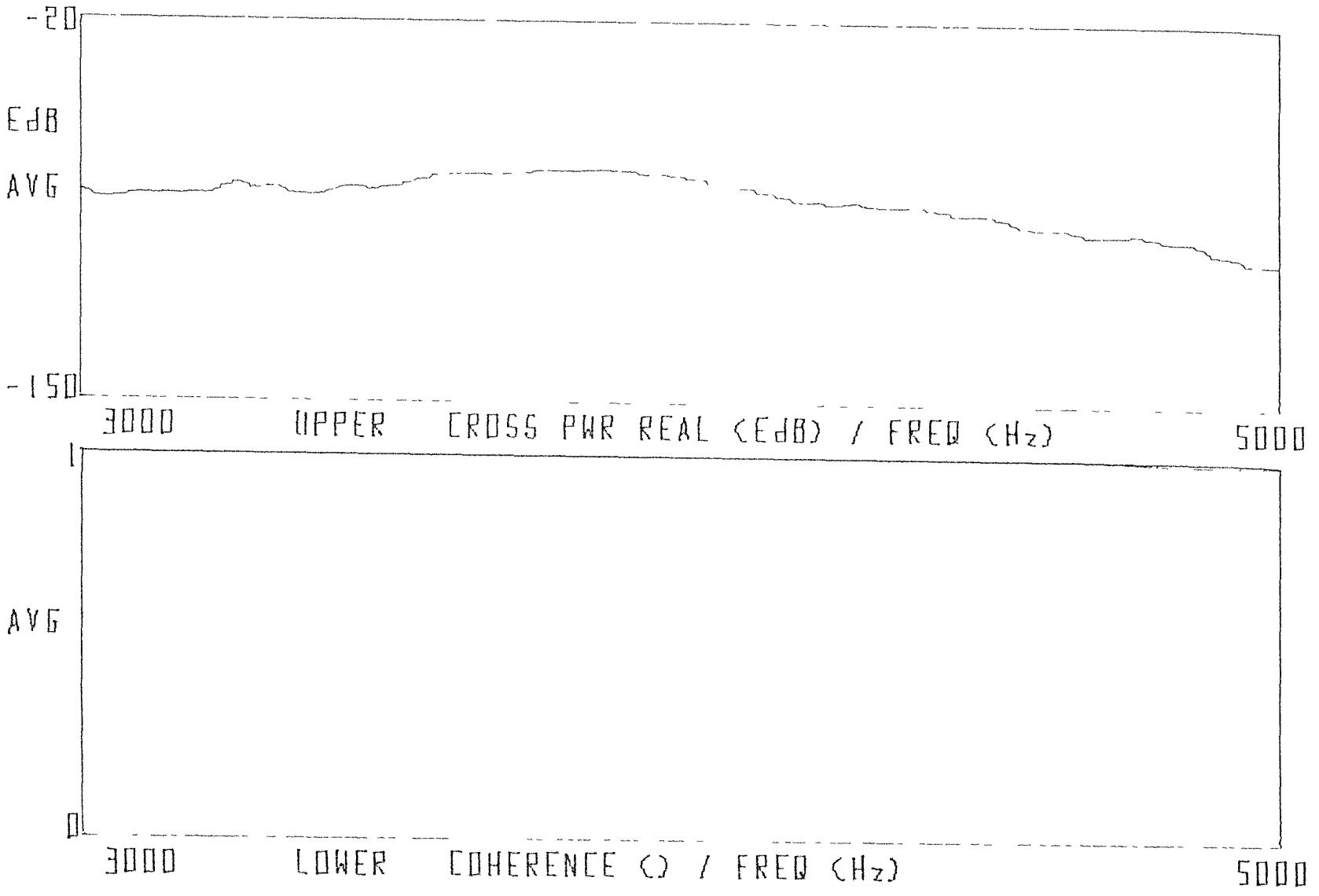

Figure (7.8): The real part of cross power spectra and the coherence function between the force signal and the velocity signal at the driving point of a plate.

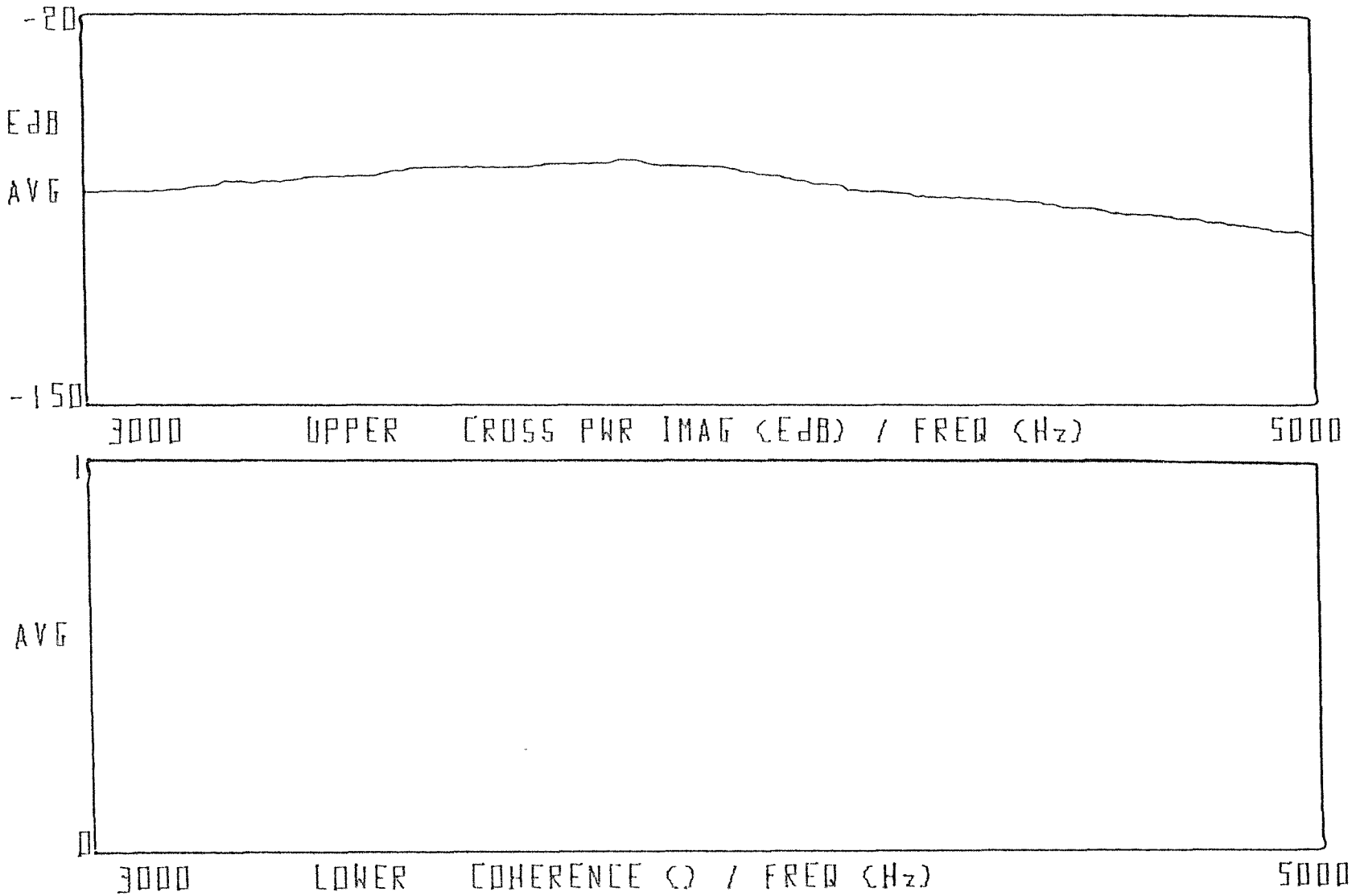

Figure (7.9): The imaginary part of cross power spectra and the coherence function between force and velocity at the driving point of a plate.

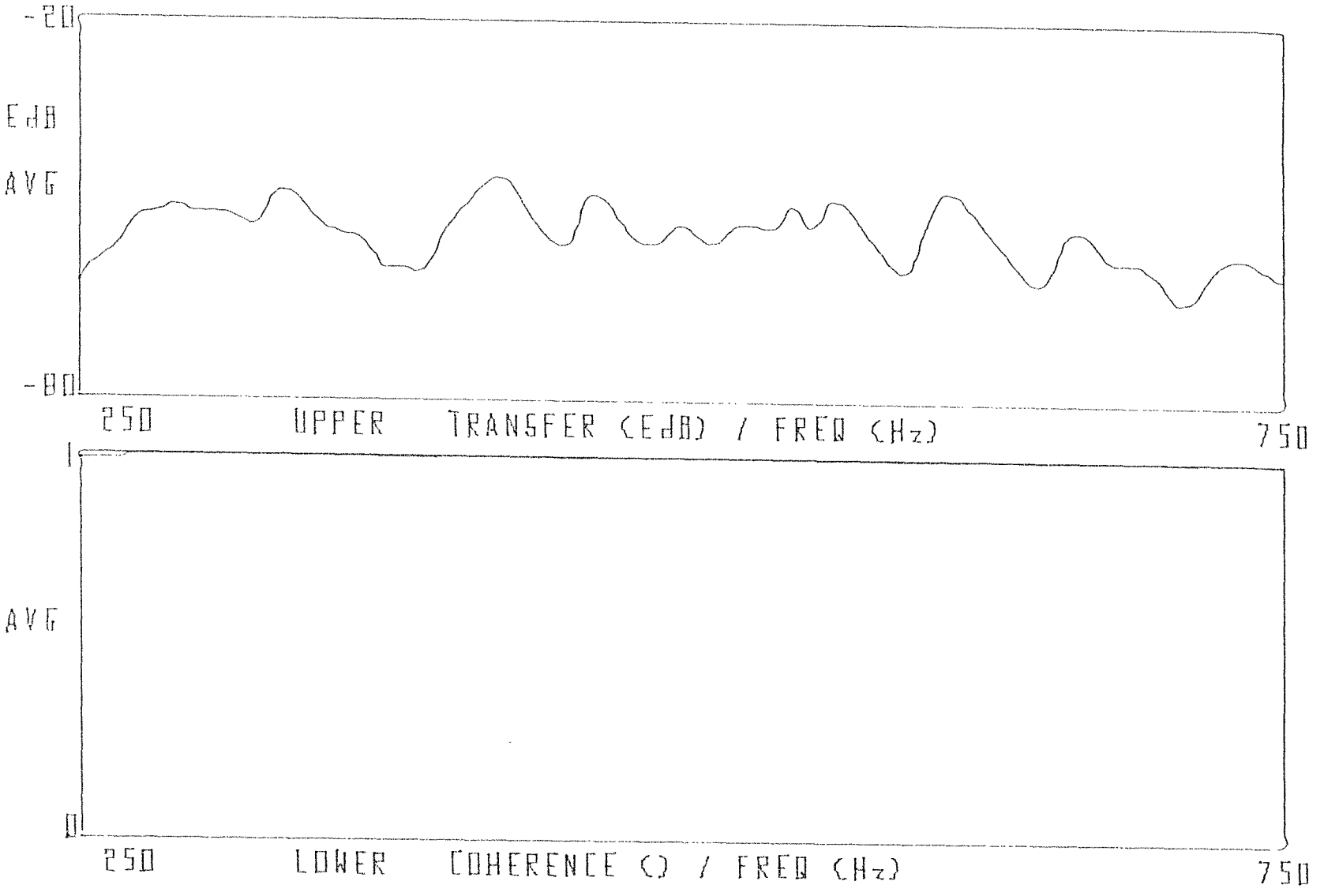

Figure (7.10): **The transfer function and the coherence function between the force signal and the velocity signal at the driving point of the plate in the frequency range 250-750 Hz.**

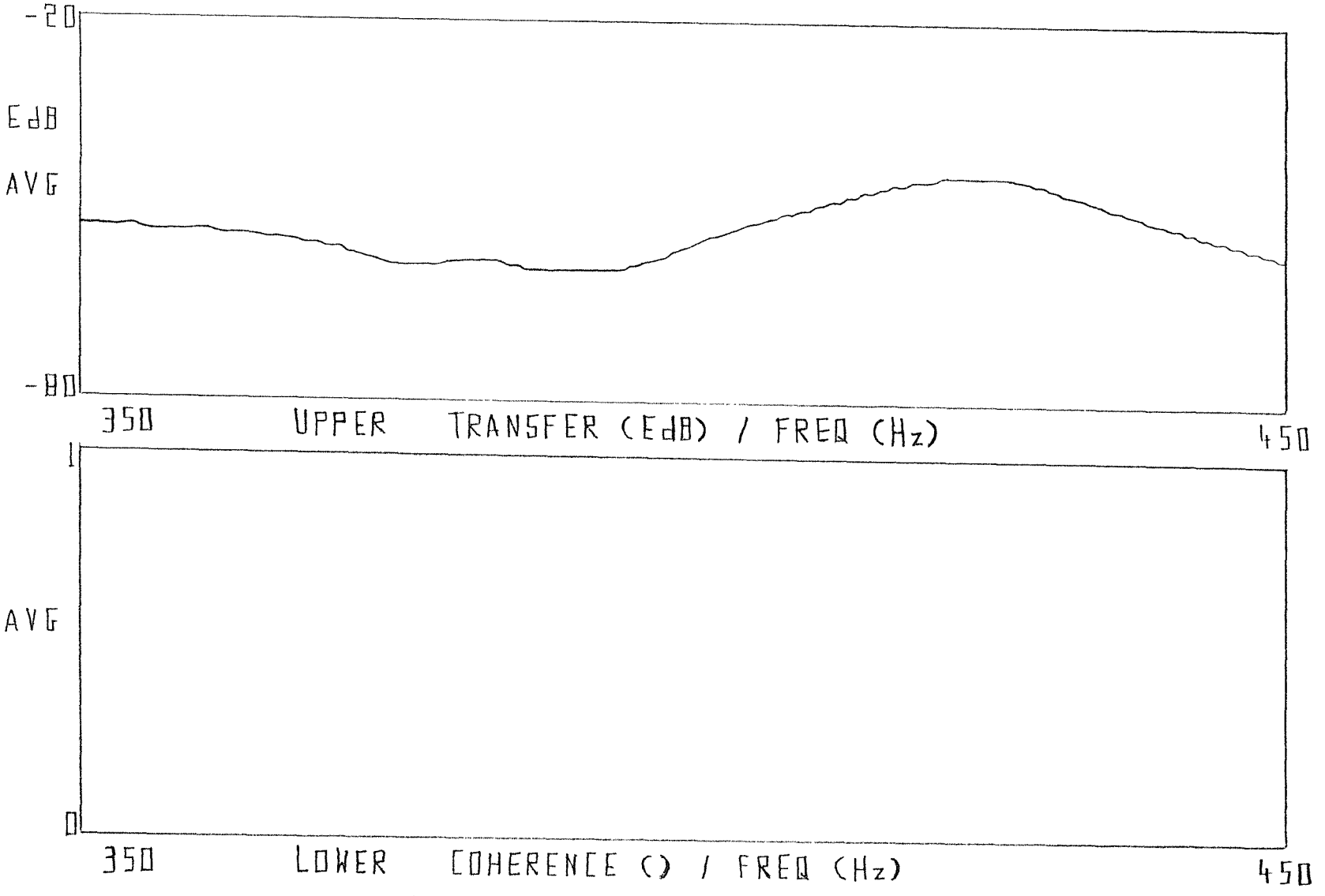

Figure (7.11): The transfer function and the coherence function between the force signal and the velocity signal at the driving point of the plate in the frequency range 350-450 Hz.

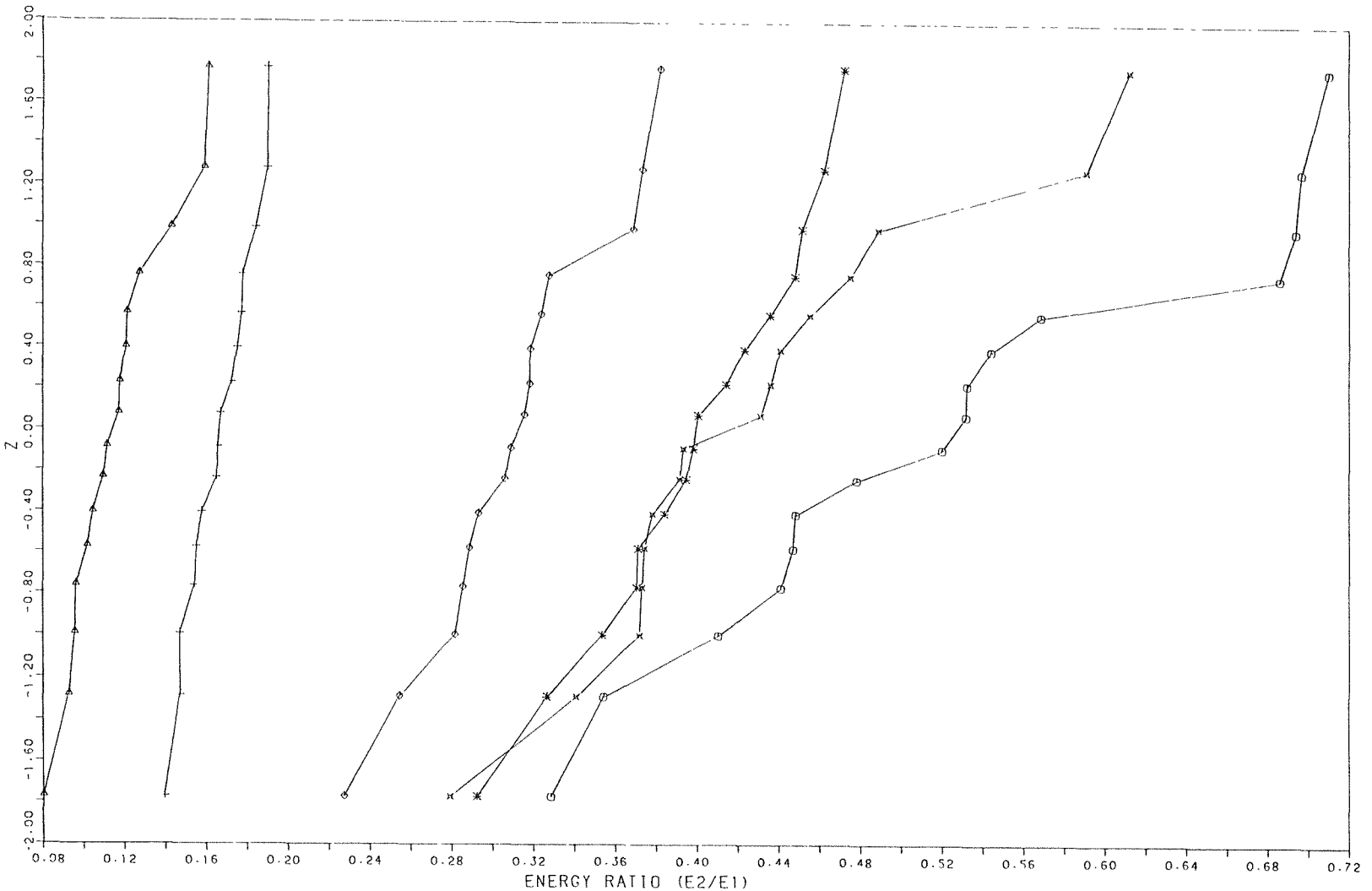

Figure (7.12): Cumulative distribution function of the experimentally determined energy ratio of two coupled plates.

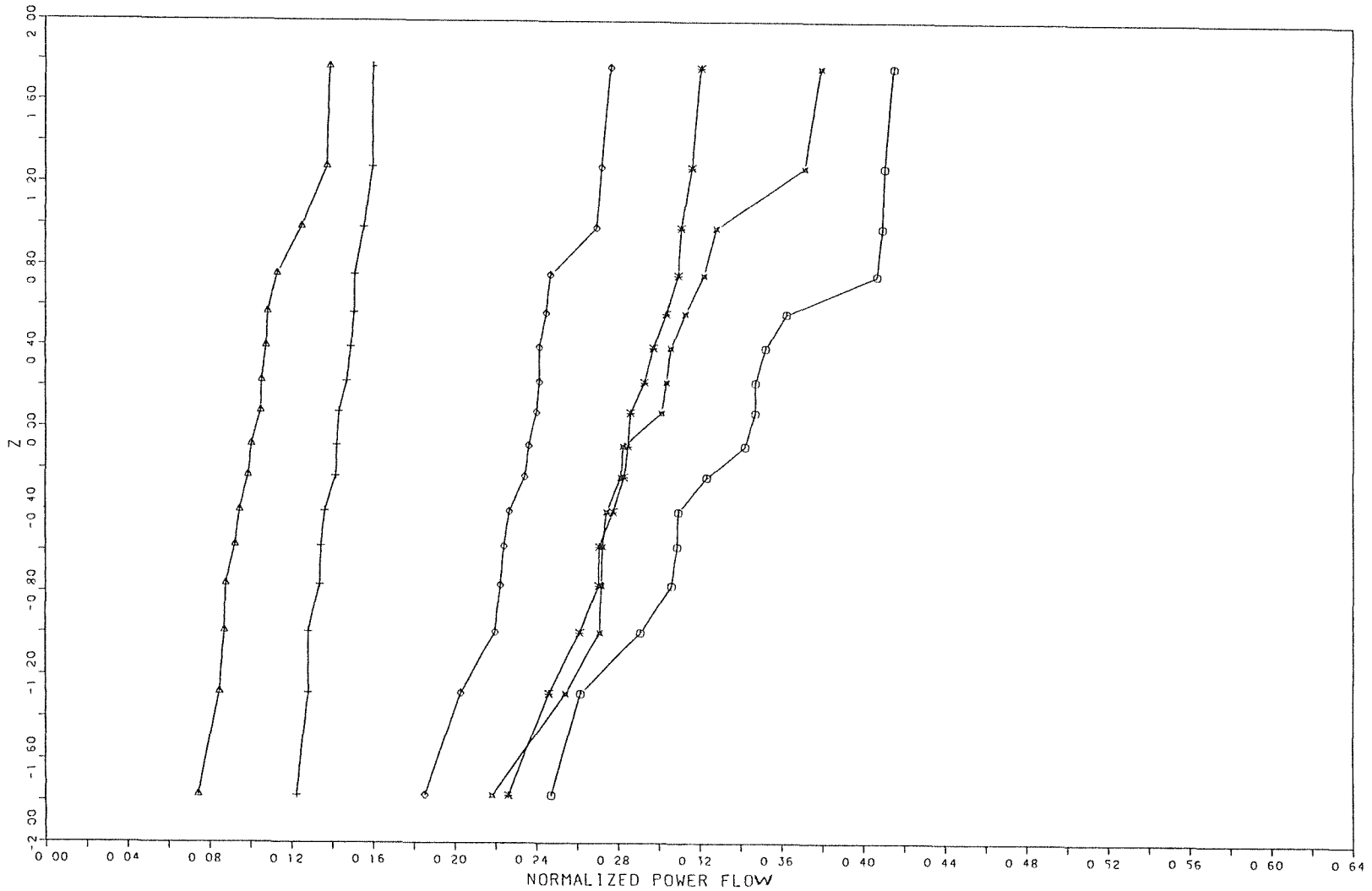

Figure (7.13): Cumulative distribution function of the normalized power flow between two coupled plates.

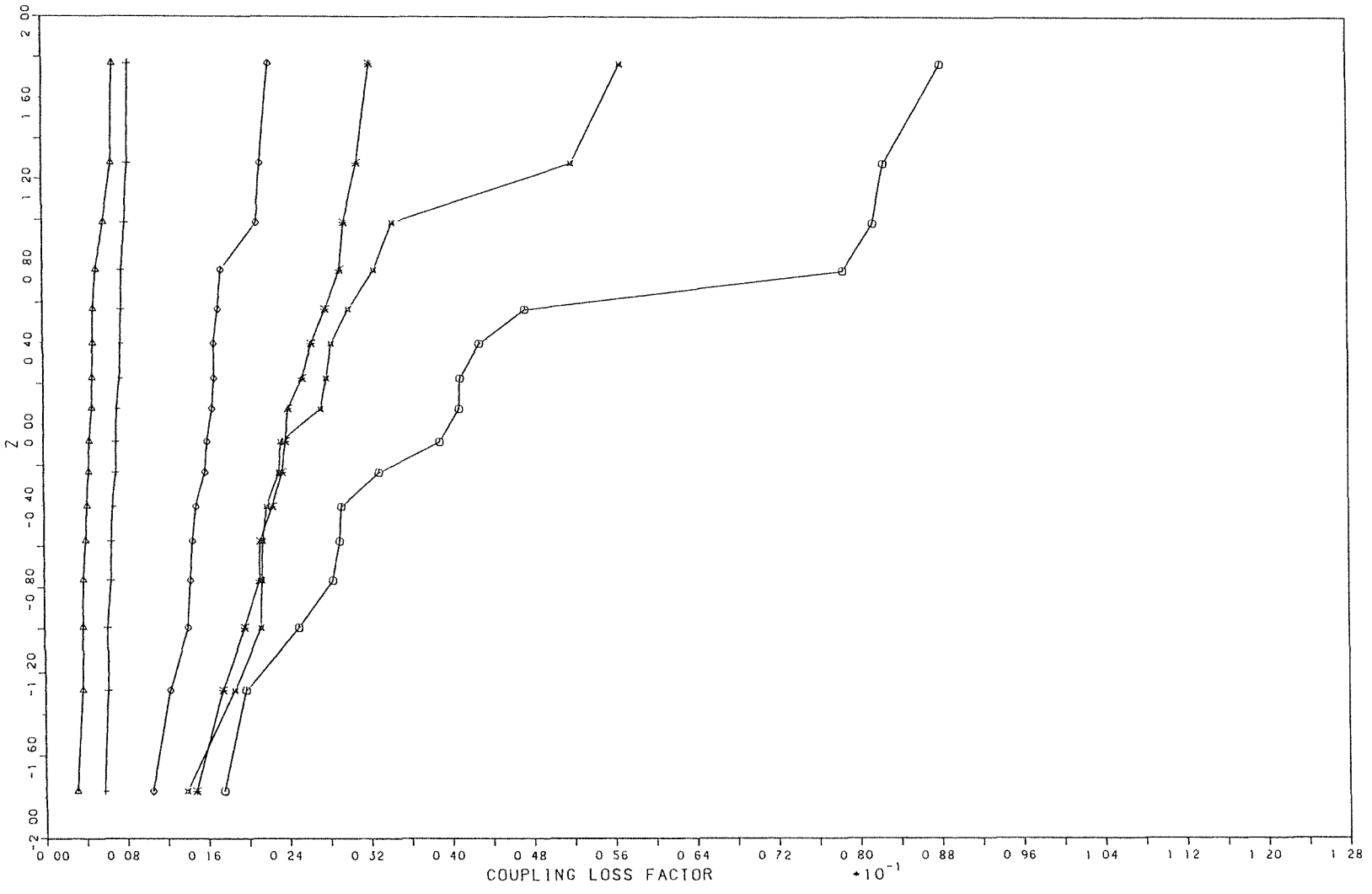

Figure (7.14): Cumulative distribution function of the coupling loss factor of two coupled plates system.

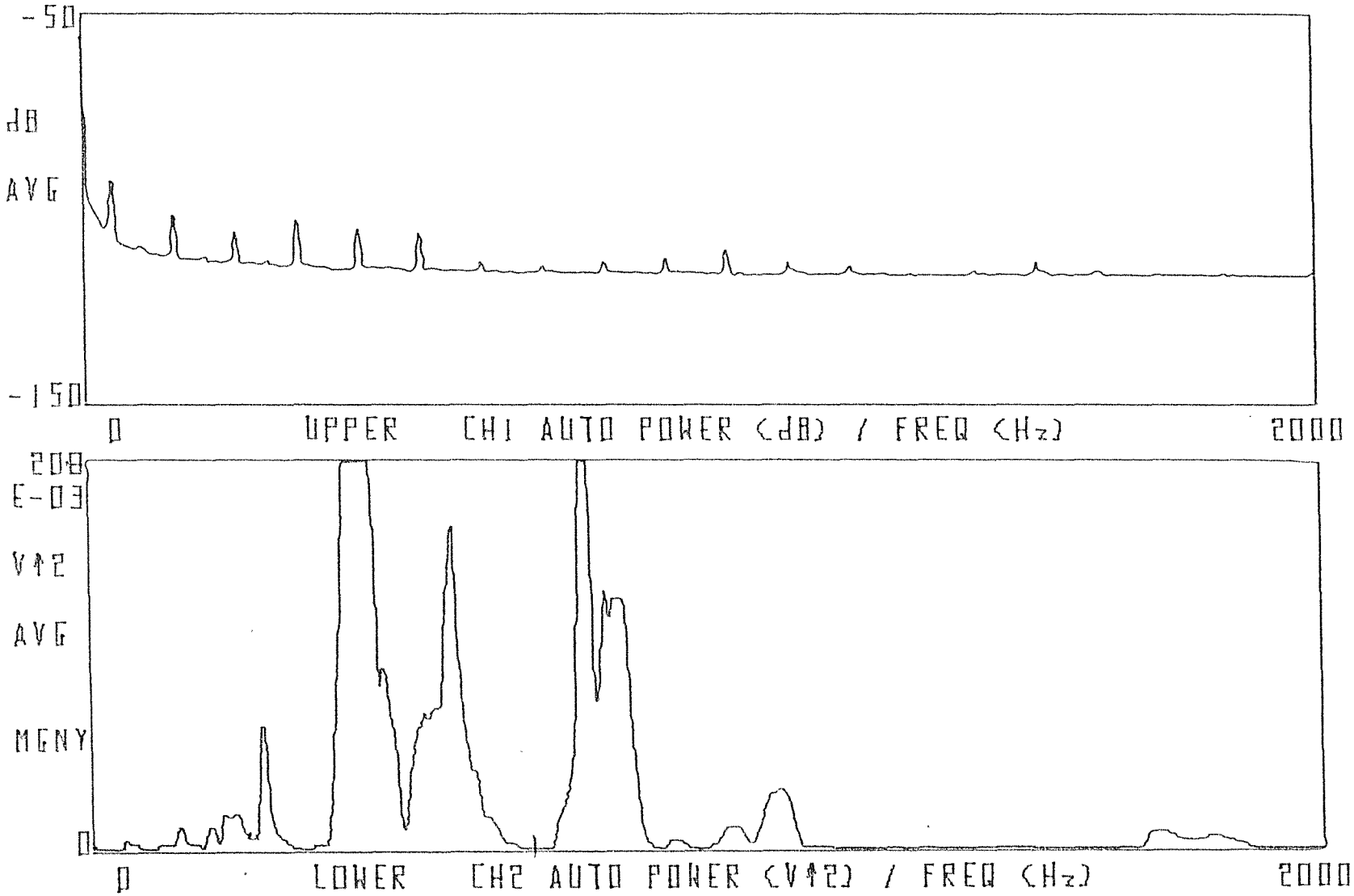

Figure (7.15): Auto power spectra of two acceleration signals in the frequency range 0-2000 Hz. Top : input signal, bottom: output acquired on the supporting,wooden frame, sorrounding the coupled plates.

CHAPTER 8

CONCLUSIONS

The problem that we set out to solve was that of investigating the uncertainty of the prediction associated with the use of Statistical Energy Analysis. We sought an approach that would be easy to apply for most of the coupled vibrating elements. This approach is based on using the exact response estimates of coupled systems to derive SEA parameters (power flows and coupling loss factors) and to investigate the sensitivity of prediction of these parameters to geometric perturbations of the coupled systems by employing the Monte Carlo technique.

SEA type estimates for the time-average quantities of interest were obtained as averages across ensembles of similar, but not identical, systems. The latter were generated from the perturbations of one of the (input) random parameters of the coupled systems. Results were then compared with those obtained from the travelling wave method.

In Chapter 2 of the thesis we presented the study of power flow between two, multi-mode coupled beams. Perturbation analysis was carried out using one of the geometric parameters (length ratio) of the coupled system as an input random variable. From this analysis we concluded that the travelling wave method overestimates the mean value of coupling loss factor under the condition of low average modal overlap factor (M_{av}) of the coupled beams system. In addition, it was concluded that the estimate of coupling loss factor approaches, asymptotically, that of the travelling wave method at high modal overlap ($M_{av} \geq 1$).

The mean power flow between the coupled beams decreases as the average modal overlap factor increases. The reason for this was that the latter factor was increased by increasing the internal loss factors of both beams. This led to an increase in the absorbed energy of the directly driven beam which consequently reduces the amount of energy transfered to the receiver beam. An attempt to increase the modal overlap factor by increasing the modal densities of the beams was made difficult because of computation difficulties (overflow problems).

The calculations of the variance for the coupling loss factor and the normalized power flow, across the ensemble of coupled beams systems, has shown that the probability of obtaining an estimate for any of those quantities which is close to its mean value increases as the modal overlap factor increases: the normalized variance (variance/ (mean)^2) decreases as M_{av} increases. This conclusion was explained by the reason that the frequency response of the coupled beams system is dominated by well separated resonant peaks at the low modal overlap condition which are highly sensitive to the introduced perturbations in structural details. This leads to significant changes in the response of the system. The small changes have little effect on the smoothed frequency response function at higher modal overlap.

From the comparison between the variance of the coupling loss factor and the variance of the normalized power flow at different modal overlap factor values, it was concluded that although the coupling loss factor is a widely used quantity in SEA calculations, it is highly sensitive to changes in system parameters compared with the power flow. The reason for this is that the coupling loss factor contains two other elements (modal energies of the coupled subsystems) beside the power flow. These elements vary almost independently and their sensitivities highly affect the variance of the coupling loss factor. This high sensitivity of coupling loss factor is unimportant when carrying out theoretical predictions, because the vibrational energies of the subsystems are the main concern which are determined by the actual power flows. But it has serious implications in experimental investigations when using SEA hypothesis to deduce the coupling loss factors from only one or two sets of data. On the face of the results of the present work, the experiments could produce very high value or very low value for the coupling loss factor at low modal overlap, which means that the reliability of the produced estimates could be very low.

The reliability of the computed mean values of coupling loss factor and the normalized power flow was examined by calculating the 95 per cent confidence intervals, assuming normal distributions for the calculated means (irrespective of the apparent distributions of the computed samples). That was justified by the considerations of the central limit theorem. It was concluded that the 95 per cent confidence intervals for the frequency averaged values of the above quantities are wider at low modal overlap than those at higher modal overlap because of the typical, general behaviour of the variance with modal overlap.

From the constructions of the cumulative probability distributions of the computed samples of coupling loss factor and the normalized power flow, a conclusion

was drawn that as the average modal overlap factor increases and takes the value of unity and greater, the distributions approach that of the normal distribution. The latter distribution has been assumed for the sample of the input perturbed variable. At low modal overlap the distributions were found not normal and therefore, the confidence intervals for the coupling loss factor and the normalized power flow are not predictable for any particular set of data.

Sensitivity analysis on the effect of small changes (random perturbations) in the properties of the coupling mechanism (stiffness) showed that these changes have little effect on the predicted mean values of the normalized power flow between the coupled beams in all modal overlap conditions.

The other case analysed in Chapter 2, which has a special importance in practice, was the coupling between a large system of high modal density (long beam) and a small system of low modal density (short beam). The important conclusion drawn from this case was that the modal overlap factor of the long beam dominates the analysis and has the same effect on the mean and the variance of the coupling loss factor and the normalized power flow as that of the average modal overlap factor of the long-long beams model. Therefore it was concluded that only one beam needs to have high modal overlap when using SEA to analyse a system of two coupled beams.

The results obtained from the experimental investigations on two, multi-mode coupled beams, which are presented in Chapter 3, support qualitatively those obtained from the theoretical calculations and similar conclusions were drawn. The experimental investigation on two coupled resonant modes showed that the SEA relationship is invalid for coupled systems under harmonic excitation. This conclusion was obtained from the comparison between the total vibrational energies of two coupled short beams.

From the analysis of two-dimensional models of coupled plates presented in Chapter 4, similar conclusions to the above were drawn concerning the means, the variances and the cumulative probability distributions of the coupling loss factor and the normalized power flow. It was shown that the position of the applied force has a considerable effects on the computed means and normalized variances of the power flow and the coupling loss factor of the two coupled plates system. Points of excitation which are located near the coupled edges of the plates produce relatively large values for the mean and the variance. This was attributed to the effect of the nearfield waves near the junction. These waves contribute to the amount of energy transmitted across the coupling line. Therefore these points of excitation have not been considered

because they produce biased results which affect the reliability of the averages. From the comparison between results obtained from single point excitation and others obtained from averaging over many points, it was concluded that averaging over many points adequately simulates the statistical independence for the purpose of SEA.

The investigation of the effect of the modal count of the coupled plates system on the sensitivity of predictions has shown that as the number of resonant modes in the analysis band increases at a given value of average modal overlap factor ($M_{av} \geq 1$), the computed mean value of coupling loss factor approaches, asymptotically, the diffuse field estimate and the variance takes relatively small values. An empirical relationship was demonstrated,relating the variance of the coupling loss factor to the number of modes, and the average modal overlap factor of the coupled plates system. This relationship may be constructed for other coupled systems, following a similar approach, and can be used to assess the uncertainty of the prediction of the quantity of interest.

Pure tone analysis on two coupled plates indicated that unacceptably high uncertainty should be expected if broadband predictions are applied to systems under pure tone excitation. This was demonstrated by the comparison between the variance values of power flow due to pure tone excitation and due to a band of white noise excitation.

The analysis of three coupled plates showed almost similar behaviour, for the means and the variances of coupling loss factor and the normalized power flow, to those of the two coupled plates model. The conclusion drawn from this case was that, approximately identical coupling loss factors between any two coupled plates can be obtained although plate 1 is driven directly while plates 2 and 3 received indirect excitations.

The analysis of power flow between two coupled rods is presented in Chapter 5. As concluded above, the coupling loss factor is a highly sensitive quantity to variations in system parameters compared with the power flow which has clearer physical significance in practice. Therefore the purpose of this analysis was to study in detail the power flow equation and to investigate the effects of subsystems parameters on the process of energy exchange. Two different coupled rods systems were examined. The general conclusions drawn from the results of coupling loss factor and the normalized power flow between two, coupled long rods support those obtained from the previous cases (coupled beams and coupled plates systems). It has been

shown that the maximum power flow between two coupled rods occurs at the natural frequencies of the coupled system. In addition, numerical results have shown that the peaks in the power flow spectrum can be obtained, generally, under the condition when the sum of the reactive parts of the impedances of the uncoupled rods vanishes. This condition has high probability of occurrence but it is not guaranteed for all peaks of power flow in the frequency band of interest.

The analysis of short-long rods system has shown that, for a fixed length value for the short (directly driven) rod, the integral of normalized power flow increases as the modal overlap factor of the long (receiver) rod increases. The normalized power flow exhibits a fixed value which is frequency independent when the modal overlap of the long rod takes the value of unity and greater.

The parametric study of the power flow equation has shown that the real part of the impedance of the indirectly driven rod is a dominant parameter in controlling the power flow between the rods in all modal overlap conditions. The numerical results of this parameter explain the asymptotic fixed value of the power flow at high modal overlap of the long rod and also explain the fall of the estimate of the power flow below that of the infinite system at low modal overlap.

Based upon the well understood behaviour of normalized power flow between the coupled rods and using the SEA relationship, an explanation for the behaviour of the coupling loss factor in different modal overlap conditions was obtained.

The study of the sensitivity of the panel radiation efficiency of an acoustically excited panel-box system was carried out using the same approach applied for the previous cases of coupled beams and coupled plates systems. The random variable used for the perturbation analysis was the thickness of the simply supported panel. It was concluded that the sum of the half-power bandwidths of the panel and the acoustic modes has a great effect on the sensitivity of the prediction of the radiation efficiency to the introduced perturbations. The variance of the radiation efficiency has the tendency to decrease as the above sum increases. For a given 1/3 octave frequency bandwidth, this was considered as a pure effect for the average modal overlap factor of the coupled system. It was also shown that the variance of the radiation efficiency is highly sensitive to the frequency bandwidth of the analysis. It decreases as the centre frequency of the band increases. That was attributed to the increase in the number of acousto-structural mode pairs in the frequency band of interest.

The sensitivity of the computed radiation efficiency to systematic changes in the modal density of the acoustic volume was also investigated. It was concluded that when the modal overlap is high (i.e., the modal density of the acoustic volume is high) these changes have no influence on the sensitivity of prediction.

The study of the cumulative probability distribution of the radiation efficiency supported the conclusions which have been obtained from the analyses of previous coupled systems that the distribution approaches normality at high modal overlap.

The energy ratio of two coupled plates was the quantity of interest in the experimental investigations presented in Chapter 7. This quantity was selected, rather than the power flow between the coupled plates, because of the practical difficulties associated with the measurements of the latter quantity. Results for the mean and the normalized variance of energy ratio were obtained across the ensemble of coupled plates systems, and in different frequency bands. The ensemble of systems was generated by perturbing the dynamics of the coupled system. Similar conclusions to those obtained from previous cases were drawn. Results for the normalized power flow and the coupling loss factor of the coupled plates system were infered from the measured values of energy ratio by using SEA relationship. Peculiar results for the means, the variances and the cumulative probability distributions of energy ratio, normalized power flow and coupling loss factor were reported in the 1/3 octave frequency band centred at 630 Hz. Relatively small values for the mean and the normalized variance were reported in comparison with those obtained at the adjacent frequency bands which contain almost the same number of modes. Surprisingly, the cumulative probability distributions in this particular band has almost the shape of normal distribution unlike the distributions at the adjacent bands which had similar average modal overlap. The reason for the low mean value was attributed to the relatively low response of the wooden frame, surrounding the plates, at this particular frequency band. No explanation has been found for the low variance and for the normal distribution of energy ratio in this frequency band because of the lack of time needed to do further tests.

8.1 Recommendations for Future Work

As the present work has been generally concerned with the study of the uncertainty that originates from the variations of the geometry of coupled systems, it is recommended that the area of uncertainty which originates from the definition and the

modelling of the different boundary conditions of the coupled systems need to be considered in detail. Also it is important to try to develop and study an analytical formula for the variance of the response of coupled systems as the present investigations are based on numerical calculations. The other area of research recommended for further work is the investigation of power flow between multiply connected subsystems with parallel paths as the present work is concentrated on serially connected subystems.

REFERENCES

1. R. H. Lyon, G. Maidanik 1962 *The Journal of the Acoustical Society of America* **34**, 623-639. Power flow between linearly coupled oscillators.

2. T. D. Scharton, R. H. Lyon 1968 *The Journal of the Acoustical Society of America* **77**, 1332-1342. Power flow and energy sharing in random vibration.

3. M. P. Kakar 1969 *Proceedings of the British Acoustical Society Meeting "Sonically induced vibration of structures"*. Power flow between linearly coupled oscillators.

4. J. Woodhouse 1981 *The Journal of the Acoustical Society of America* **69**, 1695-1709. An approach to the theoretical background of statistical energy analysis applied to structural vibration.

5. D. E. Newland 1966 *Journal of Sound and Vibration* **3**, 262-276. Calculation of power flow between coupled oscillators.

6. D. E. Newland 1968 *The Journal of the Acoustical Society of America* **43**, 553-559. Power flow between a class of coupled oscillators.

7. F. J. Fahy 1970 *Ph.D Thesis, The University of Southampton.* Acoustically induced vibration of containing structures.

8. R. H. Lyon, E. Eichler 1964 *The Journal of the Acoustical Society of America* **36**, 1344-1354. Random vibration of connected structures.

9. R. H. Lyon, T. D. Scharton 1965 *The Journal of the Acoustical Society of America* **31**, 253-261. Vibrational energy transmission in a three element structure.

10. R. G. White, J. G. Walker 1982 *Ellis Horwood Publishers* . Noise and vibration. Chapter 7 by F. J. Fahy. Statistical Energy Analysis.

11. R. H. Lyon 1975 *Cambridge, MA: MIT press* . Statistical Energy Analysis of dynamical systems: Theory and applications.

12. F. J. Fahy 1974 *The Shock and Vibration Digest* **6**, 14-33. Statistical Energy Analysis: A critical review.

13. C. H. Hodges, J. Woodhouse 1986 *Reports on Progress in Physics* 49, 107-170. Theories of noise and vibration transmission in complex structures.

14. H. G. Davis 1972 *The Journal of the Acoustical Society of America* **51**, 387-392. Exact solutions for the response of some coupled multimodal systems.

15. H. G. Davis 1972 *The Journal of the Acoustical Society of America* **51**, 393-401. Power flow between coupled beams.

16. H. G. Davis 1977 *The Journal of Applied Mechanics* **54**, 507-514. Random vibration of distributed systems strongly coupled at discrete points.

17. H. G. Davis, M. A. Wahab 1981 *Journal of Sound and Vibration* **77**, 311-321. Ensemble averages of power flow in randomly excited coupled beams.

18. H. G. Davis, S. I. Khandoker 1982 *Journal of Sound and Vibration* **84,** 557-562. Random point excitation of coupled beams.

19. P. J. Remington, J. E. Manning 1975 *The Journal of the Acoustical Society of America* **57**, 374-379. Comparison of SEA power flow predictions with an "exact" analysis.

20. D. A. Bies, S. Hamid 1980 *Journal of Sound and Vibration* **70**, 187-204. *In situ* determination of loss factor and coupling loss factor by the power injection method.

21. J. L. Guyader, C. Boisson, C. Lesueur 1982 *Journal of Sound and Vibration* **81**, 81-92. Energy transmission in finite coupled plates, Part I: Theory.

22. C. Boisson, J. L. Guyader, P. Millot, C. Lesueur 1985 *Acustica* **58**, 223-233. Etude numérique de la transmission d'énergie vibratoire entre structures assemblées: cas d'assemblages en L, T et +.

23. A. J. Keane, W. G. Price. 1987 *Journal of Sound and Vibration* **117**, 363-386. Statistical Energy Analysis of strongly coupled systems.

24. E. K. Dimitriadis, A. D. Pierce. 1988 *Journal of Sound and Vibration* **123**, 397-412. Analytical solution for the power exchange between strongly coupled plates under random excitation: A test of statistical energy analysis concept.

25. J. C. Sun, N. Lalor, E. J. Richards 1987 *Journal of Sound and Vibration* **112**, 321-330. Power flow and energy balance of non-conservatively coupled structures, I: Theory.

26. J. C. Sun, L. C. Chow, N. Lalor, E. J. Richards 1987 *Journal of Sound and Vibration* **112**, 331-343. Power flow and energy balance of non-conservatively coupled structures, II: Experimental verification of theory.

27. F. J. Fahy, D. Y. Yao 1987 *Journal of Sound and Vibration* **114**, 1-11. Power flow between non-conservatively coupled oscillators.

28. J. C. Sun, N. L. Ming 1988 *Proceedings of Inter-Noise 88*, 323-326. Distributive relationships of dissipated energy by coupling damping in non-conservatively coupled structures.

29. G. Maidanik 1962 *The Journal of the Acoustical Society of America* **34**, 809-826. Response of ribbed panels to reverberant acoustic field.

30. F. J. Fahy 1969 *Journal of Sound and Vibration* **10**, 490-512. Vibration of containing structures by sound in the contained fluid.

31. F. J. Fahy 1970 *Journal of Sound and Vibration* **13**, 171-194. Response of a cylinder to random sound in contained fluid.

32. W. E. Boyce, B. E. Goodwin 1964 *Journal of the Society of Industrial Mathematics* **12**, 613-629. Random transverse vibrations of elastic beams.

33. P. H. Prasthofer, C. W. Beadle 1975 *Journal of Sound and Vibration* **42**, 477-493. Dynamic response of structures with statistical uncertainties in their stiffness.

34. R. A. Ibrahim 1987 *Applied Mechanical Review* **40**, 309-328. Structural dynamics with parameter uncertainties.

35. L. Cremer, M. Heckl, E. Ungar 1973 *Springer-Verlag*. Structure-Borne Sound.

36. B. M. Gibbs, C. L. S. Gilford 1976 *Journal of Sound and Vibration* **49**, 267-286. The use of power flow methods for the assessment of sound transmission in building structures.

37. F04ADF, F04, 1977 *Nag Fortran Library Routine Document:* 1172/367, MK5.

38. D01AKF, D01 1981 *Nag Fortran Library Routine Document:* 1796/0, MK8.

39. P. W. Smith, R. H. Lyon 1965 *NASA CR-160*. Sound and structural vibration.

40. E. E. Ungar 1964 *McGraw-Hill*. Mechanical vibrations, Mechanical design and system handbook.Sound.

41. M. J. Crocker, A.J. Price 1969 *Journal of Sound and Vibration* **9**, 469-486. Sound transmission using statistical energy analysis.

42. M. R. Schroeder, K. H. Kuttruf 1962 *The Journal of the Acoustical Society of America* **34,** 76-80. On frequency response curves in rooms. Comparison of experimental, theoretical and Monte Carlo results for average frequency spacing between maxima.

43. N. Dimitris, P. E. Chorafas 1960 *D. Van Nostrand Co. Inc.* Statistical processes and reliability engineering.

44. G05DDF, G05, D01 1977 *Nag Fortran Library Routine Document:* 1451/0, MK5.

45. T. A. Ryan, B. L. Joiner, B. F. Ryan 1976 *Duxbury Press Boston.* Minitab Student Handbook.

46. G. R. Khabbaz 1970 *The Journal of the Acoustical Society of America* **47**, 392-393. Comparison of mechanical coupling factor by two methods.

47. S. H. Crandall, R. Lotz 1971 *The Journal of the Acoustical Society of America* **49**, 352-356. On the coupling loss factor in statistical energy analysis.

48. P. W. Smith 1979 *The Journal of the Acoustical Society of America* **65**, 695-698. Statistical models of coupled systems and the transition from weak to strong coupling.

49. C. Chatfield 1983 *Chapman and Hill.* Statistics for technology.

50. N. Pinder 1986 *ISVR Technical Report 16.* Experimental work associated with acoustic design manual for statistical energy analysis.

51. M. Heckl 1962 *The Journal of the Acoustical Society of America* **34**, 803-808. Measurement of absorption coefficient in plates.

52. S. M. Stearn 1970 *Ph.D Thesis, The University of Southampton.* Stress distributions in randomly excited structures.

53. R. H. Lyon 1969 *The Journal of the Acoustical Society of America* **45**, 545-558. Statistical analysis of power injection and response in structures and rooms.

54. F. J. Fahy 1970 *Journal of Sound and Vibration* **11**, 481-483. Letter to the Editor. Energy flow between oscillators: special case of point excitation.

55. F. J. Fahy 1970 *Journal of Sound and Vibration* **9**, 506-508. Reply to the letter to the editor. Damping in plates by M. J. Crocker and A. J. Price.

56. F. J. Fahy, R. Pierri 1977 *The Journal of the Acoustical Society of America* **62**, 1297-1298. Application of cross spectral density to measurements of vibrational power flow between connected plates.

57. R. H. Kurzwell, E. E. Ungar 1984 *Air Flight Dynamic Laboratory Report AFWAL-TR-83-3125.* Preliminary evaluation of waveguide vibration absorbers.

58. C. H. Hodges, J. Woodhouse 1989 *Journal of Sound and Vibration* **130**, 237-251. Confinement of vibration by one-dimensional disorder, I: Theory of ensemble averaging.

59. C. H. Hodges, J. Woodhouse 1989 *Journal of Sound and Vibration* **130**, 253-268. Confinement of vibration by one-dimensional disorder, II: a numerical experiment on different ensemble averages.

60. K. Tamm, O. Weis 1959 *Acustica* **9**, 275-288. Untersuchungen uber periodische wellen, exponentielle und komplexe nahfelder im begrenzten festkorper.

61. T. D. Scharton 1971 *The Journal of the Acoustical Society of America* **50**, 373-381. Frequency-averaged power flow into one-dimensional acoustic system.

List of illustrations

Figure

2.17 The normalized variance of the normalized power flow, between a long and a short coupled beams, against modal overlap factor of the long beam.

2.18 Cumulative distribution function of the coupling loss factor, of the long-short coupled beams system, at different modal overlap conditions for the long beam.

2.19 Cumulative distribution function of the normalized power flow, between a long and a short coupled beams, at different modal overlap values for the long beam.

2.20 Cumulative distribution function of the normalized power flow, between two, long coupled, at different average modal overlap conditions. Samples are generated from the perturbations of the stiffness of the coupling element.

****

3.1.a Coupled beams system

3.1.b Test rig

3.1.c The coupling element

3.2 The real part of the driving point transfer function, between a force and a velocity, of uncoupled beam, L = 3.4 m, η = 0.015.

3.3. The real part of the driving point transfer function and the coherence function, between a force and a velocity, of coupled beams system, L_1 = 3.42 m, L_2 = 3.22 m, $\eta_1 = \eta_2 = 0.03$.

3.4. The instrumentation.

3.5 A typical resonant mode of an uncoupled beam having natural frequency of 280 Hz.

3.6 A typical real part of a cross power spectrum, between a force and a velocity at the driving point of the coupled beams system.

3.7 The real part and the imaginary part of the cross spectrum between the displacement of the directly driven beam and the velocity of the receiver beam at the coupling point. $\eta_1 = \eta_2 = 0.09$, L_2 = 3.3.

3.8 Auto power spectra of the velocities of the coupled beams. $\eta_1 = \eta_2 = 0.055$, L_2 = 3.05 m. Top: driven beam, bottom: receiver beam.

3.9 Auto power spectra of the velocities of the coupled beams. $\eta_1 = \eta_2 = 0.09$, L_2 = 3.3 m. Top: driven beam, bottom: receiver beam.

3.10 The experimentally determined mean value and the 95 per cent confidence interval for the mean of coupling loss factor, of two coupled beams system, against average modal overlap factor of the coupled system.

3.11 The mean value and the 95 per cent confidence intervals for the measured mean of normalized power flow ($\bar{P}_{12}/\bar{P}_{in}$), between two coupled beams system, against average modal overlap factor of the coupled system.

3.12 The normalized variance of the experimentally determined coupling loss factor, of two coupled beams system, against average modal overlap factor of the coupled system.

3.13 The normalized variance of the measured normalized power flow, between two coupled beams system, against average modal overlap factor of the coupled system.

3.14 Cumulative distribution function of the coupling loss factor, estimated from the measurements on two coupled beams system, at different average modal overlap conditions.

3.15 A comparison between the measured and the calculated spectra of input power to a two, short coupled beams system.

3.16 A comparison between the measured and the calculated spectra of power flow of a two, short coupled beams system.

3.17 A comparison between the measured and the calculated spectra of the directly driven beam's total energy of a two short coupled beams system.

3.18 A comparison between the measured and the calculated spectra of the receiver beam's total energy of a two short coupled beams system.

****

4.1 Two coupled plates system

4.2 The spectrum of input power to a two, large coupled plates system.

4.3 Shear forces and moments acting on a plate element.

4.4 The spectrum of power flow between two, large coupled plates.

4.5.a The spectrum of the total energy of the directly driven plate of the two coupled plates system.

4.5.b The spectrum of the total energy of the receiver plate of the two coupled plates system.

4.6 Wave number diagram of a simply supported plate in flexure.

4.7 Semi-infinite coupled plates system.

4.8 The estimate of coupling loss factor (diffuse field estimate) of an infinite coupled plates system, against frequency.

4.9 The mean value and the 95 per cent confidence intervals for the mean of coupling loss factor, of two coupled plates system, against average modal overlap factor of the coupled system.

4.10 The mean value and the 95 per cent confidence intervals for the mean of normalized power flow (P_{12}/P_{in}), between two coupled plates system, against average modal overlap factor of the coupled system.

4.10.a Modal energy ratio of two coupled plates against average modal overlap factor.

4.11 The normalized variance of the coupling loss factor, of two coupled plates system, against average modal overlap factor of the coupled system.

4.12 The normalized variance of the normalized power flow, between two coupled plates system, against average modal overlap factor of the coupled system.

4.13 Cumulative distribution function of the coupling loss factor, of the two, coupled plates system, at different average modal overlap conditions.

4.14 Cumulative distribution function of the normalized power flow, between two coupled beams system, at different average modal overlap conditions.

4.15 The selected locations for the excitation of the coupled plates system.

4.16 The spatial distribution of the modulus of the nearfield amplitude (located near the coupling line) along lines parallel to the x-axis of the driven plate. The force is located at $x = x_0 = 1.6$ m, Y_0 denotes the position of the force along y-axis. $x = 0$ is the position of the coupling line

4.17 The mean value and the 95 per cent confidence intervals for the mean of coupling loss factor, of two coupled plates system, against average modal overlap factor of the coupled system. The results are obtained due to a single point of excitation located at $x = x_0 = 0.3$ m and $y = y_0 = 0.6$ m.

4.18 The normalized variance of the coupling loss factor, of two coupled plates system, against average modal overlap factor of the coupled system. The results are obtained due to the single point of excitation mentioned in. (4.18) above.

4.19 The effect of the position of the applied force on the mean value of the coupling loss factor of the coupled plates system. The results are obtained due to the excitation of the system at points which are located along a line parallel to the x-axis, $y_0 = 0.45$ m.

4.20 The effect of the position of the applied force on the mean value of the coupling loss factor of the coupled plates system. The results are obtained due to the excitation of the system at points which are located along a line parallel to the y-axis, $x_0 = 0.4$ m.

4.21-4.25 The spectrum of input power to the coupled plates system in different frequency bands.

4.26 The effect of the number of coupled modes of a two-plate system on the mean value of the coupling loss factor.

4.27 The effect of the number of coupled modes of a two-plate system on the normalized variance of the coupling loss factor.

4.28 An empirical relationship between the normalized variance of coupling loss factor, the number of coupled modes and the average modal overlap factor of two coupled plates system.

4.29 A comparison between pure tone and frequency band results of the normalized variance of power flow between two coupled plates.

4.30 Three coupled plates system.

4.31 The mean value and the 95 per cent confidence intervals for the mean of coupling loss factor (η_{12}), of the coupled plates 1 and 2 in a three coupled plates system, against average modal overlap factor of the coupled system.

4.32 The mean value and the 95 per cent confidence intervals for the mean of coupling loss factor (η_{23}), of the coupled plates 2 and 3 in a three coupled plates system, against average modal overlap factor of the coupled system.

4.33 A comparison between the mean values of coupling loss factors η_{12} and η_{23} of three coupled plates system.

4.34 The normalized variances of the coupling loss factors η_{12} and η_{23}, of three coupled plates system, against average modal overlap factor of the coupled system.

4.35 The mean values of normalized power flow $\bar{P}_{12}/\bar{P}_{in}$ and $\bar{P}_{23}/\bar{P}_{in}$, between three coupled plates, against average modal overlap factor of the coupled system.

4.36 The normalized variances of the normalized power flow $\bar{P}_{12}/\bar{P}_{in}$ and $\bar{P}_{23}/\bar{P}_{in}$, between three coupled plates, against average modal overlap factor of the coupled system.

4.37 Cumulative distribution function of the coupling loss factor (η_{12}), of the coupled plates 1 and 2 in a three coupled plates system, at different average modal overlap conditions.

4.38 Cumulative distribution function of the normalized power flow ($\bar{P}_{12}/\bar{P}_{in}$), between the coupled plates 1 and 2 in a three coupled plates system, at different average modal overlap conditions.

****

5.1. Coupled rods system. $S_2/S_1 = 6$ (S is a cross section area).

5.2 Semi-infinite coupled rods system.

5.3 Input power spectrum in a 1/3 octave band centred at 5000 Hz. Force is applied on rod 1. $L_2/L_1 = 0.65$, $\eta_1 = \eta_2 = 0.001$, $M_{av} = \sqrt{M_1 M_2} = 0.008$

5.4 Do. $M_{av} = 0.08$

5.5 Do. $M_{av} = 0.4$

5.6 Do. $M_{av} = 1.6$

5.7 Do. $M_{av} = 3.2$

5.8 Power flow spectrum, $L_2/L_1 = 0.65$, $\eta_1 = \eta_2 = 0.001$, $M_{av} = \sqrt{M_1 M_2} = 0.008$

5.9 Do. $M_{av} = 0.08$

5.10 Do. $M_{av} = 0.4$

5.11 Do. $M_{av} = 1.6$

5.12 Do. $M_{av} = 3.2$

5.13 Band results of injected power (P_{in}) to coupled rods system against average modal overlap factor (M_{av}). $L_2/L_1 = 0.65$, $\eta_1 = \eta_2 = 0.001$.

5.14 Band results of the normalized power flow ($\bar{P}_{12}/\bar{P}_{in}$) between coupled rods against average modal overlap factor (M_{av}). $L_2/L_1 = 0.65$, $\eta_1 = \eta_2 = 0.001$.

5.15 Coupling loss factor of coupled rods system against average modal overlap factor (M_{av}). $L_2/L_1 = 0.65$, $\eta_1 = \eta_2 = 0.001$.

5.16 Normalized power flow ($\bar{P}_{12}/|V_1|^2$) and the real parts of the impedances of the uncoupled rods. $L_2/L_1 = 0.65$, $\eta_1 = \eta_2 = 0.001$, $M_{av} = \sqrt{M_1 M_2} = 0.008$

5.17 Normalized power flow ($\bar{P}_{12}/|V_1|^2$) and the moduli of the imaginary parts of the uncoupled rods. $L_2/L_1 = 0.65$, $\eta_1 = \eta_2 = 0.001$, $M_{av} = \sqrt{M_1 M_2} = 0.008$.

5.18 The imaginary part of the driving point impedance (I_o) of the coupled rods system. $L_2/L_1 = 0.65$, $\eta_1 = \eta_2 = 0.001$, $M_{av} = \sqrt{M_1 M_2} = 0.008$

5.19 Normalized power flow ($\bar{P}_{12}/|V_1|^2$) and the moduli of the imaginary parts of the uncoupled rods. $L_2/L_1 = 0.64$, $\eta_1 = \eta_2 = 0.001$, $M_{av} = \sqrt{M_1 M_2} = 0.008$.

5.20. Band results of normalized power flow ($\bar{P}_{12}/\bar{P}_{in}$) between a short and a long coupled rods against the the modal overlap factor of the long (undriven) rod (M_2). $M_1 = 0.01$, $\eta_1 = \eta_2 = 0.001$.

5.21 Coupling loss factor of short-long rods system against modal overlap of the long rod (M_2).

5.22-26 The spectrum of normalized power flow ($\bar{P}_{12}/\bar{P}_{in}$) between short and long rods for different M_2 values and a fixed M_1 value of 0.01.

5.27-29 A comparison between the specra of the real parts (R_1, R_2) of the impedances of the uncoupled rods and that of the driving point coupled system (R_o) for differen M_2 values and a fixed M_1 value of 0.01.

5.30-32 A comparison between the specra of the imaginary parts (I_1, I_2) of the impedances of the uncoupled rods and that of the driving point coupled system (I_o) for different M_2 values and a fixed M_1 value of 0.01.

5.33 The frequency-integral of the real part of the impedance of the receiver rod of the short-long rods system, against modal overlap factor (M_2).

****

6.1 Panel-Box system

6.2-8 The population of radiation efficiency (1/3 octave frequency band averages) of the simply supported panel in a Panel-Box system, obtained for a sample of panel thickness values and for a given value of the sum of half power bandwidths of the acoustic and structural modes ($\beta_r + \beta_m$).

6.9 The number of acousto-structural mode pairs, of the Panel-Box system, against the parameter ($\beta_r + \beta_m$) in a 1/3 octave frequency band centred at 5000 Hz and for different box depth values.

6.10 The modal densities of a 3 mm simply supported plate and an acoustic cavity (of different depth values).

6.11 The normalized variance of the radiation efficiency of the panel against the centre frequency of the 1/3 octave frequency band for different ($\beta_r + \beta_m$) values.

6.12 The normalized variance of the radiation efficiency of the panel against the value of ($\beta_r + \beta_m$) in different 1/3 octave frequency bands.

6.13-16 The radiation efficiency of a 3 mm panel for three different values of box depth and a given value of ($\beta_r + \beta_m$).

6.17 Cumulative distribution function of the radiation efficiency of the panel at different average modal overlap conditions, in a 1/3 octave frequency band centred at 4000 Hz.

6.18 Cumulative distribution function of the radiation efficiency of the panel for different ($\beta_r+\beta_m$) values, in a 1/3 octave frequency band centred at 5000 Hz.

****

7.1 Test rig

7.2 Experimental set-up

7.3 Experimental set up for the measurement of the input power to the plate.

7.4-7.6 Typical auto spectra of the plate velocity in different frequency bands.

7.7 The transfer function and the coherence function between the force signal and the velocity signal at the driving point of the plates in the frequency range 3000-5000 Hz.

7.8 The real part of cross power spectra and the coherence function between the force signal and the velocity signal at the driving point of the plate.

7.9 The imaginary part of cross power spectra and the coherence function between force and velocity at the driving point of the plate.

7.10 The transfer function and the coherence function between the force signal and the velocity signal at the driving point of the plate in the frequency range 250-750 Hz.

7.11 The transfer function and the coherence function between the force signal and the velocity signal at the driving point of the plate in the frequency range 350-450 Hz.

7.12 Cumulative distribution function of the measured energy ratio of two coupled plates in different frequency bands.

7.13 Cumulative distribution function of the normalized power flow, between two coupled plates, in different frequency bands.

7.14 Cumulative distribution function of the coupling loss factor, of two coupled plates, in different frequency bands.

7.15 Auto power spectra of two acceleration signals in the frequency range 0-2000 Hz. Top : input signal, bottom: output acquired on the supporting wooden frame surrounding the coupled plates.

APPENDIX I

GENERAL PROCEDURE OF SEA MODELLING

Complex dynamical systems can be modelled as a number of connected, simple subsystems. Each subsystem may be modelled as a set of interacting simple oscillators (natural modes) and hence the coupled structures can be represented and analyzed as interacting sets of oscillators. Therefore the analysis of vibration of coupled oscillators is of fundamental importance in SEA.

Consider the two coupled subsystems shown schematically in the figure below.

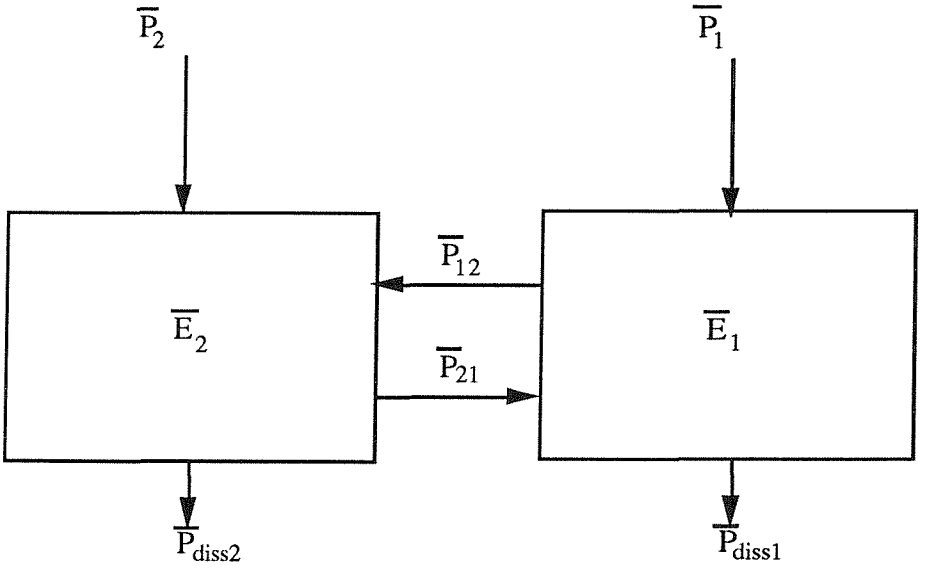

The time-average power inputs $\overline{P}_1$ and $\overline{P}_2$ are those produced by the external random forces on subsystems 1 and 2 respectively. The energy losses of one subsystem may result from various mechanisms, such as internal dissipation, friction at the boundaries or acoustic radiation. It is assumed that the coupling mechanisms are lossless, i.e.,

conservative. The energy balance equations of the two coupled components may be described by

$$\bar{P}_1 = \bar{P}_{diss1} + \bar{P}_{12} - \bar{P}_{21}, \qquad \text{(I.1.a)}$$

and

$$\bar{P}_2 = \bar{P}_{diss2} + \bar{P}_{21} - \bar{P}_{12}, \qquad \text{(I.1.b)}$$

where $\bar{P}_{diss1}$ and $\bar{P}_{diss2}$ are the time averaged rate of energy dissipations by subsystems 1 and 2 respectively, and $(\bar{P}_{12} - \bar{P}_{21})$ represents the net time averaged power flow between subsystems 1 and 2. It may be assumed that the power dissipated in one subsystem is proportional to the total stored vibrational energy of that subsystem i.e.

$$\bar{P}_{diss1} = \omega_c \eta_1 \bar{E}_1 \ , \qquad \text{(I.2.a)}$$

and

$$\bar{P}_{diss2} = \omega_c \eta_2 \bar{E}_2 \ , \qquad \text{(I.2.b)}$$

where ω_c is the centre frequency of the band of interest and η_1 and η_2 are the average modal dissipation loss factors of the subsystems 1 and 2 respectively. $\bar{E}_1$ and $\bar{E}_2$ represent the total stored energies of the subsystems. By analogy with the exact result for two coupled oscillators, the SEA *hypothesis* assumes that the power flows $\bar{P}_{12}$ and $\bar{P}_{21}$ are also proportional to the stored energies of the subsystems, i.e.,

$$\bar{P}_{12} = \omega_c \eta_{12} \bar{E}_1 \ , \qquad \text{(I.3.a)}$$

$$\bar{P}_{21} = \omega_c \eta_{21} \bar{E}_2 \ , \qquad \text{(I.3.b)}$$

where η_{12} and η_{21} are defined as the coupling loss factors. As indicated below, this is not an entirely satisfactory assumption because power transfer from one subsystem to another

occurs only at the connections and would be more reasonably expected to be proportional to subsystem energy *density* and not to the total energy. Equations (I.1.a) and (I.1.b) are then written as

$$\bar{P}_1 = \omega_c \left[\eta_1 \bar{E}_1 + \eta_{12} \bar{E}_1 - \eta_{21} \bar{E}_2\right] , \qquad \text{(I.4.a)}$$

and

$$\bar{P}_2 = \omega_c \left[\eta_2 \bar{E}_2 + \eta_{21} \bar{E}_2 - \eta_{12} \bar{E}_2\right]. \qquad \text{(I.4.b)}$$

This is an *ad hoc* extension of the exact relationship which holds for two conservatively coupled oscillators [1], namely that the energy flow between each oscillator of one subsystem and each oscillator of a coupled subsystem are independent of all other oscillators energies. The power flow between oscillator i of subsystem 1 and oscillator j of subsystem 2 may be written as

$$\bar{P}_{ij} = \omega_c \left[\eta_{ij}\bar{U}_i - \eta_{ji}\bar{U}_j\right] . \qquad \text{(I.5)}$$

Where $\bar{U}_i$ and $\bar{U}_j$ are the total stored energies of the oscillators. In this case of an 'isolated' oscillator pair, $\eta_{ij} = \eta_{ji}$ therefore

$$\bar{P}_{ij} = \omega_c \eta_{ij}\left[\bar{U}_i - \bar{U}_j\right] . \qquad \text{(I.6)}$$

If it is assumed that there are N_1 oscillators in subsystem 1 and N_2 oscillators in subsystem 2 and further that the energies of the oscillators in each subsystem are equal (i.e., equipartition of modal energy is satisfied within each subsystem), the net power flow from subsystem 1 to subsystem 2 may be written as

$$(\bar{P}_{12})_{net} = \omega_c \left[\frac{\bar{E}_1}{N_1} - \frac{\bar{E}_2}{N_2}\right] \sum_{i}^{N_1} \sum_{j}^{N_2} \eta_{ij} , \qquad \text{(I.7)}$$

where $\frac{\bar{E}_1}{N_1}$ and $\frac{\bar{E}_2}{N_2}$ are termed the average modal energies of subsystem 1 and 2 respectively and are proportional to the energy densities. By comparing equation (I.7) with equations (I.3.a) and (I.3.b), we may write

$$\eta_{12} = \frac{1}{N_1} \sum_{i}^{N_1} \sum_{j}^{N_2} \eta_{ij} \ , \qquad \text{(I.8)}$$

$$\eta_{21} = \frac{1}{N_2} \sum_{i}^{N_1} \sum_{j}^{N_2} \eta_{ij} \ . \qquad \text{(I.9)}$$

These are termed the 'modal average coupling loss factors' thus,

$$N_1\eta_{12} = N_1\eta_{12} \ . \qquad \text{(I.10)}$$

This is known as the reciprocity relation. Normally it is written in terms of the asymptotic modal densities (n_1 and n_2) of the subsystems as

$$n_1\eta_{12} = n_2\eta_{12} \ , \qquad \text{(I.11)}$$

where

$$n_1(\omega) = N_1/\Delta\omega$$

$$n_2(\omega) = N_2/\Delta\omega \ .$$

APPENDIX II

MODAL DENSITIES OF SOME UNIFORM SYSTEMS

System	Motion	Modal density, $n(\omega)$	Auxiliaryexpressions
Beam, Rod	Longitudinal	$L/\pi C_l$	$C_L = \sqrt{\frac{Y}{\rho}}$
Beam	Flexure	$(L/2\pi)\ (\omega\Gamma_b C_l)^{-1/2}$	$\Gamma_b C_L = \sqrt{\frac{YI}{\rho A}}$
Plate	Flexure	$A_s/(4\pi\Gamma_p C_l)$	$\Gamma_p C_L = \sqrt{\frac{B}{\rho h}}$
String	Lateral	$L/\pi C_s$	$C_s = \sqrt{\frac{T}{\rho A}}$
Shaft	Torsion	$L/\pi C_t$	$C_T = \sqrt{\frac{GK}{\rho J}}$

Membrane	Lateral	$A_s\omega/2\pi C_m^2$	$C_m = \sqrt{\frac{S}{\rho h}}$
Acoustic volume	Sound	$\frac{V\omega^2}{2\pi^2 C_o^3} + \frac{A_s\,\omega}{4\pi C_o^2}$	

DEFINITIONS FOR THE TABLE

A	Cross secion area
A_s	Surface area
C_o	Acoustic wave speed
C_l	Longitudinal wave speed
C_m	Membrane wave speed
C_s	String wave speed
C_t	Torsional wave speed
B	Plate rigidity
Y	Young's modulus
h	Thickness
I	Second moment of area of cross section
J	Polar moment of area of cross section
L	Length
S	Membrane tension force/unit edge length
T	String tension force
V	Volume
Γ_b	Radius of gyration of beam cross section
Γ_p	Radius of gyration of plate cross section
ω	Frequency in radians/second
ρ	material density

APPENDIX III

THE NORMAL DISTRIBUTIOM

The normal distribution or "Gaussian distribution" is a continuous distribution whose characterstics are often found in practice. It is some times called the bell-shaped distribution. The expression describing the frequency function of this distribution is written as [49]

$$f(x) = \frac{1}{\sigma\sqrt{2\pi}} \mathrm{Exp}\left\{ - \frac{(x-\mu)^2}{2\sigma^2} \right\} \quad , \qquad -\infty < x < +\infty \quad \text{(III.1)}$$

where μ and σ are the mean and the standard deviation respectively such that

$$-\infty < \mu < +\infty \ ,$$

and

$$\sigma > 0 \ .$$

The graphs of $y = f(x)$ defined by the above equation are that all are bell-shaped and symmetrical and die out quickly at the tails. A graph of the normal curve is given in the figure below.

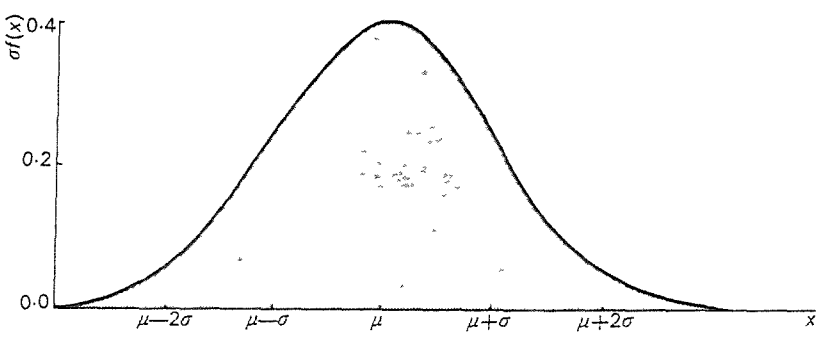

The probability density function is negligible for values of x which are more than 3σ away from μ. It can be shown that

$$\int_{-\infty}^{\infty} f(x)\, dx = 1 \qquad \text{for all values of } \mu \text{ and } \sigma.$$

It can also be shown that

$$\text{mean} = \int_{-\infty}^{\infty} x\, f(x)\, dx = \mu \ ,$$

$$\text{Variance} = \int_{-\infty}^{\infty} (x-\mu)^2 f(x)\, dx = \sigma^2 \ .$$

The cumulative distribution function can be defined as the integral of p.d.f which gives the probability of obtaining a value for a random variable X which is less than or equal to a given value x, i.e.,

$$F(x) = \text{probability } (X \leq x)$$

$$= \int_{-\infty}^{x} \frac{1}{\sigma\sqrt{2\pi}} \text{Exp}\left\{ -\frac{(u-\mu)^2}{2\sigma^2} \right\} du \qquad \text{(III.2)}$$

The cumulative distribution function with zero mean and standard deviation of 1.0 can be obtained from the standard statistical tables. This particular normal distribution is often called the standard normal distribution. The c.d.f of any other

normal distribution can also be obtained from the standard tables by making the transformation

$$Z = \frac{X-\mu}{\sigma}$$

where the random variable X has mean μ and standard deviation σ. Therefore, the standardized variable Z has zero mean and standard deviation of 1.0, as required.

For a particular value x, of X, the corresponding value of the standarized variable is given by

$$z = \frac{x-\mu}{\sigma} \quad , \qquad \text{(III.3)}$$

where z is the number of standard deviations by which x departs from μ. Some particular useful values of the cumulative distribution function F(z) is given below

z	0	1	2	2.5	3.0
F(z)	0.5	0.84	0.977	0.994	0.9987

III.a Student *t* distribution

Suppose x_i, i = 1, 2, 3, ..., n is a random sample of n observations from a poulation whose mean is μ and whose variance is σ^2. If the population is normal then the distribution of $\bar{x}$ is $N(\mu,\sigma^2/n)$. If σ^2 is unknown it can be estimated from s^2, the variance of the sample. The distribution of $(\bar{x}-\mu)/(s/\sqrt{n})$ is approximately normal and the approximation improves as n increases. The exact distribution is called the *t* - distribution with n-1 degrees of freedom. Like the standard normal distribution it is symmetric with mean zero.

If $\bar{x}$ and s^2 are calculated from a sample size n, the $100(1-\alpha)$ per cent confidence interval of the true (population) mean is given by

$$\bar{x} \pm t\left(\frac{\alpha}{2}, n-1\right) \frac{s}{\sqrt{n}} \qquad \text{(III.4)}$$

where $t\left(\frac{\alpha}{2}, n-1\right)$ is the percentage point such that a proportion of $\frac{\alpha}{2}$ of the t -distribution with (n-1) degrees of freedom lies above it. These percentage points can be obtained from statistical tables.

APPENDIX IV

FORMULAE FOR POWER FLOW AND INPUT POWER FOR COUPLED RODS

Consider the coupled system shown in the figure below.

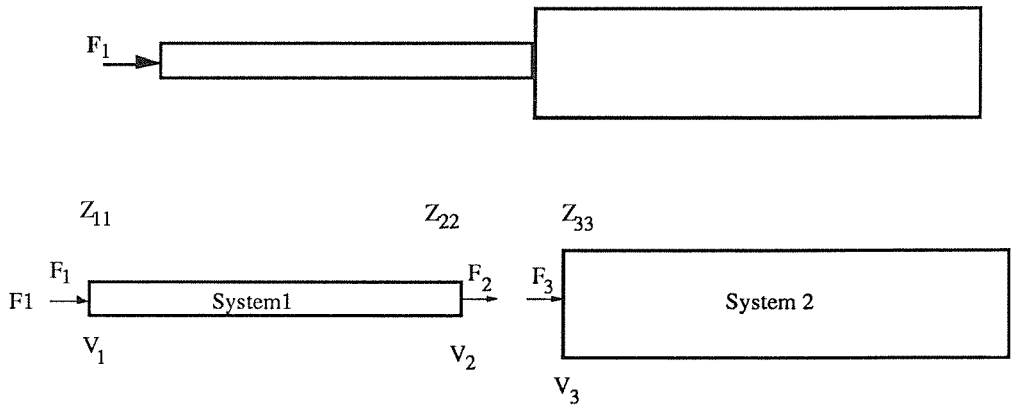

For system 1 the velocities V_1 and V_2 can be written as

$$V_1 = \frac{F_1}{Z_{11}} + \frac{F_2}{Z_{12}} \ , \qquad \text{(IV.1)}$$

and

$$V_2 = \frac{F_2}{Z_{22}} + \frac{F_1}{Z_{21}} \ , \qquad \text{(IV.2)}$$

where Z_{11}, Z_{12} and Z_{21} are the direct and the transfer impedances of the first system. Similarly, for the second system , the velocity V_3 is given by

$$V_3 = \frac{F_3}{Z_{33}} \quad , \qquad \text{(IV.3)}$$

where Z_{33} is the direct impedance of the second system at the coupling point. When the systems are coupled, the boundary conditions at the coupling point are

$$V_3 = V_2 \quad , \qquad \text{(IV.4)}$$

and

$$F_3 + F_2 = 0 \quad . \qquad \text{(IV.5)}$$

From equations (IV.3), (IV.4) and (IV.5), V_2 can be written as

$$V_2 = \frac{-F_2}{Z_{33}} \quad . \qquad \text{(IV.6)}$$

By the substitution of (IV.6) into (IV.2), then

$$\frac{-F_2}{Z_{33}} = \frac{F_1}{Z_{21}} + \frac{F_2}{Z_{22}} \quad . \qquad \text{(IV.7)}$$

By the substitution of (IV.7) into (IV.1), then

$$V_1 = \frac{F_1}{Z_{11}} - \frac{F_1 Z_{22}\, Z_{33}}{Z_{12} Z_{21} (Z_{22} + Z_{33})} \quad , \qquad \text{(IV.8)}$$

and

$$Z_o = \frac{F_1}{V_1} = \frac{1}{\frac{1}{Z_{11}} - \frac{Z_{22}\,Z_{33}}{Z_{12}Z_{21}(Z_{22}+Z_{33})}} \quad , \qquad \text{(IV.9)}$$

where Z_o is the driving point impedance of the coupled system. The force and the velocity at the coupling point can now be written as

$$F_3 = -F_2 = \frac{F_1}{Z_{21}(\frac{1}{Z_{22}}+\frac{1}{Z_{33}})} \quad , \qquad \text{(IV.10)}$$

and

$$V_3 = V_2 = \frac{F_1 Z_{22}}{Z_{21}(Z_{22}+Z_{33})} \quad . \qquad \text{(IV.11)}$$

The time averaged power flow between the coupled systems can be written as

$$\bar{P}_{12} = \frac{1}{2} |V_3|^2 \, \mathrm{Re}\{Z_{33}\} \quad .$$

The substitution for V_3 and Z_{33} produces the following expression for time averaged power flow

$$\bar{P}_{12} = \frac{1}{2} \left| \frac{F_1 Z_{22}}{Z_{21}(Z_{22}+Z_{33})} \right|^2 \mathrm{Re}\{Z_{33}\} \quad . \qquad \text{(IV.12)}$$

The time averaged input power can be written as

$$\bar{P}_{in} = \frac{1}{2} |V_1|^2 \, \mathrm{Re}\{Z_o\} \quad .$$

The substitution for V_1 and Z_0 from above gives,

$$\bar{P}_{in} = \frac{|F_1|^2}{2} \mathrm{Re}\left\{\frac{Z_{11}Z_{12}Z_{21}(Z_{22}+Z_{33})}{Z_{12}Z_{21}(Z_{22}+Z_{33})-(Z_{11}Z_{22}Z_{33})}\right\} \left|\frac{Z_{12}Z_{21}(Z_{22}+Z_{33})-(Z_{11}Z_{22}Z_{33})}{Z_{11}Z_{12}Z_{21}(Z_{22}+Z_{33})}\right|^2$$

(IV.13)